AN ABSTRACT OF THE THESIS OF

Yochanan Kushnir for the degree of Doctor of Philosophy in Atmospheric Sciences presented on 13 December 1984.

Title: Subseasonal Variability in a Two-Level Atmospheric General Circulation Model

Abstract approved: _____

Dr. Steven K. Esbensen

The dynamical processes which maintain atmospheric disturbances in regions of strong wintertime variability of the northern hemisphere are examined using data from a GCM simulation. Time series of the dependent variables and diabatic heating components from 10 Northern Hemisphere winters simulated by the Oregon State University two-level GCM are used. Variance and covariance analyses are performed to determine the geographical distribution of the intensities and transport properties of high-frequency (periods between 2.5 and 10 days) and low-frequency (periods between 10 days and a season) eddies. These are compared with existing observations and the discrepancies are discussed in terms of their dynamical consistency with the time-mean circulation.

The energetics of high-frequency and low-frequency eddies are studied. It is found that the behavior of high-frequency eddies is consistent with baroclinic instability theory. Low-frequency eddies appear to be maintained mainly by a high-latitude baroclinic energy cycle. Energy conversions characteristic of barotropic processes are also significant at jet-stream-latitudes. The process of wave-energy dispersion is found to be an important factor governing the geographical distribution of low-frequency activity at middle latitudes.

The nature of the systems causing low-frequency variability over the North Pacific Ocean is examined by applying complex EOF analysis to the time series of geopotential height anomalies. The first eigenmode of this analysis describes a wave of planetary scale extending

from northeastern Asia to the Gulf of Mexico across the North Pacific basin. While the phase of this wave retrogrades along the continental borders of the ocean basin, energy propagates in the opposite direction and penetrates as far as the central North Atlantic. The dynamical characteristics of this disturbance are examined by complex covariance analysis between the first mode's principal component and the dependent-variable fields. It is found that the disturbance grows mainly through baroclinic processes with some contribution from barotropic processes.

On the basis of these results it is proposed that the observed differences between the high- and low-frequency disturbances result from their being generated in different geographical regions where sphericity and the properties of the stationary flow cause baroclinic growth of structurally different modes.

Subseasonal Variability in a Two-Level Atmospheric General Circulation Model

by

Yochanan Kushnir

A THESIS

submitted to

Oregon State University

in partial fulfillment of

the requirements for the

degree of

Doctor of Philosophy

Completed December 13, 1984

Commencement June 1985

APPROVED:

Redacted for Privacy

Associate Professor of Atmospheric Sciences in charge of major

Redacted for Privacy

Chairman of the Department of Atmospheric Sciences

Redacted for Privacy

Dean of Graduate School

Date thesis is presented December 13, 1984

Typed by Naomi W. Zielinski for Yochanan Kushnir

To My Parents

ACKNOWLEDGEMENTS

It goes without saying that the road leading to the conclusion of a dissertation is long and tedious. This road however, could also turn into a significant experience, as it was in this case. This is mostly due to the guidance, teaching, support and friendship that were offered to me by my research advisor, Dr. Steven Esbensen, to whom I am grateful for all of these.

I would like to thank the help and support from the other members of my doctoral committee, Dr. Ronald Adams, Dr. Young-June Han, Dr. Clayton Paulson and Dr. Michael Schlesinger. In particular I would like to acknowledge the fruitful discussions with Drs. Han, Paulson and Schlesinger.

Thanks go to Dr. Lawrence Gates for his support and for making this study possible under the roof of the Climatic Research Institute at Oregon State University.

The permanent staff of the Climatic Research Institute, in particular Bob Mobley and Bill McKie, were extremely helpful and supportive in the performance of the computations and the graphics involved in this study. I also am sincerely indebted to the typing efforts of Naomi Zielinski and Michelle Holcomb who helped me meet all the deadlines involved.

Last but not least, I would like to thank my wife, Dina, and my daughters, Tamar and Hadas, for their love, patience and understanding during the long days in which my attention could not be with them.

The research upon which this thesis is based was supported by the National Science Foundation under grant ATM 8205992.

TABLE OF CONTENTS

CHAPTER 1: INTRODUCTION

CHAPTER 2: HISTORICAL REVIEW

2.1 Short time-scale fluctuations
2.2 Long time-scale fluctuations
2.3 GCMs as a medium for dynamical studies

CHAPTER 3: MODEL, DATA AND METHODOLOGY

3.1 The model
3.2 Data preparation
3.2.1 Interpolation to pressure levels
3.2.2 Filtering
3.3 Methodology of the diagnostics
3.4 The wintertime mean circulation

CHAPTER 4: STATISTICAL PROPERTIES OF GEOPOTENTIAL HEIGHT FLUCTUATIONS

4.1 Spatial distribution of time fluctuations
4.2 Horizontal structure of geopotential height fluctuations
4.3 Temporal properties of geopotential height fluctuations
4.4 Interpretation

CHAPTER 5: DYNAMICAL CHARACTERISTICS OF THE MODEL'S WINTERTIME VARIABILITY. PART A: SPATIAL DISTRIBUTION OF EDDY ACTIVITY AND TRANSPORTS

5.1 Intensity of time fluctuations of dynamical variables
5.2 Eddy transport properties
5.3 Recapitulation

CHAPTER 6: DYNAMICAL CHARACTERISTICS OF THE MODELS'S WINTERTIME VARIABILITY. PART B: EDDY ENERGETICS

6.1 Formulation of eddy energetics
6.2 The energy cycle of high-frequency eddies
6.3 Energetics of low-frequency eddies
6.4 A hemispheric view of eddy energetics

CHAPTER 7: THE LIFE CYCLE OF LOW-FREQUENCY DISTURBANCES . . . 115

7.1 Methodology of identifying and following low-frequency disturbances 115
7.2 The structure of the North Pacific low-frequency disturbances 129
7.3 The life cycle and maintenance of North Pacific low-frequency disturbances 139

CHAPTER 8: SUMMARY, CONCLUSIONS AND SUGGESTIONS FOR FURTHER RESEARCH 153

REFERENCES 158

APPENDICES 165

APPENDIX: EDDY ENERGY EQUATIONS 165

LIST OF FIGURES

Figure — Page No.

3.1. Surface elevation above sea level over the northern hemisphere as used in the model's boundary conditions. Contour interval: 500 m. 20

3.2. The power response curves of the three low-pass filters used in this study: (a) 2.5 day low-pass (half power frequency at 0.4 day^{-1}), (b) 10 day low-pass (half power frequency at 0.1 day^{-1}) and (c) 40 day low-pass (half power frequency at 0.025 day^{-1}). 24

3.3. (a) The simulated wintertime mean 400 mb geopotential height field. Contour interval: $.5x10^2$ m. This figure and those that follow in this chapter are based upon 2.5 day low-pass filtered data from ten simulated winters (Dec. through Feb.). (b) The observed 500 mb geopotential height field, from Blackmon (1976), Fig. 3b. Contour interval: 50 m. Here and in all other figures of model results the mapped area extends to the equator. Observations start at 20°N. 27

3.4. (a) The simulated wintertime mean 400 mb zonal wind component. Contour interval: 5 m s^{-1}; negative contours are dashed. (b) As in (a) but for observations at 500 mb (taken from Blackmon et al., 1977, Fig. 6a). Contour interval 4 mb^{-1}. Observations start at 20°N. 29

3.5. The simulated wintertime means of the: (a) vertical zonal wind shear as measured by the difference between the 400 and 800 mb zonal wind. (b) 400 mb absolute vorticity field. Contour interval: (a) 5 m s^{-1}, (b) 10^{-5} s^{-1}; in (a) zero line is dotted and negative contours are dashed. 30

3.6. The simulated wintertime mean 400 mb meridional wind component. Contour interval: 2 m s^{-1}; negative contours are dashed. 31

3.7. The simulated wintertime mean 400 mb negative of vertical pressure velocity. Contour interval $20x10^{-5}$ mb s^{-1}; negative contours are dashed. 33

Figure Page No.

3.8. The simulated wintertime mean 800 mb temperature. Contour interval 3 deg C; negative contours are dashed. 35

4.1. Simulated vs. observed mid-tropospheric r.m.s. geopotential height: (a) Simulated 2.5 day low-pass. (b) Observed unfiltered. (c) Simulated 2.5-10 day anomaly. (d) Observed 2.5-6 day anomaly. (e) Simulated 10 day low-pass anomaly. (f) Observed 10 day low-ass anomaly. Simulated data are at 400 mb and observations are at 500 mb. Observations are from Blackmon (1976). Contour interval is 10 m except in (a) and (e) where it is 20 m. Observations start at 20°N. 37

4.2. The ratio between the simulated 10 day low-pass anomaly wintertime 400 mb geopotential height r.m.s and that of the total 2.5 day low-pass anomaly. Contour interval: 0.1. 41

4.3. The wintertime local correlation between the simulated 400 and 800 mb geopotential height. (a) 2.5 to 10 day fluctuations. (b) 10 day low-pass fluctuations. Contour interval: 0.1; negative contours are dashed. 43

4.4. Simultaneous correlation of the simulated 400 mb geopotential height anomaly at 34°N, 145°W with that at all other grid points. (a) 2.5 day low-pass fluctuations. (b) 10 day low-pass fluctuations. (c) 2.5 to 10 day fluctuations. Contour interval: 0.1; negative contours are dashed and the zero line is dotted. 45

4.5. Composite of simultaneous one-point-correlation maps of the simulated 400 mb geopotential height with base-grid-points within the 20 to 40°N latitude belt (see text for further details). (a) 2.5 to 10 day fluctuations. (b) 10 day low-pass fluctuations. Contour interval: 0.1; negative contours are dashed and the zero line is dotted. 48

Figure Page No.

4.6. Composite of simultaneous one-point-correlations of the 400 to 800 mb geopotential height anomalies (400 mb at base point and 800 mb elsewhere). Base grid points are within the 20 to 40°N latitude belt (see text for further details). (a) 2.5 to 10 day fluctuations. (b) 10 day low-pass fluctuations. Contour interval: 0.1; negative contours are dashed and the zero line is dotted. 50

4.7. Composite of simultaneous one-point-correlation maps of the simulated 400 mb geopotential height with base-grid-points within the 40 to 60°N latitude belt (see text for further details). (a) 2.5 to 10 day fluctuations. (b) 10 day low-pass fluctuations. Contour interval: 0.1; negative contours are dashed and the zero line is dotted. 51

4.8. Composite of simultaneous one-point-correlations of the 400 to 800 mb geopotential height anomalies (400 mb at base point and 800 mb elsewhere). Base grid points are within the 40 to 60°N latitude belt (see text for further details). (a) 2.5 to 10 day fluctuations. (b) 10 day low-pass fluctuations. Contour interval: 0.1; negative contours are dashed and the zero line is dotted. 52

4.9. Composite of simultaneous one-point-correlations of the 400 to 800 mb geopotential height anomalies with base grid points are within the 60 to 80°N latitude belt (see text for further details). (a) 2.5 to 10 day fluctuations. (b) 10 day low-pass fluctuations. Contour interval: 0.1; negative contours are dashed and the zero line is dotted. 53

4.10. Composite of simultaneous one-point-correlation maps of the simulated 400 mb 10 day low-pass geopotential height anomaly with base-grid-points within the Equator to 20°N latitude belt. Contour interval: 0.1; negative contours are dashed and the zero line is dotted. 55

Figure Page No.

4.11. Composite of one-point-correlation maps of the simulated 400 mb 2.5 to 10 day geopotential height fluctuations with base-grid-points within the 20 to 40°N latitude belt. (a) Base-grid-point leads all other points by 3 days. (b) Base-grid-point lags all other points by 3 days. Contour interval: 0.1; negative contours are dashed and the zero line is dotted. 56

4.12. Composite of one-point-correlation maps of the simulated 400 mb 10 day low-pass geopotential height fluctuations with base-grid-points within the 20 to 40°N latitude belt. (a) Base-grid-point leads all other points by 3 days. (b) Base-grid-point lags all other points by three days. Contour interval: 0.1; negative contours are dashed and the zero line is dotted. 57

4.13. Composite of one-point-correlation maps of the simulated 400 mb 10 day low-pass geopotential height fluctuations with base-grid-points within the 40 to 60°N latitude belt. (a) Base-grid-point leads all other points by 3 days. (b) Base-grid-point lags all other points by three days. Contour interval: 0.1; negative contours are dashed and the zero line is dotted. 58

4.14. The stationary wave number of the energy propagating wave as a function of latitude (see text Hoskins and Karoly, 1981 for further details) for the model's 400 mb zonal mean current. Dashed line is the 400 mb simulated zonal angular velocity in m s^{-1}. 62

5.1. The simulated wintertime 800 mb temperature r.m.s. of (a) 2.5 to 10 day fluctuations, (b) 10 day low-pass fluctuations. Contour interval 1°C. 64

Figure Page No.

5.2. The simulated wintertime 400 mb variance of wind velocity components. (a) 2.5 to 10 day zonal wind fluctuations. (b) 2.5 to 10 day meridional wind fluctuations. (c) 10 day low-pass zonal wind fluctuations. (d) 10 day low-pass meridional wind fluctuations. Contour interval: 20 m^2 s^{-2}. 66

5.3. The ratio of the meridional to zonal length scale of the simulated eddies at 400 mb as implied by the variances of the wind velocity components (see text for further details). (a) 2.5 to 10 day fluctuations. (b) 10 ay low-pass fluctuations. Contour interval: 0.2. 69

5.4. The simulated wintertime variance of the vertical pressure velocity at 400 mb. (a) 2.5 day low-pass fluctuations. (b) 2.5 to 19 day fluctuations. (c) 10 day low-pass fluctuations. Contour interval: 2×10^{-7} mb^2 s^{-2}. 71

5.5. The simulated wintertime covariance between the zonal and meridional wind components (northward zonal momentum transport) at 400 mb. (a) 2.5 to 10 day fluctuations. (b) 10 day low-pass fluctuations. Contour interval: 10 m^2 s^{-2}; negative contours are dashed. 74

5.6. The horizontal tilt of the simulated eddies at 400 mb as inferred by their velocity covariance matrix (see text for further details). (a) 2.5 to 10 day fluctuations. (b) 10 day low-pass fluctuations. The arrows represent the major axis of eddy asymmetry. Length of arrow is proportional to eddy eccentricity and its direction with respect to the parallels is the horizontal tilt. The underlying contours are those of eddy kinetic energy (contour interval: 20 m^2 s^{-2}), indicating the eddy intensity. 76

Figure Page No.

5.7. Simulated and observed wintertime covariance between the meridional wind component and temperature (northward heat transport). (a) Simulated 2.5 to 10 day fluctuations. (b) Simulated 10 day low-pass fluctuations. (c) Observed 2.5 to 6 day fluctuations. (d) Observed 10 day low-pass fluctuations. Contour intervals are 2° C m s^{-1} in (a) and (c) and 4° C m s^{-1} in (b) and (d). Simulation results are at 800 mb; observations at 850 mb. Observations start at 20°N. 78

5.8. The simulated wintertime negative covariance between the vertical pressure velocity and temperature (upward heat transport) at 800 mb. (a) 2.5 to 10 day fluctuations. (b) 10 day low-pass fluctuations. Contour intervals are 40×10^{-5} °C mb s^{-1} in (a) and 80×10^{-5} °C mb s^{-1} in (b). 81

5.9. The simulated wintertime negative covariance between the vertical pressure velocity and horizontal velocity components at 400 mb. (a) Vertical northward momentum transport of 2.5 to 10 day fluctuations. (b) Vertical northward momentum transport of 10 day low-pass fluctuations. (c) Vertical westward momentum transport of 2.5 to 10 day fluctuations. (d) Vertical westward momentum transport of 10 day low-pass fluctuations. Contour interval: (a), (b) and (d) 80×10^{-5} m mb s^{-2}, (c) 40×10^{-5} m mb s^{-2}; the zero contour is dotted and negative contours are dashed. 83

Figure Page No.

6.1. The horizontal distribution of various terms in the wintertime vertically integrated energy budgets of the simulated 2.5 to 10 day disturbances. (a) Eddy APE. (b) Eddy kinetic energy. (c) Time-mean to eddy APE conversion by horizontal processes. (d) Time-mean to eddy APE conversion by vertical processes. (e) Eddy APE to kinetic energy conversion. (f) Time-mean to eddy kinetic energy conversion by horizontal processes. (g) Time-mean to eddy kinetic energy conversion by vertical processes. (h) Eddy geopotential flux convergence. (i) Generation of APE by eddy diabatic processes. (j) net of processes c, d, e, and i. (k) net of processes e, f, g, and h. See text for further details. Contour interval: (a) 0.5×10^5 J m^{-2}, (b) 1×10^5 J m^{-2}, (c), (d), (e), (f) and (j) 0.5 W m^{-2}, (g) and (i) 0.25 W m^{-2}, (h) and (k) 1 W m^{-2}. Negative contours are dashed and the zero contour is dotted. 90

6.2. Horizontal distribution of vertically integrated time-mean to eddy kinetic energy conversion terms for 2.5 to 10 day disturbances. (a) Term (2) of KKEH. (b) The sum of terms (1) and (4) of KKEH. See equation (6.1) and text for further details. Contour interval 0.5 W m^{-2}; negative contours are dashed and zero contour is dotted. 97

6.3. (a) Simultaneous correlation between the simulated 2.5 to 10 day fluctuations in precipitation at 50°N and 120°W and 400 mb geopotential height fluctuations elsewhere. (b) Same as (a) but for 38°N 70°W. Contour interval 0.1; negative contours are dashed and zero contour is dotted. 100

6.4. The horizontal distribution of various terms in the wintertime vertically integrated energy budgets of the simulated 10 day lowpass disturbances. (a) Eddy APE. (b) Eddy kinetic energy. (c) Time-mean to eddy APE conversion by horizontal processes. (d) Time-mean to eddy APE conversion by vertical processes. (e) Eddy APE to kinetic energy conversion. (f) Time-mean to eddy kinetic energy conversion by horizontal processes. (g) Time-mean to eddy kinetic energy conversion by vertical processes. (h) Eddy geopotential flux convergence. (i) Generation of APE by eddy diabatic processes. (j) net of processes c, d, e, and i. (k) net of processes e, f, g, and h. See text for further details. Contour interval: (a) and (b) 1×10^5 J m^{-2}, (c), (d), (e), (f) and (j) 1 W m^{-2}, (g) and (i) 0.5 W m^{-2}, (h) and (k) 2 W m^{-2}. Negative contours are dashed and the zero contour is dotted. 101

6.5. Horizontal distribution of vertically integrated time-mean to eddy kinetic energy conversion terms for 10 day lowpass disturbances. (a) Term (2) of KKEH. (b) The sum of terms (1) and (4) of KKEH. See equation (6.1) and text for further details. Contour interval 1 W m^{-2}; negative contours are dashed and zero contour is dotted. 109

6.6. Energy diagram for simulated low- and high-frequency disturbances. Values are Northern Hemisphere averages. Numbers in boxes denote the APE and KE amounts in 10^5 J m^{-2}. Values along arrows denote conversion rates in W m^{-2}. Direction of arrows represent the direction of the conversion. Net values at bottom refer to net of all processes accounted for here (see text). 112

Figure

Page No.

7.1. The first and only mode of CEOF analysis applied to a simple eastward propagating wave with a non-dimensional length of 10 in the x-direction and 21 in the y-direction and a period of 20. (a) Amplitude and phase of spatial eigenvector, denoted by the length and direction of the arrows with reference to the x-axis. (b) amplitude and phase of temporal expansion coefficient (principal component), denoted by full and broken lines respectively. 118

7.2. The spatial eigenvector of CEOF analysis applied to a standing wave of length 10 in the x-direction and 21 in the y-direction. 120

7.3. The spatial eigenvector of CEOF analysis applied to a standing wave packet propagating energy in the x-direction with a group velocity of 5. 121

7.4. The first eigenvector of a CEOF expansion of the normalized 10 day low-pass simulated geopotential height anomaly over the Northern Hemisphere between 10 and 58°N. The length of the arrow is proportional to the local amplitude and the direction with respect to the side of the page is the relative phase. This mode explains 14.05% of the total normalized variance. 123

7.5. The amplitude and phase of the principal component corresponding to the first hemispheric eigenmode of 10 day low-pass geopotential height anomaly of Fig. 7.4. Amplitude is read on the left ordinate and phase (in degrees) on the right. The time interval between two consecutive tic-marks on the abscissa is one day. 124

7.6. The first eigenvector of a CEOF expansion of the normalized 10 to 40 day band-pass simulated geopotential height anomaly over the Pacific quadrant of the Northern Hemisphere. The length of the arrow is proportional to the local amplitude and the direction with respect to the side of the page is the relative phase. This mode explains 27.31% of the total normalized variance. 126

Figure Page No.

7.7. The amplitude and phase of the principal component corresponding to the first Pacific eigenmode of 10 to 40 day band-pass geopotential height anomaly of Fig. 7.6. Amplitude is read on the left ordinate and phase (in degrees) on the right. The time interval between two consecutive tic-marks on the abscissa is one day. The small arrows indicate the peaks of the cycles chosen for later composites. 127

7.8. The phase and amplitude of the principal component of the Pacific eigenmode at the peak of its 'outbreak', projected on the complex plain. The arrows point at the days used for later composites. 130

7.9. (a) The average geopotential height anomaly in the 11 days of peak Pacific mode amplitudes chosen for compositing (see Fig. 7.7). (b) The reconstructed average pacific mode for the same 11 days (see text for further details). Contour interval 20 m; negative contours are dashed and the zero line is dotted. 131

7.10. The reconstructed 400 mb 10 to 40 day geopotential height anomaly of a typical, fully developed Pacific mode. Contour interval 20 m; negative contours are dashed and the zero contour is dotted. 133

7.11. The reconstructed 800 mb 10 to 40 day geopotential height anomaly of a typical, fully developed Pacific mode. Contour interval 20 m; negative contours are dashed and the zero contour is dotted. 135

Figure Page No.

7.12. The reconstructed 400 mb 10 to 40 day velocity field of a typical, fully developed Pacific mode. (a) zonal component. (b) meridional component. Contour interval 2 m s^{-1}; negative contours are dashed and the zero contour is dotted. 136

7.13. The reconstructed 800 mb 10 to 40 day temperature anomaly of a typical, fully developed Pacific mode. Contour interval 2 °C; negative contours are dashed and the zero contour is dotted. 137

7.14. The reconstructed 400 mb 10 to 40 day vertical pressure velocity anomaly of a typical, fully developed Pacific mode. Contour interval 5 mb day^{-1}; negative contours (rising motion) are dashed and the zero contour is dotted. 138

7.15. The reconstructed 800 mb 10 to 40 day diabatic heating rate anomaly of a typical, fully developed Pacific mode. Contour interval 0.2 °C day^{-1}; negative contours are dashed and the zero contour is dotted. 140

7.16. A time series of the vertically integrated kinetic energy of simulated 10 to 40 day fluctuations averaged over the Northern Hemisphere Pacific sector. Units are in 10^5 J m^{-2}. 141

7.17. The horizontal distribution of leading terms in the energy budget of the total simulated 10 to 40 day disturbances. (a) APE. (b) Kinetic energy. (c) Time-mean to eddy APE conversion. (d) APE to kinetic energy conversion. (e) Time-mean to eddy kinetic energy conversion. (f) Geopotential flux convergence. (g) Eddy APE generation through diabatic processes. Contour interval in (a) and (b) is 1×10^5 J m^{-2}, in (c), (d) and (f) 1 W m^{-2}, in (e) 0.5 W m^{-2} and in (g) 0.25 W m^{-2}. 143

Figure Page No.

7.18. The horizontal distribution of leading terms in the energybudget of the simulated 10 to 40 day disturbances corresponding only to the Pacific mode. (a) APE. (b) Kinetic energy. (c) Time-mean to eddy APE conversion. (d) APE to kinetic energy conversion. (e) Time-mean to eddy kinetic energy conversion. (f) Geopotential flux convergence. (g) Eddy APE generation through diabatic processes. Contour interval in (a) and (b) is 0.2×10^5 J m^{-2}, in (c), (d) and (f) 0.4 W m^{-2}, in (e) 0.2 W m^{-2} and in (g) 0.1 W m^{-2}. 147

7.19. The composite energy cycle of disturbances described by the first Pacific mode. Kinetic energy and APE are in units of 10^3 J m^{-2} and the conversion terms are in 10^{-2} W m^{-2}. The abscissa is in days where day zero denotes the day of maximum mode amplitude. The values represent an area average over the Pacific Quadrant of the Northern Hemisphere from 90°E eastward to 60°W. 151

SUBSEASONAL VARIABILITY IN A TWO-LEVEL ATMOSPHERIC GENERAL CIRCULATION MODEL

CHAPTER 1: INTRODUCTION

The study of the general circulation of the atmosphere has historically been concerned with achieving two major goals, namely the understanding of the maintenance of both the semi-permanent and fluctuating features of the atmosphere. This study pertains to the latter. In particular, we are concerned with wintertime atmospheric variability on time scales of a few days to a season.

Since the beginning of this century there has been a continuing scientific interest in atmospheric variability on subseasonal time scales. This interest has been motivated primarily by the urge to develop and improve the skill of weather forecasting. While much is known today about the origin and life cycles of atmospheric fluctuations on time scales of a few days, many uncertainties remain with regard to fluctuations with longer periods. In recent years there has been growing evidence that these slower fluctuations have spatial structures and distributions that are distinctively different from those of short-time-scale fluctuations.

Confident that long-time-scale fluctuations are the result of large-scale dynamical processes, we have set forth to investigate their maintenance and life cycles and compare them with short-time-scale fluctuations. We have chosen to use data simulated by a relatively simple atmospheric General Circulation Model (GCM). This was done not only because of the completeness and consistency of GCM data but also because this GCM is an important member in the hierarchy of models that can be used to study the dynamics of atmospheric circulation systems. Our goal is to contribute to the growing understanding of these disturbances and eventually to improve our forecasting capabilities.

One of the first attempts to investigate the problem of subseasonal low-frequency variability dates to the 1930s when a group

of scientists headed by C. G. Rossby had set forth to investigate the dynamical behaviour of planetary-scale features which appear on weekly-averaged weather maps. In their theoretical and observational studies (e.g., Rossby, 1939 and 1945; Namias and Clapp, 1944 and Cressman, 1948), it was argued that such systems generally behave like forced, barotropic, potential vorticity conserving flows, in contrast to the more rapidly varying and smaller scale baroclinic weather systems.

In early spectral studies of atmospheric variables, Shapiro and Ward (1960) and Ward and Shapiro (1961) noted the relatively large amount of power associated with fluctuations with periods longer than those of weather disturbances (which before then were believed to be the major cause for atmospheric variability). Being alert to studies by the Rossby group and others, they were also looked without much success for significant peaks at low frequencies. These observations led them to suggest that the large power at low frequencies is a result of the basically random fluctuations caused by weather disturbances that have a moderate degree of short term persistence. They claimed this would dampen the high-frequency power and cause a so-called "red-noise spectrum."

A major difficulty in these early studies was the dynamical description of the elusive unperiodic behaviour of the planetary waves. It was quite typical for these systems to follow extended periods of quasi-stationarity by rapid intensification or decay, westward as well as eastward propagation and sudden changes in shape. This behavior simply added to the pessimistic views of Ward and Shapiro. However, more evidence supporting the hypothesis that low-frequency fluctuations have more specific dynamical origins came with the increase in the length, density and spatial coverage of weather records. This enabled Sawyer (1970) to compare the geographical distribution of short (< 10 days) and long (20 to 60 day) time-scale fluctuations of geopotential height over the Northern Hemisphere. His results showed that not only are the latter much stronger than the former everywhere, but also that the regions of maxima in the two categories are well separated from each other. Blackmon (1976) and

Blackmon et al. (1977 and 1979) extended Sawyer's study using a larger data set. Their results and those of Lau (1978 and 1979a) clearly demonstrated that while fluctuations on a time scale of a week are caused by baroclinic, highly transient, cyclone-scale waves, those with time scales longer than ten days are caused by much less mobile planetary-scale disturbances with an equivalent barotropic vertical structure.

More recently Wallace and Gutzler (1981) and Blackmon et al. (1984a and b) have studied the horizontal structure of systems causing atmospheric variability and have further illuminated these differences between high- and low-frequency disturbances. Studies by Holopainen et al. (1982), Hoskins et al. (1983) and Lau and Holopainen (1984) revealed the differences in the role played by fluctuations on short- and long-time scales in the maintenance of the time-mean flow in terms of intensity and location.

Rossby's much acclaimed pioneering effort to explain the behavior of planetary-scale waves in the atmosphere was naturally followed by many theoretical studies on the subject, some of which were direct extensions of his ideas. This was the case with the study by Hoskins et al. (1977) who investigated the effect of sphericity on the dispersion of Rossby waves. Their results and those obtained more recently by Hoskins and Karoly (1981) have shown that the modal structure of forced disturbances on the sphere look remarkably similar to the spatial correlation patterns of Wallace and Gutzler (1981). The agreement between wave-dispersion theory and observations was further demonstrated by the lagged correlation analysis of Blackmon et al. (1984b).

Hypothesizing that low-frequency modes might be generated internally in the atmosphere, without the dependence on "external" forcing, Simmons et al. (1983) tested the stability properties of a barotropic atmosphere in which the basic flow was zonally asymmetric, to random perturbations. They have found that (realistic) zonal asymmetry can make the flow barotropically unstable and that the most unstable mode also resembles some of Wallace and Gutzler's (1981) patterns. Frederiksen (1982 and 1983) showed that similar modes could

also develop in a stratified zonally asymmetric flow and grow through both baroclinic and barotropic processes.

The theories on vacillation (Lorenz, 1963) and multiple equilibria (Charney and Devore, 1979) have described the generation and life cycle of quasi-periodic, low-frequency, planetary-scale modes which feed on nonlinear scale-interactions. Egger and Schilling (1983) have used quasi-nonlinear dynamics to show that advection by synoptic-scale eddies can cause a geographical distribution of low-frequency variablity reminiscent of that observed.

In all these theoretical studies simplified dynamical models have been used and comparisons with observations were usually made on a qualitative basis. The difficulty of putting these comparisons on a more quantitative basis stems in part from the limitations of atmospheric observations and in part from the difficulty involved in isolating the low-frequency modes in the data. Observations provide very little quantitative information on the forcing mechanisms in the atmosphere. The spatial resolution and relative inaccuracy of observations over the oceans are serious problems, and the isolation of dynamically meaningful, low-frequency modes in observations is a problem that dates back to the pioneering studies of the thirties and forties noted above.

Recently it has been shown that general circulation models offer a reasonably good simulation of atmospheric variablity on short and long time scales (e.g. Hayashi and Golder, 1977; Blackmon and Lau, 1980; and Lau, 1981). These models generate comprehensive, dynamically consistent and spatially and temporally homogeneous information on the simulated atmospheric state. In the hierarchy of numerical models, GCMs are the most complex and achieve the closest description of real atmospheric processes. GCM data should therefore serve as an important tool in the study of atmospheric variability.

The Oregon State University (OSU) GCM (Schlesinger and Gates, 1980 and Ghan et al., 1982) is a relatively simple two-level primitive equation model with a horizontal resolution of 4° latitude by 5° longitude, and parameterizations of the major sub-grid-scale physical processes. In other words, the model has adequate dynamical

complexity yet offers an efficient description of the atmospheric state. As such the model is an important link between the idealized models used in theoretical studies and the observations.

Recently the OSU model was used to simulate ten years of the atmospheric circulation with its boundary conditions varying through a fixed annual cycle. The history of state variables generated by this run is used here to study the variability of the wintertime northern hemisphere atmosphere with an emphasis on the low frequencies. In Chapter 2, the history of observational studies and theory on subseasonal variability is reviewed. Chapter 3 describes the model, the data and the basic features of the simulated wintertime mean circulation. Chapter 4 considers the hemispheric distribution of the geopotential height fluctuations and with their spatial and temporal properties. In Chapter 5 the intensity of fluctuations in other dynamical variables are examined. The energy cycle of the model eddies is studied in Chapter 6. Finally, in Chapter 7, an attempt is made to describe the life cycle of low-frequency disturbances by examining the structure and energetics of a composite low-frequency mode over the North Pacific region.

CHAPTER 2: HISTORICAL REVIEW

Atmospheric variability occurs over an extremely broad spectrum of time periods, yet skill in prediction has been achieved only in the domain of relatively short-period disturbances. Although many attempts have been made to devise methods for predicting fluctuations on time scales longer than a week, they have generally not been successful enough to be useful. This has sometimes been attributed to the inherent unpredictability of the atmospheric flow (e.g. Lorenz, 1963a). However, it is conceivable that this is also due to the lack of complete dynamical understanding of the processes leading to and maintaining the low-frequency variability of the atmosphere.

In this chapter we shall review the observations and theory on the two major classes of atmospheric variability: that on short time-scales, with periods on the order of two days to a week and that on long time-scales, with periods between about two weeks and a season.

2.1 Short time-scale fluctuations

Most efforts to achieve skill in predicting atmospheric variability have been directed toward the so-called synoptic time scales of about two days to a week. Fluctuations in the circulation on these time scales have been associated with the life cycle and migration of weather cyclones. The theory on the behavior of such systems was first formulated by the Bergen School of Meteorology (e.g., Bjerknes and Holmboe, 1944). Later the properties of weather cyclones were explained by the theory of baroclinic instability proposed by Charney (1947) and Eady (1949) and extended by studies like those of Simmons and Hoskins (1976 and 1978) and Frederiksen (1978 and 1980) to more realistic situations.

Based on the existing theoretical models of baroclinic instability, the main properties of the disturbances may be summarized in terms of their location, temporal and spatial scales, and transport properties. Specifically, baroclinic disturbances are generated in

latitudes where the vertical component of the earth's vorticity is sufficiently large and where the prevailing air current (or basic state) has a large horizontal temperature gradient. Under the conditions prevailing in the earth's atmosphere the horizontal scale of these eddies, as governed by the static stability and the northward gradient of the earth's vorticity, is on the order of a few thousand kilometers (zonal wavenumbers 6 to 9) and their periods are on the order of several days (less than 10). The transport properties of baroclinic eddies are a manifestation of their three-dimensional structure. Baroclinic eddies transport heat from warmer to colder regions, drawing potential energy from the underlying current. Upward motion in the warmer air on their equatorward side and downward motion in the poleward lying colder air converts their acquired potential energy into kinetic energy. Baroclinic eddies also generally transport zonal momentum against the gradient of the basic flow's westerly momentum.

That some atmospheric disturbances, namely those with a time scale of a week, show such properties was clearly shown by the work of Hartmann (1979), Blackmon (1976), Blackmon et al. (1977) and Lau (1978 and 1979a). Hartmann used spectral analysis with time series of middle-latitude Atlantic weather-ship soundings to show that traveling waves with periods of 4 to 5 days have transport properties and vertical structures typical of theoretical baroclinic eddies. Blackmon (1976) calculated the spatial distribution of the intensity of geopotential height fluctuations over the Northern Hemisphere during the winter season. Using spherical harmonic analysis and time filtering he divided his data by period bands and spatial scale. The 2.5 to 6 day fluctuations had maximum intensities slightly northward and downstream from the jet-stream maxima, and a relatively small scale (zonal wavenumber 5 to 7). Blackmon et al. (1977) calculated the 2.5 to 6 day band covariance between the zonal and the meridional component of the wind and between the meridional wind and temperature. They showed that the observed eddies behave as predicted by theory, transporting momentum into the jet stream regions and heat northward, with maxima in the fluxes just northeastward of the jet stream maxima. Lau (1978

and 1979a) examined the vertical structure of the intensity and transport properties of observed eddies with short time scales. He showed the dependence of this structure on the geographical location with respect to the major jet streams. His results clearly confirmed that observed fluctuations with a time scale of a week are driven by the process of baroclinic energy conversions and have the life cycle predicted by baroclinic instability theory. Recently Blackmon et al. (1984a and b) used spatial correlation analysis applied to northern hemisphere winter data to show that short time scale fluctuations actually look like weather cyclones. They appear as a train of low- and high-pressure cells with a wave length of about 4000 km, propagating eastward with a phase speed of about 12 m/sec. This study and that of Hoskins et al. (1983) have also shown that observed cyclonic eddies are larger in their meridional scale than in their zonal scale, in accordance with the theoretical result of Simmons and Hoskins (1976) and Frederiksen (1978).

The effect of the baroclinic-eddy transfer properties on the time-mean flow was studied by Holopainen et al. (1982), Hoskins et al. (1983) and Lau and Holopainen (1984). Their results have shown that these eddies act like a sink for the underlying flow's potential and kinetic energy, although sources of kinetic energy due to eddy westerly momentum-flux convergence exist as well.

The simulation of baroclinic eddies by GCM's has been shown to be reasonably good. Hayashi and Golder (1977) used space-time spectral analysis with time series of the GFDL GCM simulation of the northern hemisphere winter. They identified fluctuations with a four-day period and a zonal wavenumber of 7 that behave like the observed and theoretical baroclinic eddies. These waves were moving eastward and had a baroclinic vertical structure. Their relationship to the location of the jet streams and the distribution of transport properties were similar to those observed. Blackmon and Lau (1980) applied variance and covariance analysis to the GFDL GCM simulation and concluded that, apart from internally consistent shifts in the location of the major model features and a small underestimation of the simulated intensity of baroclinic activity, the model simulated the generation,

intensification and decay of baroclinic eddies quite well. Mullen (1980) carried out these analyses with time series of northern hemisphere winter data simulated by the OSU GCM, and was led to similar conclusions regarding its performance on short time scales.

2.2 Long time-scale fluctuations

The theory and observations we have reviewed demonstrate the important role that the background circulation plays in determining the properties and life cycle of baroclinic eddies. Fluctuations of the circulation on time scales longer than the life cycle of baroclinic eddies and on spatial scales of the cyclone tracks are not only common but are also responsible for the largest part of atmospheric variability (e.g., Sawyer, 1970). Since the beginning of the century, investigators have observed a variety of planetary-scale, "low-frequency" fluctuations in the global circulation. These differ in their geographical location as well as in their temporal and spatial scales. Some have time scales longer than a season (e.g., Walker and Bliss, 1932; Horel and Wallace, 1981, and Namias and Cayan, 1981), while others occur on subseasonal time scales and usually have smaller dimensions (e.g., Namias and Clapp, 1944; Willet, 1948; Rex, 1950a and b; Namias, 1950 and Wallace and Gutzler, 1981). The latter disturbances are the low-frequency features of interest in this study. Attempts have also been made to use dynamical as well as statistical models to predict low-frequency disturbances (Namias, 1953; Nicholls, 1980), yet operationally these methods have not achieved a satisfactory degree of skill.

One of the major road blocks on the way to developing methods for predicting atmospheric low-frequency variability has been the lack of a complete dynamical understanding of their origin and maintenance. The first comprehensive dynamical studies on this subject were those by Rossby (1939 and 1945). In these studies a simplified dynamical model was proposed to explain the behavior of long, quasi-stationary waves in middle latitudes that were observed on weekly-averaged synoptic charts. It was suggested that these features behave like the

barotropic, linear response of a β-plane atmosphere to large-scale local forcing such as orographic lifting. Under the law of conservation of potential vorticity, this response would take in the form of the so-called Rossby waves which tend to move westward relative to the environmental flow and thus can become stationary in a westerly current. Rossby also showed that under these assumptions, the wave energy would disperse quite rapidly downstream generating a wave pattern of hemispheric dimensions. These forced waves would then fluctuate in time in response to variations in the intensity of the zonal current.

Namias and Clapp (1944) and Cressman (1948, 1949 and 1958) tested Rossby's theory using observed data and suggested some changes to make it more useful as a tool for forecasting. The difficulties involved in such use of the theory were the overly simplified dynamics behind it, and the problem of determining and predicting the strength of the zonal current.

Over the years Rossby's theory continued to be the subject of many observational studies. In most of these studies the movement and intensity of the low wavenumber zonal harmonics were calculated using space-time spectral analysis methods (see review by Madden, 1979). Most of the observations indicated the existence of rapidly retrograding waves with a period of about 5 days which were interpreted as free Rossby modes. In a few other cases (e.g., Pratt and Wallace, 1976) much longer periods of about 20 days were detected. The dynamical interpretation of these spectral studies, however, was complicated by accumulating evidence showing that low-frequency variability had a strong regional character. Evidence on the regional character of low-frequency variability dates back to the discovery of the so-called "blocking" phenomenon. This middle latitude phenomenon is characterized by a persistent local, large-scale interruption in the prevailing westerly flow. It takes the form of a dipole-like pair of cellular geopotential height anomaly centers (positive center poleward) causing a split in the jet stream (Rex, 1950a). Rex (1950b) compiled more than a hundred cases of blocking in the Northern Hemisphere, extracted from 14 years of data. He found that they tend to occur in two

geographical locations: in the eastern Atlantic around 10°W, and in the eastern Pacific around 150°W. These blocks normally extend over a period of 12 to 16 days without appreciable movement and tend to occur most frequently in winter and spring. Later Sawyer (1970) mapped the geographical distribution of low-frequency variability during the winter season over most of the Northern Hemisphere. He showed that geopotential height fluctuations with long-time periods (20 to 60 days) are stronger and geographically separate from those on short time scales (< 10 days). He found that the maxima in the low-frequency 500 mb geopotential height r.m.s. are located over the extreme northern Atlantic and Pacific oceans. Sawyer also observed the high correlation between the 500 mb geopotential height fluctuations and those of the 1000 to 500 mb thickness in the low-frequencies. He studied the spatial structure and time behavior of disturbances causing these fluctuations by using lagged spatial correlation analysis and found them to be dominated by north-south oriented, standing dipole-like patterns. These observations lead him to conclude that they were closely related to the blocking phenomenon.

Blackmon (1976) extended Sawyer's analysis using a larger data set having full-hemispheric coverage over a longer time period. He distinguished between fluctuations with time scales longer than 10 days and those with shorter time scales. Using spherical harmonics he classified the 500 mb variability into three categories according to their spatial dimensions. He found that most of the low-frequency fluctuations are caused by planetary scale systems with zonal scales of wavenumber 1 to 3 and a north-south dipole-like structure. He also found them to be propagating very slowly westward. Blackmon et al. (1977) calculated the low frequency r.m.s. in the low-tropospheric thermal field. They found the maxima to be located over the high latitude continents, shifted from the maxima in the geopotential height r.m.s. field, and attributed these to shallow systems of a highly baroclinic nature. In contrast, the oceanic systems were later shown to be of an equivalent barotropic nature (Blackmon et al., 1979). The momentum and heat transports by the low-frequency eddies were found to be much stronger than those of the cyclonic, high-frequency eddies,

and their maxima were shifted further northward and downstream from the jet stream maxima. These observations were verified by Holopainen et al. (1982), Hoskins et al. (1983) and Lau and Holopainen (1984) who studied the eddy transport properties from the point of view of their influence on the time-mean flow. Hoskins et al. (1983) have further shown that these transport properties can be used to diagnose the shape, horizontal scale and vertical tilt of the eddies. Their calculations have demonstrated that in contrast to their high-frequency counterparts, low-frequency eddies have zonal dimensions which are relatively longer than their meridional dimensions and generally a smaller vertical tilt.

The tendency to display quasi-stationary, large-scale north-to-south oriented dipole-like spatial correlation patterns is an important aspect of the atmospheric low frequency fluctuations. These patterns are often referred to in the literature as "teleconnections." Wallace and Gutzler (1981) have reviewed almost half a century of teleconnection-related studies, and re-examined and classified the various patterns on the basis of monthly-mean geopotential height data. Their results indicate that teleconnection patterns in different regions are quite independent of each other. They have also noted their equivalent-barotropic nature. Recently Blackmon et al. (1984a) examined the spatial correlations of 500 mb geopotential height fluctuations on even shorter time scales and found that 10-3 day disturbances display similar teleconnection patterns. Blackmon et al. (1984b) have also used time-lagged correlation analysis to examine the time behavior of the low-frequency teleconnection patterns in the atmosphere and found them to be quasi-stationary in phase. The only marked temporal change they found was a downstream increase in the pattern intensity with time. They interpreted this as a manifestation of a process of horizontal energy dispersion in the form of Rossby waves.

The observational evidence on the behavior of low-frequency eddies, in particular their generally equivalent barotropic structure and the quasi-stationary nature of their oscillations have recently re-awakened interest in Rossby's (1939 and 1945) linear, barotropic

wave dispersion models. Hoskins et al. (1977) compared Rossby's original β-plane model with a spherical, barotropic atmosphere model. In contrast to the simpler case studied by Rossby where the energy dispersed only in the zonal direction, they found that the spherical geometry imposed a two-dimensional dispersion pattern on the perturbations of their model atmosphere. In the ideal case of a zonal, constant angular-velocity flow, the forced Rossby waves dispersed along a great circle path. Some of the important conclusions from this study were that tropical forcing can influence the middle and high latitudes and vice versa, and that interaction between the two hemispheres is also possible. The results also indicated that with realistic basic flow and energy dissipation rates, the likelihood of a Rossby-wave resonance is greatly reduced. Grose and Hoskins (1979) used a similar model to study the stationary response to topographic forcing. They showed that the Rossby wave response to a realistic earth orography may explain a large part of the observed stationary wave pattern in the upper troposphere. More recently, Hoskins and Karoly (1981) extended this theory by using a hemispheric baroclinic model. They studied the response to both orographic and thermal forcing with the following results:

a. The stationary response of the atmosphere to local forcing consists of a local baroclinic part and a remote equivalent barotropic part.

b. Under realistic dissipation rates, the remote response has a large meridional (equator to pole) and zonal (half a hemisphere or more) extent, downstream from the region of forcing.

c. The downstream response is in the form of a wavetrain arranged along a a great-circle-like path, where the intensity of the waves and their zonal dimensions are larger in higher latitudes.

The results of Hoskins and Karoly's numerical experiment were in good qualitative agreement with Wallace and Gutzler's (1981) observed teleconnections. Hoskins and Karoly interpreted the local response to forcing in the context of quasi-geostrophic dynamics and successfully applied kinematic barotropic wave theory and geometric optics to explain the properties of the remote response.

Hoskins and Karoly's success in showing the good agreement between linear stationary theory and observations has motivated other investigators to generalize the simple theoretical models. Branstator (1983) has applied kinematic wave theory to the results of a simple numerical model to show the response of zonally asymmetric barotropic flows to stationary forcing. He demonstrated the possible existence of reflection zones and wave guides in the jet stream regions. Others have studied the response to different forcing mechanisms and regions of generation, sometimes with conflicting results. Webster (1981) simulated a deep-heating mechanism and found that forcing the atmosphere in the subtropics creates the strongest response in middle latitudes. This observation agreed with Hoskins and Karoly's (1981) and Simmons (1982) results using "deep heating" in various latitudes. Hendon and Hartmann (1982) have used prescribed deep heating with an ocean - atmosphere sensible heat flux feedback to show that middle-latitude forcing has a stronger remote response than tropical forcing. They also noted that surface friction can further reduce the remote response and have concluded that tropical forcing effects on the middle latitudes could not be of dominant importance. Kang (1984) has used a non stationary linear baroclinic model with parameterizations of cumulus and sensible heating, and of surface friction and found that if those mechanisms are allowed to operate everywhere the middle-latitude response to tropical forcing could be significant.

A crucial part of the two-dimensional wave dispersion theory is the existence of an "external" forcing mechanism to generate the vorticity source. Some investigators have raised the question of whether low-frequency modes could be generated by an "internal" mechanism such as instability. One of the first attempts to answer this question dates back to the late 1940s and is related to the detection of

quasi-periodic oscillations in the strength of the westerlies in the middle latitudes (Cressman, 1950; Namias, 1950). These fluctuations are locally manifested by shifts in the jet stream locations, changes in their intensity and dimensions, meandering and splitting. The changes have been observed to occur with periods ranging from several days to several weeks. Namias (1950) suggested that these fluctuations are the dynamical response of the atmosphere to the existing requirement to balance the north-south basic thermal gradient by transporting heat northward. To facilitate such transports, large-scale eddies as well as weather cyclones will be generated, with their intensity and frequency of occurrence depending on the strength of the thermal gradient. Hide (1953) observed this phenomenon in rotating heated tank experiments and named it "vacillation." Lorenz (1963b) modeled vacillation using a highly truncated, two-level, quasi-geostrophic baroclinic model on a β-plane. He was able to show that under a relatively strong imposed north to south temperature gradient, high enough rotation rates and a critical amount of friction, an instability develops. This instability involves a periodic change of flow from a more wavy form to a more zonal form. Earlier, Thompson (1957) and Arakawa (1961) showed that baroclinicity is not a necessary requirement for achieving vacillation. The quasi-nonlinear barotropic models they used became barotropically unstable when a sharp jet formed, and a transfer of kinetic energy from the mean state to the unstable mode occurred. The growing mode caused a weakening and splitting of the jet. More recently Quinet (1974) studied the energetics of vacillation in a model similar to the one used by Lorenz (1963b) and found that two types of energy transformations are involved: one in which the dominating transformation is between the mean state and the eddy available potential energy, and another in which there is a transformation between the mean state and the eddy kinetic energy. He named these "potential energy" and "kinetic energy" vacillations, respectively.

One of the drawbacks of vacillation as a theory of low-frequency oscillations is that it appears to exist only in highly truncated models. An increase of the number of degrees of freedom in the models

increases the complexity of the modeled flow and higher baroclinic modes compete with the planetary-scale modes to fulfill the energy balance requirements. Some observational evidence, in the form of time series of hemispheric energy budget components, however, points at the possibility that vacillation cycles are responsible for part of the low-frequency atmospheric variability. Webster and Keller (1975) examined upper-tropospheric, constant-level balloon data from the Southern Hemisphere and identified long-term fluctuations in the kinetic energy field. McGuirk and Reiter (1976) found similar long-period fluctuations in the total northern hemisphere available potential energy. The dominant period of the fluctuations found in both studies was about three weeks.

Charney and DeVore (1979) suggested that atmospheric anomalies which persist for relatively long time periods could also result from nonlinear interactions between planetary waves and the zonal-mean flow in the presence of orography. The feedback mechanism between a forced Rossby wave and the "form drag" it creates on the zonal mean flow in the presence of a mountain will result in several equilibrium solutions, depending on the number of degrees of freedom allowed. The differences between these equilibrium solutions are in the relative amplitudes of their wavy part. In highly truncated barotropic flows these equilibria are stable, but, if the number of degrees of freedom is increased or the flow is allowed to be stratified, the equilibrium solutions can become unstable. Thus transformations between several equilibrium solutions are possible. Charney et al. (1981) applied this model to realistic one-dimensional orography and compared the results with observed west to east cross sections of planetary wave amplitude during a number of blocking episodes. They claimed good agreement between the two.

Different internal instability mechanisms, able to create low-frequency fluctuation in a simplified dynamical model were recently proposed by Simmons et al. (1983) and Frederiksen (1982 and 1983). Simmons et al. have shown that a basic state with a realistic zonal and meridional asymmetry is barotropically unstable to small perturbations. The leading modes of this instability have long

periods (one month and longer) and planetary structures similar to some of the teleconnection patterns of Wallace and Gutzler (1983). They have further shown that the growth of the unstable eddies is governed not only by eddy northward momentum flux over regions of strong meridional shear of the basic state, but also by the fact that these eddies acquire a zonal elongation at the jet exit regions. Frederiksen showed the existance of similar large-scale, dipole-like modes in a two-level quasi-geostropic model with a relatively large static stability. These modes grew faster than purely barotropic ones and some had shorter periods on the order of 15 to 20 days.

A third approach to low-frequency variability was that proposed by Green (1977) and more recently by Egger and Schilling (1983). Their idea was that organized patterns of convergence of momentum and heat due to high-frequency eddies may induce a low-frequency response. Egger and Schilling pointed at the existence of such organized pattern in nature, in the form of the high-frequency storm tracks. By using the known spatial and temporal statistical distribution of momentum transport along the the storm tracks, Egger and Schilling obtained forced low-frequency solutions to the quasi-geostrophic barotropic vorticity equation. The time-averaged low-frequency response to this quasi-nonlinear forcing was found to have limited agreement with observations.

In recent years it has been shown that some of the important observed features of low-frequency variability are quite well simulated by GCM's. Blackmon and Lau (1980) looked at the variances and covariances of geopotential height, temperature and velocity in the GFDL model. They found that the model simulates reasonably well the various properties of low-frequency disturbances like the location in space of the activity centers and their horizontal and vertical structure. Mullen (1980) has found a similar agreement between the OSU low-frequency fluctuations and observations. Lau (1981) studied the teleconnection patterns appearing in the GFDL GCM simulation and found similar patterns to those observed by Wallace and Gutzler. Qiu and Esbensen (1984) looked for teleconnections in the monthly mean geopotential height field of the OSU GCM simulation, and have

carefully documented their spatial distribution and character. Their results indicate that this GCM with its fixed boundary conditions is able to simulate most of the observed patterns.

2.3 GCMs as a medium for dynamical studies

The use of GCMs as a medium for dynamical studies has been quite limited. Gall (1976) used a GCM and a linear model to estimate the importance of nonlinearity in the process of baroclinic instability. Lau (1981) used GCM data to depict the weather types that accompany low-frequency changes in the atmospheric state.

The use of GCM data for the dynamical studies of atmospheric variability is appealing particularly because, as has been shown by observations, most centers of variability occur over the world oceans where observational errors are large and the dynamical consistency between field variables is low. In contrast GCMs offer a full comprehensive set of field variables including information on diabatic heating components and friction.

There exists, however, another important reason for using GCMs in dynamical studies. These models offer the most complete mathematical description of large-scale atmospheric processes. As such they should be used as a link between the simplified and specifically designed models used for theoretical studies and the diagnosis of observations.

Hoskins (1983) has recently reiterated the importance of using dynamical models of various complexity combined with evolving conceptual models and observations, to understand the behavior of the atmosphere on various temporal and spatial scales. In this study we take the approach suggested by Hoskins, and by comparing model results and observations on one hand and the results of theoretical studies on the other, we try to gain a better understanding of tropospheric variability in the wintertime northern hemisphere.

CHAPTER 3: MODEL, DATA AND METHODOLOGY

The data used in this study are derived from the six-hourly history of state variables generated by the OSU atmospheric GCM. This model has been run in a so-called control-experiment mode for ten simulated years under a fixed annual cycle of solar radiation and sea surface temperatures. This chapter gives a brief description of the model, the major steps taken during the preparation of the data for this study, the methodology of the data diagnostics, and a description of the basic features of the model's wintertime mean circulation over the northern hemisphere.

3.1 The Model

The OSU atmospheric GCM has been described by Schlesinger and Gates (1980) and was fully documented by Ghan et al. (1982). The model is based on the primitive set of equations formulated in terrain-following σ-coordinates. It has a 4° latitude and 5° longitude horizontal resolution and is divided into two equal-mass layers in the vertical. The model's top at 200 mb acts like a material surface. The model's horizontal differencing scheme is formulated on the so-called "B"-grid, using the Arakawa (1966) kinetic energy and enstrophy conserving scheme. The vertical differencing is also designed to satisfy essential integral constraints.

The model includes a detailed parameterization of the major physical processes such as the transfer of solar and terrestrial radiation, and the hydrological cycle. Also parameterized are sub-grid scale processes such as cumulus convection, surface friction, and the exchange of heat and moisture at the earth's surface. The model's boundary conditions include smoothed orographic features its distribution over the northern hemisphere shown in Fig. 3.1, and a prescribed classification of the surface type (this is allowed to change by the accumulation and melting of snow). Also prescribed are a fixed annual cycle of ocean-surface temperatures and sea-ice coverage both based upon climatology, and the incoming solar radiation at the model's top.

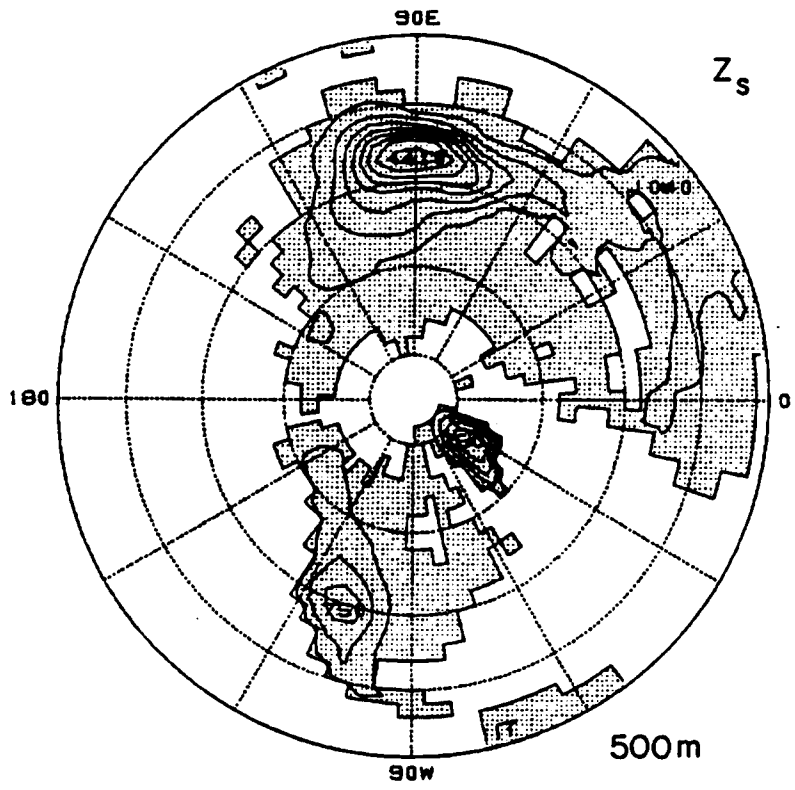

Fig. 3.1. Surface elevation above sea level over the northern hemisphere as used in the model's boundary conditions. Contour interval: 500 m.

The latter varies through a local diurnal cycle. Because its sea surface conditions do not change from one year to another, the model does not contain a major mechanism governing interannual variability. This, however, is a desirable feature in our case since we are interested only in the subseasonal part of the atmospheric variability.

The model outputs the six-hourly atmospheric state described by the horizontal and vertical distribution of all of its prognostic variables including the distribution of surface pressure. These can be used in a post-processing mode to determine diagnostic variables such as the distribution of the diabatic heating components. A ten-year record of this history of states exists in the archive of the model's control experiment. This record provided the data set for this study.

3.2 Data preparation

3.2.1 Interpolation to pressure levels

Most of the model results are presented on its σ = 1/4 and 3/4 levels. Over the oceans these levels correspond roughly to the 400 and 800 mb pressure levels, but over land the deviation from constant pressure surfaces can be quite large. To facilitate dynamical interpretation and comparison with observations, the model σ = 1/4 and 3/4 level variables were interpolated to the pressure levels of 400 and 800 mb. The interpolation was carried out in a model consistent way based on the procedures suggested by Gates et al. (1971). In these the wind velocity components are assumed to vary linearly with pressure, and the potential temperature (θ) to vary linearly in the κ-power of pressure (κ being the ratio between the dry-air gas constant and the specific heat of dry air at constant pressure). The temperature on pressure surfaces (T) is calculated from the interpolated value of potential temperature. The latter is also used to calculate the geopotential height of the constant pressure surfaces, from a model consistent form of the hydrostatic equation. The diabatic heating rate (Q) at the σ levels of 1/4 and 3/4 is derived from the values of the model primary variables using the model's subroutines.

It is then interpolated to pressure levels by assuming that $\frac{\Theta}{T} Q$ varies linearly in the p^{κ} space (this assumption is consistent with the vertical dependence of Θ and the thermodynamic energy equation). Finally, the vertical pressure velocity $(\omega \equiv \frac{dp}{dt})$ is first derived at the $\sigma = 1/4$ and $3/4$ from a model consistent expression for the adiabatic cooling term in the thermodynamic energy equation $(\omega\alpha)$. The resulting two ω values and the assumption that $\omega = 0$ at the model's top, are interpolated to pressure levels by using a parabolic fit in pressure (this fit is consistent with the linear wind profile as implied by the mass continuity equation).

The consistency and quality of these interpolation procedures were checked by performing a sample heat and mass budgets on pressure levels, the results of which were found to be satisfactory.

3.2.2 Filtering

The use of time filtering in this study was intended primarily to achieve a separation between relatively short-time-scale fluctuations and long-time scale ones. Our choice of the "cut-off" time-scale at 10 days is based on the observational studies of Sawyer (1970), Blackmon (1976) and others (see Introduction). Some justification for this choice also results from the theoretical modelling of atmospheric baroclinic processes which indicates that the life cycle of most baroclinic waves varies between 2 and 10 days (see e.g., Simmons and Hoskins, 1978). This is also roughly the typical dissipation time in the atmosphere. Thus, disturbances that are sustained beyond this cut-off time should be dynamically different from those associated with migratory weather cyclones.

We have attempted to check the validity of this choice by using sample time spectra of geopotential height fluctuations at various geographical locations. Not surprisingly, these spectra closely resembled a "red-noise" spectrum in the low frequencies. In most of these, however, we found an indication of a "synoptic time-scale" peak at periods of 5 to 7 days, separated from the low-frequency "red-noise" peak.

Following the pressure interpolation step, the time series of the prognostic and derived variables sampled four times per day were filtered in time to eliminate fluctuations with periods shorter than about 2 days. This effectively removed diurnal variations from the data and permitted a data sampling rate of one sample per day. This procedure was applied to data from 10 simulated northern hemisphere winters. In this study the winter season was chosen because it is characterized by stronger variability than in other seasons. Winter is defined as the 90-day period beginning on the 1st of December. Since each winter had to be filtered separately, we have "padded" the time series of each by the 30 days of GCM data on each side. These padded data were used only in the time filtering; they were ignored in the diagnostics. Here and in all other filtering operations, a 4-pole symmetric tangent-Butterworth recursive filter, developed from the algorithm presented by Kaylor (1977) was used. The power response curve of the 2.5 day low-pass filter is shown in Fig. 3.2.

Next the daily normals of each variable were evaluated in the following way: let $a_{mn}(\underline{x},p)$ be the field value at location $\underline{x}$ and pressure level p on day n of year m (m=1 to 10, n = -30 to 120), then the daily normal $\hat{a}_n(\underline{x},p)$ is given by

$$\hat{a}_n(\underline{x},p) = \frac{1}{10} \sum_{m=1}^{10} a_{mn}(\underline{x},p) \qquad (3.1)$$

The daily anomaly $a'_{nm}(\underline{x},p)$ given by:

$$\hat{a}'_{mn}(\underline{x},p) = a_{mn}(\underline{x},p) - \hat{a}_n(\underline{x},p) \qquad (3.2)$$

In this way the invariant part of the annual cycle and its harmonics were removed from the data.

The time series of daily anomalies were then further filtered with a 10 day low-pass recursive filter to separate between high- and low-frequency fluctuations (see Fig. 3.2 for the power response curve). By subtracting this anomaly time series from the "total signal" (2.5 day low-pass), the 2.5 to 10 day band-pass anomaly fields were constructed.

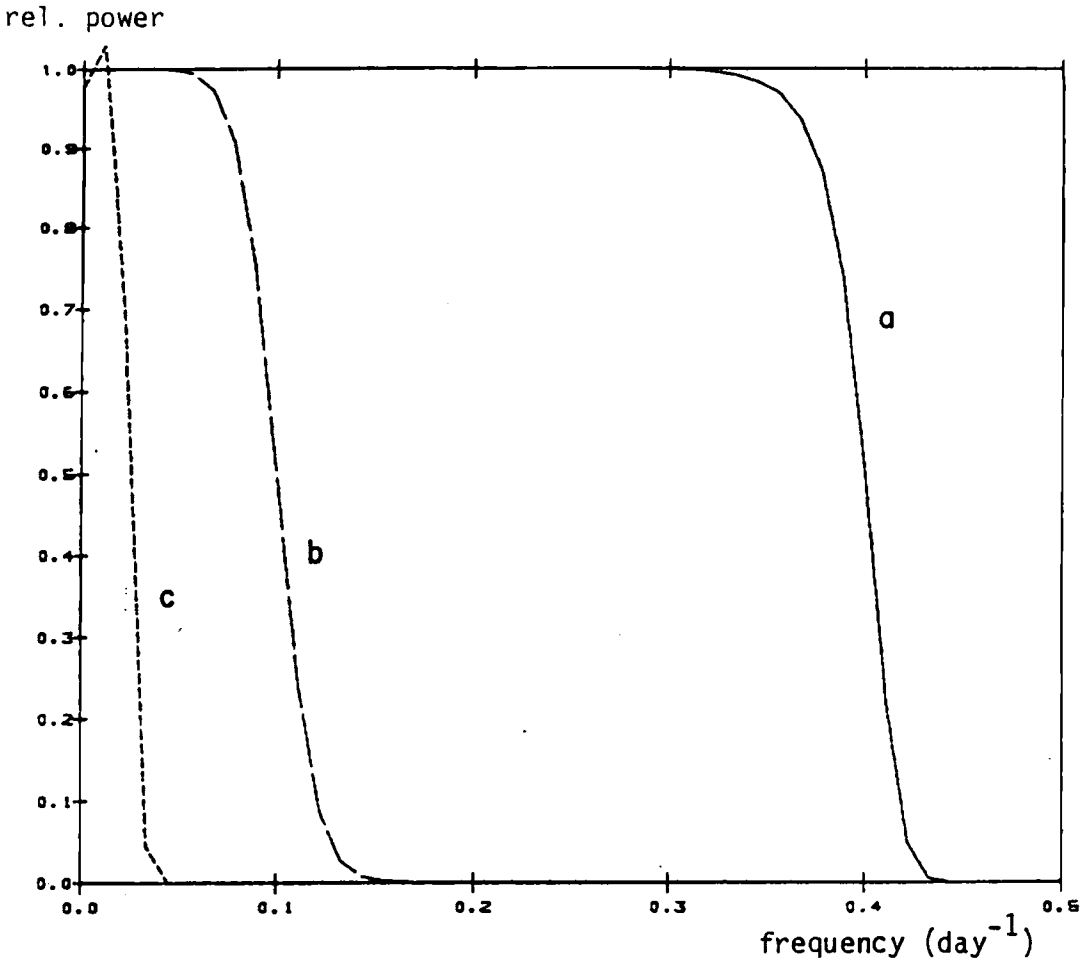

Fig. 3.2. The power response curves of the three low-pass filters used in this study: (a) 2.5 day low-pass (half power frequency at 0.4 day^{-1}), (b) 10 day low-pass (half power frequency at 0.1 day^{-1}) and (c) 40 day low-pass (half power frequency at 0.025 day^{-1}).

The final results of these analyses describe the dynamical state of the wintertime mean circulation and fluctuations in three time-scale categories:

a. those with periods of 2.5 days to a season, the total signal;
b. those with periods of 2.5 to 10 day, the high-frequency part of the signal;
c. those with periods of 10 days to a season, the low-frequency part of the signal.

3.3 Methodology of the diagnostics

Most of the diagnosis presented in this study is based on analyses of variance and covariance. The variance of an anomaly field $a'(\underline{x},p)$ is given by

$$\left\langle a'(\underline{x},p)^2 \right\rangle_t = \frac{1}{10\times 90} \sum_{m=1}^{10} \sum_{n=1}^{90} [a'_{mn}(\underline{x},p)]^2 \qquad (3.3)$$

and the covariance between field a' and field b' is given by:

$$\left\langle a'(\underline{x},p_1)b'(\underline{x}_2,b_2) \right\rangle_t = \frac{1}{10\times 90} \sum_{m=1}^{10} \sum_{n=1}^{90} [a'_{mn}(\underline{x}_1 p_1)b'_{mn}(\underline{x}_2,p_2)] \qquad (3.4)$$

(where we allow for a spatial cross covariance calculation). Note that Eqs. (3.3) and (3.4) are slightly biased estimators. The root mean square (r.m.s.) value is simply the square root of the variance, and the correlation between two fields is defined as:

$$\mathrm{Corr}\langle a,b\rangle = \frac{\langle a'(\underline{x}_1 p_1)b'(\underline{x}_2 p_2)\rangle_t}{\langle a'(\underline{x}_1,p_1)^2\rangle_t^{\frac{1}{2}} \langle b'(\underline{x}_2,p_2)^2\rangle_t^{\frac{1}{2}}} \qquad (3.5)$$

The model uses a staggered "B"-grid thus, in some cases a' and b' are not defined at the same geographical location (as is the case with the covariance between either velocity component and the temperature or geopotential height fields). In these cases a model consistent grid transformation was performed.

The model fields are presented here on a polar azimuthal equidistant map projection on which two regions having the same map area also have the same true geographical area. The continental outline of the model was retained for the purpose of consistency.

During the subsequent presentation and discussion of the results, frequent comparisons are made with existing observations. To limit the number of figures presented in this study, the reader will be referred to the literature where these observations are presented.

3.4 The wintertime mean circulation

Before we turn to the discussion of the simulated eddy statistics, it is important that we describe the basic features of the simulated wintertime mean circulation. Although this circulation includes the modifying effect of the eddies it may be viewed as the basic environment in which the latter are generated and maintained. This view is justified by studies like those of Lau (1979b) and Holopainen et al. (1982) which show that it is the mean circulation that plays a dominant role in maintaining local dynamical balances on a seasonal time scale, while the eddies play a secondary role.

The wintertime mean simulated 400 mb geopotential height field is shown in Fig. 3.3a. When this is compared to observations shown in Fig. 3.3b (taken from Blackmon, 1976, Fig. 3b; see also Lau et al., 1981, Fig. II.A.1.d for the 300 mb geopotential height), we find that the model simulates the general character of the stationary wave patterns quite well. In particular we note the position of the three major troughs over North America, Europe, and far eastern Asia, and the three main ridges between them. There are however some differences between the simulation and observations. We find that in the simulation there is only one smooth broad ridge over the Pacific whereas in observations the anticyclonic circulation over the Pacific is confined to the north, over the Aleutians and the Bering Sea, while over the eastern part of the Pacific there exists a weak oceanic trough west of the North American coast and a ridge over the western slopes of the Rockies. Over the Atlantic the model tends to

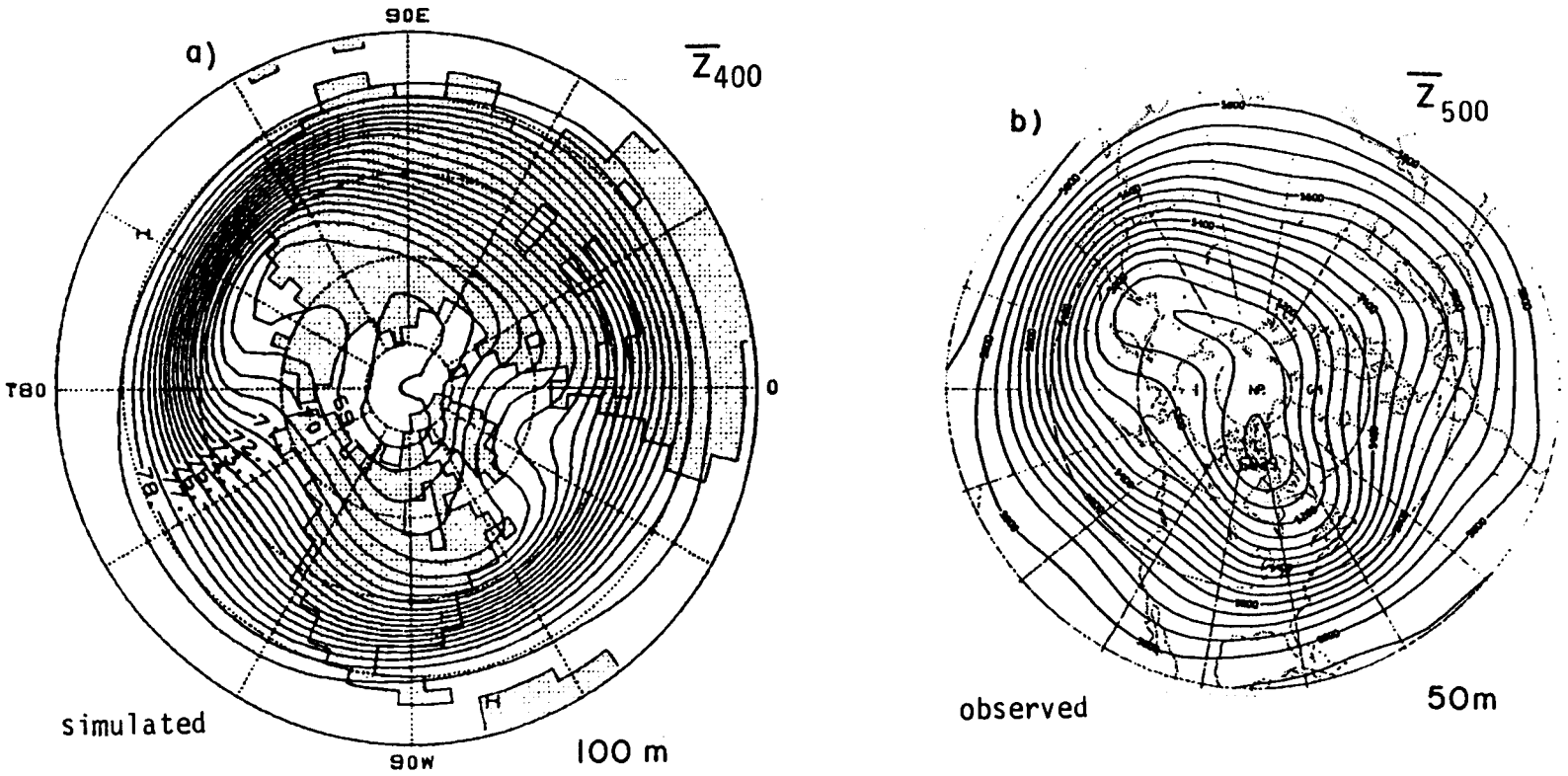

Fig. 3.3. (a) The simulated wintertime mean 400 mb geopotential height field. Contour interval: $.5 \times 10^2$ m. This figure and those that follow in this chapter are based upon 2.5 day low-pass filtered data from ten simulated winters (Dec. through Feb.). (b) The observed 500 mb geopotential height field, from Blackmon (1976), Fig. 3b. Contour interval: 50 m. Here and in all other figures of model results the mapped area extend to the equator. Observations start at 20°N.

overestimate the amplitude of the ridge and underestimate the intensity of geopotential height gradient in the region between the eastern U.S. and Canada on the one hand and Greenland and Iceland on the other (the Atlantic jet stream). Instead we note the more zonal belt of strong gradients between the U.S. and the Iberian Peninsula.

The model simulated 400 mb mean-zonal wind distribution is shown in Fig. 3.4a. The observed field at 500 mb, taken from Blackmon et al. (1977) Fig. 6a is shown in Fig. 3.4b (see also Lau et al. (1981) Fig. II.A.3.b). The model simulates the two major jet streams over the Pacific and Atlantic and the jet over the Mediterranean area. However, consistent with the simulated geopotential height field, we find that the Pacific jet lies westward and southward of its observed position and that the Atlantic jet is much more zonal than in observations. The model also overestimates the intensity of the jet streams, and their meridional gradients are much stronger than in observations. The vertical shear of the mean zonal wind (Fig. 3.5a) is also stronger than in observation and its maxima are shifted westward.

The mean 400 mb meridional wind is shown in Fig. 3.6. We note that the meridional wind distribution over the Pacific and Atlantic is consistent with the broad ridges in the geopotential height field; this differs somewhat from observations (Lau et al., 1981, Fig. II.A.4.b).

At this point we may try to consider the baroclinic instability of the wintertime circulation. In his study of baroclinic instability, Phillips (1954) determined that for the case of a homogeneous zonal current on a β-plane the flow will become baroclinically unstable if the vertical wind shear is stronger than a threshold value determined by β and the static stability of the flow. Frederiksen (1980) has generalized Phillips' criterion for a zonally and meridionally varying basic state in a spherical geometry, and showed that the meridional gradient of the basic current's absolute vorticity replaces the original β. The simulated wintertime mean absolute vorticity is shown in Fig. 3.5b. When this field is compared to observations (Lau et al., 1981, Fig. II-A.7) we find that the simulated meridional

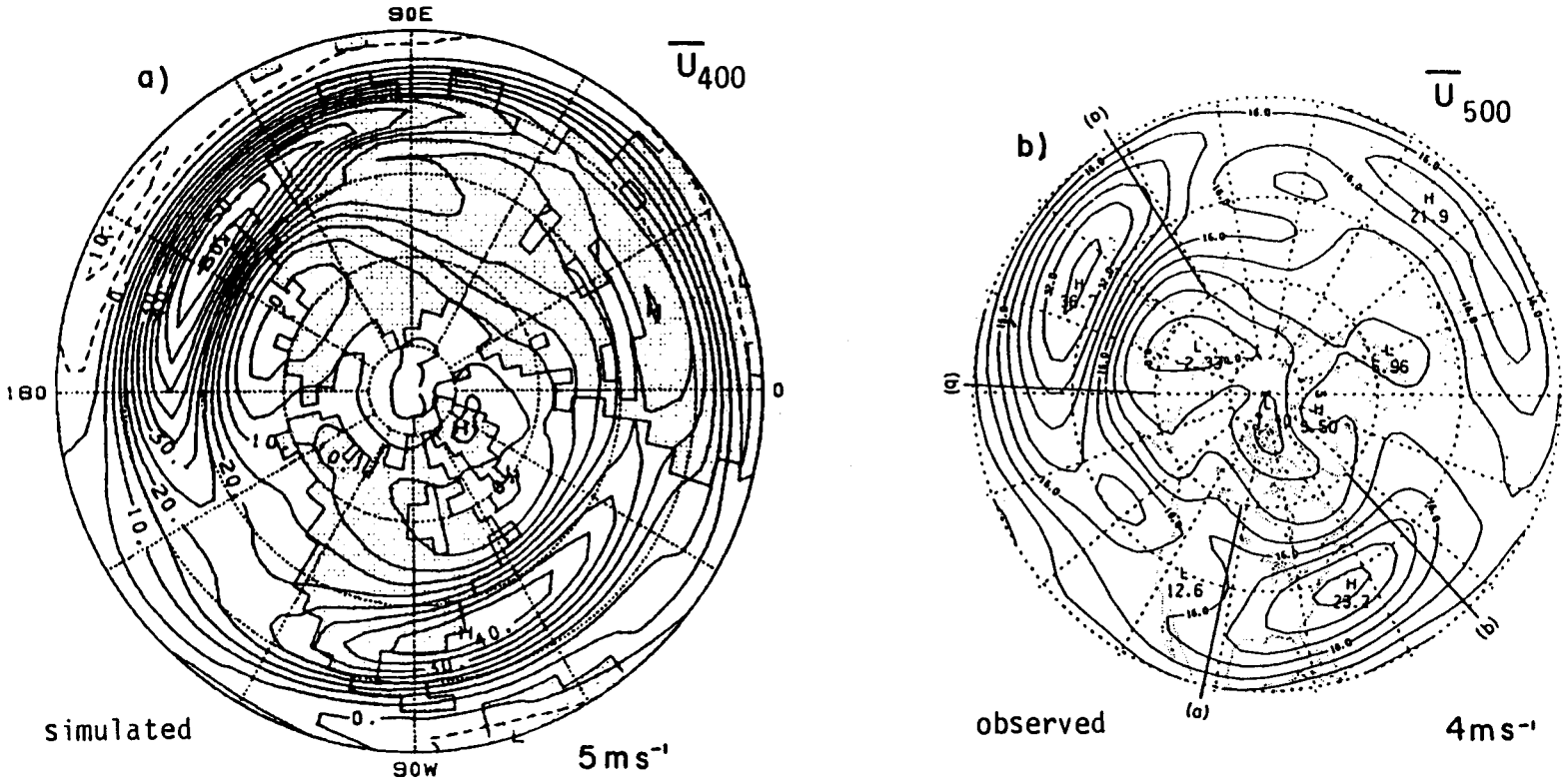

Fig. 3.4. (a) The simulated wintertime mean 400 mb zonal wind component. Contour interval: 5 m s^{-1}; negative contours are dashed. (b) As in (a) but for observations at 500 mb (taken from Blackmon et al, 1977, Fig. 6a). Contour interval 4 ms^{-1}. Observations start at 20°N.

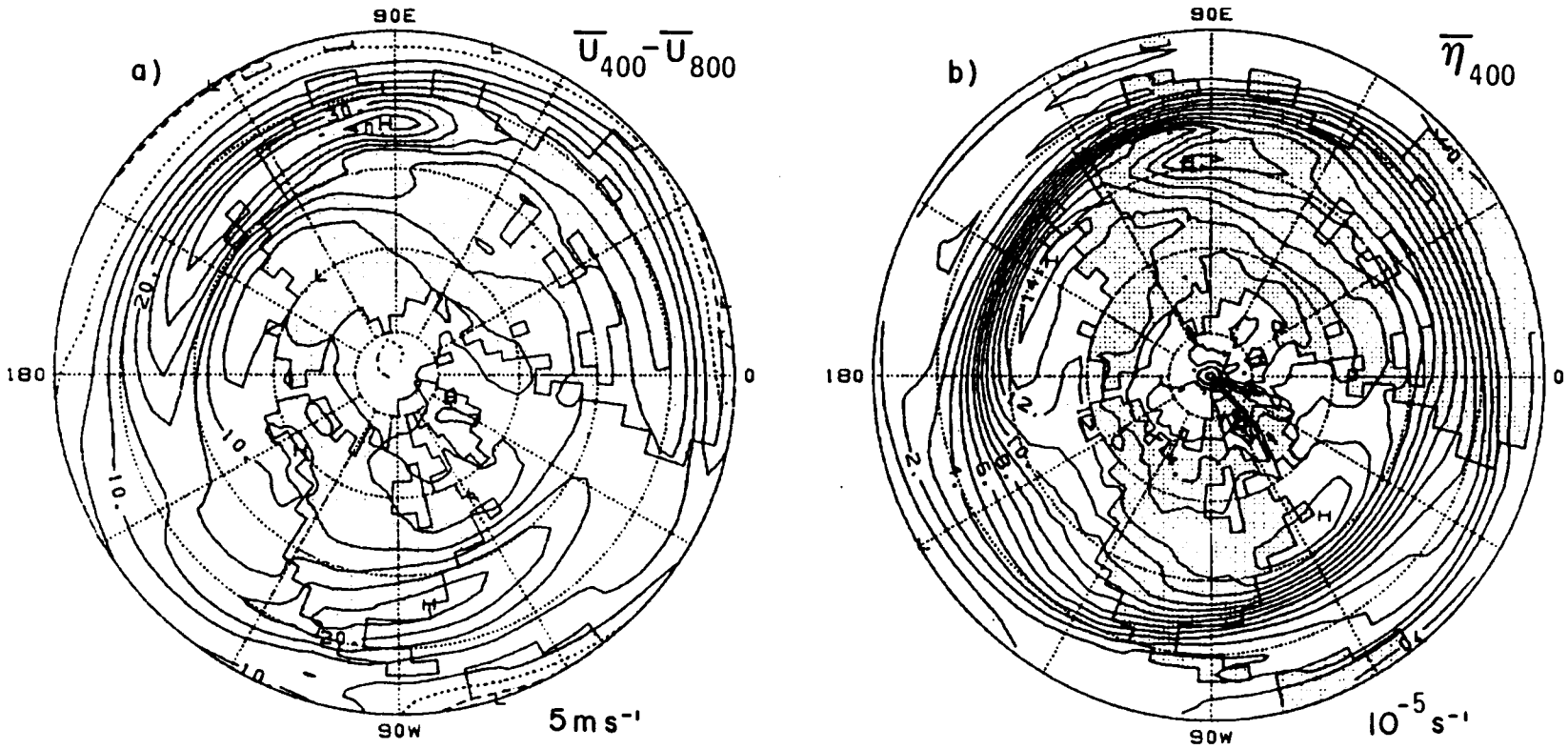

Fig. 3.5. The simulated wintertime means of the: (a) vertical zonal wind shear as measured by the difference between the 400 and 800 mb zonal wind. (b) 400 mb absolute vorticity field. Contour interval: (a) 5 m s^{-1}, (b) 10^{-5} s^{-1}; in (a) zero line is dotted and negative contours are dashed.

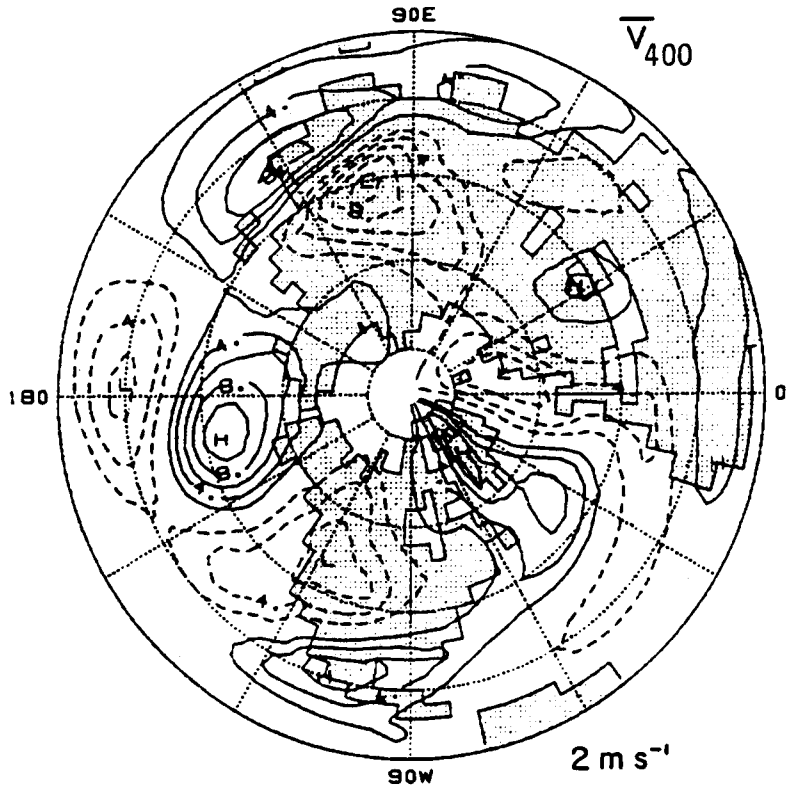

Fig. 3.6. The simulated wintertime mean 400 mb meridional wind component. Contour interval: 2 m s^{-1}; negative contours are dashed.

gradient of absolute vorticity in the regions of strong vertical shear is twice as large as observed. This effect should offset the model's stronger model vertical shear and thus we should not expect the model's baroclinic regions to extend much beyond the jet streaks. The model and observations should differ in the relative location of the baroclinic zones. We expect these zones to be shifted eastward and southward from their observed locations in accordance with the shift in the locations of the major jet-stream maxima.

In this context we would also like to draw the reader's attention to the possibility of high-latitude baroclinic instability in the regions of enhanced vertical shear and weak absolute vorticity gradients of the seasonally averaged circulation over Siberia, Greenland and especially over the extreme North Pacific ocean basin. In these high latitudes where the Coriolis parameter is relatively large, instability will occur at weaker shears than those encountered at middle latitudes (see also Pedloski, 1964 and Moura and Stone, 1976).

Figure 3.7 presents the negative of the vertical pressure velocity field at 400 mb (i.e. upward motion is positive). This field carries the clear signature of the model's orography (Fig. 3.1) but also shows a broad zonal band of sinking motion over the subtropics and rising motion over high latitudes. When comparing this field with observations (Lau, 1979a, Fig. 1) we notice that the model tends to somewhat overestimate the sinking motions and underestimates the rising motions. The flow in the vicinity of the western mountain ridges of North America is different from the observed, with the dipole-like feature in the model oriented northwest to southeast instead of the observed west-to-east orientation. This is consistent with the difference in the Pacific geopotential height distribution in the two data sets. Interestingly observations do not show the considerable vertical motion over Greenland where the mountain chain is quite high, while in the model's simulation, there exists a strong dipole there. It should be remembered that the vertical motion field presented by Lau is not directly observed but was derived from observations using an NWP model.

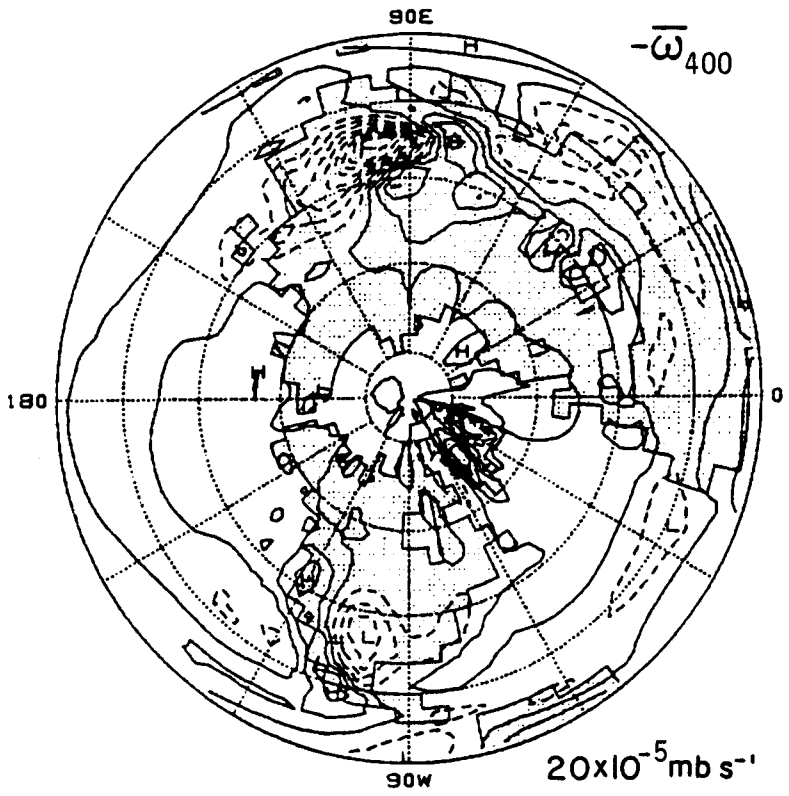

Fig. 3.7. The simulated wintertime mean 400 mb negative of vertical pressure velocity. Contour interval 20×10^{-5} mb s^{-1}; negative contours are dashed.

Finally the wintertime averaged temperature field at the 800 mb level is shown in Fig. 3.8. We notice that the phase and intensity of the major continental troughs and oceanic ridges are quite well simulated (see Lau et al., 1981, Fig. II.A.2.b).

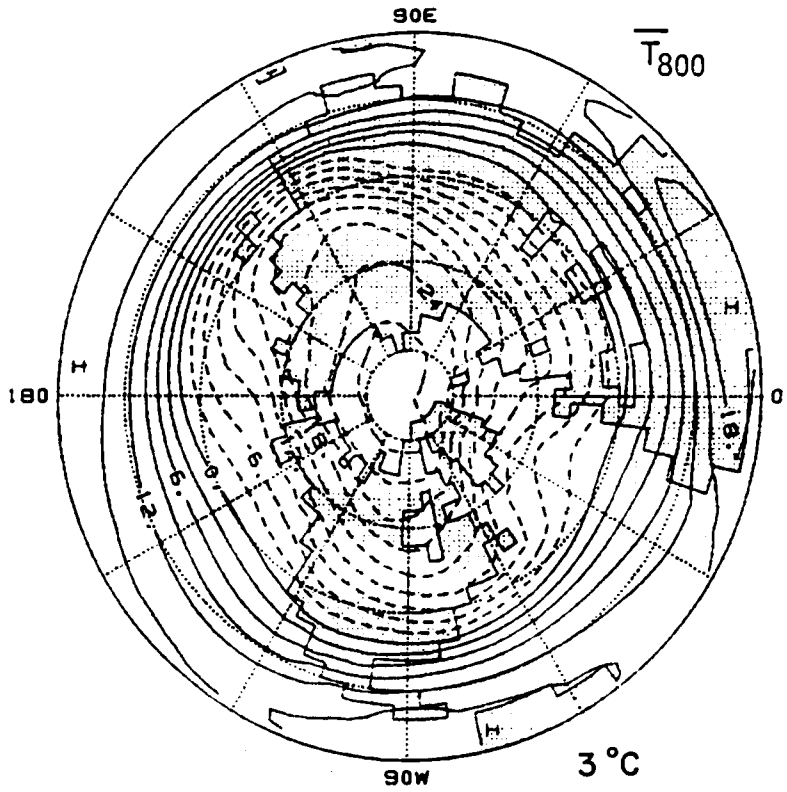

Fig. 3.8. The simulated wintertime mean 800 mb temperature. Contour interval 3 deg C; negative contours are dashed.

CHAPTER 4: STATISTICAL PROPERTIES OF THE MODEL'S GEOPOTENTIAL HEIGHT FIELD

Atmospheric low-frequency variability has been studied mainly through the analysis of geopotential height data. This approach was justified a-posteriori by the tendency of these fluctuations to show equivalent barotropic and quasi-geostrophic behavior. The r.m.s. of the geopotential height fluctuations (usually that at 500 mb) has been used to measure the eddy intensity and to identify the regions of high eddy activity (e.g., Sawyer, 1970; Blackmon, 1976). The shape, spatial scales, and time behavior of the disturbances causing these fluctuations have been inferred from spatial correlation analysis (e.g., Wallace and Gutzler, 1981; Blackmon et al., 1984a and b). In the following pages, results of similar types of analyses applied to the simulated geopotential height field will be presented. These results will serve as an overview of the properties of the model's wintertime variability.

4.1 Spatial distribution of time fluctuations

Figure 4.1a presents the distribution of the total, simulated 400 mb r.m.s. geopotential height and Fig. 4.1b. The observed counterpart at 500 mb from Blackmon 1976 (see also Lau et al., 1981 Fig. II.B.1.c). We notice the regional differences in the intensity of the geopotential height time fluctuations. The maxima occur at middle and high latitudes where the major stationary ridges are located. This is in general agreement with observations particularly in the case of the Pacific and Siberian maxima. The major discrepancy between the model and the observations is in the r.m.s. distribution over the North Atlantic basin. Here the model has two distinct but relatively weak local maxima instead of the single strong observed maximum. Other discrepancies are the 10 degree northward shift in the location of the Pacific maximum and the 10 degree southward shift of the Siberian maximum compared to observations. There are also relatively stronger r.m.s. deviations in the model over the Sea of Japan.

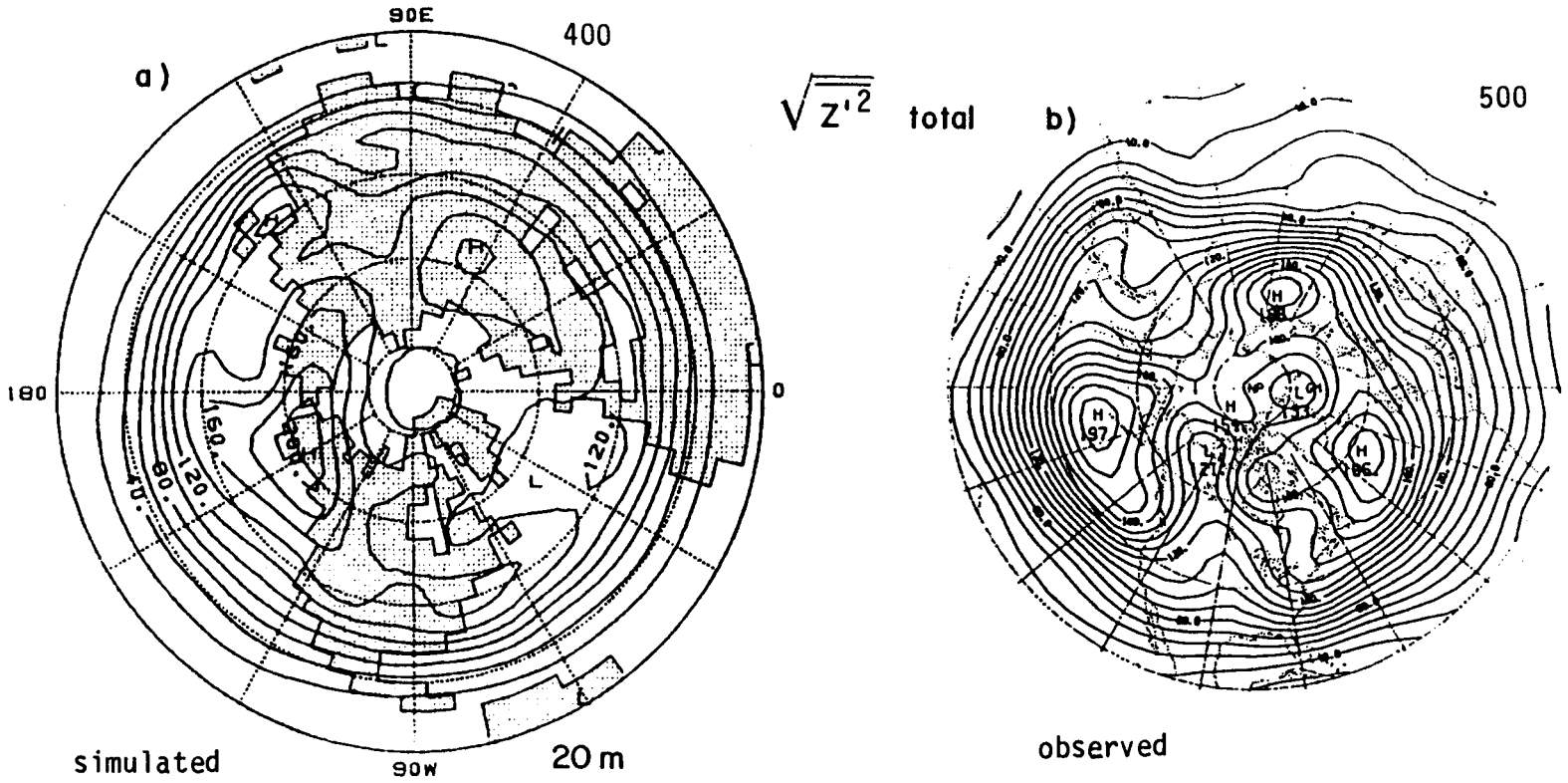

Fig. 4.1. Simulated vs. observed mid-tropospheric r.m.s. geopotential height: (a) Simulated 2.5 day low-pass. (b) Observed unfiltered. (c) Simulated 2.5-10 day anomaly. (d) Observed 2.5-6 day anomaly. (e) Simulated 10 day low-pass anomaly. (f) Observed 10 day low-pass anomaly. Simulated data are at 400 mb and observations are at 500 mb. Observations are from Blackmon (1976). Contour interval is 10 m except in (a) and (e) where it is 20 m. Observations start at 20°N.

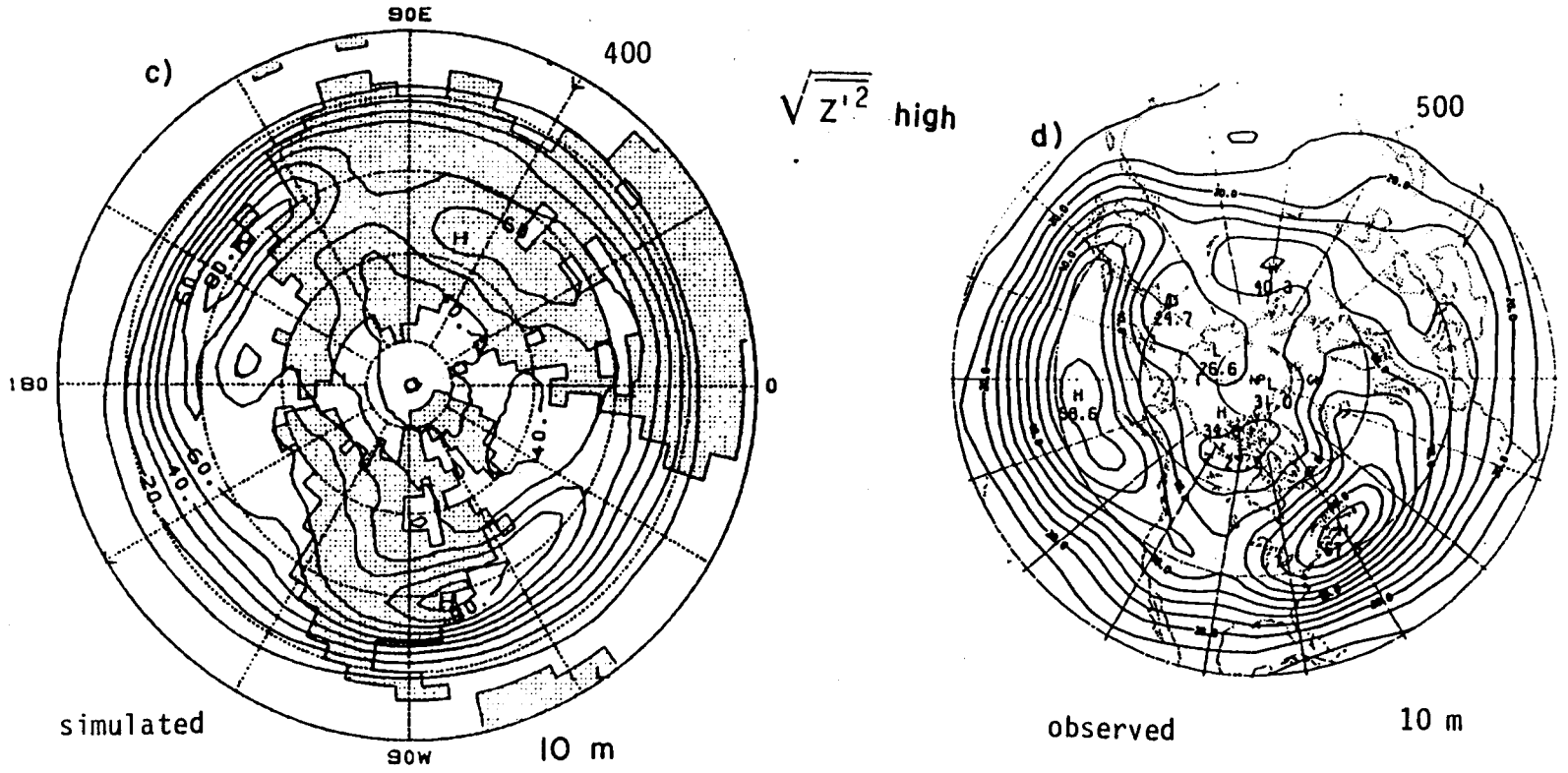

Fig. 4.1 (continued)

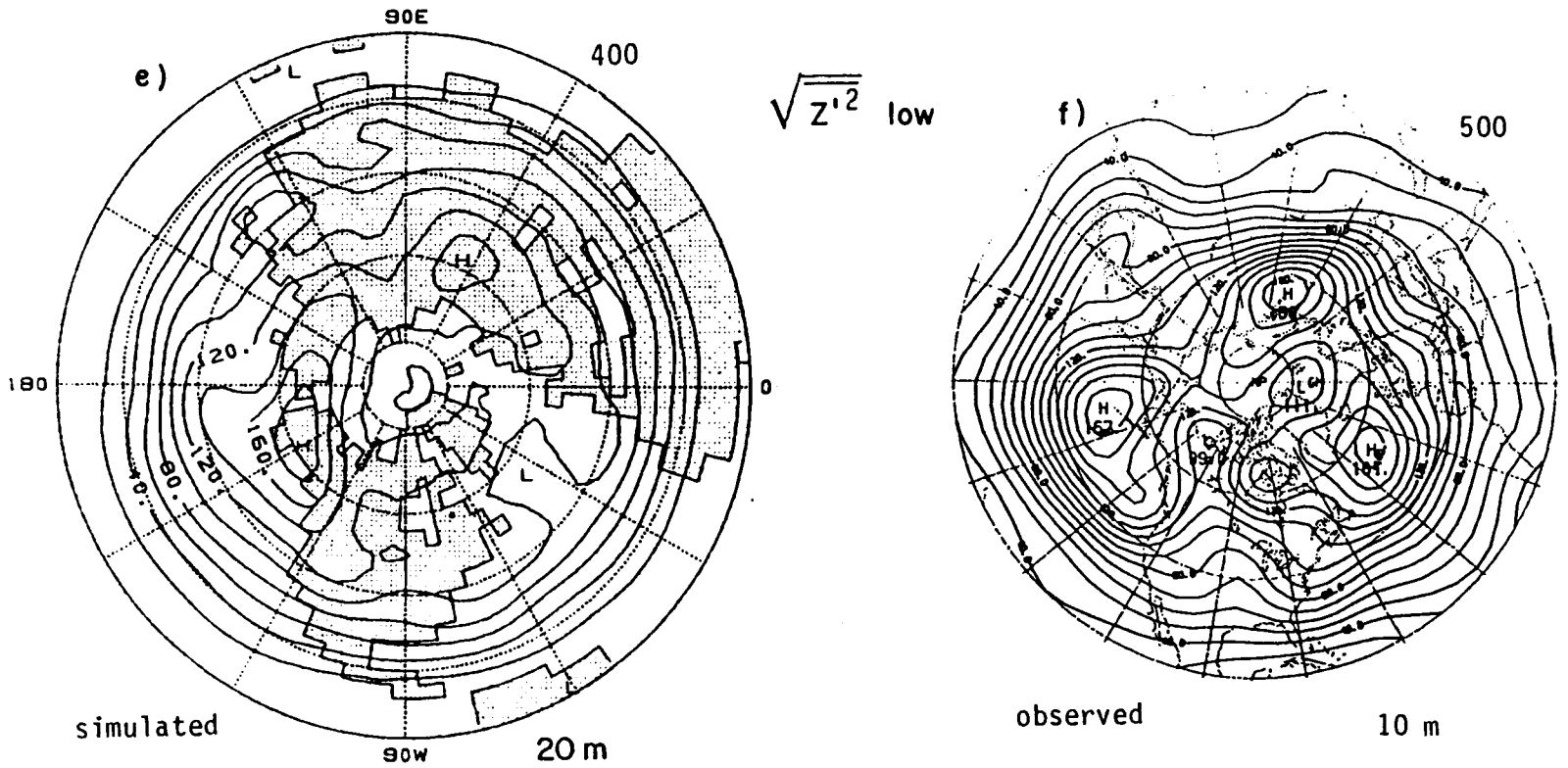

Fig. 4.1 (continued)

It is likely that the peculiar model r.m.s. distribution over the Atlantic is related to the difference between the simulated and observed stationary wave pattern there.

Figures 4.1c and e present the r.m.s. deviations of the model's 400 mb geopotential height field for the two frequency bands addressed in this study, namely the high-frequency fluctuations (2.5 to 10 day band) and the low-frequency fluctuations (10 day lowpass), respectively. As expected, the low-pass fluctuations dominate the r.m.s. field. This has already been noted by Sawyer (1970) and Blackmon (1976). To illustrate this fact we have calculated the ratio between the low-pass and the total r.m.s. fields. The results of this calculation are presented in Fig. 4.2. It is seen that the low-pass r.m.s. deviations have values between 70 and 90% of the total. The regions where this ratio is relatively small are obviously those where the high-frequency r.m.s. field reaches its maxima. These regions were referred to by Blackmon et al. (1977) as the "storm tracks" regions, where the eddies show properties which are characteristic of migratory baroclinic weather disturbances. As in observations (Fig. 4.1d and 4.1f taken from Blackmon, 1976), the maxima of the r.m.s. fields in the two frequency bands are well separated from each other, with the high-frequency storm tracks lying southwestward of the regional low-frequency maxima.

Here again we find some discrepancies between the model and observations. In the low frequencies the patterns are quite similar to those of the total r.m.s. field, thus we find the already-noted shifts in the location of the major "centers of action." The distribution of the r.m.s. field over the Atlantic is poorly simulated. The model's low-frequency fluctuations are too strong over the western Atlantic and too weak over its central and eastern parts. We also note that the spurious local maximum over the Sea of Japan appears in the low-pass pattern suggesting a low-frequency origin. In the high-frequency band, we notice the westward and southward location of the storm tracks relative to observations. These discrepancies amount to about 10 degrees of latitude and up to 40 degrees of longitude; the longitudinal difference is especially large over the Pacific. In

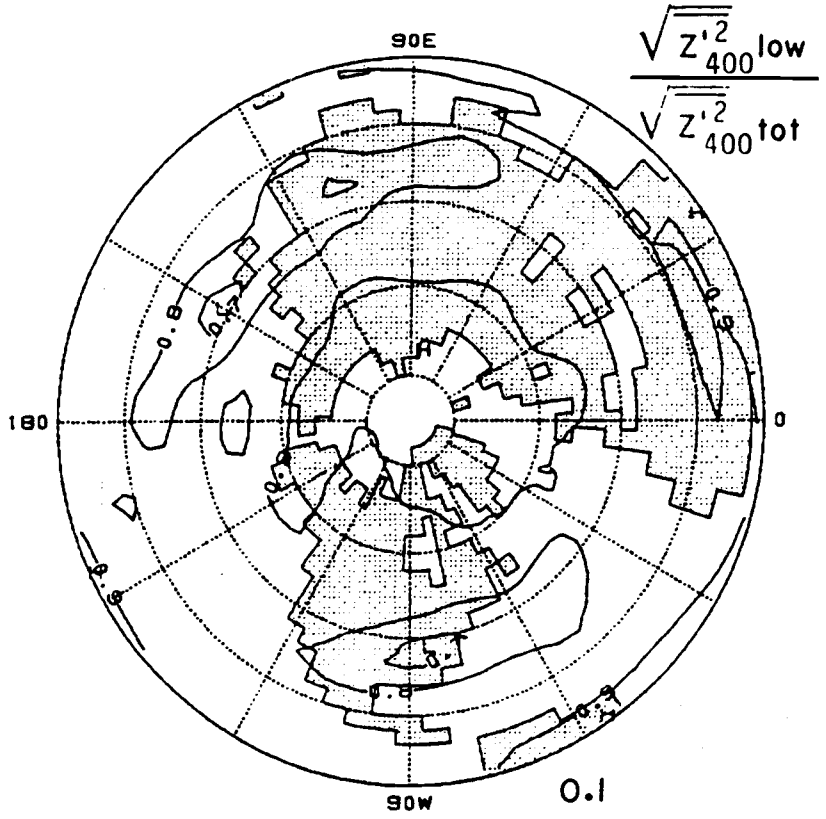

Fig. 4.2. The ratio between the simulated 10 day low-pass anomaly wintertime 400 mb geopotential height r.m.s and that of the total 2.5 day low-pass anomaly. Contour interval: 0.1.

observations the storm tracks are located some 10 degrees longitude downstream from the jet maximum and about 5 degrees northward. In the simulation the latitudinal shift is similar but the jet maxima and the maxima of the high-frequency r.m.s. field lie on the same meridian. Other differences are the shorter eastward extent of the model's Pacific storm track compared to observations, the lack of the observed north-eastward extension of the Atlantic storm track in the simulation and the large simulated r.m.s. values over the west coast of North America. Some of the discrepancies in the simulated high frequency r.m.s. distribution are consistent with the structure of the model's mean wintertime circulation (see further discussion in Chapter 5).

Blackmon et al. (1979) have studied the vertical structure of the observed time fluctuations by correlating the 500 mb geopotential height fields to that at 1000 mb. They have noted the large regional dependence of the correlation field and the differences between high- and low-frequency fluctuations (see their Figs. 2b and c). In this study we have correlated the 400 and 800 mb geopotential height fields in the two eddy categories (Fig. 4.3a and b). The results are in good agreement with observations, showing regions of relatively high correlations (barotropy) over the oceans and regions of relatively low and even negative correlation (baroclinicity) over the continents, in the two frequency bands. The baroclinicity is particularly strong on the lee sides of the major orographic obstacles (part of it may have resulted from the extrapolation from the elevated σ levels to the 800 mb level in these regions). The vertical structure of the high frequency eddies (Fig. 4.3a) changes from relatively baroclinic over the western oceans to barotropic over the eastern oceans. This agrees with observations and is consistent with the theoretical life cycle of baroclinic eddies (Simmons and Hoskins, 1978). Low-frequency eddies are more barotropic than their high-frequency counterparts almost everywhere, but even they show strong baroclinicity over the continents. In both frequency bands we find that the degree of correlation between the 400 and the 800 mb geopotential height field is relatively higher over regions of high 400 mb r.m.s. values, an indication that the stronger time fluctuations are caused by vertically coherent and penetrating systems.

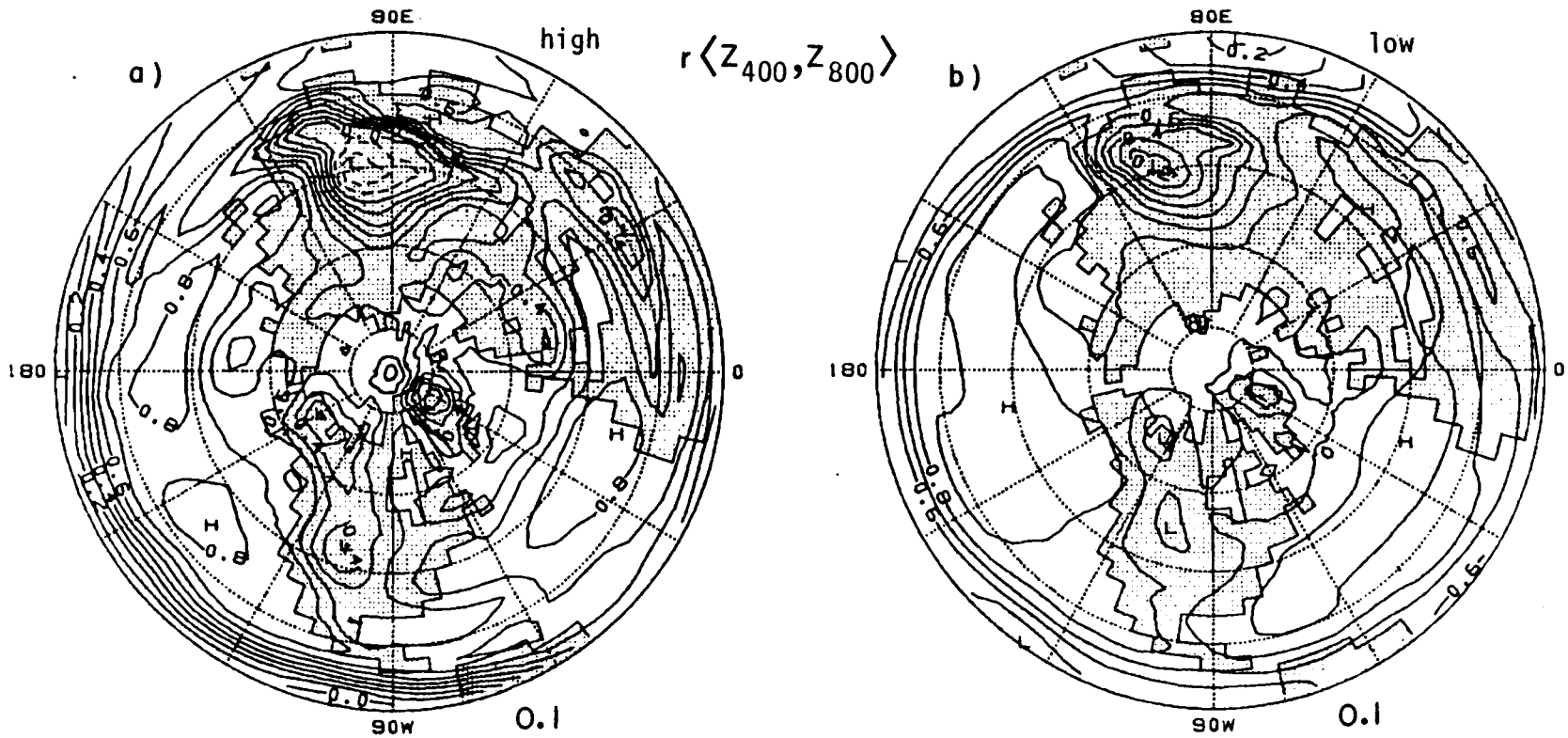

Fig. 4.3. The wintertime local correlation between the simulated 400 and 800 mb geopotential height. (a) 2.5 to 10 day fluctuations. (b) 10 day low-pass fluctuations. Contour interval: 0.1; negative contours are dashed.

4.2 Horizontal structure of geopotential height fluctuations

We now turn our attention to the horizontal structure of the disturbances causing the model geopotential height fluctuations. This structure can be unveiled by using simultaneous spatial correlation analysis in the form referred to as one-point-correlation analysis. In this method the time series of geopotential height anomalies at a given field point, the so-called "base grid point," is correlated against all other field points. If the fluctuations at the base grid point are completely uncorrelated to those centered on any other point, the resulting pattern will resemble a 'δ' function at the base point. If, on the other hand, the fluctuations are caused by large scale patterns such as waves or standing oscillations, the pattern with the largest amount of variance will appear. Finite sampling, noise, and the other patterns in the field will smooth or distort the prominent pattern. Thus, a standing wave which theoretically would appear as a step function (with values of +1 surrounding the base point and -1 at the other side of the surrounding nodal lines), will appear as a dipole-like pattern with values changing gradually from 1 at the base point and a negative value with magnitude smaller than 1 at other locations. The distance between the base grid point and the centers of the correlation field minimum offers a rough measure of half the wavelength of the dominant wave disturbances.

In Fig. 4.4 we have shown the result of applying the one-point-correlation analysis method to a model grid point at 34°N, 145°W. In Fig. 4.4a, we have used the total 400 mb geopotential height anomaly as our time series. We note that the emerging pattern resembles a large-scale wave with five extrema representing the wave troughs and crests and four nodes in between. The zonal scale of the wave may be inferred from distance between every other node along a latitude circle. In this case, the wave length along the 30°N parallel is about 6000 km which corresponds to a zonal wavenumber 6. In the meridional direction there appears to be one nodal point on each meridian. Thus, the wave's meridional scale is somewhat larger than the zonal scale. This is also reflected in the slight south-to-north

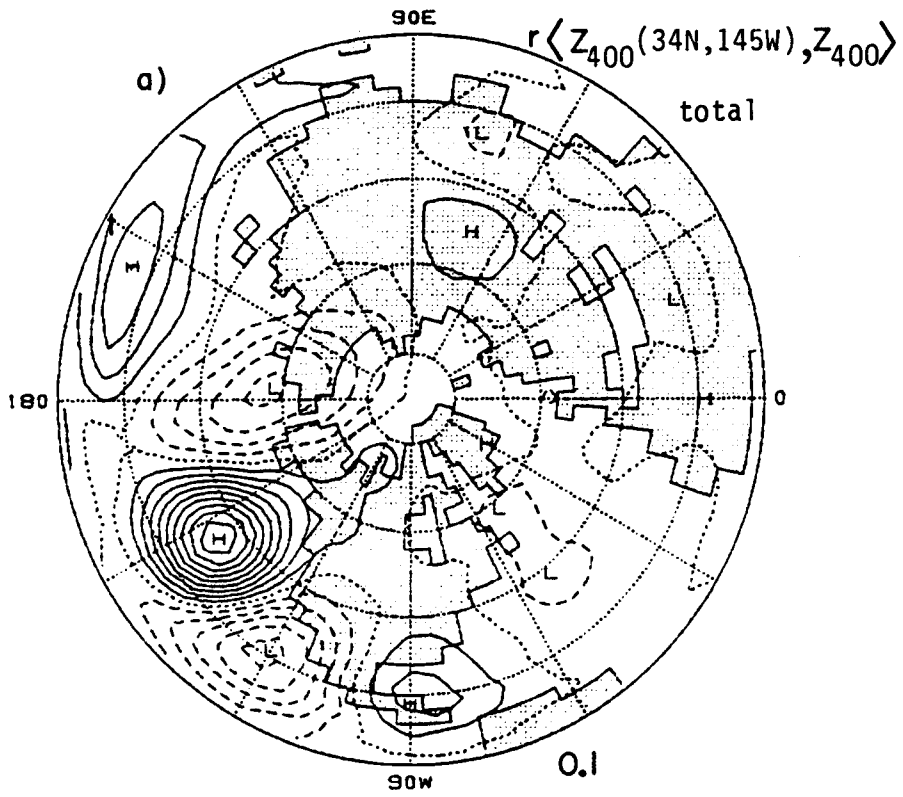

Fig. 4.4. Simultaneous correlation of the simulated 400 mb geopotential height anomaly at 34°N 145°W and that at all other grid points. (a) 2.5 day low-pass fluctuations. (b) 10 day low-pass fluctuations. (c) 2.5 to 10 day fluctuations. Contour interval: 0.1; negative contours are dashed and the zero line is dotted.

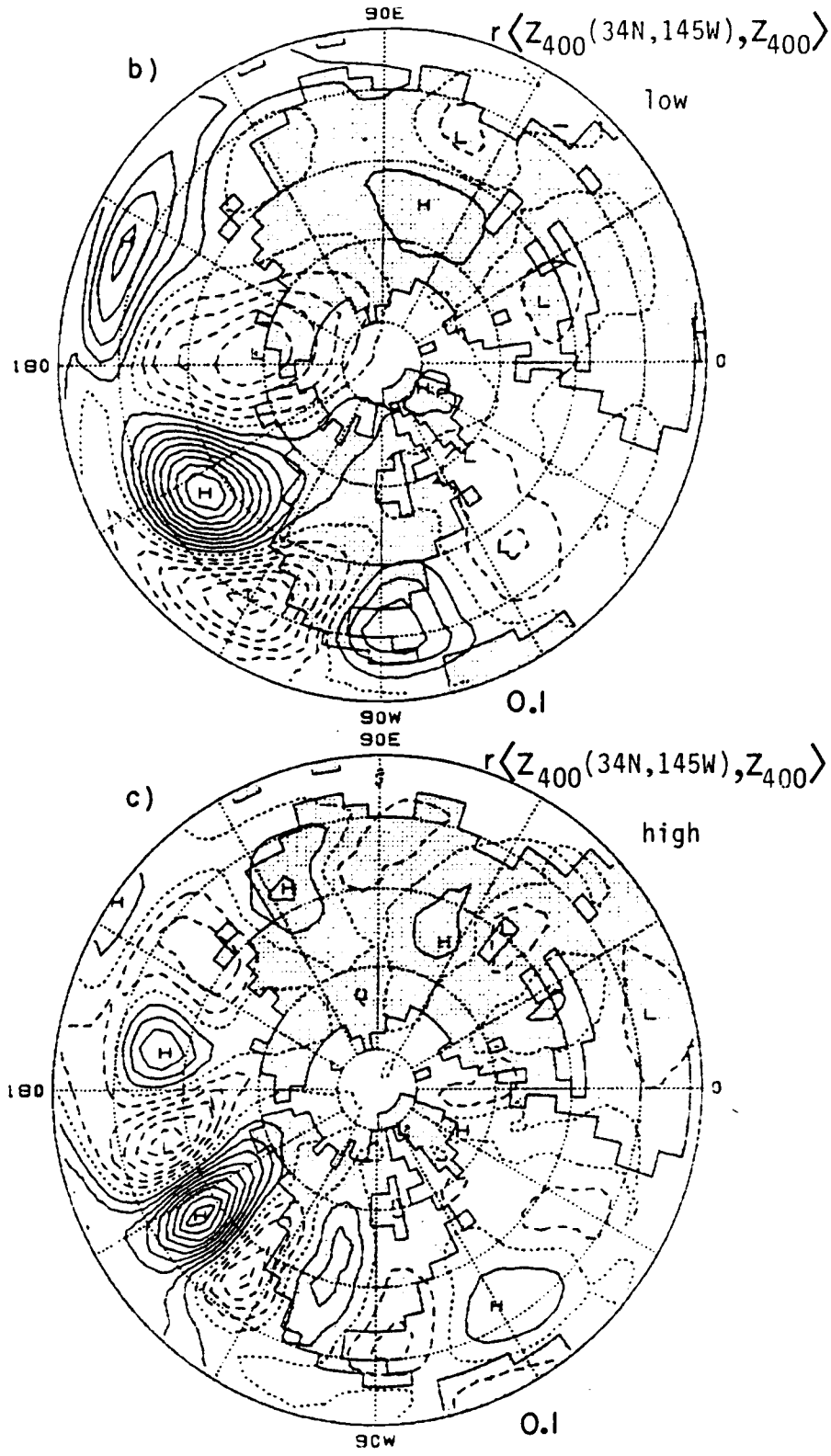

Fig. 4.4 (continued)

elongation of the patterns. Finally we note that the locus of all extrema is a line that curves in a great-circle-like arc and is thus not parallel to a latitude circle.

Using only the low-frequency part of the signal we obtain the result shown in Fig. 4.4b. We notice that the picture is generally similar to the previous one. This is not surprising since we have already seen that most of the geopotential height variance lies in the low-frequencies. The removal of the high-frequency "noise" results in larger values at the remote extrema and a slight increase in the area of positive correlations surrounding the base point.

Figure 4.4c shows the one-point-correlation field of the same base point, but for the high-frequency part of the signal. Removing the masking effect of the low-frequency fluctuations reveals that the underlying disturbance is still wave-like but that its structure is different. The pattern is arranged almost exactly along a latitude circle. Its wavelength is about 4000 km at 30°N which is equivalent to a zonal wavenumber of 9. We now find no nodes on the meridians which indicates a meridional scale that is much larger than the zonal scale.

To generalize our observations and acquire an overview of the typical characteristics of the eddies over the middle latitude northern hemisphere middle latitudes, we have repeated this type of analysis every 15 degrees longitude around the whole latitude circle of 30°N and along the latitude circles at ±4 degrees and ±8 degrees away. We have then composited the results by rotating all base grid points to the 90°W meridian, shifting them also north or south as needed to the 30°N parallel. The result is thus equivalent to a "zonally averaged" one-point-correlation field in the 20 to 40°N latitude belt and does not reflect existing longitudinal variation in the eddy structure (see later in Chapter 5). The composites for both the high- and low-frequency bands are shown in Fig. 4.5a and b respectively and are qualitatively similar to the single case we have studied earlier. An added dimension to these results is gained by repeating the composite, but this time correlating the base grid point value at 400 mb with the 800 mb geopotential height anomaly at all other field points. The

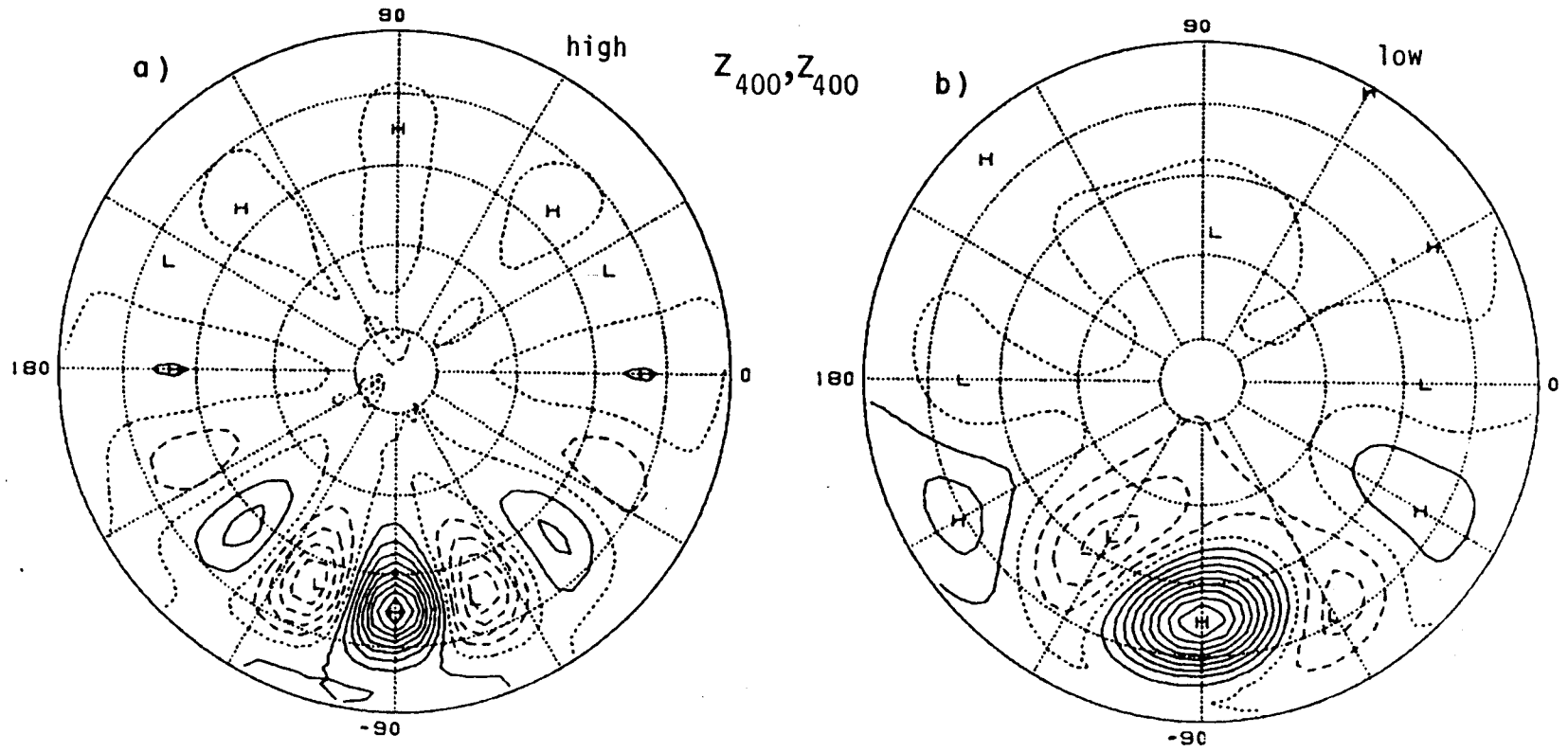

Fig. 4.5. Composite of simultaneous one-point-correlation maps of the simulated 400 mb geopotential height with base-grid-points within the 20 to 40°N latitude belt (see text for further details). (a) 2.5 to 10 day fluctuations. (b) 10 day low-pass fluctuations. Contour interval: 0.1; negative contours are dashed and the zero line is dotted.

results shown in Fig. 4.6 are an indication to the vertical structure of the disturbances. In the high-frequency band (Fig. 4.6 a) the structure is baroclinic, with the extrema shifted eastward about 1/8 of a wave-length. In contrast, the low-frequency disturbance (Fig. 4.6 b) is much more barotropic (the shift is equivalent to about 1/12 of a wave length).

When the composite is repeated for the 40 to 60°N latitude belt, the high-frequency pattern (Fig. 4.7a) does not change substantially. Its zonal scale is still about wavenumber 9, much smaller than its meridional scale. The pattern is less parallel to a latitude circle and its intensity and lateral extent have been reduced, an indication that its intensity and frequency of occurrence has been reduced. A similar weakening of the pattern is also noticeable in the low-frequency composite (Fig. 4.7b), but here additional differences are evident. The meridional scale has now decreased with an indication of a complete wave cycle along one quarter of a meridian. In the zonal direction, there is an indication of the existence of lower harmonics, in particular, a wavenumber 2 signature. At the center of the pattern there is still a dominant imprint of a wavenumber 6 curving along a great-circle-like arc from 30°N and 60° west of the bast-grid-point to 50°N and back to 20°N and about 60° east of the base-grid-point.

The 40 to 60°N composite of the 400 to 800 mb one-point-correlations is shown in Fig. 4.8. The results for the high and low frequencies (parts a and b of the figure, respectively) are qualitatively the same as in the 20 to 40°N composite.

Finally, the composites at even higher latitudes, namely the 60 to 80°N belt, are presented in Fig. 4.9. Since there is not much high-frequency activity over these latitudes (see Fig. 4.1c) we are not surprised to find the high-frequency composite (Fig. 4.5a) looking as if it were based on random spatially uncorrelated noise. In the low-frequency composite (Fig. 4.9b) we find an indication of a regional see-saw between low and high latitudes. That this is the character of the underlying disturbance is supported by compositing the low-frequency one-point-correlation fields over the Equator to 20°N

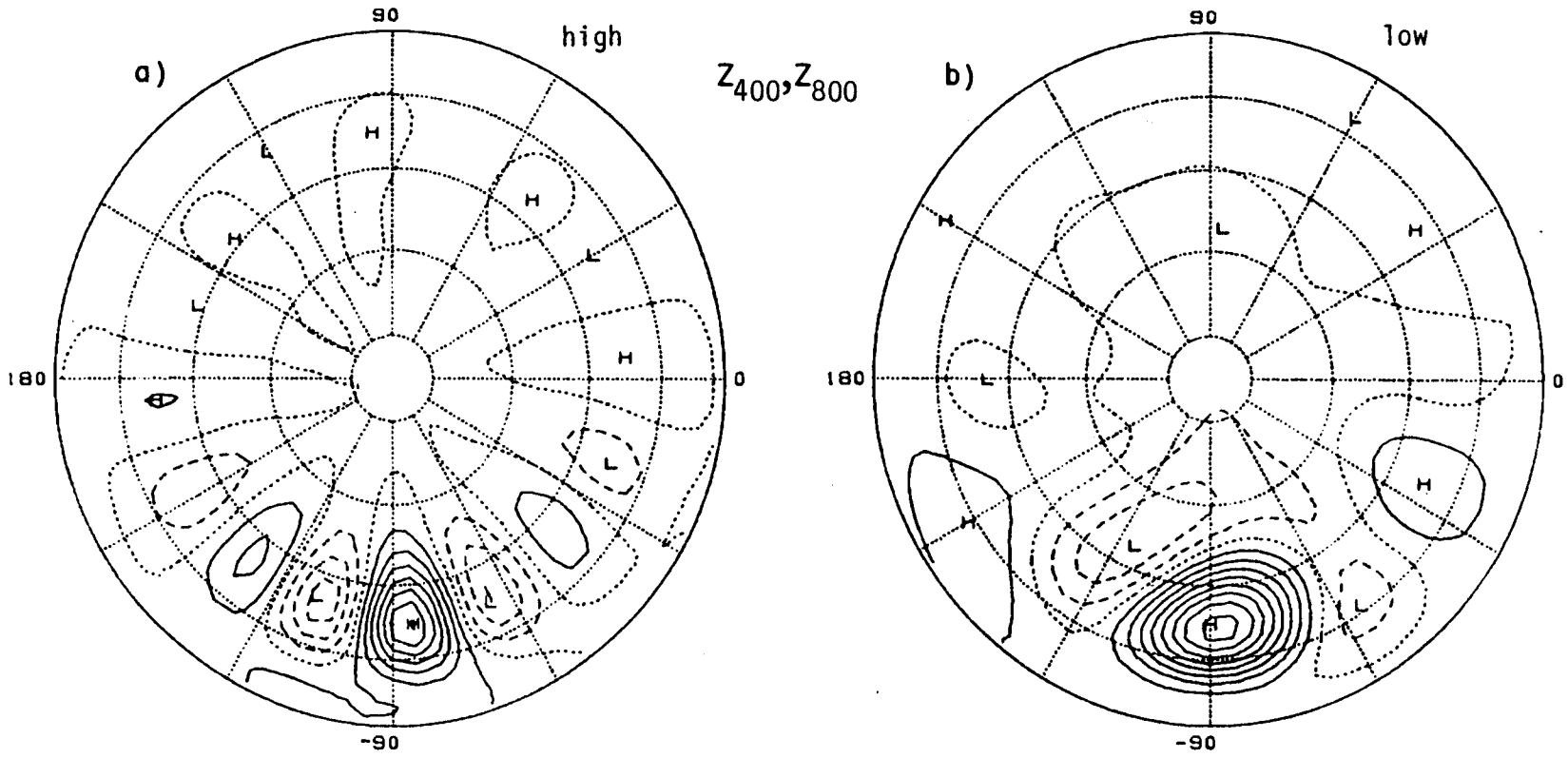

Fig. 4.6. Composite of simultaneous one-point-correlations of the 400 to 800 mb geopotential height anomalies (400 mb at base point and 800 mb elsewhere). Base grid points are within the 20 to 40°N latitude belt (see text for further details). (a) 2.5 to 10 day fluctuations. (b) 10 day low-pass fluctuations. Contour interval: 0.1; negative contours are dashed and the zero line is dotted.

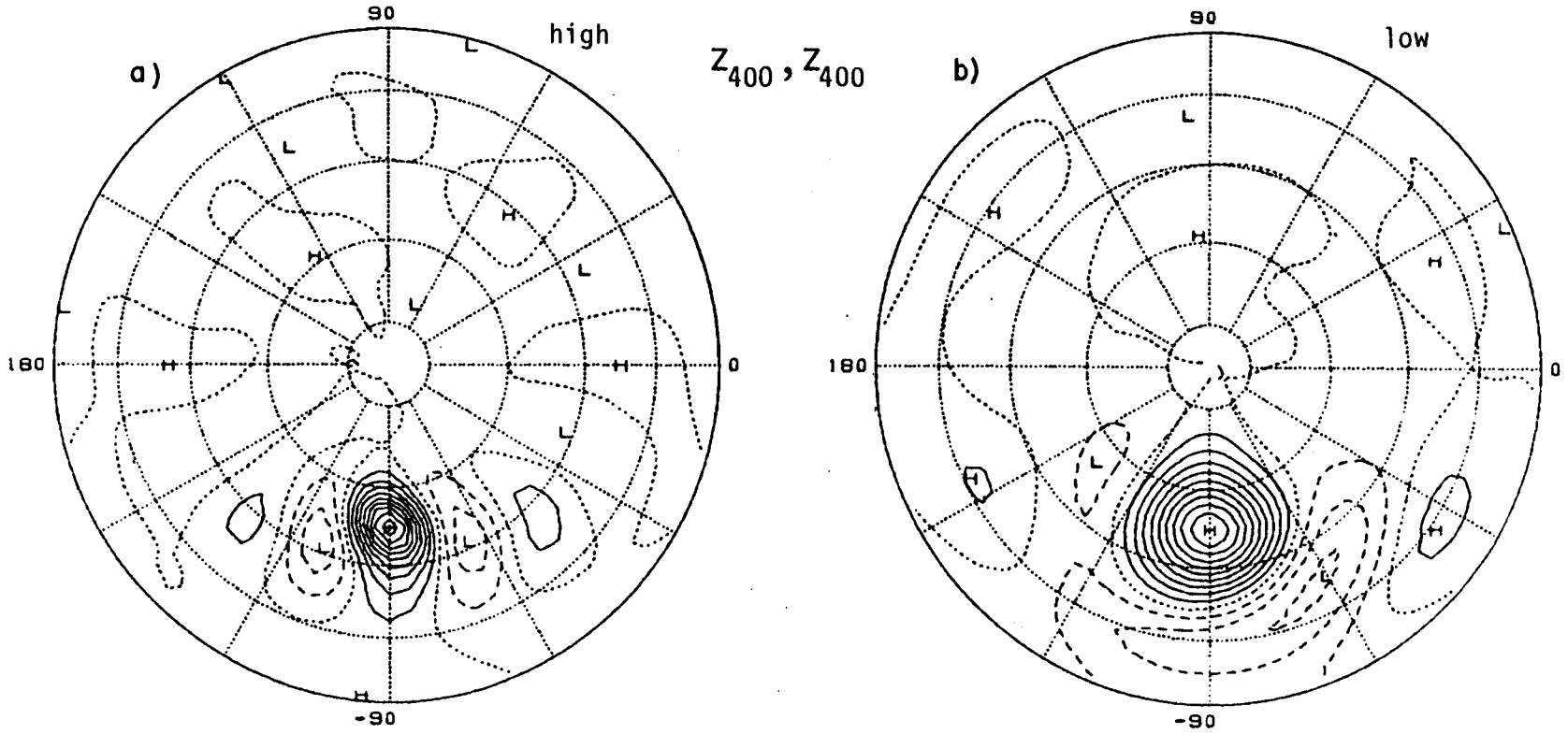

Fig. 4.7. Composite of simultaneous one-point-correlation maps of the simulated 400 mb geopotential height with base-grid-points within the 40 to 60°N latitude belt (see text for further details). (a) 2.5 to 10 day fluctuations. (b) 10 day low-pass fluctuations. Contour interval: 0.1; negative contours are dashed and the zero line is dotted.

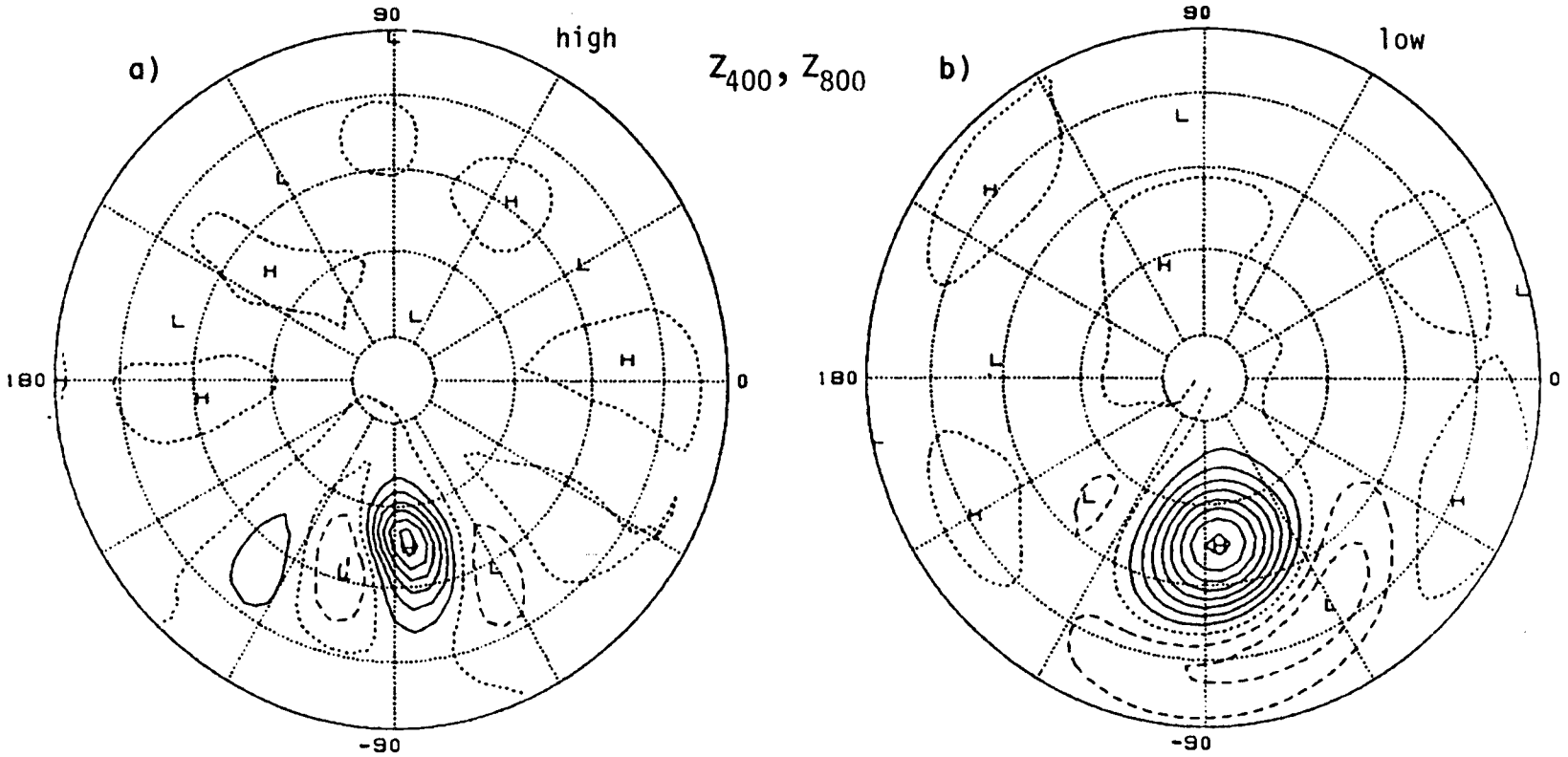

Fig. 4.8. Composite of simultaneous one-point-correlations of the 400 to 800 mb geopotential height anomalies (400 mb at base point and 800 mb elsewhere). Base grid points are within the 40 to 60°N latitude belt (see text for further details). (a) 2.5 to 10 day fluctuations. (b) 10 day low-pass fluctuations. Contour interval: 0.1; negative contours are dashed and the zero line is dotted.

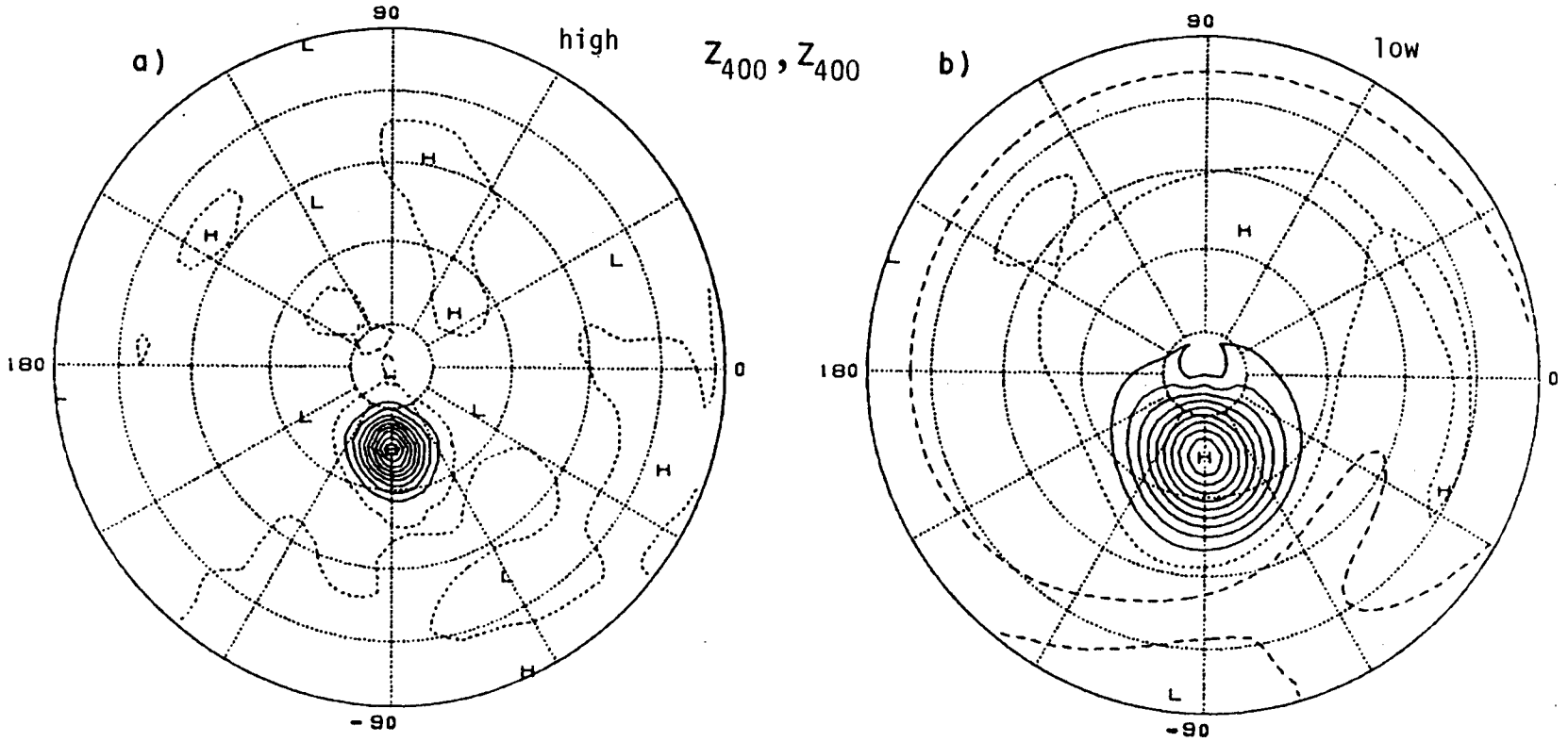

Fig. 4.9. Composite of simultaneous one-point-correlations of the 400 to 800 mb geopotential height anomalies with base grid points are within the 60 to 80°N latitude belt (see text for further details). (a) 2.5 to 10 day fluctuations. (b) 10 day low-pass fluctuations. Contour interval: 0.1; negative contours are dashed and the zero line is dotted.

latitude belt. The results shown in 4.10 are an almost exact reversal of the high-latitude composite of Fig. 4.9b.

4.3 Temporal properties of geopotential height fluctuations

The temporal behavior of the disturbances causing the geopotential height fluctuations can be studied through the use of time-lagged one-point-correlation analysis. This method was used by Sawyer (1970), Lau (1981), and Blackmon et al. (1984b) and involves introducing a time lag between the height series at the base grid point and all the other field points. We have chosen to present the results at two different time lags of ±3 days. A shift in the centers of high and low correlations between these figures will indicate phase propagation. These results will again be presented in the form of 20 degrees latitude belt composites.

Figure 4.11a shows the high-frequency composite when the base grid point leads all others by 3 days (this is the -3 day lag composite) and Fig. 4.11b shows the high-frequency composite with the base point lagging all other points by 3 days (the +3 day lag composite). Comparing these figures to each other and to Fig. 4.5a (the zero-day-lag composite) we conclude that what we see is an eastward moving wave disturbance. Note that the structure of the wave is virtually unchanged by the time shifting. Also note that in three days the high-correlation center at the base point is completely replaced by a low center. An examination of intermediate lags reveals that the displacement of the extrema is achieved through phase propagation with a speed of about 12 m/s or a period of about 4 days. A similar behavior is indicated by the 40 to 60°N lag correlation composites which are not shown here.

The low-frequency lag correlation composites are shown in Fig. 4.12a and b (-3 day lag and +3 day lag at 20 to 40°N) and Fig. 4.13a and b (-3 and +3 day lag at 40 to 60°N. The striking feature of these composites is the almost complete stationarity of the large positive center at the base grid point. The surrounding centers do shift around somewhat. In the 40 to 60°N composite, the high

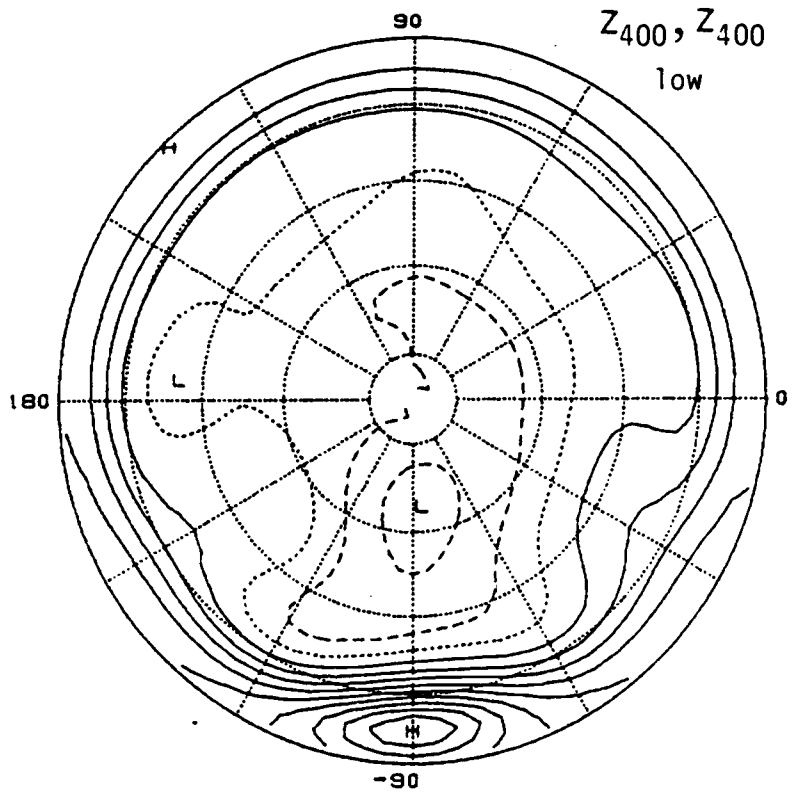

Fig. 4.10. Composite of simultaneous one-point-correlation maps of the simulated 400 mb 10 day low-pass geopotential height anomaly with base-grid-points within the Equator to 20°N latitude belt. Contour interval: 0.1; negative contours are dashed and the zero line is dotted.

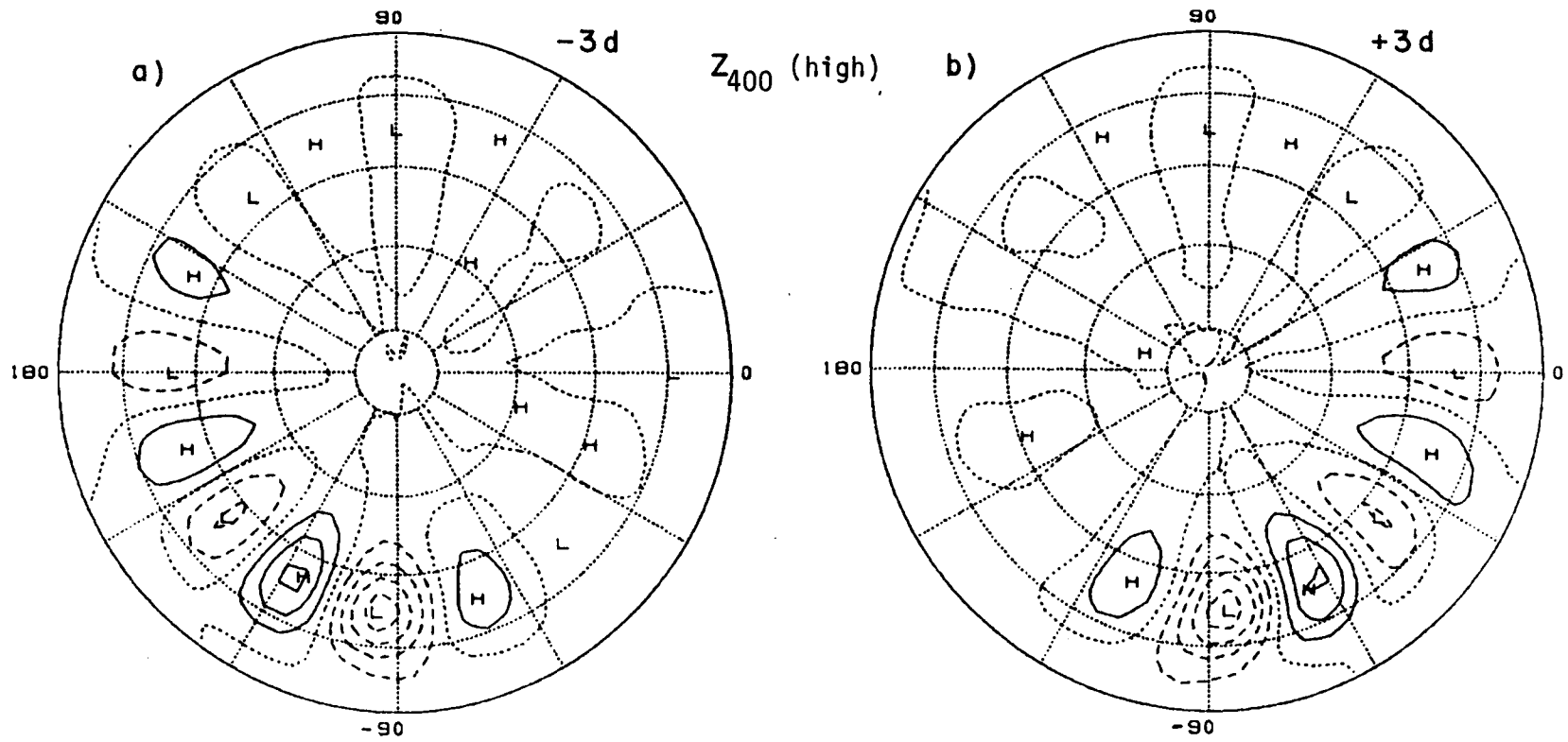

Fig. 4.11. Composite of one-point-correlation maps of the simulated 400 mb 2.5 to 10 day geopotential height fluctuations with base-grid-points within the 20 to 40°N latitude belt.
(a) Base-grid-point leads all other points by 3 days.
(b) Base-grid-point lags all other points by three days.
Contour interval: 0.1; negative contours are dashed and the zero line is dotted.

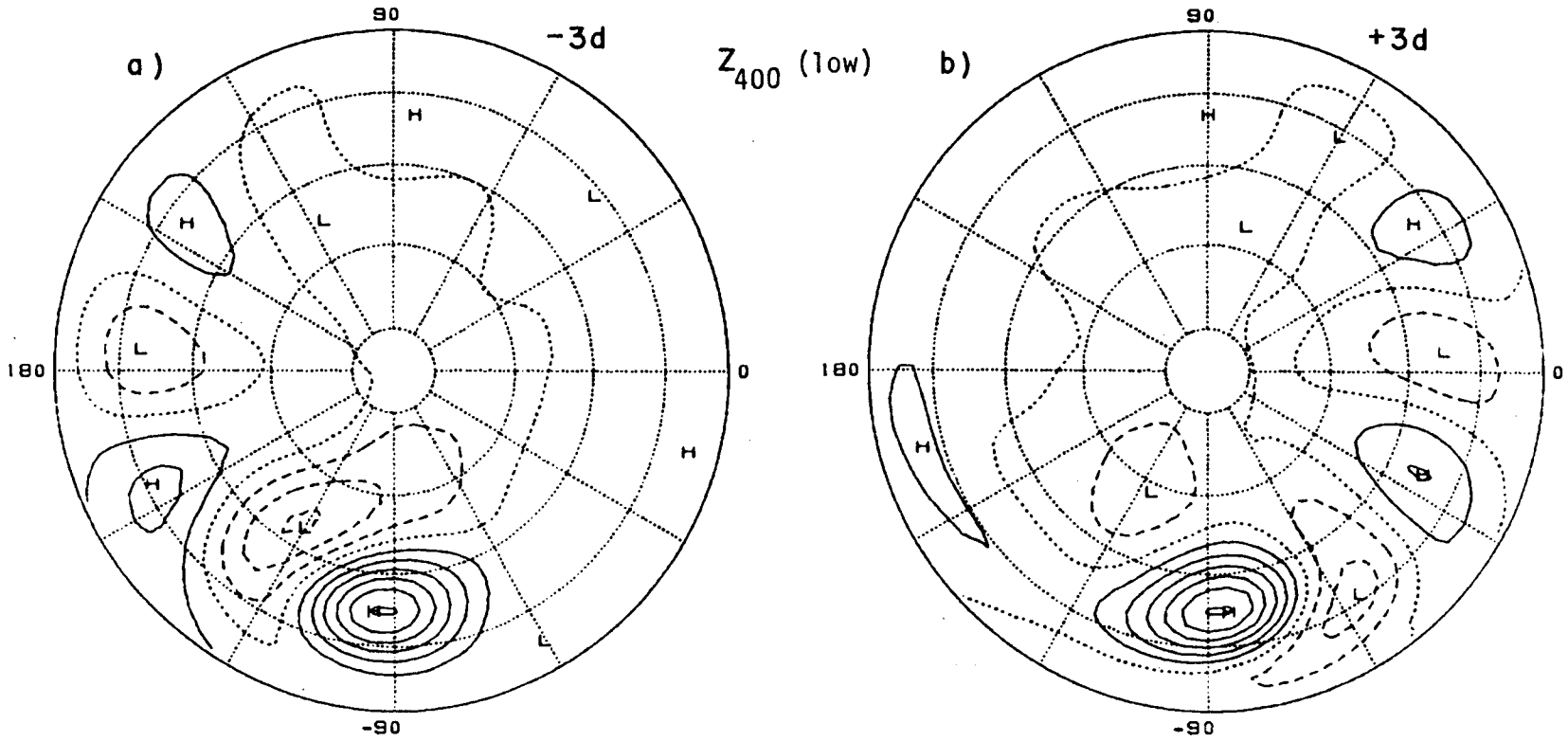

Fig. 4.12. Composite of one-point-correlation maps of the simulated 400 mb 10 day low-pass geopotential height fluctuations with base-grid-points within the 20 to 40°N latitude belt. (a) Base-grid-point leads all other points by 3 days. (b) Base-grid-point lags all other points by three days. Contour interval: 0.1; negative contours are dashed and the zero line is dotted.

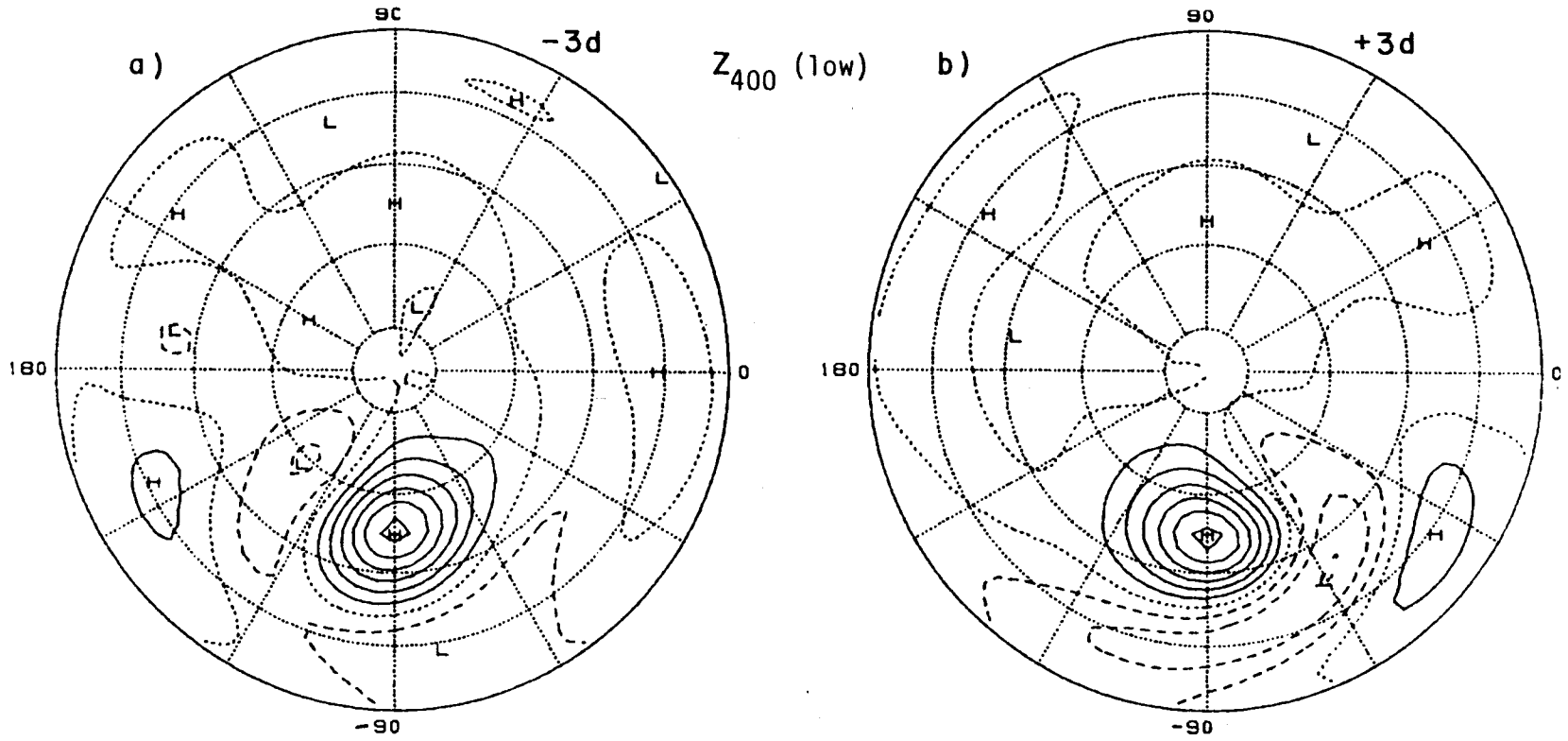

Fig. 4.13. Composite of one-point-correlation maps of the simulated 400 mb 10 day low-pass geopotential height fluctuations with base-grid-points within the 40 to 60°N latitude belt. (a) Base-grid-point leads all other points by 3 days. (b) Base-grid-point lags all other points by three days. Contour interval: 0.1; negative contours are dashed and the zero line is dotted.

latitude minimum and middle latitude maximum west of the center meridian retrograde during the 6 day period separating Fig. 13a from b. At the same time the minimum east of the center meridian moves northeastward.The 20 to 40°N composite is more stationary. While the phase of the patterns remains almost stationary, there are large changes in the magnitude of the correlation values with time. Both the high- and low-frequency composites show a tendency for the intensity to increase on the eastern half of the field as time goes by. While this is followed by phase changes in the high-frequency composites it is so in the low frequencies. The low-frequency behavior could be interpreted as an eastward dispersion of energy (see Chapter 4.4). It is difficult to assess the rate of dispersion from these figures. Taking for example the 20 to 40°N composite where the dispersion is quite zonal, we notice that at the -3 day lag field (Fig. 4.12a) there are virtually no patterns east of the base point. In the zero-day-lag field (Fig. 4.5b) a well defined low-high pattern appears and extends almost 90 degrees westward of the base-grid-point. Thirty degrees further downstream at 30°N, no significant pattern shows in the -3 day lag field while a weak high exists at zero-day lag. At +3 day lag (Fig. 4.12b) this high center intensifies. These observations imply a dispersion rate of 20 to 30 degrees per day. In the 40 to 60°N composite the dispersion is less zonal and it is even more difficult to estimate its rate.

4.4 Interpretation

The results presented here clearly indicate the OSU Atmospheric GCM offers a good simulation of the atmospheric wintertime variability. While the model may not reproduce all the features in exactly their observed geographical location or intensity, it does so with the basic spatial and temporal character of the fluctuations (see Blackmon et al., 1984a and b). We have also noticed the internal consistency between such features as the location of the major troughs and jet streams and that of the centers of high- and low-frequency variability.

It is evident from all we have presented so far that some definite statistical and structural differences exist between high- and low-frequency fluctuations. These agree with and give theoretical support to similar differences that appear in observations (e.g., Blackmon, 1976; Blackmon et al. 1984a and b). These differences may be summarized as follows:

a. The major part of the wintertime mid-troposphere geopotential height variability is caused by low-frequency fluctuations. These low-frequency fluctuations are strongest over the high-latitude northeastern ocean basins and Siberia.
b. The relative role of high-frequency fluctuations in causing atmospheric variability is largest over the jet-stream regions, i.e., the 20 to 40°N latitude belt over the western ocean basins and the Mediterranean.
c. While high-frequency disturbances have short zonal and large meridional scales, low-frequency disturbances have medium to large zonal scales and smaller meridional scales.
d. While high-frequency fluctuations are strongly baroclinic, low-frequency fluctuations are more barotropic.
e. High-frequency fluctuations are caused by rapidly propagating waves while low-frequency fluctuations are caused by almost stationary or slightly retrograding wave disturbances.

These results strongly suggest that the model's high-frequency variability can be interpreted as traveling waves obtaining their energy from a baroclinic energy cycle. We shall return to this point in the following chapters. The causes for the low-frequency variability are so far not apparent. We can, however, interpret some of our results on the basis of the theory on the dispersion of energy by Rossby waves on a sphere. We note first that the composite one-point correlation figures qualitatively resemble theoretical barotropic and baroclinic wave dispersion patterns as shown for example by Hoskins et al.(1977) and Hoskins and Karoly (1981). But the resemblance goes even beyond this qualitative aspect in the following:

a. As predicted by Rossby-wave dispersion theory, the zonal scale of the waves penetrating to higher latitudes is larger than those at lower latitudes while the meridional scale of the former is smaller than that of the latter.
b. The zonally-short and meridionally-long waves disperse energy rapidly in a purely zonal direction. The zonally-long and meridionally-short waves disperse energy more slowly along a poleward penetrating great-circle-like path.

The agreement between our composites and wave dispersion theory can be even further emphasized by calculating the stationary total wavenumber (K_s in Hoskins and Karoly's, 1981 notation) as a function of latitude, based on the model's zonally-averaged seasonal-mean zonal wind component. This profile is presented in Fig. 4.14. We find reasonable agreement between the scale of the waves shown by the composites in different latitude belts and that implied by the K_s profile.

The results of the low-frequency time-lagged correlation analysis also seem to indicate the source of the dispersing energy. In the 20 to 40°N composites (4.12a and b) there is a relatively strong negative center northeast of the main positive one at -3 day lag and a relatively weaker negative center southwest of the main positive one at +3 day lag. In the high latitude composite (4.13a and b) the negative feature of the +3 day lag figure is stronger. These results suggest that the energy for these disturbances is most frequently generated at higher latitudes.

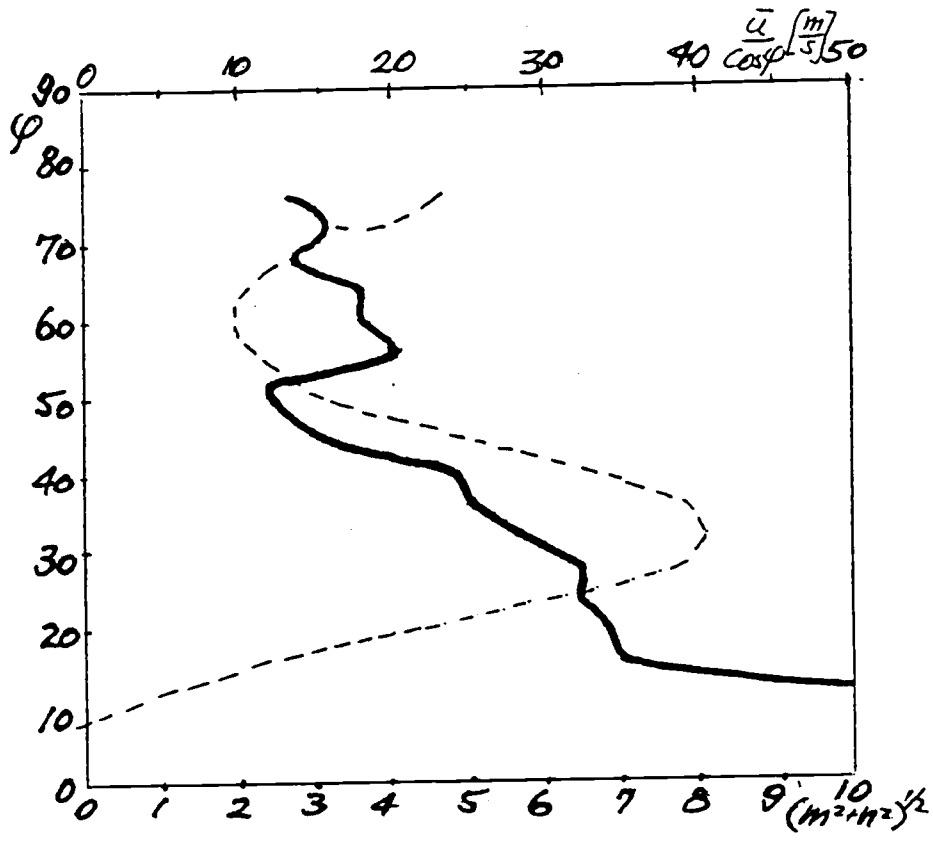

Fig. 4.14. The wavenumber of the stationary energy-propagating wave as a function of latitude for the model's 400 mb mean zonal current (see text and Hoskins and Karoly, 1981 for further details). The simulated 400 mb zonal mean angular velocity is shown by the dashed line.

CHAPTER 5: DYNAMICAL CHARACTERISTICS OF THE MODEL'S WINTERTIME VARIABILITY. PART A: SPATIAL DISTRIBUTION OF EDDY ACTIVITY AND TRANSPORTS

In the previous chapter we have found that the model's variability on subseasonal time scales is caused by large-scale, horizontally, and in most cases vertically, coherent disturbances. This is in complete qualitative agreement with observations. An understanding of the dynamics of these systems cannot be achieved without an examination of the other dependent variable fields and their mutual phase relationships. These properties will be dealt with in this chapter, through the application of variance and covariance analyses to the fields of eddy temperature and velocity. Since similar analyses have been applied in the past to observations, a comparison between those with the model-based results is possible. We will demonstrate that this comparison can provide further understanding of the dynamics of the eddies. The observational studies of Blackmon (1976), Blackmon et al. (1977 and 1979), Lau (1979a and b) and Lau et al. (1981) will provide the basis for the comparison.

It should be noted that Mullen (1980) examined some of the eddy statistics from the first 3 years of the OSU GCM simulation that forms the basis of this study. His results compare quite well with ours, pointing at the stability of the statistics and the small amount of interannual variability in this model simulation.

5.1 Intensity of time fluctuations of dynamical variables

The r.m.s. values of the temperature field at the 800 mb level for the high- and low-frequency eddies is shown in Fig. 5.1a and b, respectively and their observed counterparts are given by Blackmon et al. (1977, Fig. 9) and Lau et al. (1981, Fig. II-B.2). In the high frequencies there is good agreement between the regions of high 800 mb temperature r.m.s. and that of the geopotential height (Fig. 4.1c). However, the temperature r.m.s. is larger near the continental baroclinic features of Figs. 4.3a than over the storm tracks. The

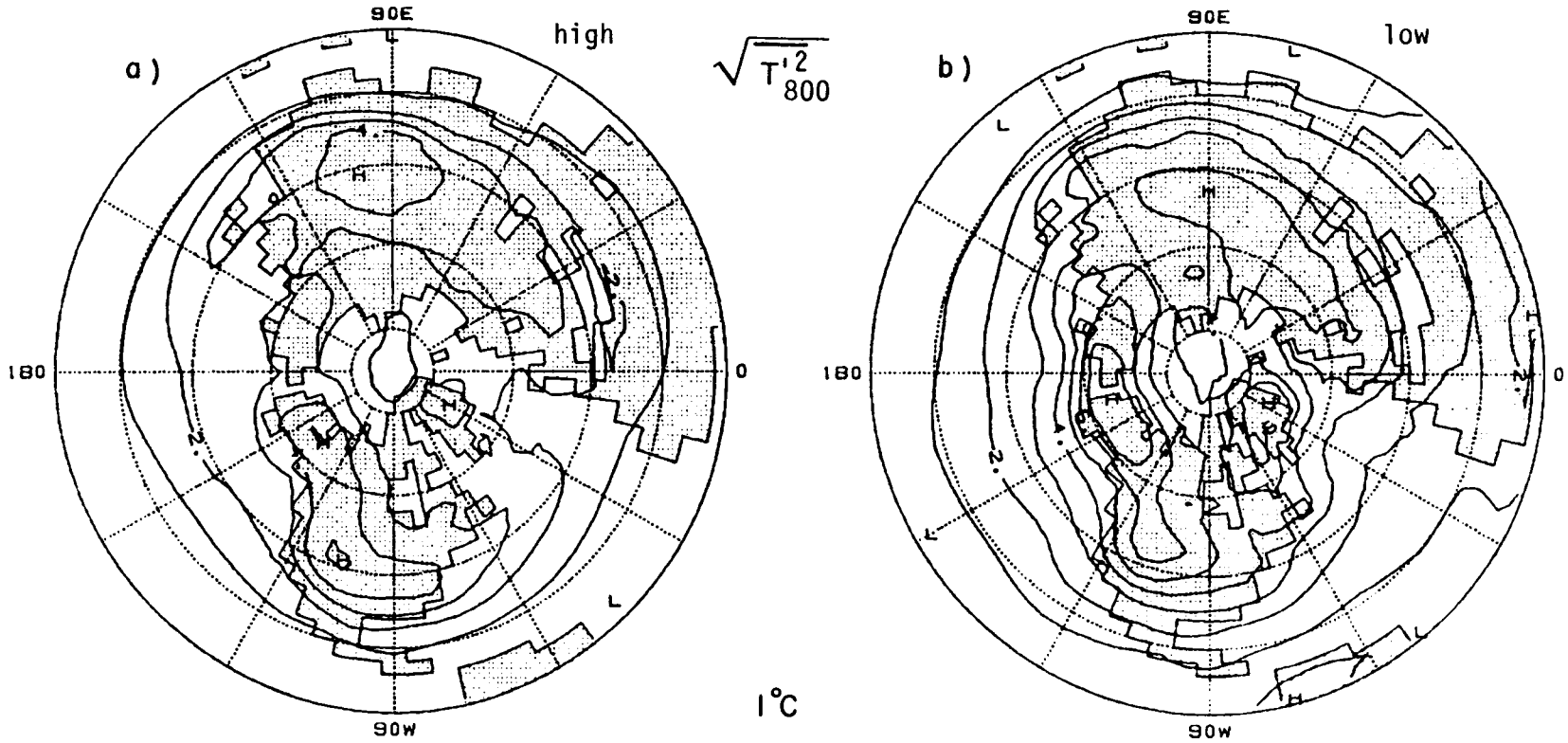

Fig. 5.1. The simulated wintertime 800 mb temperature r.m.s. of (a) 2.5 to 10 day fluctuations, (b) 10 day low-pass fluctuations. Contour interval 1°C.

continental r.m.s. values diminish at the 400 mb level (not shown) indicating that the continental minima in the 400 to 800 mb geopotential height correlations are caused by shallow systems virtually confined to the model's lowest layer. This agrees with observations. An interesting spurious model feature is the temperature (and geopotential height) r.m.s. center over western U.S. and Canada. In observations this local maximum is relatively weak and occurs east of the Rockies; it is more in phase with the orography. The oceanic maxima in the temperature r.m.s. field exist both at 800 and 400 mb, a fact which reiterates the differences in the dynamical nature of continental and maritime disturbances. Here again there is qualitatively good agreement with observations. The differences between the simulation and observations are consistent with those of the geopotential height r.m.s.

The low-frequency temperature r.m.s. values agree better with observation. In this part of the spectrum there is also a better agreement between the temperature r.m.s. values and those of the geopotential height at 400 mb, which is another indication of the stronger barotropy of these fluctuations.

Figure 5.2 presents the variance of the zonal and meridional wind components in the two frequency categories. The high frequency $\overline{u'^2}$ and $\overline{v'^2}$ fields (Figs. 5.2a and b, respectively) compare well with observations (Blackmon et al., 1977 Figs. 5a and b) except for some shifts in the location of the maxima which are consistent with the shifts in the storm tracks noted earlier. In the regions of maximum variance, $\overline{v'^2}$ is much larger than $\overline{u'^2}$ indicating that the high-frequency eddies tend to have larger meridional scales than zonal scales. As in observations, the zonal-wind variance maxima tend to be broader and less elliptical than those of the meridional wind.

Blackmon et al. (1977) have examined the low-frequency variance of the zonal and meridional wind components and found them to be "chaotic", not well related to one another and to the geopotential height r.m.s. field. This is apparently not the case with the model data (Figs. 5.2c and d). The general character of these fields can be depicted by a "geographical" classification of the variance maxima.

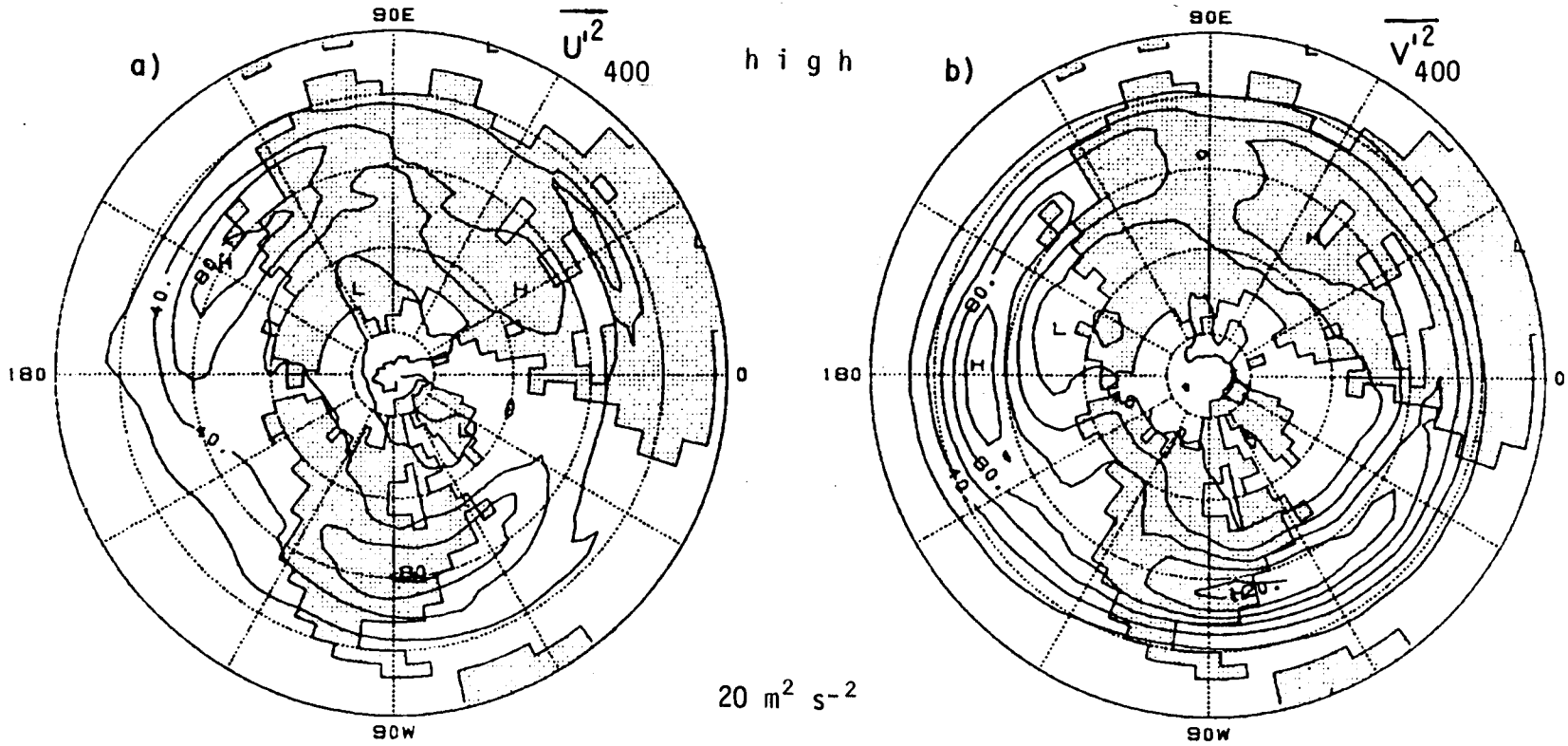

Fig. 5.2. The simulated wintertime 400 mb variance of wind velocity components. (a) 2.5 to 10 day zonal wind fluctuations. (b) 2.5 to 10 day meridional wind fluctuations. (c) 10 day low-pass zonal wind fluctuations. (d) 10 day low-pass meridional wind fluctuations. Contour interval: 20 m^2 s^{-2}.

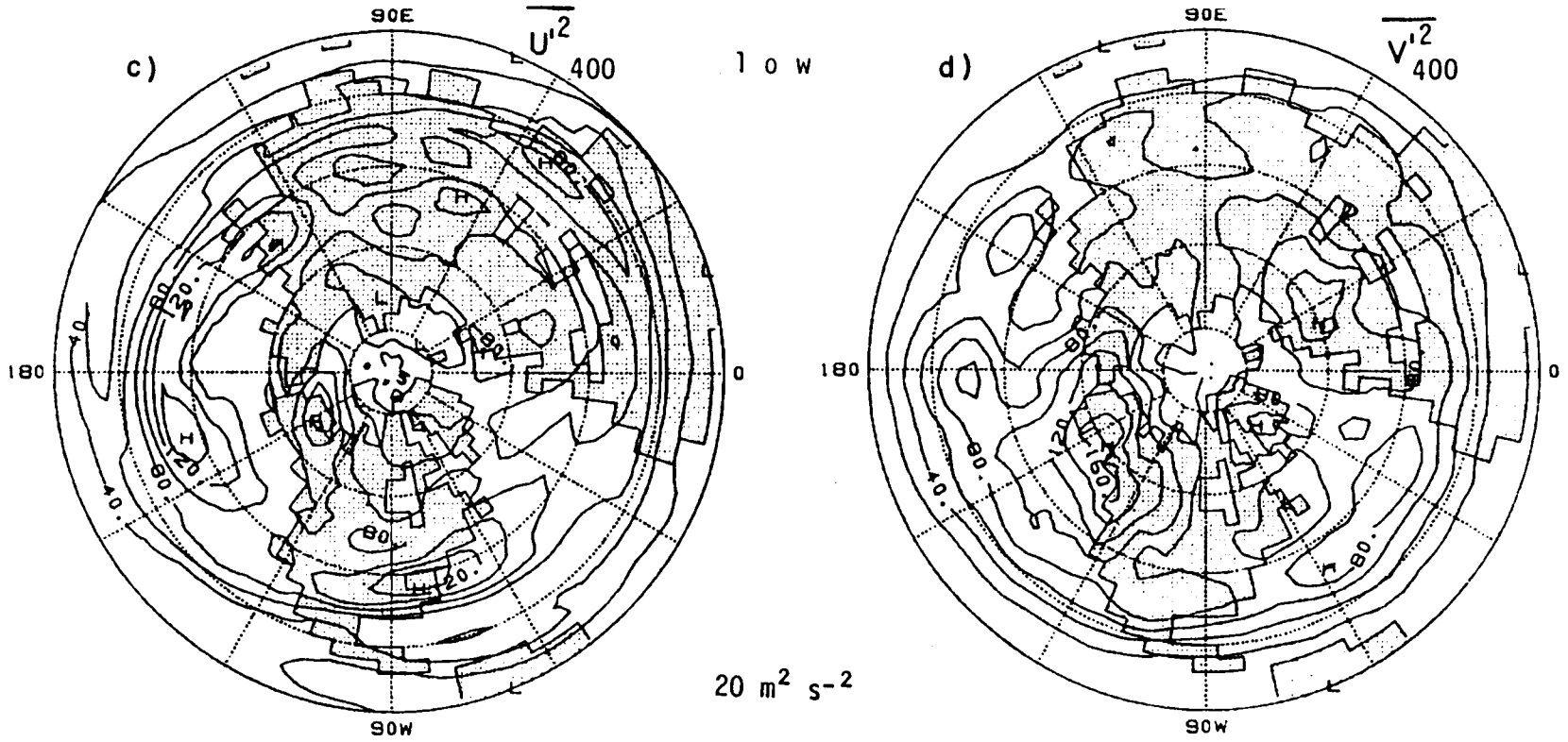

Fig. 5.2 (continued)

In each ocean basin and over Asia there exists a jet-stream-latitude maximum. These are zonally elongated and in the $\overline{v'^2}$ field tend to show a relative minimum over the local jet maximum. In contrast to the high-frequency eddies, the zonal-wind variance in these latitudes is larger than that of the meridional wind, indicating that the zonal scales of the low-frequency eddies are somewhat larger than their meridional scales. The second "type" of low-frequency wind variance centers are located over the extreme northeastern ocean basins and in northern Siberia, approximately where the maxima of the low-frequency r.m.s. geopotential height values are located (in the $\overline{v'^2}$ field the Siberian and Scandinavian centers are combined into one). Over these high-latitude centers $\overline{u'^2}$ and $\overline{v'^2}$ are of comparable magnitude.

A more quantitative way of looking at the relationship between the variance of the velocity components and the horizontal structure of the disturbance associated with them is to assume local WKBJ conditions in the eddy environment. Then, under the assumption of quasi-horizontal motion, the ratio of the meridional to zonal wind variances is proportional to the square of the ratio of the meridional to zonal wavelength. We have presented this ratio, at the two frequency categories in Fig. 5.3a and b. As we have already noted here and in the previous chapter, high-frequency eddies have large meridional and smaller zonal dimensions, while low-frequency eddies have similar zonal and meridional scales. Figure 5.3 also reveals regional differences in the shape of the eddies: high-frequency eddies (Fig. 5.3a) are "rounder" over the jet streaks (their region of generation) than over the eastern ocean basins (their region of decay). This sharpening of the eddies could be a result of the dispersion properties of Rossby waves on a sphere (waves with a low k/l ratio disperse meridionally while those with high k/l ratio disperse zonally). In the low frequencies (Fig. 5.3b) similar differences exist between the shape of western and eastern ocean eddies. The more intense high latitude low-frequency eddies are elongated in the south to north direction. All these regional shape differences also appear in local one-point correlation maps (not shown).

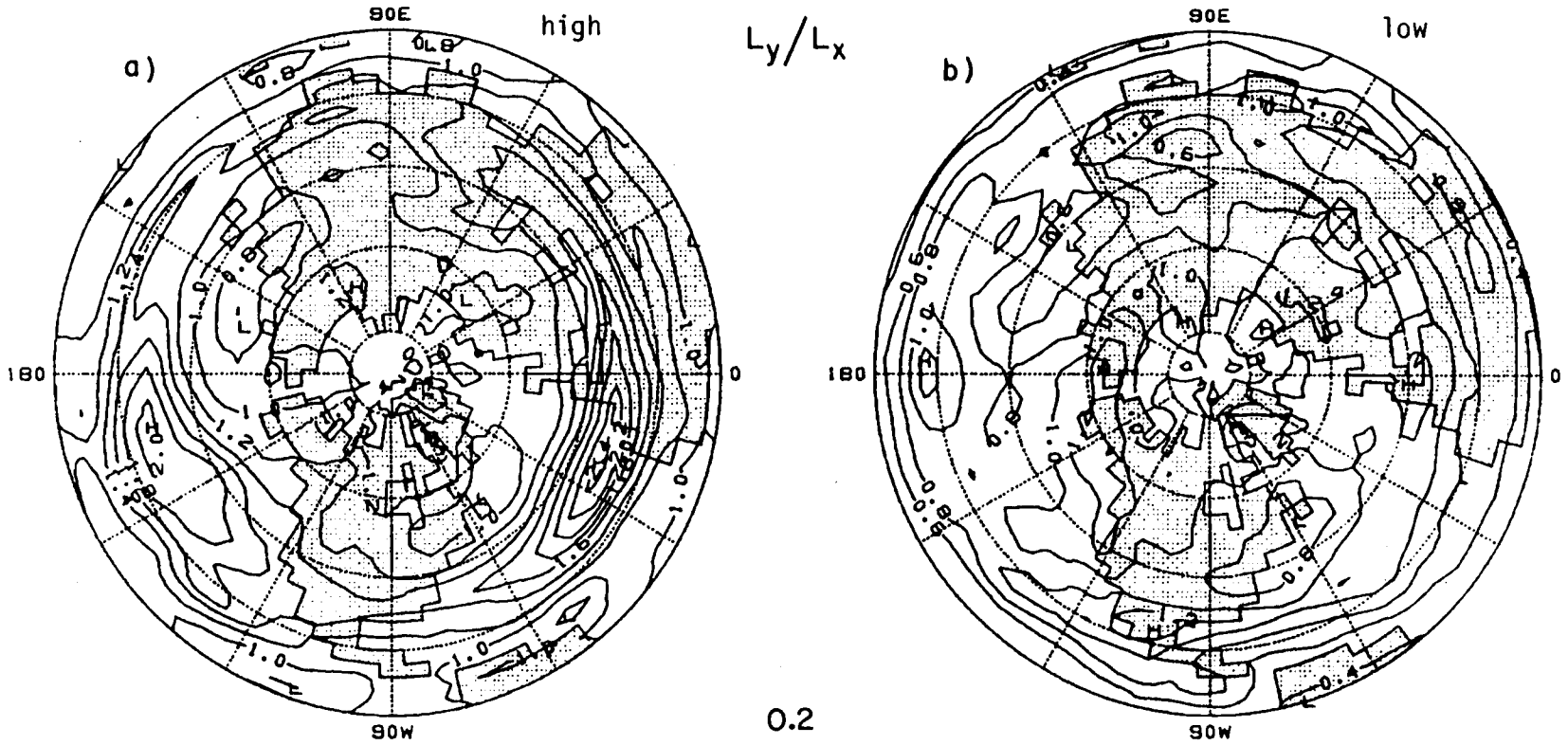

Fig. 5.3. The ratio of the meridional to zonal length scale of the simulated eddies at 400 mb as implied by the variances of the wind velocity components (see text for further details). (a) 2.5 to 10 day fluctuations. (b) 10 ay low-pass fluctuations. Contour interval: 0.2.

Finally, the variance of the vertical pressure velocity is shown in Fig. 5.4. Comparing the total variance (Fig. 5.4a) with observations (Lau, 1979b, Fig. 2) shows that the model's strongest features are related to orography while the observed features are related to the storm tracks. A more careful examination reveals that the magnitude of the model's maxima over the Himalayas and the Rockies are comparable to the observed features. It is in the storm tracks that the model's $\overline{\omega'^2}$ is weaker by a factor of about 3 compared to observation. This difference can be explained in part by the difference in the pressure level (which is 500 mb in Lau, 1979b). In subsequent sections we will judge the effects of this discrepancy on the model's vertical dynamical processes.

The distribution of the model's $\overline{\omega'^2}$ between the two frequency categories is shown in Fig. 5.4a (high frequencies) and b (low frequencies). The high-frequency r.m.s. values show relatively strong "storm track" related features while in the low frequencies the high r.m.s. values are strongly related to the orography. In contrast to the r.m.s. or variance of other variables, the vertical velocity variance is slightly dominated by the high-frequency fluctuations! Although there is no information on the observed distribution of $\overline{\omega'^2}$ between the two frequency categories, the location of the observed maxima strongly indicate that this is also the case in the real atmosphere.

5.2 Eddy transport properties

Eddy transports (the covariance between the eddy velocity components and other eddy fields) are a manifestation of the three-dimensional structure of the disturbances. This structure and its relation to the properties of the eddy environment play a crucial role in the maintenance of the eddies. We therefore examine some of the basic transport properties of the model's high- and low-frequency eddies. The implications of these properties for the maintenance of the eddies are left for later (Chapter 6).

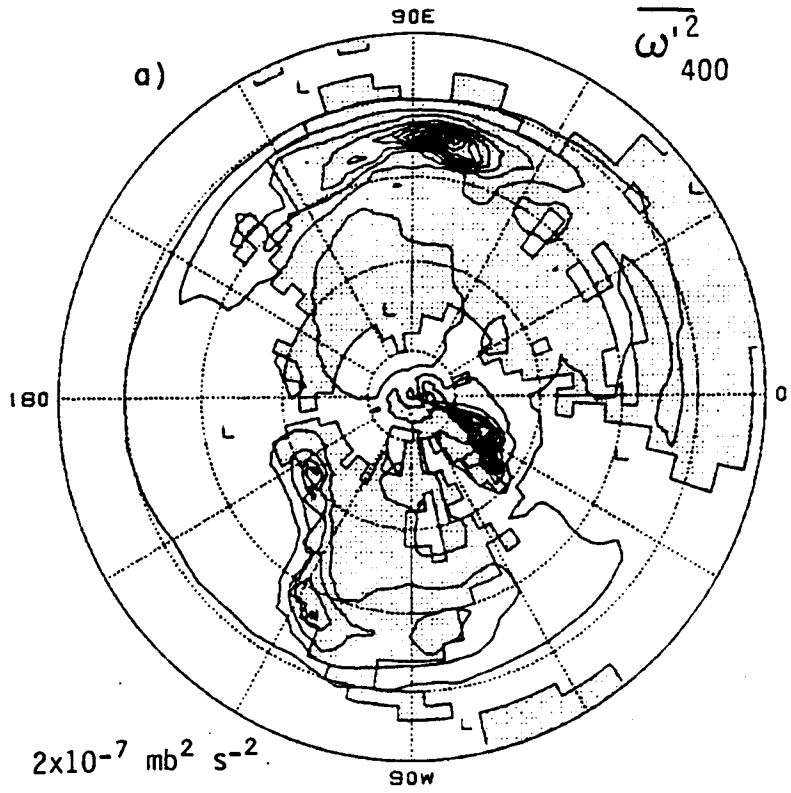

Fig. 5.4. The simulated wintertime variance of the vertical pressure velocity at 400 mb. (a) 2.5 day low-pass fluctuations. (b) 2.5 to 19 day fluctuations. (c) 10 day low-pass fluctuations. Contour interval: $2x10^{-7}$ mb^2 s^{-2}.

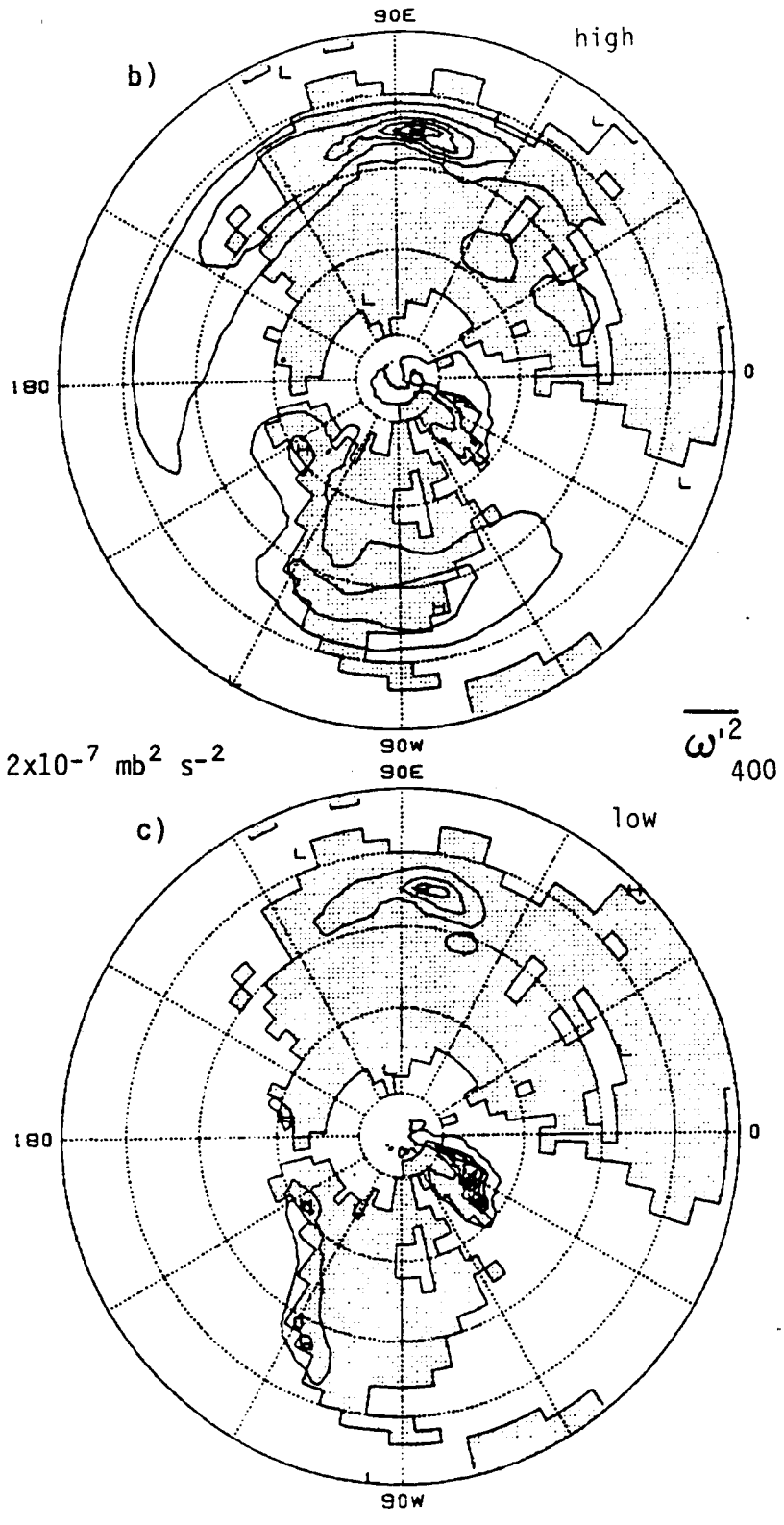

Fig. 5.4 (continued)

Figure 5.5a and b shows the northward transports of westerly momentum at 400 mb by high- and low-frequency eddies. Theory predicts that growing baroclinic eddies in a vertically and horizontally sheared basic state (jet) will usually transport westerly momentum into the region of maximum instability (e.g., Frederiksen, 1980). This is generally the case with the model's high-frequency eddies (Fig. 5.5a). In the Pacific, the maximum convergence of westerly momentum occurs about 15 degrees westward of the center of the model's Pacific storm track (as defined by the distribution of the geopotential height variance in Fig. 4.1e). In the Atlantic, the situation is different with the region of maximum convergence almost overlapping the center of the storm track. These differences between the Pacific and Atlantic storm tracks appear to be consistent with the regions of strongest instability where the vertical wind shear is strong and meridional gradient of the absolute vorticity of the seasonal mean flow is weak (see Figs. 3.5a and b). Interestingly there exists a parallel difference between these two storm tracks in observation (see e.g., Lau et al., 1981, Fig. II.B.1.f and Fig. II.C.2.c). The model features are again found to be shifted southwestward from their observed counterparts, consistent with the discrepancies in the location of the storm tracks themselves. The magnitude of the storm-track-related momentum-transport dipoles falls between the observed values at 500 and 300 mb (Lau et al., 1981, Fig. II.C.2.d).

A significant difference in the model transport pattern and observations exists over the central and eastern Pacific. Here, from about the region where the model's storm track diminishes to the west coast of North America, the model high-frequency eddies transport westerly momentum southward. In contrast, observations show that the dipole-like pattern of northward and southward transports flanking the storm track continues all across the Pacific. In this region the model's jet stream has a negative northward shear which implies strong barotropic eddy decay of the simulated eddies (see Chapter 6). A similar tendency to display a spurious (in comparison to observations) southward momentum flux exists also over the central and east Atlantic. Finally, we note that the model's peculiar storm track over

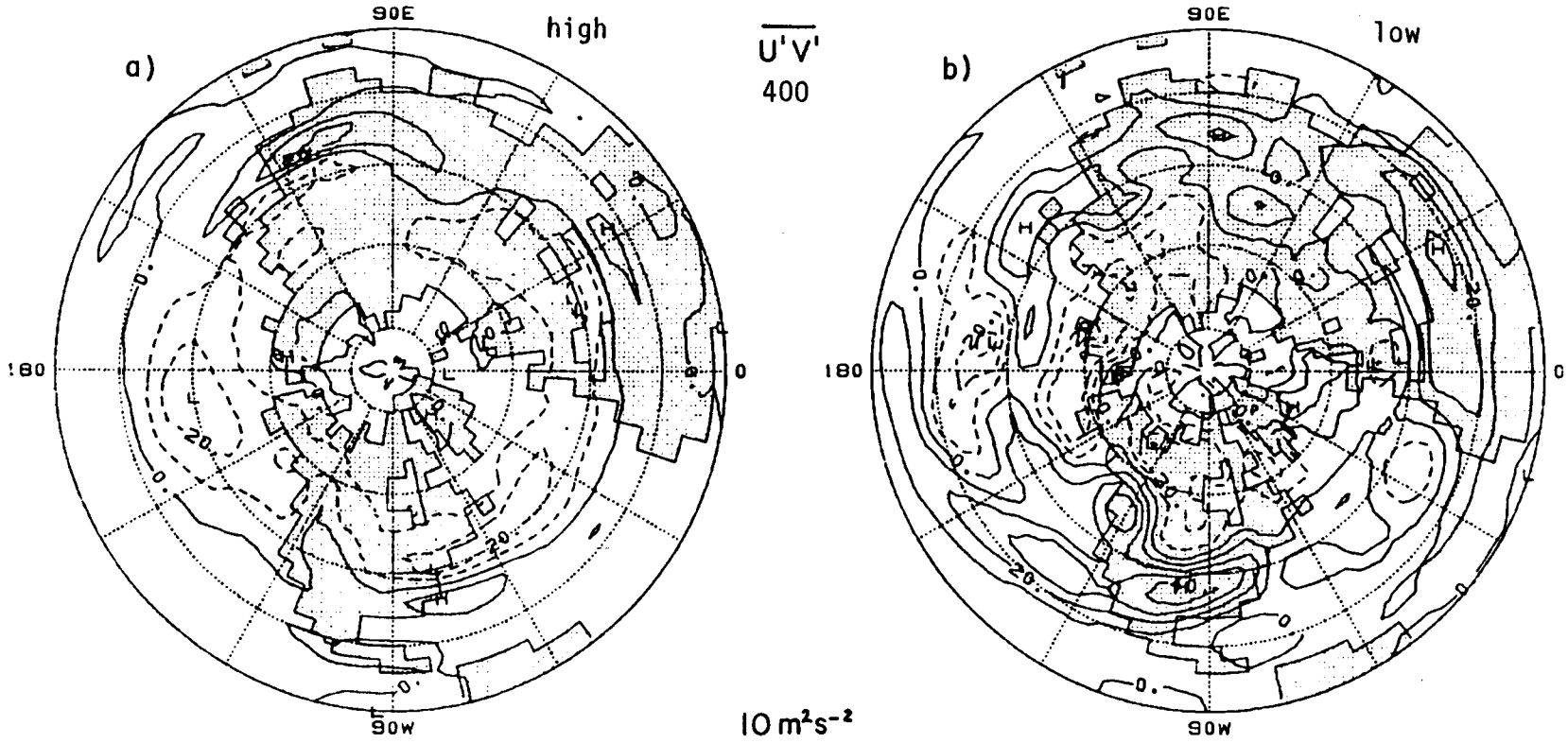

Fig. 5.5. The simulated wintertime covariance between the zonal and meridional wind components (northward zonal momentum transport) at 400 mb. (a) 2.5 to 10 day fluctuations. (b) 10 day low-pass fluctuations. Contour interval: 10 m^2 s^{-2}; negative contours are dashed.

the American Northwest is only partially flanked by a dipole transport pattern. In fact, over Alaska, the dipole pattern is reversed, with a weak northward transport to its north and a southward transport to its south.

In the low-frequencies, the northward westerly-momentum transport distribution is generally similar to observations (Lau et al., 1981, Fig. II.C.1.e and f). The maxima here are located over the eastern and western Pacific, the U.S., the Mediterranean and western Siberia, and the minima over the central Pacific, Canada, and Northeast Asia. The model minima over the Atlantic and Europe are weaker than the observed. The distribution of the transport in the low frequencies is much more complex than that at high frequencies and its implications on the maintenance of the low-frequency eddies will be made clearer in the next chapter.

At this point we can combine our knowledge of the variances of the eddy wind component and of the eddy momentum flux to pursue the question of the eddy horizontal structure even further. Hoskins et al. (1983) have shown how the eddy horizontal anisotropy can be studied from the knowledge of these quantities. This is of course a result of the quasi-horizontal, quasi-geostrophic character of both types of eddies. Thus the anisotropic part of the eddy velocity covariance matrix can give us the information on the direction of the major axis of eddy asymmetry and its length (eddy eccentricity) on the horizontal plane. The isotropic part of this matrix which is simply the kinetic energy of the eddies is an indicator of eddy intensity (see Hoskins et al., 1983, for further details). We have presented this information for the high- and low-frequency eddies in Fig. 5.6a and b. The arrows in the diagram are aligned along the major asymmetry axis for the eddies; the length of the arrows is proportional to the eddy eccentricity. The solid contours are those of the kinetic energy field. In some respects these figures reiterate some aspects of the eddy horizontal structure we have already noted earlier. Again we find the high-frequency eddies to be meridionally elongated with this elongation largest over the eastern side of the ocean basins. The low-frequency eddies are zonally elongated over the middle

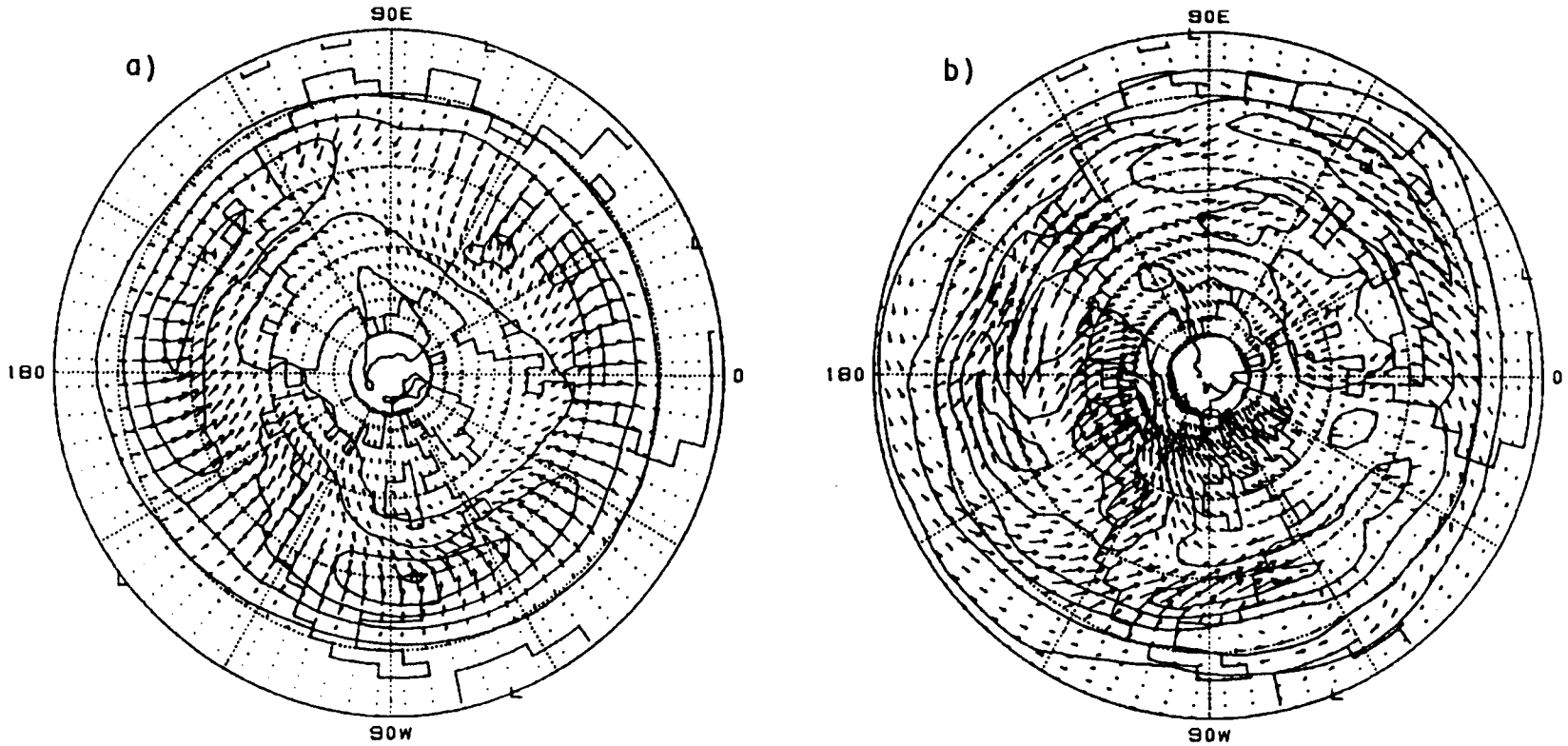

Fig. 5.6. The horizontal tilt of the simulated eddies at 400 mb as inferred by their velocity covariance matrix (see text for further details). (a) 2.5 to 10 day fluctuations. (b) 10 day low-pass fluctuations. The arrows represent the major axis of eddy asymmetry. Length of arrow is proportional to eddy eccentricity and its direction with respect to the parallels is the horizontal tilt. The underlying contours are those of eddy kinetic energy (contour interval: 20 m^2 s^{-2}), indicating the eddy intensity.

latitudes and meridionally elongated at high latitudes. The angle between the arrows and the latitude lines indicates the local tilt of the eddy trough lines, which is directly related to the direction of momentum transport they induce. In this we find that the central and eastern ocean high-frequency model eddies have a tendency to tilt in the south-east to north-west direction more than their observed counterparts (see Hoskins et al., Fig. 2), resulting in the peculiar momentum flux convergence they produce. As we shall see later in Chapter 6.2 this flux pattern is related to the barotropic decay of the high-frequency eddies in the jet-exit regions.

The eddy northward heat flux at 800 mb (the covariance between the meridional wind component and temperature fluctuations) is shown in Fig. 5.7 (high frequency) and b (low frequency). In the high frequencies there is generally good agreement between the location of the maxima in the transport and the regions of strongest instability as indicated by the vertical wind shear and the gradient of absolute vorticity of the seasonal mean circulation (Figs. 4.5a and b). Moreover, the relationship between the r.m.s. geopotential height values (Fig. 4.1c) and the region of largest instability and northward heat transport agrees with the notion that the eddies grow as they are being advected westward and achieve their maximum intensity downstream from the region of instability. Under the influence of the stronger Pacific jet, the eddies move further downstream than their Atlantic counterparts before they reach their peak. We note that the east-west axis of the transport patterns is shifted slightly northward from the jet axis a fact that is also consistent with the observations shown in Fig. 5.7c (from Blackmon et al., 1977, Fig. 7.b) and theoretical models. This is so because the northward gradient of the absolute vorticity of the basic current is weaker north of the jet axis. Again, we recognize the model peculiarities in determining the regions of maximum eddy activity (the south westward shifts from the observed locations and spurious western North American feature) which are all internally consistent. The existence of a local model heat transport maximum over Alaska indicates that the spurious storm track over this region is also associated with baroclinic instability (in Chapter 3 we

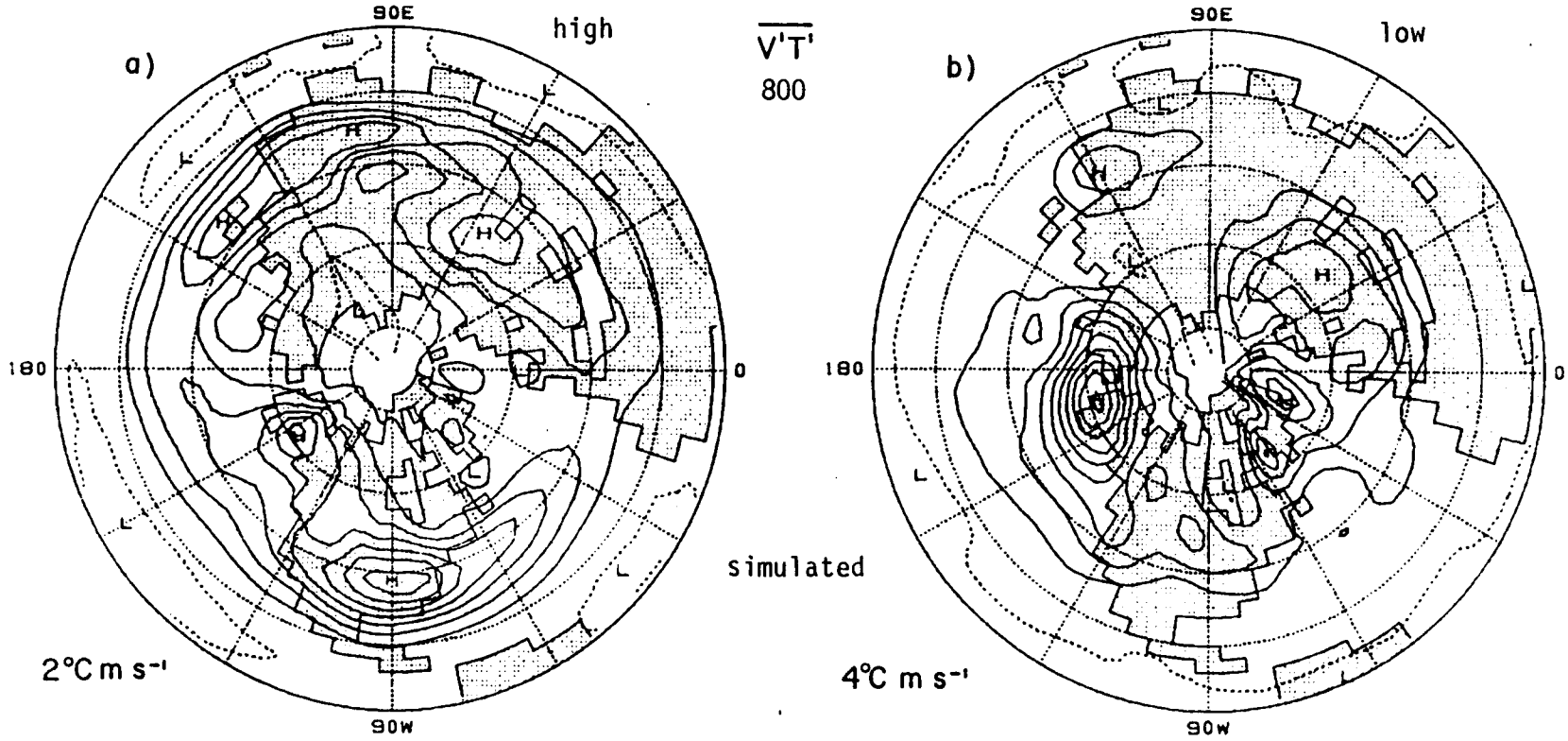

Fig. 5.7. Simulated and observed wintertime covariance between the meridional wind component and temperature (northward heat transport). (a) Simulated 2.5 to 10 day fluctuations. (b) Simulated 10 day low-pass fluctuations. (c) Observed 2.5 to 6 day fluctuations. (d) Observed 10 day low-pass fluctuations. Contour intervals are 2° C m s^{-1} in (a) and (c) and 4° C m s^{-1} in (b) and (d). Simulation results are at 800 mb; observations at 850 mb. Observations start at 20°N. Observations are from Blackmon et al. (1977).

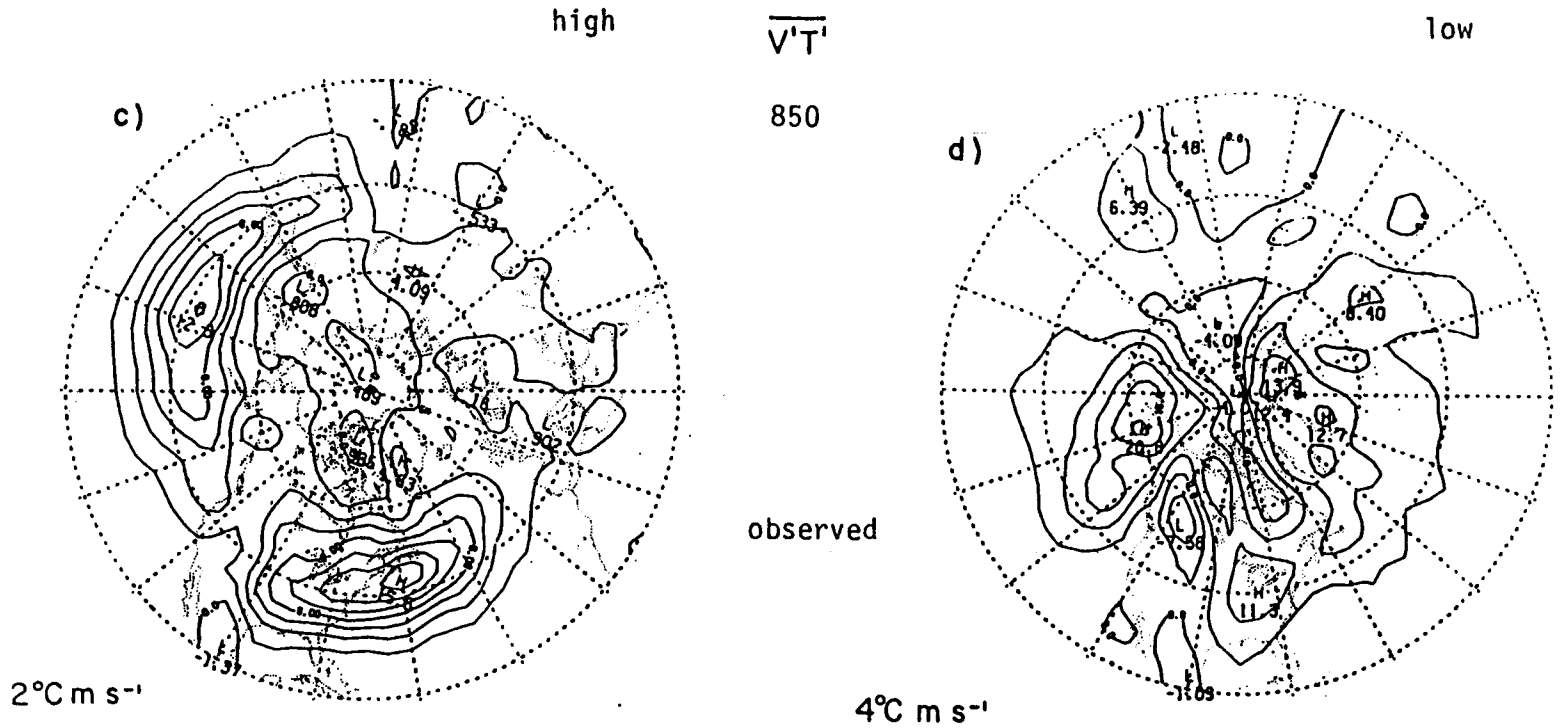

Fig. 5.7 (continued)

have found evidence for instability of the underlying circulation over this region).

The low-frequency northward heat transport (Fig. 5.7b) has distinct northern middle-latitude features. This is generally the case with the observations shown in Fig. 5.7d (from Blackmon et al., 1977, Fig. 11.6), though the model fluxes are about one and a half times larger than the observed. There also exist some difference in the locations of the transport maxima like that of the Atlantic and European sector where the model heat-transport maximum is located over Greenland while the observed maximum is over the Barens Sea. The good correspondence between the model's heat transport maxima and the maxima of the low-frequency r.m.s. geopotential height field (Fig. 4.1e) suggests that baroclinic processes play an important role in the dynamics of these eddies. This point will be elaborated on in the next chapter. Over most of the middle latitudes, low-frequency disturbances tend to have a barotropic structure, as indicated by the weak heat fluxes there.

The vertical transport of heat at 800 mb (or the negative covariance between the vertical pressure velocity and temperature fluctuations) is shown in Fig. 5.8a and b. This transport is closely related to the conversion between eddy APE and eddy kinetic energy. The spatial patterns of the vertical heat transport in both frequency bands indicate that both high and low-frequency eddies convert their APE to kinetic energy over most of the middle and high latitudes. This is in agreement with observations (the total eddy vertical heat transport was presented in Lau, 1979b, Fig. 4). The high frequency transport (Fig. 5.8a) reaches its maximum over the model's storm tracks while the low-frequency eddy transport (Fig. 5.8b) is maximum at higher latitudes. Some weak downward transport occurs over the prominent orographic features indicating a forced eddy circulation there. The magnitude of the model's transports is weaker than the observed, a fact which is consistent with the weaker variance of the vertical pressure velocity (see Section 5.2).

The theory of disturbances maintained by a baroclinic energy cycle predicts a high positive correlation between the meridional and

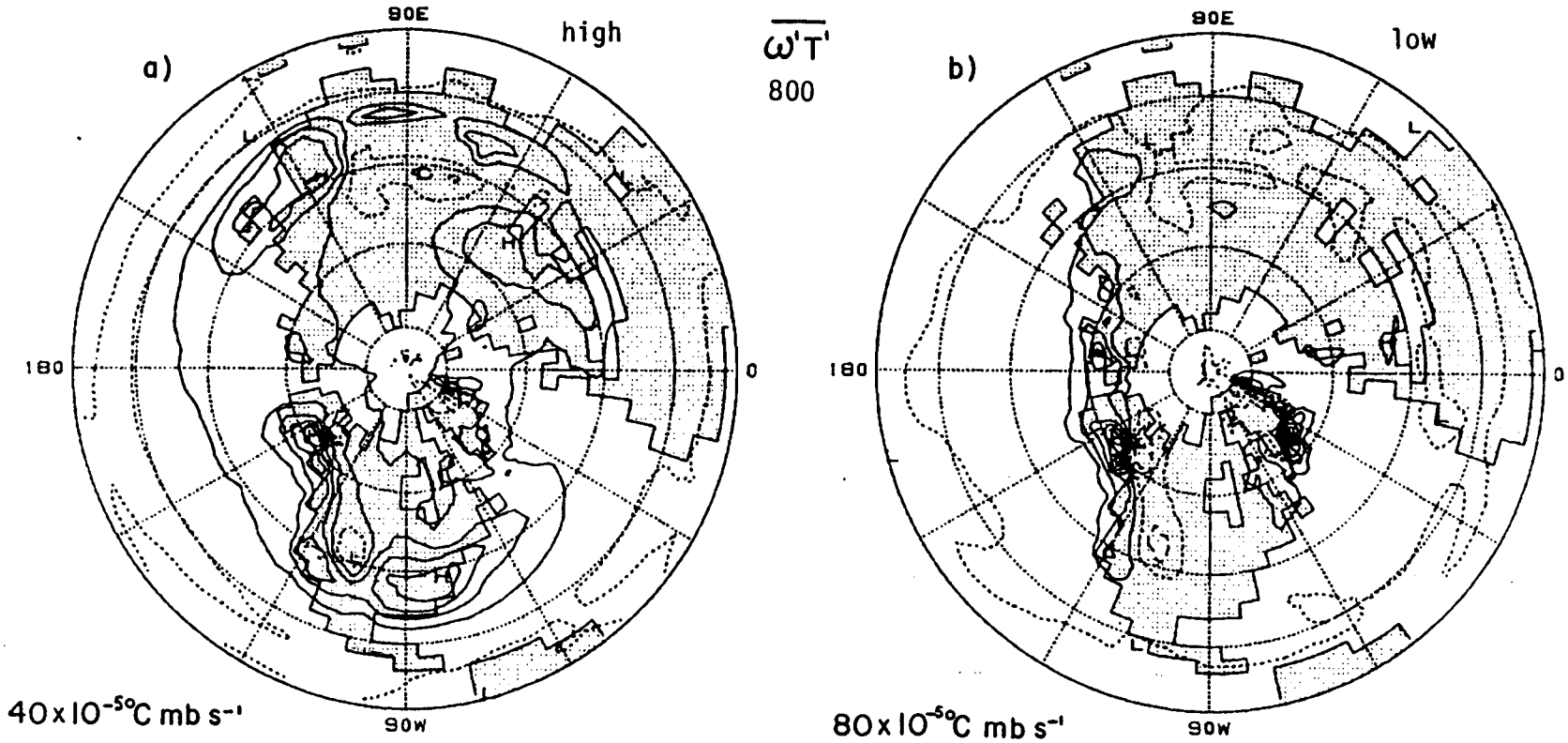

Fig. 5.8. The simulated wintertime negative covariance between the vertical pressure velocity and temperature (upward heat transport) at 800 mb. (a) 2.5 to 10 day fluctuations. (b) 10 day low-pass fluctuations. Contour intervals are 40×10^{-5} °C mb s^{-1} in (a) and 80×10^{-5} °C mb s^{-1} in (b).

vertical motions. This indeed is the case with the model's high-frequency eddies as indicated by Fig. 5.9a in which the negative covariance between the vertical pressure velocity and the meridional velocity fluctuations at 400 mb is presented. This upward transport of northerly momentum reaches a maximum over the model's storm tracks. Low-frequency eddies also show a dominant upward transport of northerly momentum. The prominent features here are associated with orography. Lau et al., (1981, Fig. II.D.5) presented only the total eddy vertical transport. However, it is quite clear that here again the model eddies generally behave like the observed eddies.

The vertical transport of westerly momentum in the high-frequency band (Fig. 5.9c) is large and downward slightly northward of the model's storm tracks and weakly downward to weakly upward south of the storm tracks. The distribution of upward and downward transport shows a strong similarity to that of northward and southward westerly momentum transport. This is a result of the horizontal structure of the eddies and their dynamics. By being elongated in the meridional direction and short in the zonal direction, the zonal wind fluctuations induced by the eddies are mainly associated with their meridional tilt. Sinking motion occurs mainly behind or in front of the trough-line, and rising motion ahead as the positive correlation $\overline{-\omega'v'}$ suggests. Together these imply that in a region of northward momentum flux (in front of the trough) u' and ω' will be positively correlated and vice versa. Upstream of the mountain ranges the zonal wind fluctuations are coherent with those of vertical motion since ω' is orographically induced (e.g., westerly fluctuations induce upward motion and easterly fluctuations, downward motion). A similar relationship between the $\overline{u'v'}$ and the $\overline{-\omega'u'}$ fields also exists in the low-frequency range. It is however weaker here because low-frequency eddies are more east-west elongated with u' not so much associated with the meridional eddy tilt.

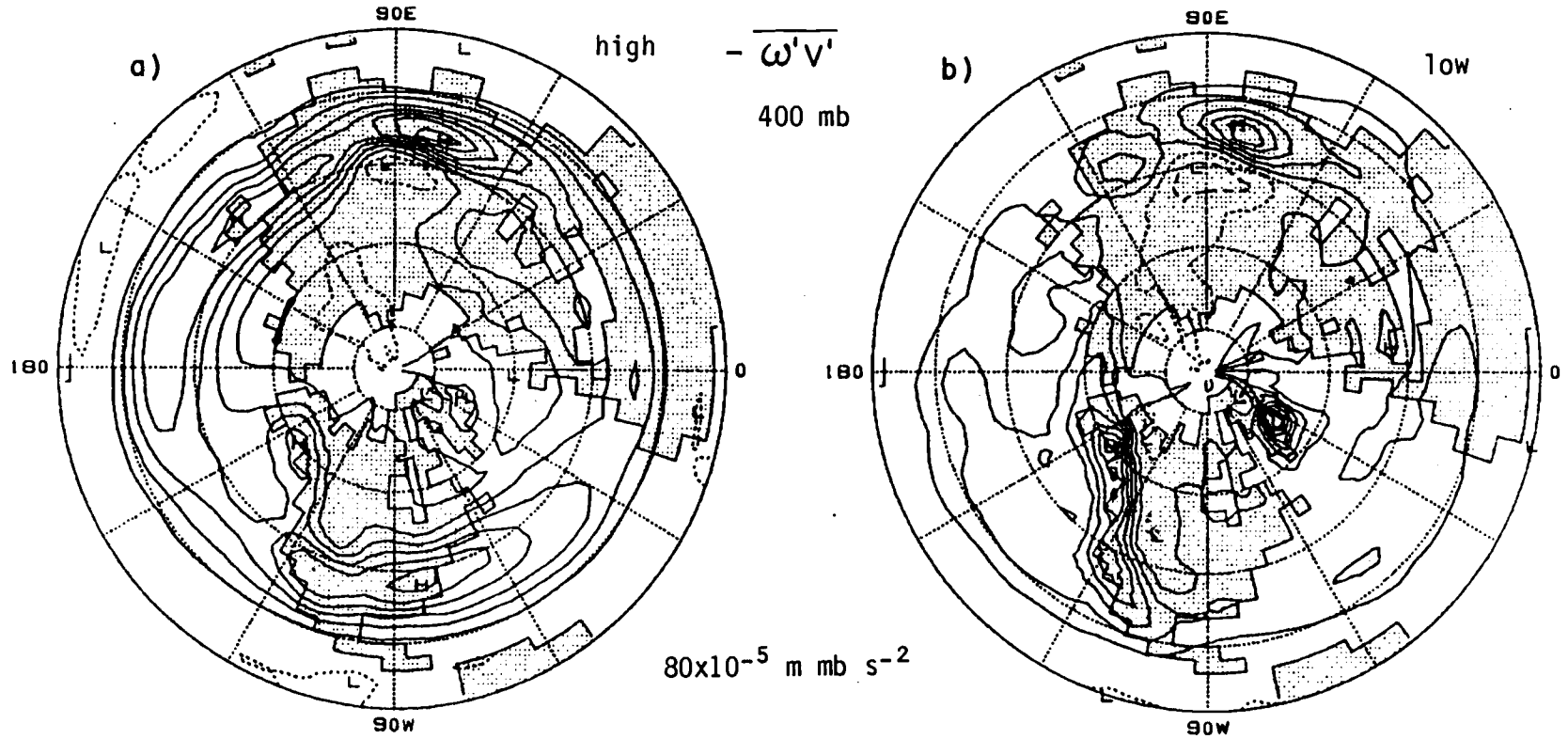

Fig. 5.9. The simulated wintertime negative covariance between the vertical pressure velocity and horizontal velocity components at 400 mb. (a) Vertical northward momentum transport of 2.5 to 10 day fluctuations. (b) Vertical northward momentum transport of 10 day low-pass fluctuations. (c) Vertical westward momentum transport of 2.5 to 10 day fluctuations. (d) Vertical westward momentum transport of 10 day low-pass fluctuations. Contour interval: (a), (b) and (d) $80x10^{-5}$ m mb s^{-2}, (c) $40x10^{-5}$ m mb s^{-2}; the zero contour is dotted and negative contours are dashed.

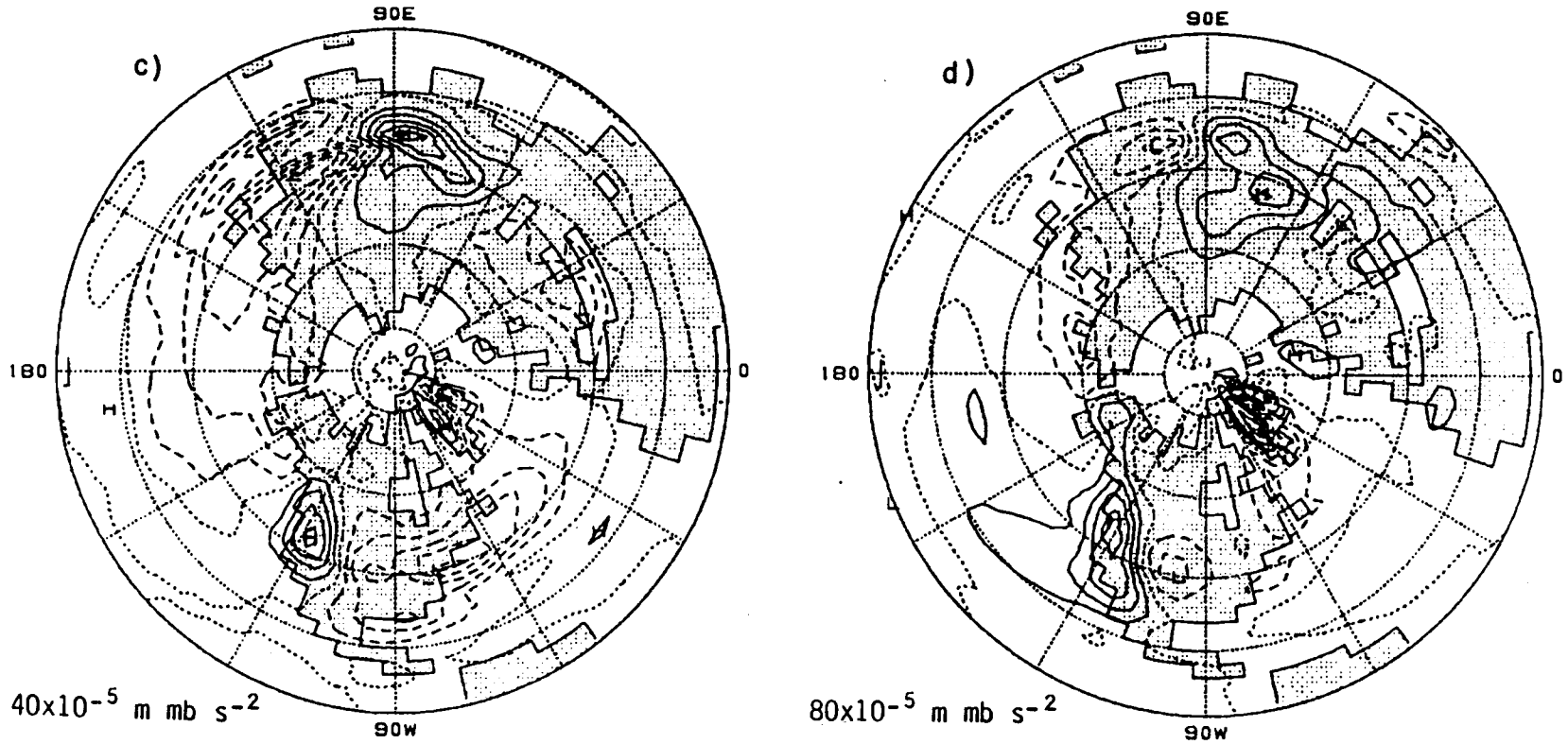

Fig. 5.9 (continued)

5.3 Recapitulation

In this chapter we have offered both a confirmation of our previous conclusion with regard to the horizontal structure of the eddies and a first impression of the nature of the dynamical processes which maintain the eddies. It is now clear that beyond their being differently distributed in space, high- and low-frequency eddies differ substantially in their horizontal shape and dimensions. However, some indications of similarities in their dynamical nature begin to appear. Both kinds of eddies show a strong positive correspondence between the temperature on one hand and the meridional and vertical wind components on the other. This clearly indicates that they both obtain energy through the baroclinic energy cycle. The regions in which the eddies grow as a result of this process, however, differ substantially as indicated by the location of the heat transport maxima.

We have gathered enough evidence to state that the results of the relatively simple, two-level model used in this study offer a realistic simulation of atmospheric processes governing the fluctuations on the subseasonal time scales studied here. We have found an internal consistency between the momentum and heat transports and the regions of strong eddy activity and the regions where the model's seasonally averaged circulation appears to be baroclinically unstable. In particular, this consistency extends to the regions in which the time mean circulation and the eddy intensities differ from observation. We therefore deduce that the model offers a qualitatively sound simulation of atmospheric processes, and continue our analysis with the goal of determining the dynamical mechanisms responsible for the disturbances in the real atmosphere, by using this GCM simulation.

CHAPTER 6: DYNAMICAL CHARACTERISTICS OF THE MODEL'S WINTERTIME VARIABILITY. PART B: EDDY ENERGETICS

One of the ways to gain insight into the dynamical processes which maintain the simulated disturbances is to examine their energy cycle. This method has been used extensively in studies of the maintenance of the global general circulation (e.g., Oort, 1964; Newell et al., 197)) and the maintenance of particular aspects of this circulation (e.g., Holopainen 1970; Lau, 1979a). In other cases it has been used to study disturbances on a regional basis using compositing methods (see Smith, 1980). Here we would like to examine the major dynamical processes involved in the energy cycle of transient eddies, on the two time scales we have dealt with so far, i.e. high-frequency eddies with a time scale of about one week and low-frequency eddies with time scales ranging from ten days to a season. The main question we would like to address is: Is there a difference in the energetics of high-frequency and low-frequency eddies? For this purpose we will examine the seasonally averaged spatial distribution of energy and its conversion from one form to another and hemispheric means of these quantities.

6.1 Formulation of eddy energetics

The maintenance of the eddy kinetic and potential energy can be studied through the examination of the kinetic energy equation and the temperature variance equation. For each eddy category, these equations are:

$$\frac{DK_E}{Dt} = -\nabla\cdot\overline{\mathbf{V}'\phi'} - \frac{\partial}{\partial p}\overline{\omega'\phi'} - \frac{R}{p}\overline{\omega'T'}$$

HFC VFC AEKE

$$-\left\{\frac{\overline{u'u'}}{a\cos\phi}\frac{\partial\bar{u}}{\partial\lambda} + \frac{\overline{u'v'}}{a}\frac{\partial\bar{u}}{\partial\phi} + \frac{\overline{u'v'}}{a\cos\phi}\frac{\partial\bar{u}}{\partial\lambda} + \frac{\overline{u'v'}}{a}\frac{\partial\bar{v}}{\partial\phi} + \frac{\overline{u'v'}\bar{u} - \overline{u'v'}\bar{v}}{a}\tan\phi\right\}$$

(1) (2) (3) (4) (5)

KKEH

$$-\overline{\omega'u'}\frac{\partial\bar{u}}{\partial p} + \overline{\omega'v'}\frac{\partial\bar{v}}{\partial p} + \overline{\mathbf{V}'\cdot\mathbf{F}'} + \overline{\mathbf{V}'\cdot\mathcal{F}_e'} + B_K \qquad (6.1)$$

KKEV F FE

$$\frac{C_p}{\bar{T}}\frac{D}{Dt}\left(\tfrac{1}{2}\overline{T'^2}\right) = \frac{C_p}{\bar{T}}\overline{Q'T'} + \frac{R}{\bar{p}}\overline{\omega'T'} - \frac{C_p}{\bar{T}}\overline{\mathbf{V}'T'}\cdot\nabla\bar{T} - \frac{C_p}{\bar{T}}\overline{\omega'T'}\frac{\partial\bar{T}}{\partial p}$$

GAE -AEKE AAEH AAEV

$$+\frac{R}{p\bar{T}}\left\{\overline{\omega'T'T'} + \overline{\omega T'^2}\right\} + \frac{C_p}{\bar{T}}\overline{T'Q_e'} + B_A \qquad (6.2)$$

QE

Here ($\bar{}$) denotes a seasonal (wintertime) average and (') an eddy quantity of either category. $K_E = \frac{1}{2}(\overline{u'^2} + \overline{v'^2})$ is the eddy kinetic energy. We also define here $A_E = \frac{C_p}{\bar{T}}(\frac{1}{2}\overline{T'^2})$, the eddy temperature variance to which we shall refer hereafter as the local eddy available potential energy or eddy APE (both K_E and A_E are thus in units of m^2/s^2). $\mathbf{F}'$ is the sub-grid-scale eddy friction and Q' the sub-grid-scale eddy diabatic heating rate. The two terms $\mathcal{F}_e'$ and Q_e' are "Reynolds-stress" terms resulting from the convergence of the eddy momentum and heat fluxes by the eddy velocity components. B_K and B_A are the terms representing the conversion of energy between the two frequency bands. All other symbols have their usual meteorological meaning. Complete derivations of Eqs. (6.1) and (6.2) are given in the Appendix.

These energy equations state that the time rate of change of the energy components is due to:

a. The conversion of energy from that of the time-mean flow to that of the eddies. These terms are grouped into those that result from horizontal processes (KKEH in the kinetic energy equation and AAEH in the APE equation) and those that result from vertical processes (KKEV and AAEV respectively).

b. The conversion from eddy APE to eddy kinetic energy (term AEKE in the kinetic energy equation or -AEKE in the APE equation).

c. The term in the kinetic energy equation representing the redistribution of kinetic energy which results from the dispersion properties of atmospheric waves, the so-called energy flux convergence term (its horizontal and vertical component are HFC and VFC, respectively).

d. The terms representing sub-grid-scale processes like frictional dissipation of kinetic energy (F) and diabatic generation of APE (GAE).

e. The eddy "Reynolds-stress" terms (FE in the kinetic energy equation and QE in the APE equation).

f. The inter-band interaction terms representing energy conversion from one eddy category to another (B_K and B_A).

We shall consider the vertical integral of the terms described in a to d. In order to simplify the integration procedure, the pressure thickness of the lower level was taken as the difference between the seasonally averaged surface pressure and 600 mb.

6.2 The energy cycle of high-frequency eddies

Baroclinic instability theory defines a baroclinic energy cycle in which the main source of total energy for disturbances is the conversion of the basic state APE into eddy APE, a result of the eddies

transporting heat down the gradient of the basic state temperature field. This eddy APE is in turn converted into eddy kinetic energy by the eddy induced vertical motion, which in a growing eddy is positively correlated with temperature. The eddies then lose their kinetic energy to the basic state (provided the latter is meridionally sheared), a result generally attributed to the effect of transporting westerly momentum into the basic state wind maximum. It is this baroclinic energy cycle that we use to explain the global energy cycle calculated from observational data (e.g., Oort, 1964). Blackmon et al. (1977), Lau (1979a and b), and Lau et al. (1981) have compiled a large amount of observational evidence indicating that this life cycle is typical of the high-frequency transient eddies in the regions of the storm tracks. Moreover, these data provide insight into the life cycle of the baroclinic high-frequency eddies by examining the changing magnitudes and directions of the eddy transports along the storm track.

The horizontal distribution of the vertically integrated energy cycle of the model's high-frequency eddies is shown in Figs. 6.1a to k. Figures 6.1a and b show the total eddy APE (as calculated from the eddy temperature variance) and kinetic energy respectively, in units of 10^5 J/m^2. The kinetic energy maxima nearly coincide with the storm tracks as defined by the 400 mb high-frequency eddy geopotential height variance (Fig. 4.1c), while the maxima in the APE over the Pacific and North America occur slightly upstream from the centers of the storm tracks. The relationships are consistent with the fact that the kinetic energy of the eddies is closely related to the intensity of the height perturbations which increases as the eddies are advected eastward by the underlying current. In the Pacific, this configuration is accentuated as a result of the stronger advective influence of the Pacific jet stream.

Figures 6.1c and d show the horizontal distribution of the vertically integrated AAEH and AAEV terms of (6.1) in units of W/m^2. We find that both these time-mean APE to eddy APE conversion rates are strongest slightly upstream from the location of their corresponding jet stream maxima and storm tracks. These are the regions where the

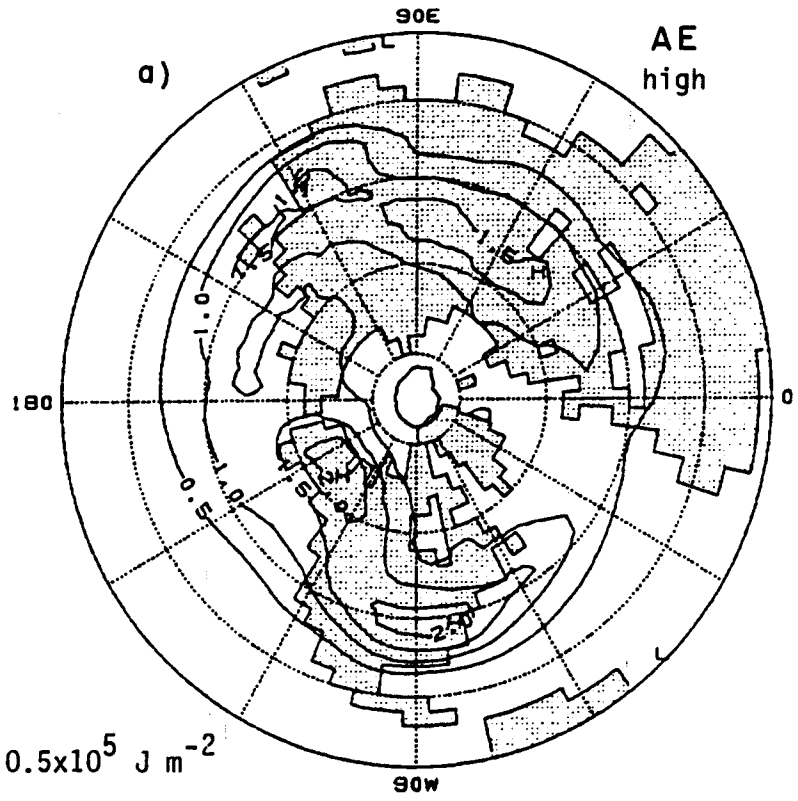

Fig. 6.1. The horizontal distribution of various terms in the wintertime vertically integrated energy budgets of the simulated 2.5 to 10 day disturbances. (a) Eddy APE. (b) Eddy kinetic energy. (c) Time-mean to eddy APE conversion by horizontal processes. (d) Time-mean to eddy APE conversion by vertical processes. (e) Eddy APE to kinetic energy conversion. (f) Time-mean to eddy kinetic energy conversion by horizontal processes. (g) Time-mean to eddy kinetic energy conversion by vertical processes. (h) Eddy geopotential flux convergence. (i) Generation of APE by eddy diabatic processes. (j) net of processes c, d, e, and i. (k) net of processes e, f, g, and h. See text for further details. Contour interval: (a) 0.5×10^5 J m^{-2}, (b) 1×10^5 J m^{-2}, (c), (d), (e), (f) and (j) 0.5 W m^{-2}, (g) and (i) 0.25 W m^{-2}, (h) and (k) 1 W m^{-2}. Negative contours are dashed and the zero contour is dotted.

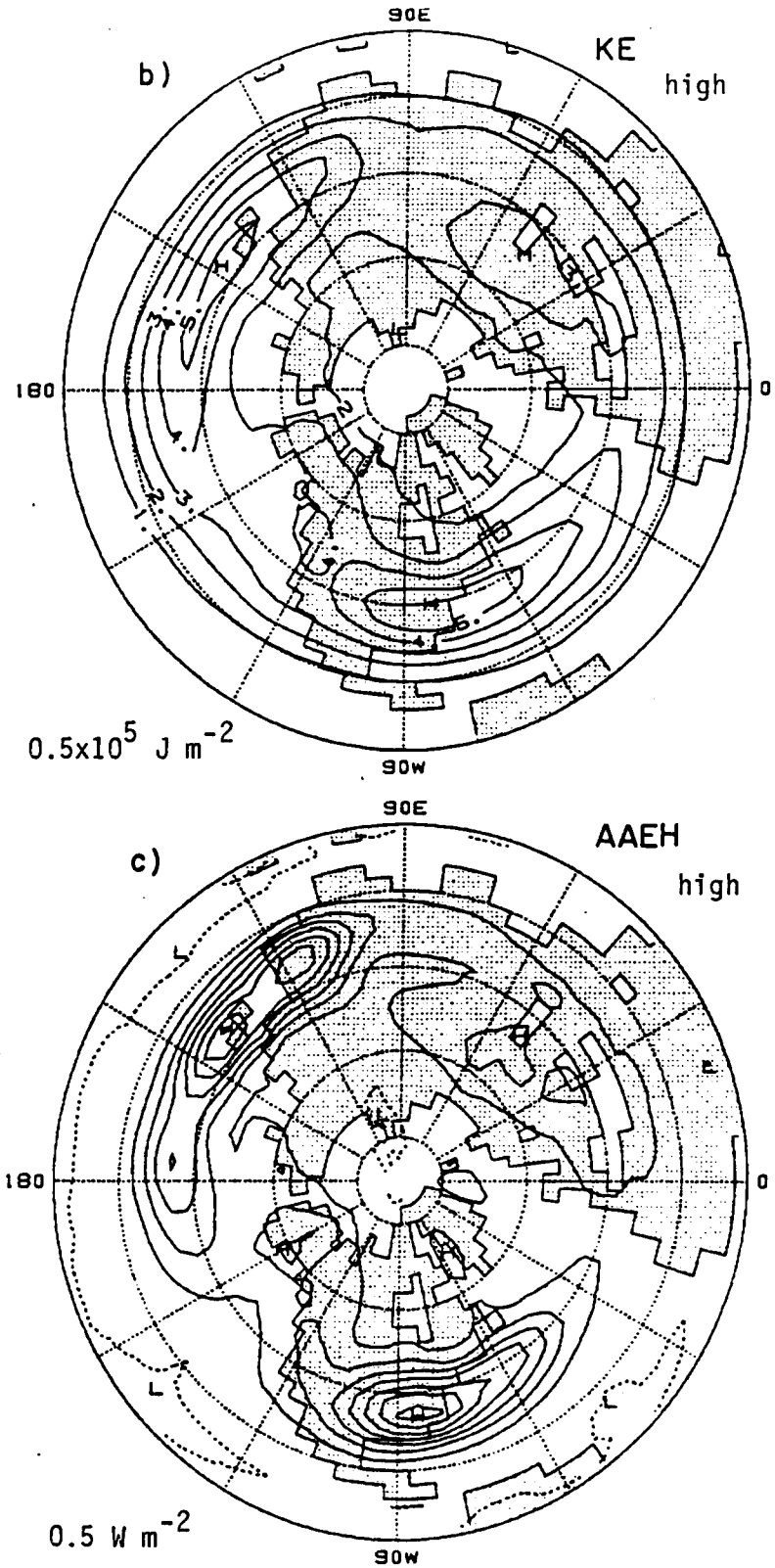

Fig. 6.1 (continued)

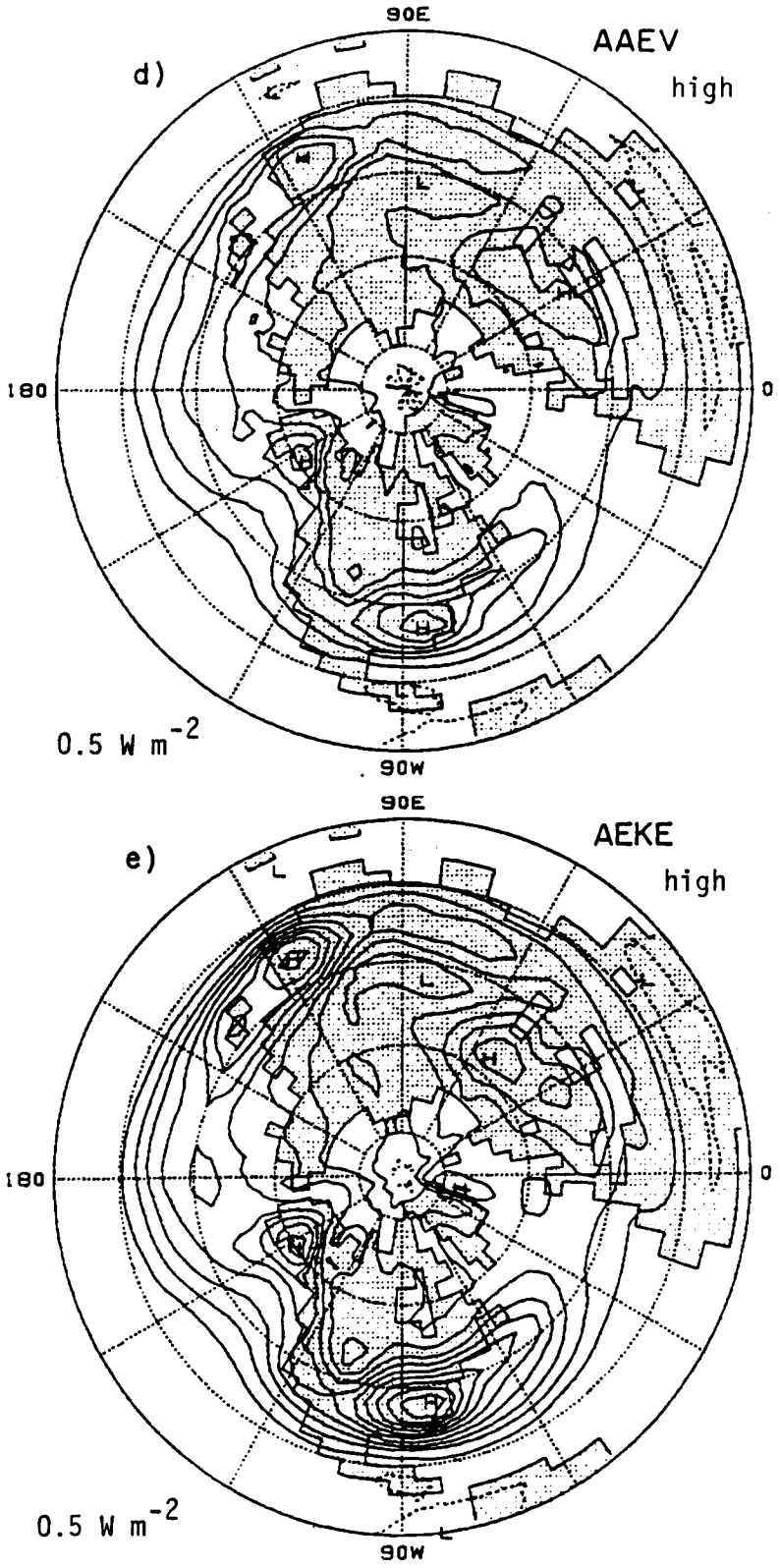

Fig. 6.1 (continued)

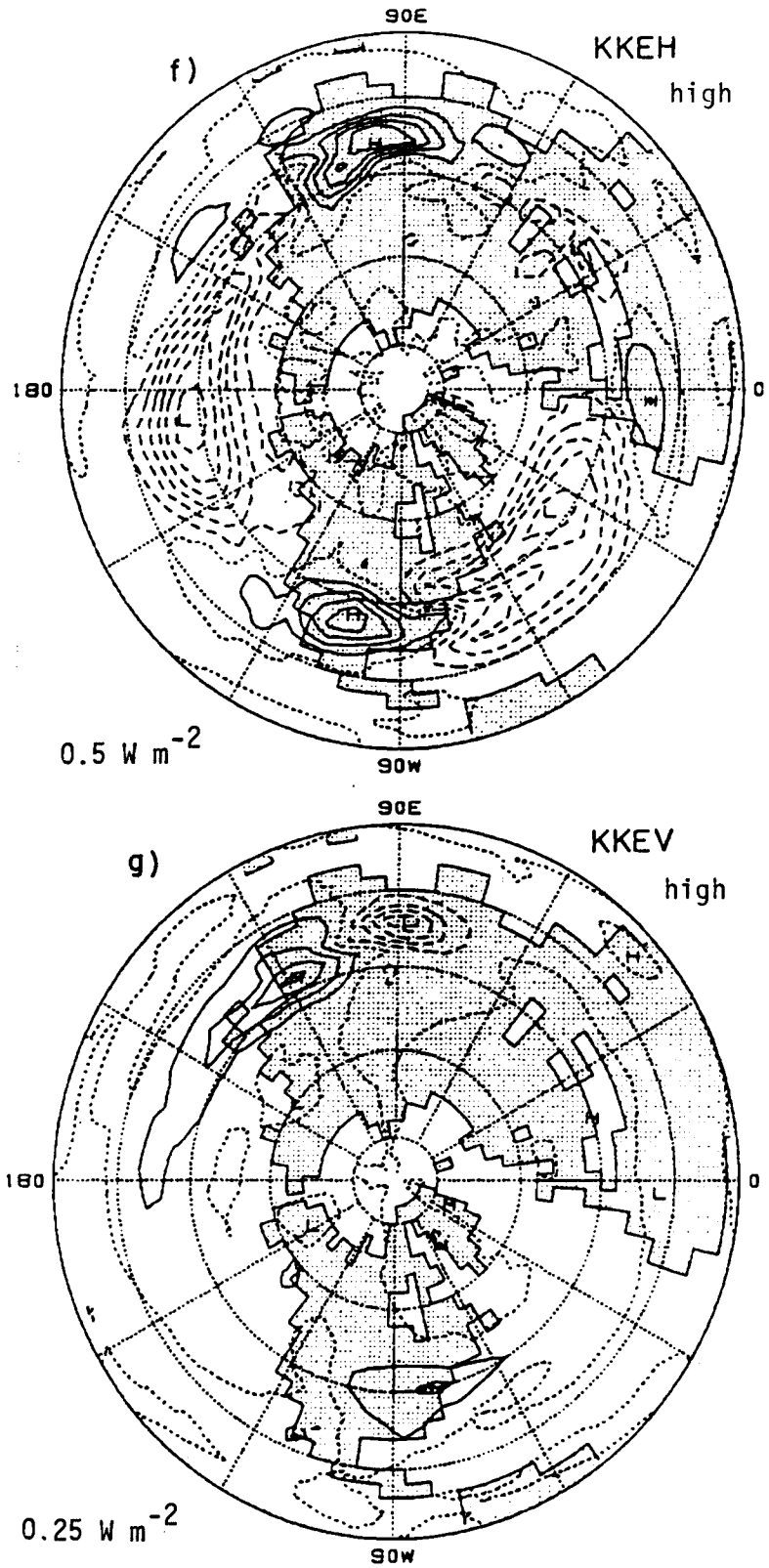

Fig. 6.1 (continued)

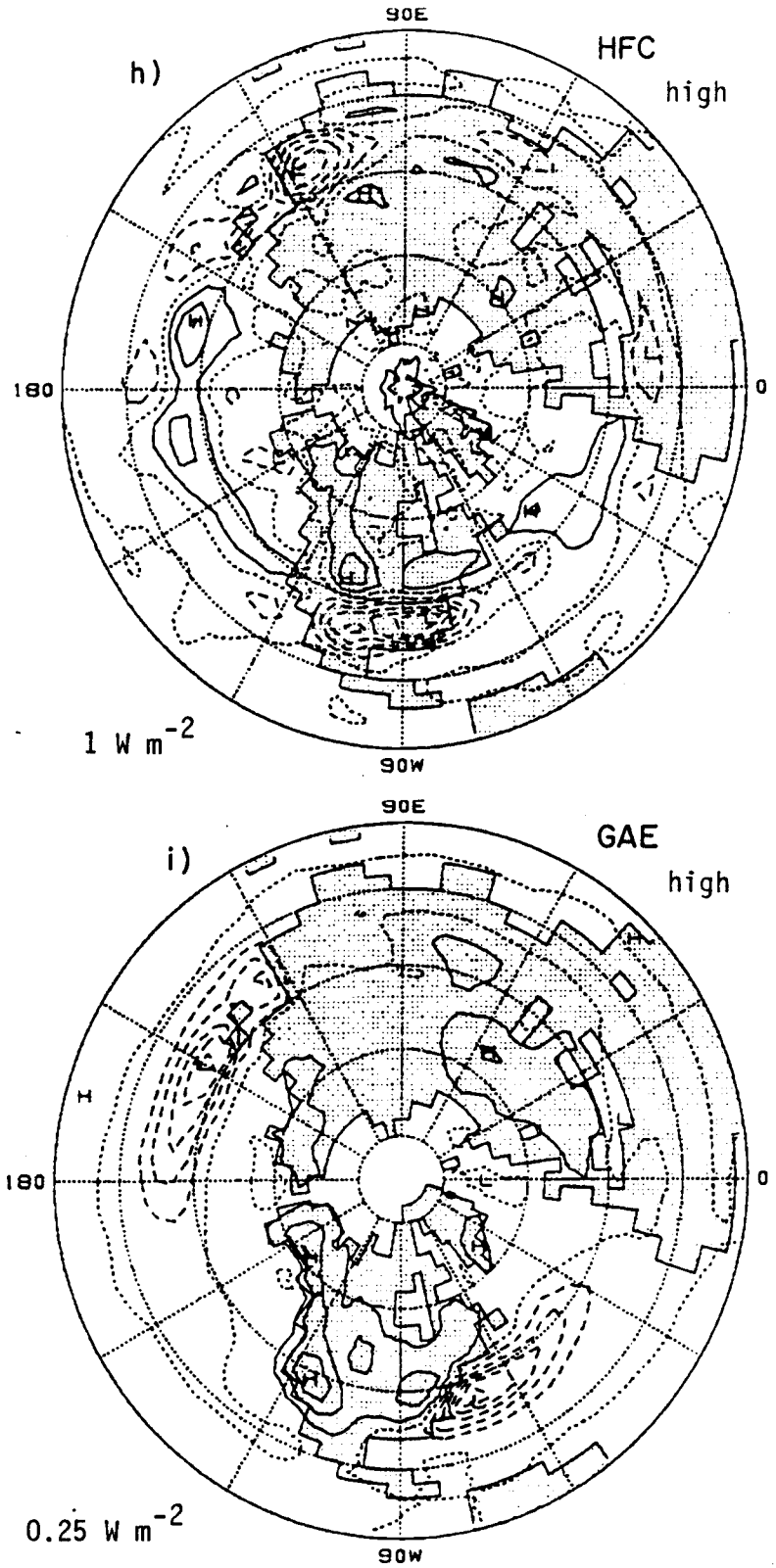

Fig. 6.1 (continued)

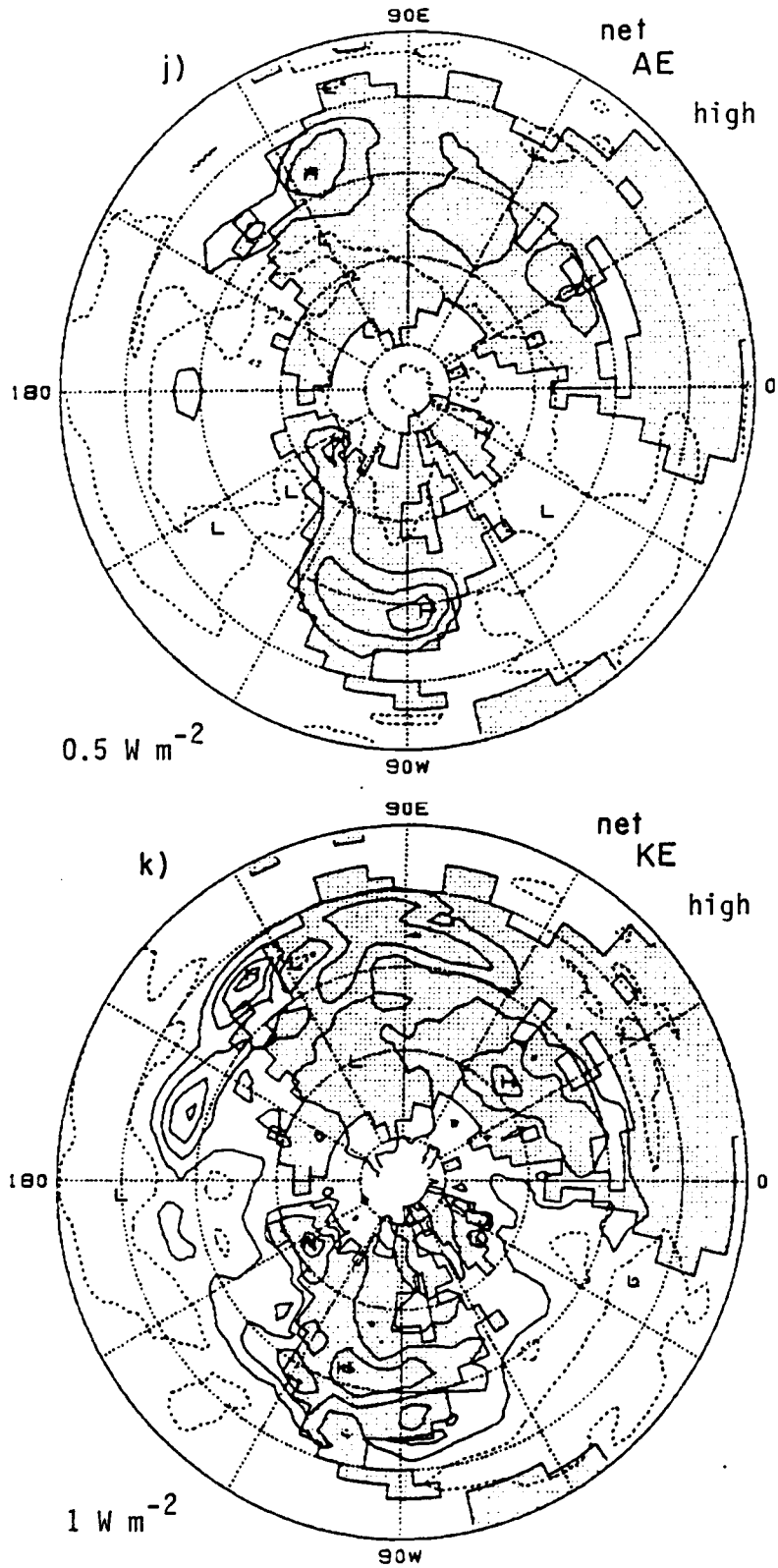

Fig. 6.1 (continued)

vertical wind shear [as measured by u(400 mb) - u(800 mb)] is strongest in the model (see Fig. 3.4). We also note that the rate of conversion of energy as a result of eddy lifting of warm air (or sinking of cold air) is of the same order of magnitude as that caused by the horizontal downgradient eddy heat transport. Over the jet streams where the horizontal gradient of the seasonal mean temperature is large, AAEH is generally larger than AAEV but over the American Northwest region and Europe AAEV is the dominant conversion term.

The rate of conversion from APE to kinetic energy is shown in Fig. 6.1e. The distribution of this term coincides with that of the terms AAEH and AAEV. From its magnitude it appears as if this term provides a considerable sink for the eddy APE as it nearly balances AAEH and AAEV. This term is also the primary source for eddy kinetic energy.

The distribution of the time-mean to eddy kinetic energy conversion rates, terms KKEH and KKEV in Eq. (6.1), are shown in Figs. 6.1f and g, respectively. The horizontal kinetic energy conversion rate is positive upstream of the storm track centers, indicating that high-frequency eddy growth is enhanced by barotropic processes. The existence of a similar effect in the real atmosphere was suggested by Lau (1979a) in his jet-entrance region cross sections and was recently demonstrated by Lau and Lau (1984) in their composite high-frequency eddy life cycle. Downstream from the centers of the storm tracks the reverse process takes place and eddy kinetic energy is destroyed in a barotropic process, part of it converted to kinetic energy of the time-mean flow. This agrees with both theory (Simmons and Hoskins, 1978) and observations (Lau, 1979a; Lau and Lau, 1984). It is of interest to see the relative importance of the five terms in KKEH. For a zonally-symmetric basic state only term (2) is nonzero (see Eq. 6.1). The horizontal distribution of this term is shown in Fig. 6.2a. Terms (1) and (4) are the largest in KKEH but they tend to cancel each other (largely because the atmospheric flow is close to being horizontally non-divergent) we have thus presented only their sum in Fig. 6.2b. We see that this sum is of equal magnitude to that of term (2), that is the longitudinal shear of the mean zonal wind and

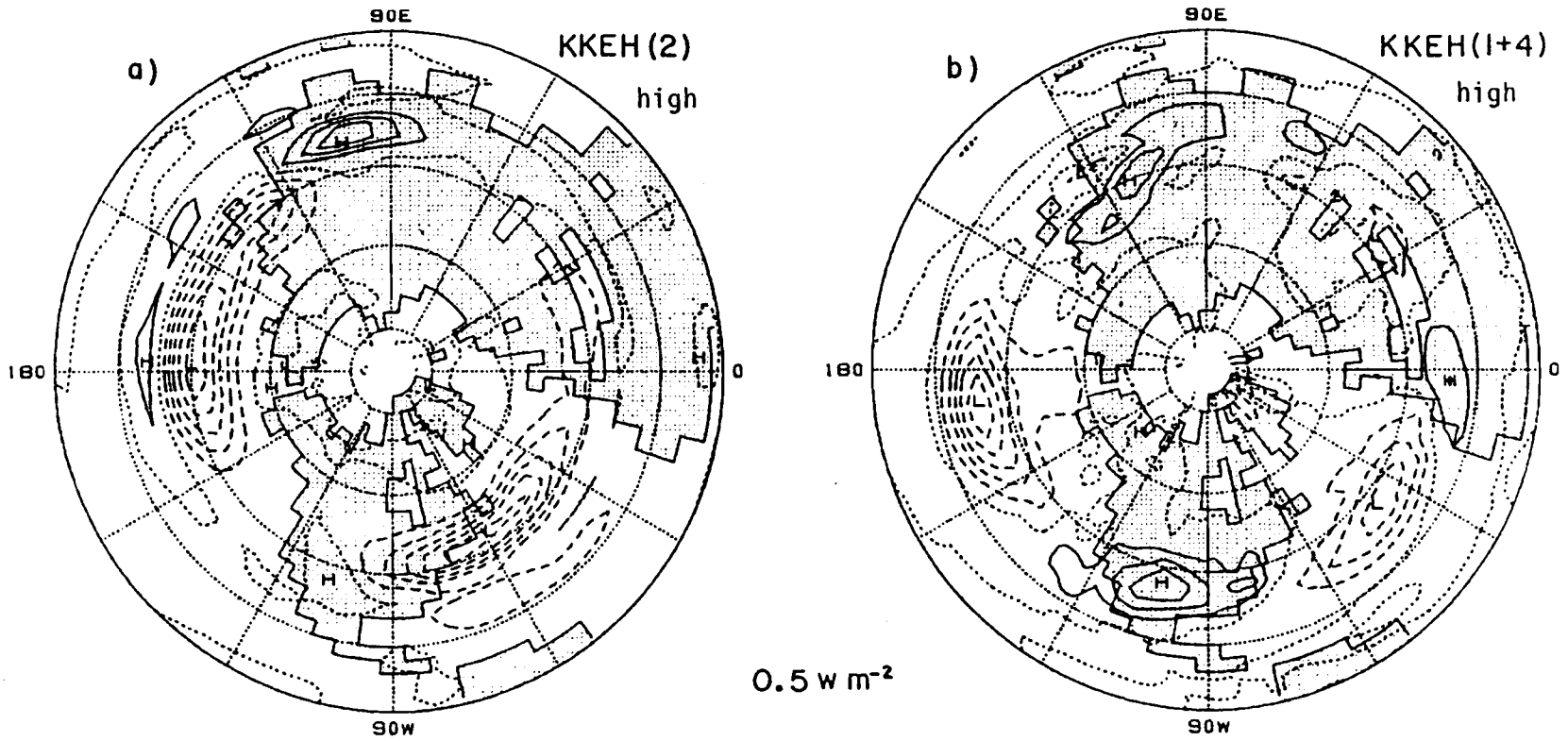

Fig. 6.2. Horizontal distribution of vertically integrated time-mean to eddy kinetic energy conversion terms for 2.5 to 10 day disturbances. (a) Term (2) of KKEH. (b) The sum of terms (1) and (4) of KKEH. See equation (6.1) and text for further details. Contour interval 0.5 W m^{-2}; negative contours are dashed and zero contour is dotted.

the latitudinal shear of the mean meridional wind play an important role in this barotropic process. Terms (3) and (5) (not shown) have a much smaller effect on KKEH. KKEV is weaker than KKEH and tends to counteract the latter, as shown in Fig. 6.1g.

Figure 6.1h presents the role of eddy dispersion in the maintenance of the local kinetic energy. This figure suggests that the eddies tend to disperse their own energy downstream from the regions of maximum kinetic energy generation (by the AEKE term). The direction of dispersion seems to be oriented from west to east almost parallel to that of the local time-mean flow. This result is not surprising since as we have already shown that these high-frequency eddies are elongated in the north-south direction and thus, tend to disperse their energy eastward relative to the basic flow.

The effect of the diabatic heating on the generation of eddy APE is shown in Fig. 6.6i. This process is described by the covariance of eddy sub-grid-scale heating and temperature (term GAE in 6.2). Over the oceanic storm tracks this covariance is negative. This is a result of condensational heating in the convective clouds, which form in the cold air advected by the eddies over the relatively warmer ocean surface. Over the continental storm tracks of North America and Europe, diabatic processes generate APE. This feature is strongest in the model's lower layer and might be unrealistic. Kim and Chang (1982) have calculated the global distribution of simulated precipitation rate by the different processes parameterized in the model. Their results show that the two-level model is unable to simulate the wintertime shallow convective precipitation which usually takes place over cool ocean and land surfaces. The precipitation over the North American continent and Europe is therefore a result of moisture flux convergence in the generally southwesterly flows. Thus, the typical situation over these regions is that a moving disturbance is preceded by warm-air precipitation followed by cold-air clearing and radiative cooling. This will obviously cause a generation of eddy APE.

In Fig. 6.3a we present the spatial correlation field between the precipitation anomaly at 50°N, 120°W and the hemispheric geopotential height field anomaly (both in the 2.5 to 10 day band). The figure

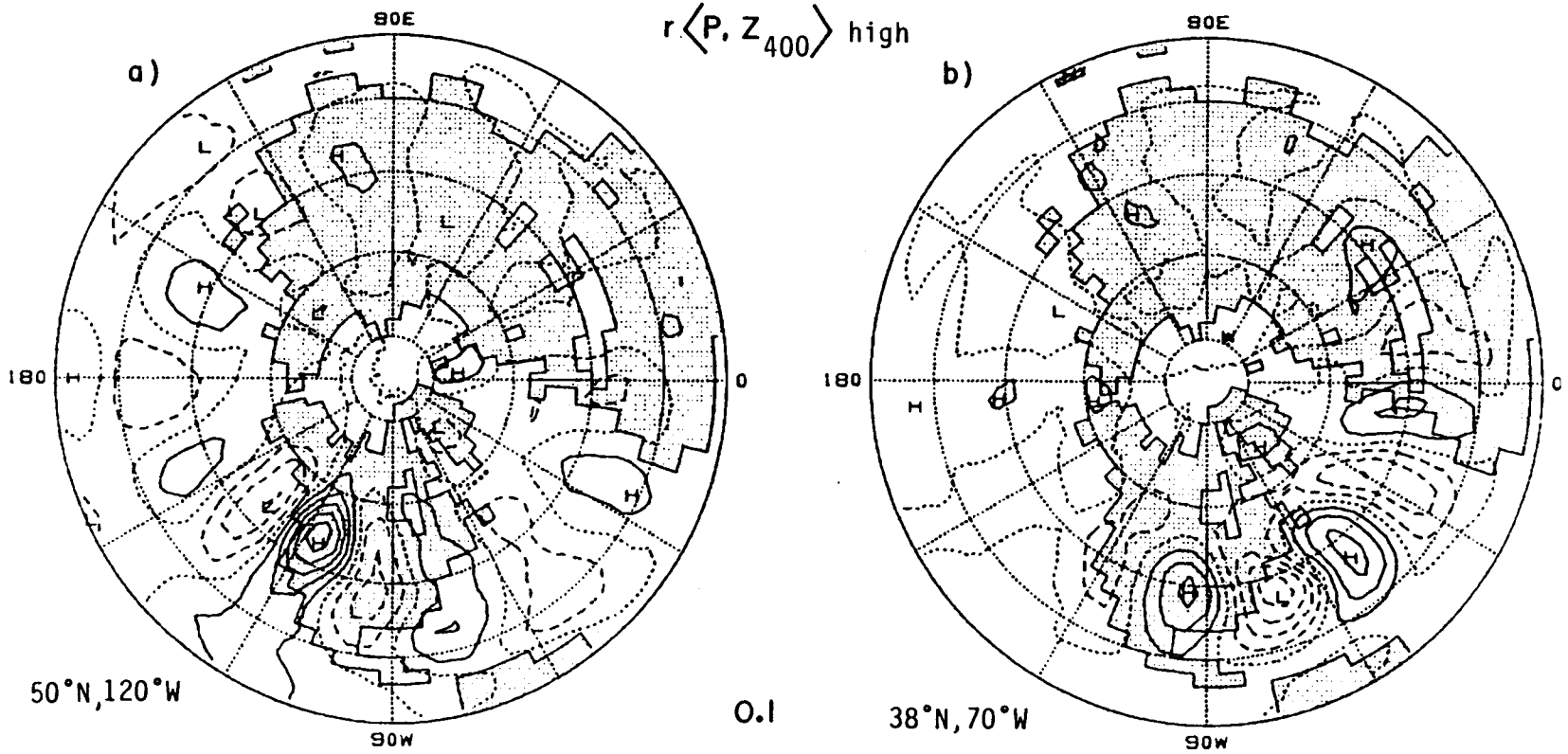

Fig. 6.3. (a) Simultaneous correlation between the simulated 2.5 to 10 day fluctuations in precipitation at 50°N and 120°W and 400 mb geopotential height fluctuations elsewhere. (b) Same as (a) but for 38°N,70°W. Contour interval 0.1; negative contours are dashed and zero contour is dotted.

clearly shows that precipitation there tends to happen in southwesterly flows. Over the storm tracks the situation is different as is represented by the 38°N, 70°W precipitation to geopotential height correlation field in Fig. 6.3b. The North American positive GAE feature has an abrupt edge along the ocean - land border line. This results from the negative correlation between sensible heating and temperature over the ocean which cancels some of the precipitation - clearing effect.

Finally, Figs. 6.1j and k show the local net of all the processes discussed above, in the APE and kinetic energy budgets, respectively. These net fields have maxima slightly upstream (in the time-mean flow sense) of the regions of maxima in the APE and kinetic energy and minima elsewhere. This is understandable on the grounds of not accounting for the advection by the time mean flow. The magnitude of the net generation is such that the mean amount of energy in the storm tracks could be generated in one or two days. It is likely that the eddy Reynolds stresses could counteract this net effect. Lau (1979b) has in fact calculated the Reynolds stress terms in the eddy kinetic energy equation showing that this is indeed the case in observations (see his Fig. 12b). Sub-grid frictional dissipation will also act more strongly in regions of large kinetic energy, thus, balancing the KE generation there.

6.3 Energetics of low-frequency eddies

The energy cycle of low-frequency eddies is presented in Figs. 6.4a to k. As in the case of high-frequency eddies we have calculated those processes described by terms AAEH, AAEV, AEKE, KKEH, KKEV, HFC, and GAE of Eqs. 6.1 and 6.2.

One of the difficulties encountered when dealing with atmospheric low-frequency eddies is the lack of a unifying theory to explain their dynamical origins and maintenance. In the introduction to this study (Chapter 2) we have pointed at some of the attempts made during the years to explain their existence and behavior. These theories can be evaluated based on the results presented here.

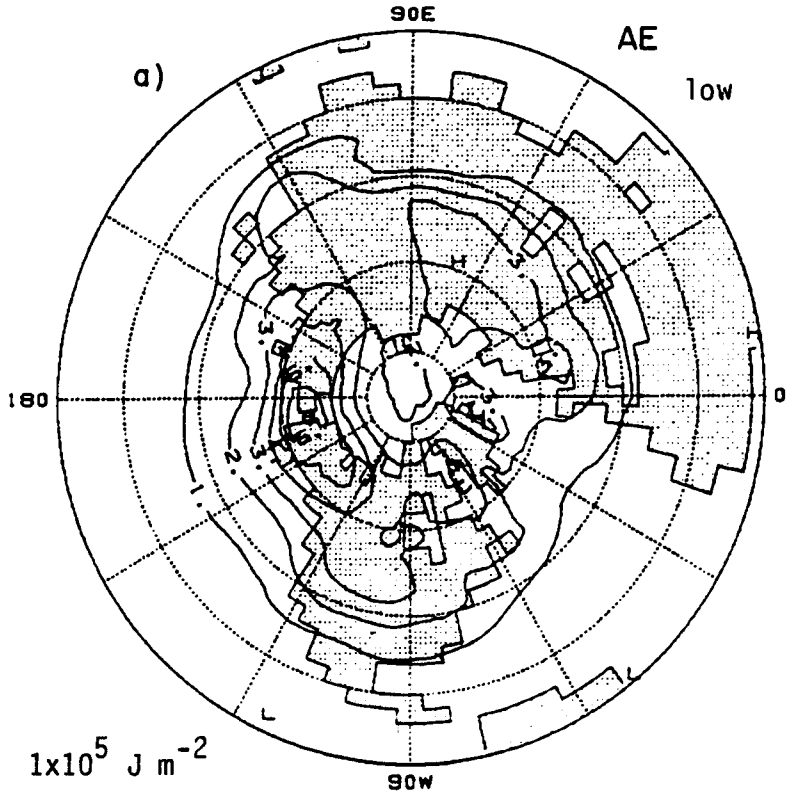

Fig. 6.4. The horizontal distribution of various terms in the wintertime vertically integrated energy budgets of the simulated 10 day lowpass disturbances. (a) Eddy APE. (b) Eddy kinetic energy. (c) Time-mean to eddy APE conversion by horizontal processes. (d) Time-mean to eddy APE conversion by vertical processes. (e) Eddy APE to kinetic energy conversion. (f) Time-mean to eddy kinetic energy conversion by horizontal processes. (g) Time-mean to eddy kinetic energy conversion by vertical processes. (h) Eddy geopotential flux convergence. (i) Generation of APE by eddy diabatic processes. (j) net of processes c, d, e, and i. (k) net of processes e, f, g, and h. See text for further details. Contour interval: (a) and (b) 1×10^5 J m^{-2}, (c), (d), (e), (f) and (j) 1 W m^{-2}, (g) and (i) 0.5 W m^{-2}, (h) and (k) 2 W m^{-2}. Negative contours are dashed and the zero contour is dotted.

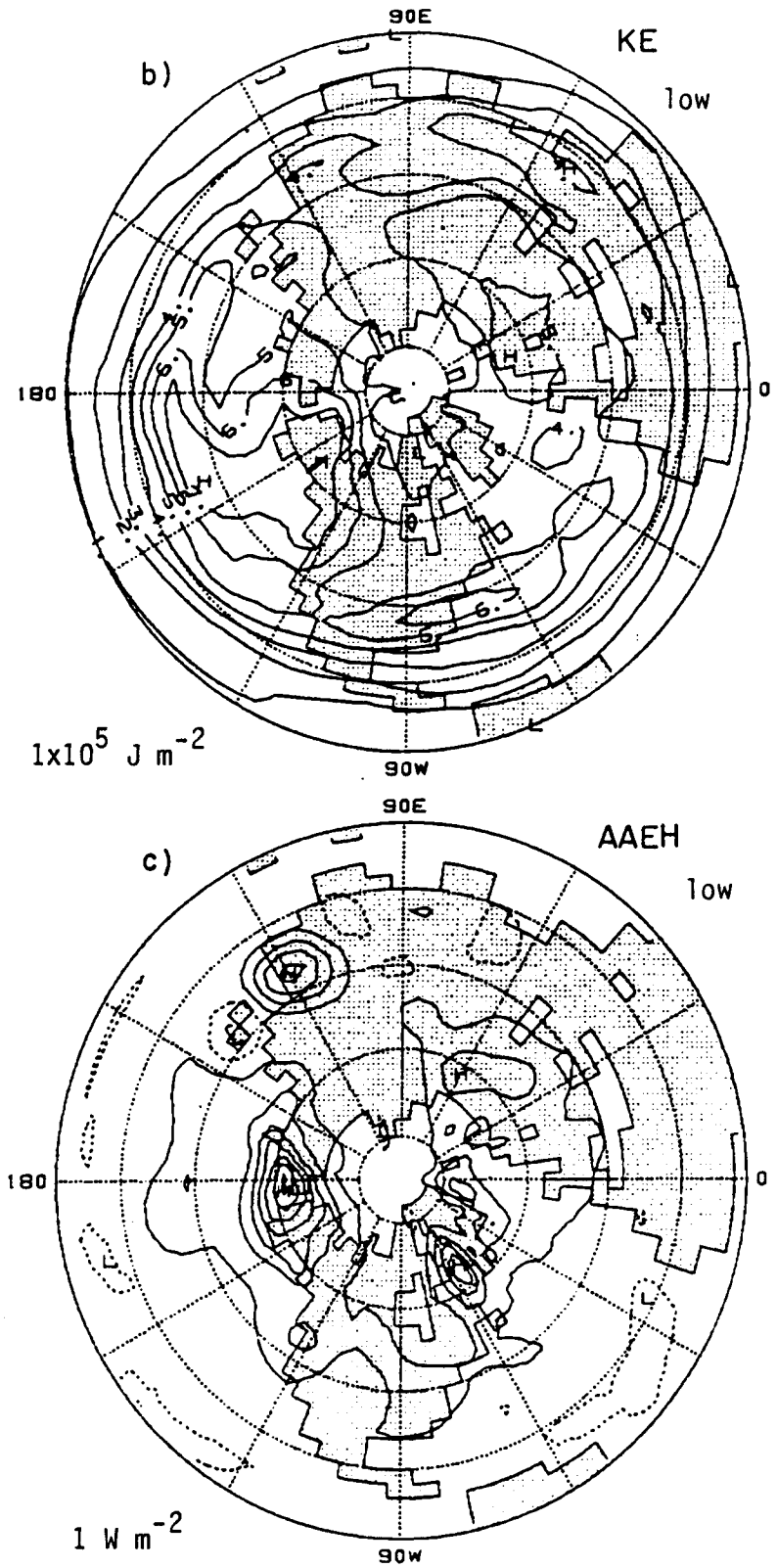

Fig. 6.4 (continued)

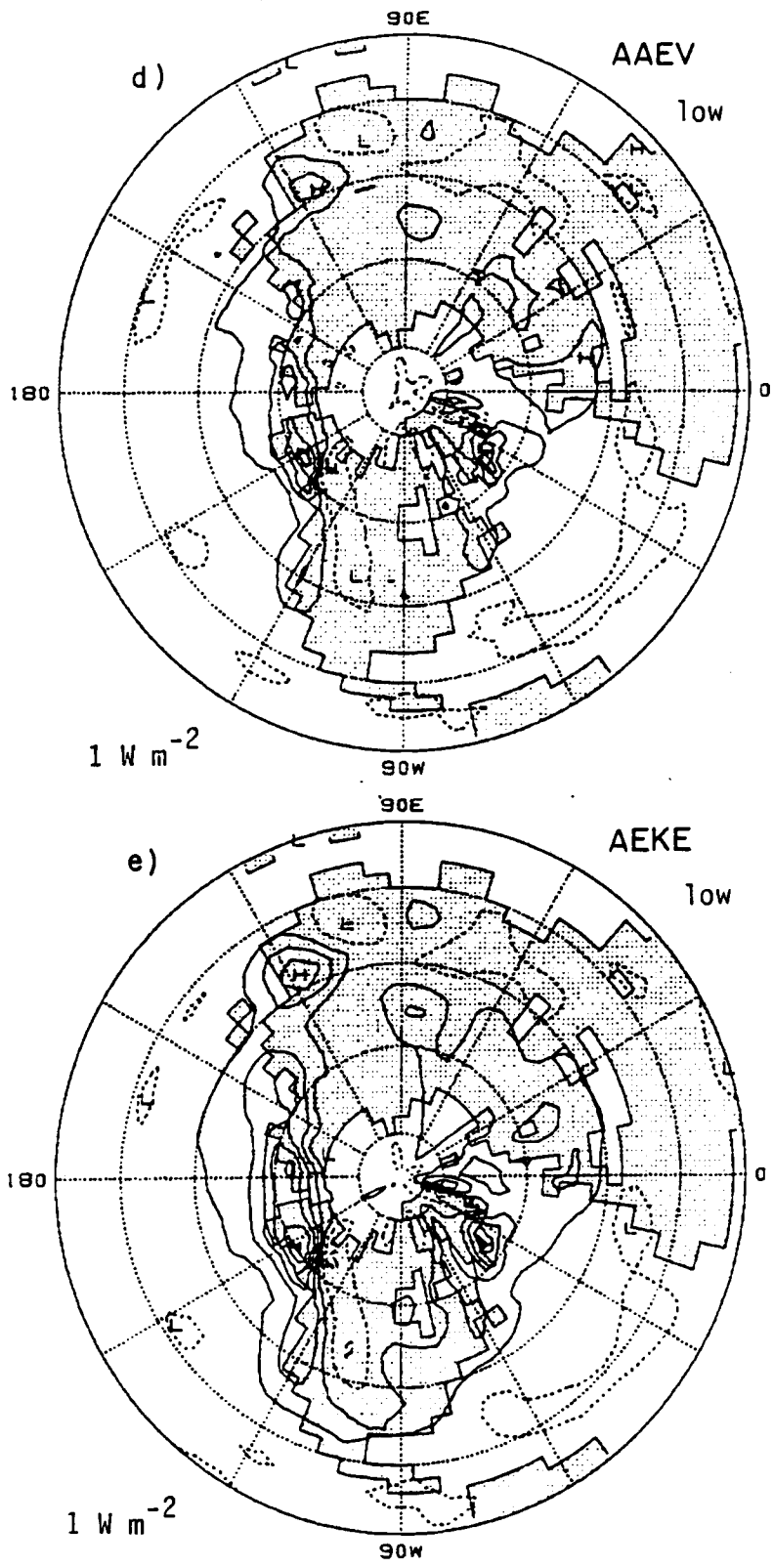

Fig. 6.4 (continued)

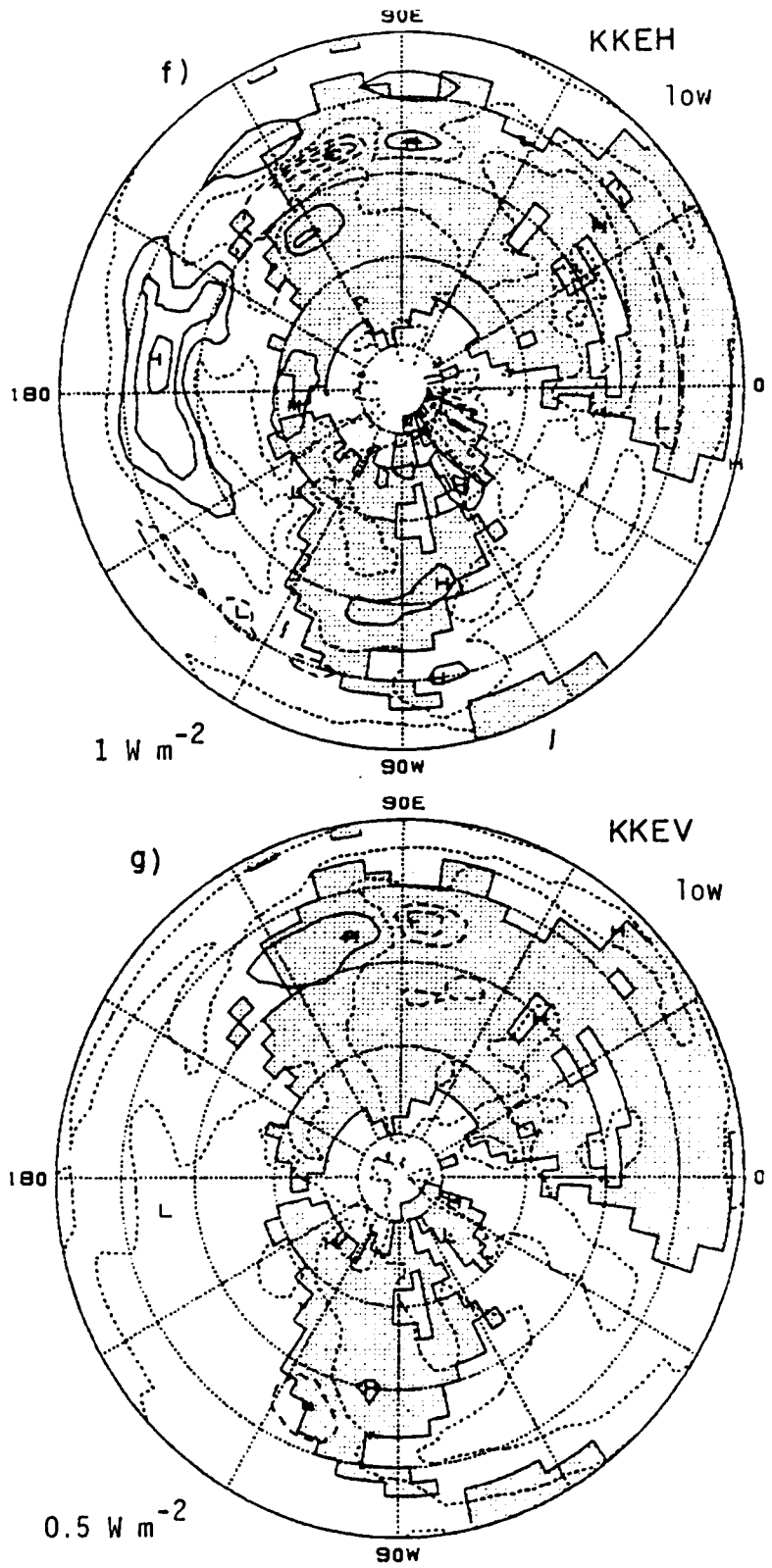

Fig. 6.4 (continued)

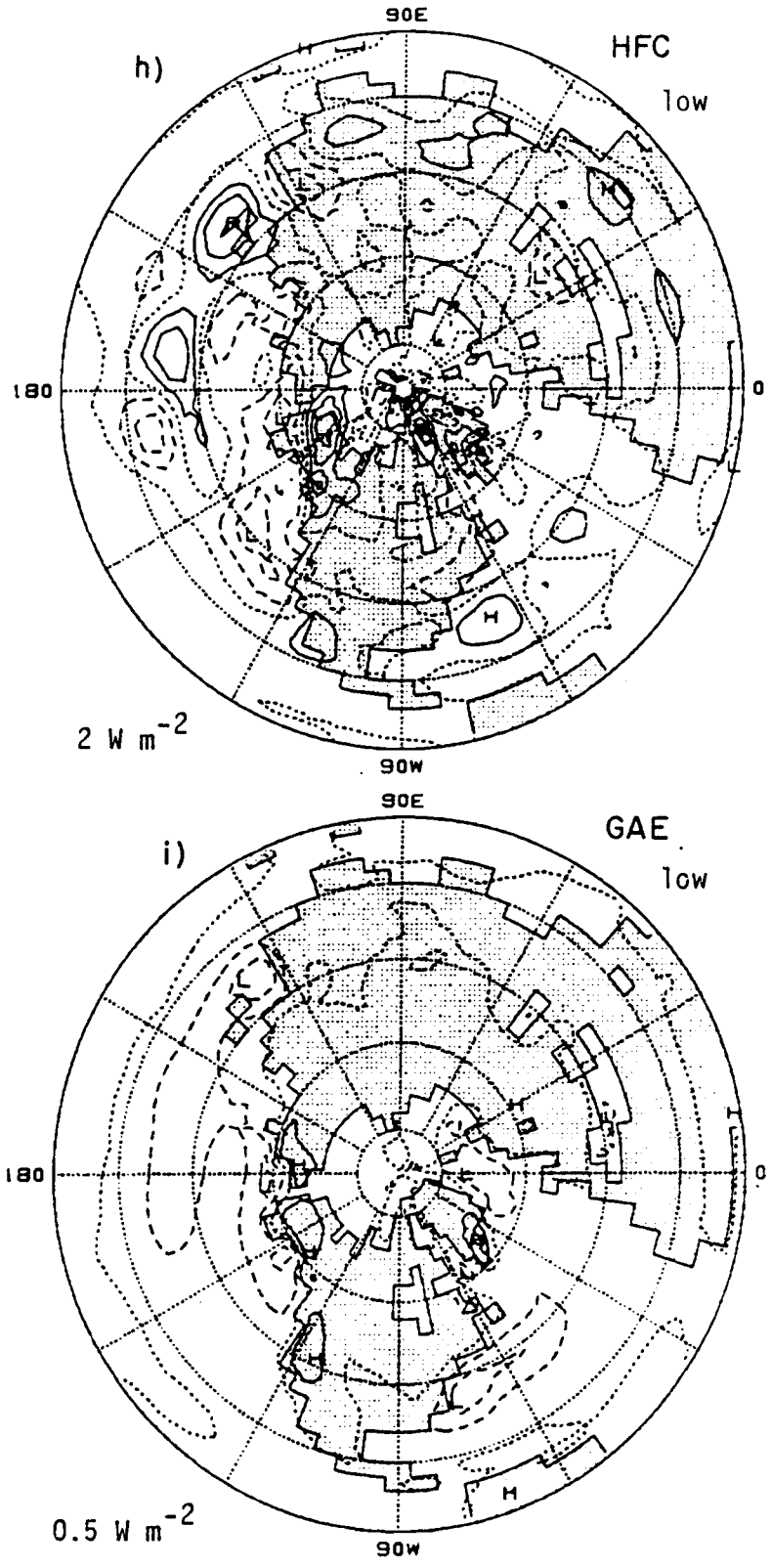

Fig. 6.4 (continued)

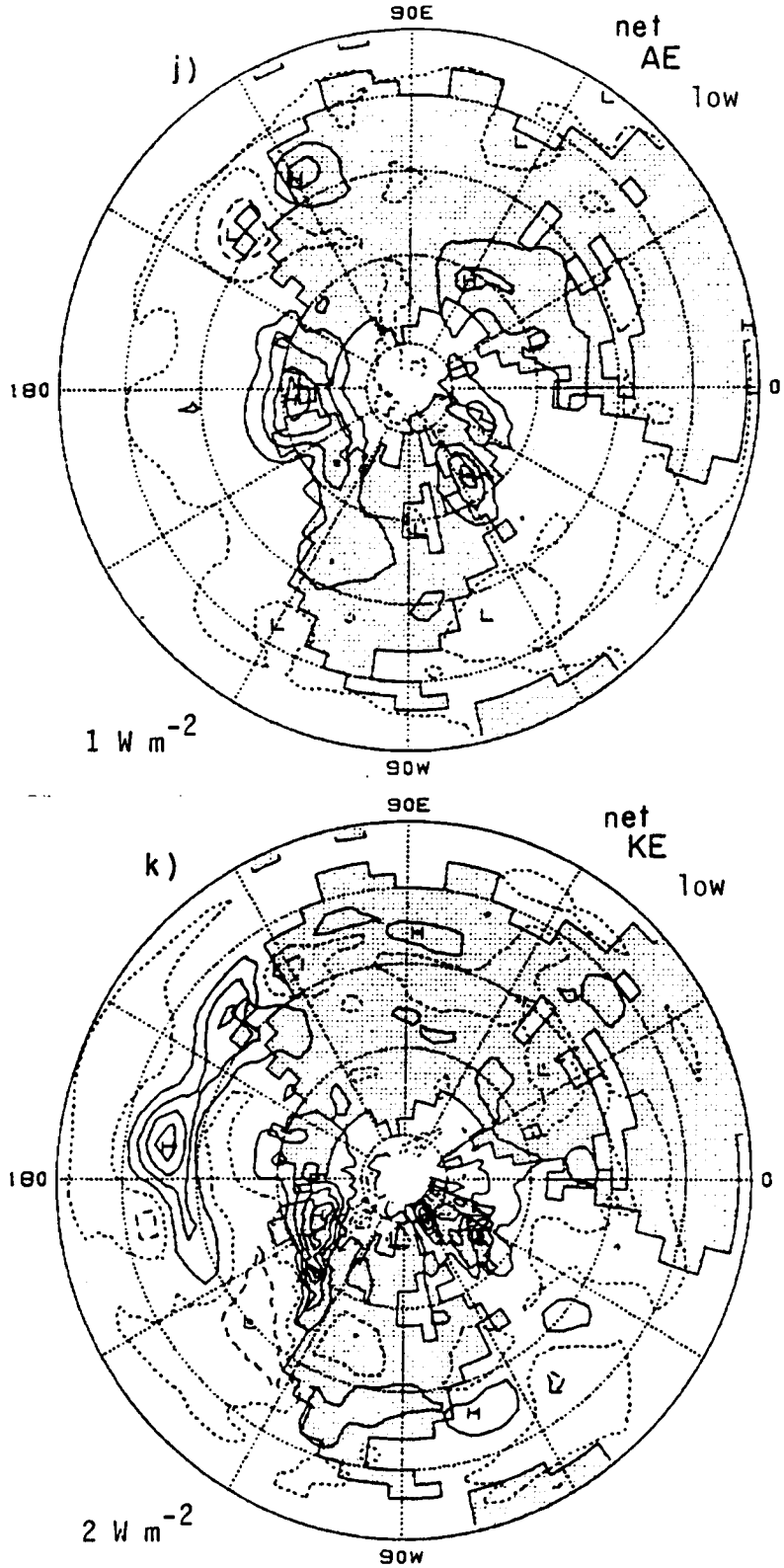

Fig. 6.4 (continued)

In examining the energy cycle of low-frequency eddies we first note that in this frequency range, the ratio between the energy associated with the fluctuations of the temperature field (Fig. 6.4a) and that associated with fluctuations in the wind field (Fig. 6.4b) is larger than in the high-frequency band (see Figs. 6.1a and b). By using scaling arguments, it can be shown that this ratio should be proportional to the square of the typical zonal wavelength of the eddies. Thus, the above observation is consistent with previous results showing that low-frequency eddies have larger scales than high frequency ones.

The next two figures (6.4c and d) present the low-frequency baroclinic APE conversion rates AAEH and AAEV. These are found to have a significantly different spatial distribution than their high-frequency counterparts and a larger magnitude. This magnitude difference is especially large in the case of AAEH. Recalling the eddy statistics presented in Chapter 5, we should not be surprised that this is so. After all, the low-frequency northward heat transport over the Bering Sea reaches values three times larger than the high-frequency transports over the storm tracks (see Figs. 5.1a and b). An examination of the winter-mean temperature field (Fig. 3.7) reveals the existence of a regional intensification of the temperature gradient over the Bering Sea and Alaska and also over Greenland and northeastern Europe (where there also exist local maxima in $\overline{v'T'}$). Consistent with these high latitude features in the thermal field we also find a local enhancement of the vertical wind shear and weak vorticity gradients as pointed out in Chapter 3.4. Thus, it seems that high latitude baroclinic energy conversions play an important role in the maintenance of low-frequency eddies. A careful examination of the data compiled by Lau et al. (1981) reveals that this should qualitatively also be the case with observations (see e.g., their Fig. II.C.3.f). An interesting feature of the AAEH field is the dipole-like feature over western China and Japan. The positive center over China is no doubt tied with the local geopotential height r.m.s. maximum over the Sea of Japan noted earlier in Chapter 4. The minimum in AAEH over Japan results from very weak meridional temperature

transports there and a positive zonal transport over a region where $\partial\overline{T}/\partial x$ is positive.

The rate of conversion from eddy APE to eddy kinetic energy is shown in Fig. 6.4e. The maxima in this figure lie close to those in the AAEH and AAEV terms indicating that the conversion of APE to kinetic energy there is tied to the generation of eddy APE. We note that this conversion is not related to the maxima of kinetic energy at the latitudes of the jet-streams. Also significant is the fact that the magnitude of this term is smaller than the sum of AAEH and AAEV (in the high-frequency band this term almost exactly balances the effect of the latter two).

The mechanism responsible, at least over the Pacific, for the jet stream eddy kinetic energy maxima is revealed in Fig. 6.4f showing the horizontal time-mean to eddy kinetic energy conversion rate (KKEH). This term is positive over the Pacific jet exit regions in the middle latitudes indicating a barotropic conversion of kinetic energy from the time mean circulation to the eddies. In Fig. 6.5a we have presented the contribution to KKEH from the "traditional" barotropic instability term associated with the meridional shear of the basic state and the eddy meridional momentum flux (term (2) of KKEH). This term has the form of small scale dipole-like features, in apparent contrast to the large scale features in its high-frequency counterpart. The positive conversion rates seem to dominate here, which is again different from the high-frequency picture. As shown in Fig. 6.5b, a significant contribution to KKEH comes from the terms (1) and (4) in Eq. 6.1. Individually these terms are even larger in magnitude but as a result of the horizontal quasi-nondivergence of the flow they partially cancel each other. In a barotropic flow, the sum of (1) and (4) may be written as:

$$-\left(\overline{u'^2} - \overline{v'^2}\right)\frac{\partial \overline{u}}{\partial x}$$

(see Simmons et al., 1983). This implies that eddies which are elon gated in the east-west direction (i.e., $\overline{u'^2} > \overline{v'^2}$) as is the case with the low-frequency eddies, lose energy to the time-mean flow at the jet-entrance regions and extract energy from it in the jet-exit

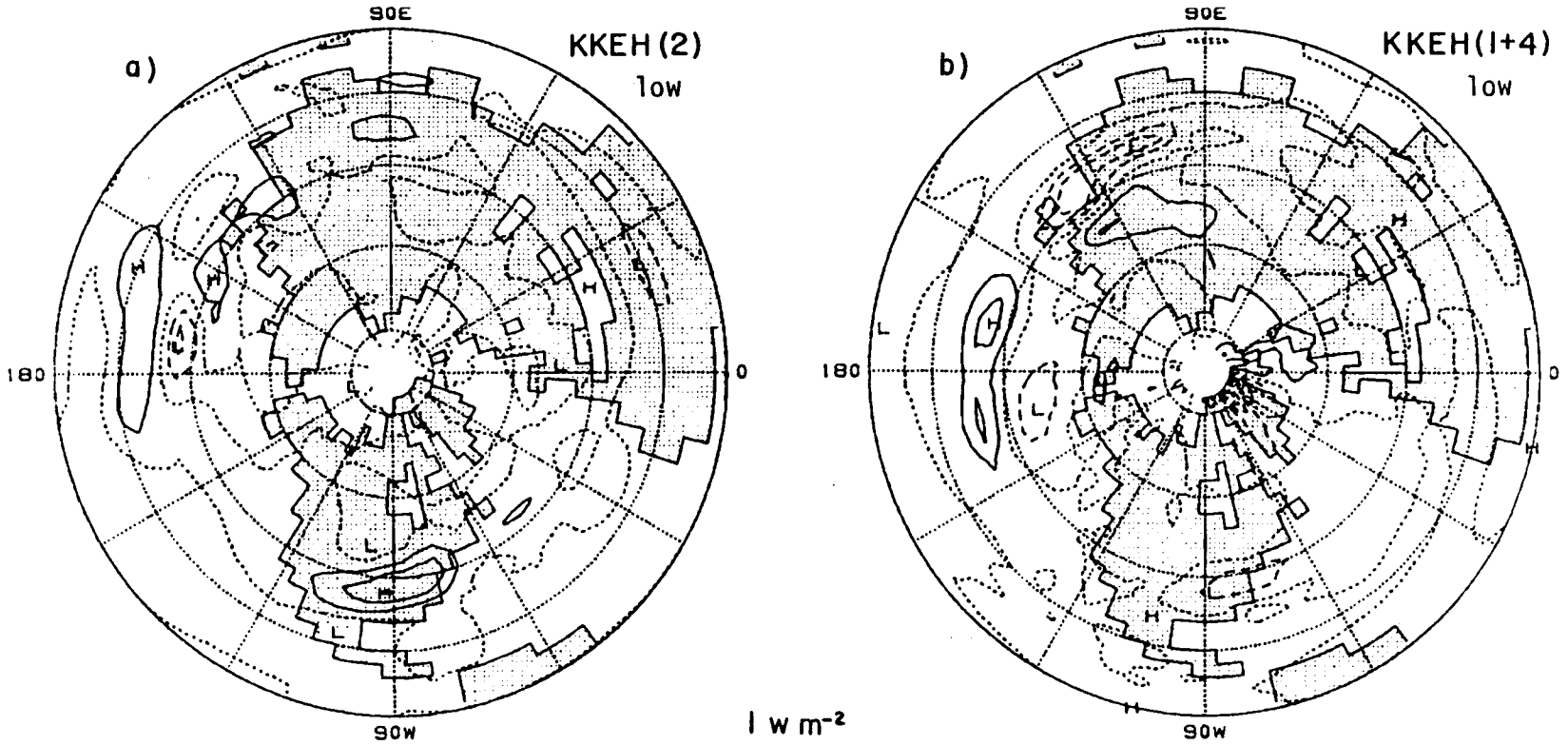

Fig. 6.5. Horizontal distribution of vertically integrated time-mean to eddy kinetic energy conversion terms for 10 day lowpass disturbances. (a) Term (2) of KKEH. (b) The sum of terms (1) and (4) of KKEH. See equation (6.1) and text for further details. Contour interval 1 W m^{-2}; negative contours are dashed and zero contour is dotted.

regions. This barotropic conversion was a key process in Simmons et al (1983) discussion of the barotropic instability of zonally asymmetric basic states. Over the Atlantic the eddies have much weaker eccentricity and the jet stream longitudinal gradient is smaller, hence the conversion rates are much smaller. The vertical kinetic energy conversion term KKEV (Fig. 6.4g) is relatively weak and shows a tendency to counteract the horizontal term. This is similar to what we have seen in the case of high-frequency eddies.

The role of wave dispersion in redistributing kinetic energy in the low-frequency band is shown in Fig. 6.4h. Since the low-frequency eddies are elongated in the east-west direction we expect them to disperse energy generally westward relative to the time mean flow (this effect should be strong at middle latitudes where the latitudinal gradient of the earth's vorticity is strong). In Fig. 6.4h, we indeed find that over the middle latitudes of the western Pacific the centers of energy flux convergence are located upstream of the region where kinetic energy is generated by the KKEH process. Over the higher latitudes of the North Pacific, where we have found a strong baroclinic generation of kinetic energy there exists a region of energy flux divergence. Further north, over Alaska, there is a region of energy flux convergence. In the middle-latitude Atlantic we find a few circular regions of convergence, where the local KE maximum exists.

The generation of potential energy by diabatic processes (term GAE in 6.2) is shown in Fig. 6.4i. The picture here is generally similar to that at the high frequencies. We again find destruction of APE over ocean areas and generally weak generation over the continents. Over the northwestern part of North America and over the far northeastern part of Asia we find a region of more pronounced GAE maxima of similar origin as their high-frequency counterparts (see Chapter 6.3).

Figures 6.4j and k show the net effect of all the individual terms we have discussed above on the potential and kinetic energy equations, respectively. Similar to what we noticed at high frequencies, the regions of eddy generation are located at or slightly upstream of the regions of eddy energy maxima, suggesting that the

processes we have reviewed are responsible for the maintenance of the eddies.

These findings thus indicate that low-frequency eddies are maintained primarily by a baroclinic energy cycle. Over the Pacific barotropic conversions contribute to eddy growth. We will now summarize these results by looking at the hemispheric means of the barious conversions presented above.

6.4 A hemispheric view of eddy energetics

The results we have so far obtained enable us to sketch a hemispheric energy box diagram for the wintertime variability. We remember that here we consider the conversions between the wintertime mean circulation and the time eddies on all spatial scales, divided into two frequency categories. Some of the links in the energy diagram are missing but we will speculate as to their effects, on the basis of other results.

When we average the kinetic and temperature variance equations over the whole Northern Hemisphere and consider this hemisphere to be a closed domain (a consideration justified post priori in the case of HFC), some of the terms vanish. This is true of all terms which can be represented in flux convergence form, which includes the terms representing the advection of eddy energy by the time mean flow, the geopotential flux convergence term (HFC) and the eddy Reynolds stress terms (FE and QE). Symbolically equations 6.1 and 6.2 now become:

$$\frac{\partial \hat{K}_E}{\partial t} = \widehat{AEKE} + \widehat{KKEH} + \widehat{KKEV} + \hat{F} + \hat{B}_k \qquad (6.3)$$

$$\frac{\partial \hat{A}_E}{\partial t} = -\widehat{AEKE} + \widehat{AAEH} + \widehat{AAEV} + \widehat{GAE} + \hat{B}_A \qquad (6.4)$$

where the hat stands for both vertical and hemispheric averaging.

Figure 6.6 presents the energy diagram for the model's wintertime circulation. Here box $\hat{K}$ stands for the kinetic energy of the seasonal mean flow and box $\hat{A}$ for the APE of the seasonal flow (defined in a way consistent with the definition of the eddy APE).

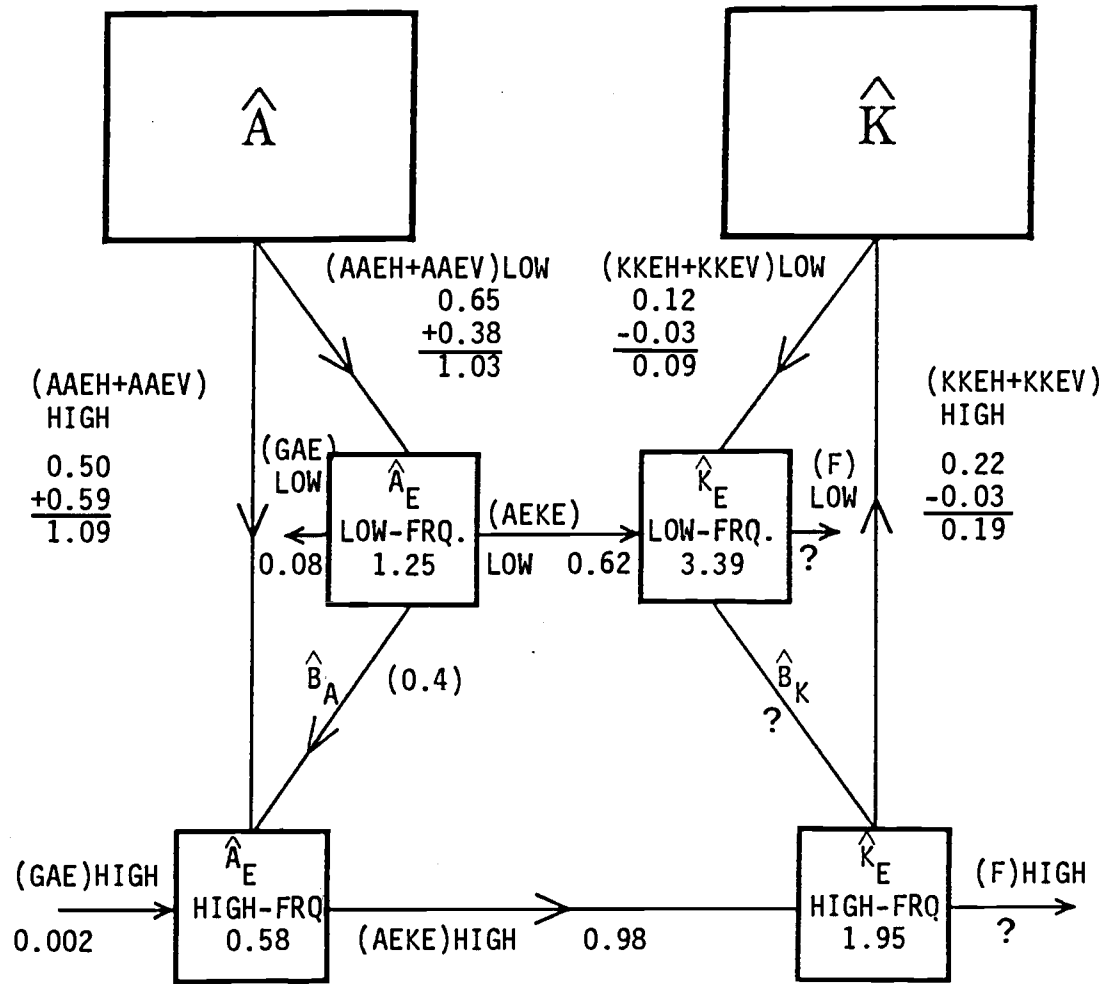

NET $\hat{A}_E$ GENERATION: LOW = 0.33
HIGH= 0.14

NET $\hat{K}_E$ GENERATION: LOW = 0.71
HIGH= 0.79

Fig. 6.6. Energy diagram for simulated low- and high-frequency disturbances. Values are Northern Hemisphere averages. Numbers in boxes denote the APE and KE amounts in 10^5 J m^{-2}. Values along arrows denote conversion rates in W m^{-2}. Direction of arrows represent the direction of the conversion. Net values at bottom refer to net of all processes accounted for here (see text).

As we have already learned, both high- and low-frequency eddies grow at the expense of the available potential energy of the time mean flow, but their baroclinic energy cycles are not exactly similar. In the high frequencies the eddies gain their APE almost equally through vertical and horizontal processes. In the low-frequencies, the horizontal processes dominate. The total conversion rate is, however, almost the same in the two categories (about 1 W/m^2). In the high frequencies, almost all of the APE generated through baroclinic processes is converted to kinetic energy through adiabatic lifting (warm air rising and cold air sinking). In the low frequencies, however, the rate of APE to kinetic energy conversion is only ~60% of the APE generation rate. That again supports our observations on the relative weakness of vertical processes in the low frequencies.

The interesting difference between the two eddy categories lies in their eddy to time-mean kinetic energy conversion. While high-frequency eddies lose their kinetic energy to the time-mean circulation at a rate of about 0.2 W/m^2, low-frequency eddies extract energy from the time-mean circulation at a rate of about 0.1 W/m^2. Although there is a 10 to 1 ratio between the hemispheric mean low-frequency baroclinic conversion rate and the barotropic conversion rates, we believe that barotropic conversions are characteristic of these eddies. As we have noted earlier the model might be exaggerating the intensity of the low-frequency baroclinic conversion; in observations the ratio between the two conversion rates might be more in favor the barotropic conversions than in the simulation although in both cases barotropic processes play only a secondary role in the energetics.

Finally we note the small role played by diabatic processes in generating or destroying eddy APE. In the high-frequency case there is a weak net generation effect which is probably due to the model's mis-handling of high-latitude shallow convection. In the low frequencies diabatic processes provide a sink for the eddy APE.

In this study we have not calculated all the terms in the energy budgets as our goal was limited to examining differences in the key processes only. However, we believe we have the basis to estimate the

effects of the processes not included, i.e, the inter-band conversion terms. It is reasonable to assume that the low-frequency fluctuations are slow enough in time and large enough in space so that locally they do not change much through the life cycle of a high-frequency eddy, and over its spatial extent (at least over one wavelength). Thus the low frequency fields serve as a "basic state" for the high-frequency eddies. It is then reasonable to believe that the high-frequency eddies will respond to baroclinic instability induced by the low-frequency field and react to it in the same way they react to the baroclinically unstable regions in the time mean flow. Thus there will be a "mini-baroclinic-cycle" which will be quite similar to the prominent one we have just reviewed. In this mini-cycle, high-frequency eddies will extract potential energy from the low-frequency flow and lose their kinetic energy to it. The low frequency rates of time-mean to eddy APE conversion and eddy APE to kinetic energy conversion suggest that B_A might be on the order of $0.4\ W\ m^{-2}$.

Before we conclude this chapter we would like to reiterate a point made earlier when examining the net fields in Figs. 6.1j and k and 6.4j and k. This point regards the strong regional confinement of the energetics of the eddies. Through their life cycle both high- and low-frequency eddies exert only a regionally restricted influence. Thus the question of eddy maintenance could, and probably should, be addressed on a regional basis.

CHAPTER 7: THE LIFE CYCLE OF LOW-FREQUENCY DISTURBANCES

In this chapter we deal only with the low-frequency disturbances. We have so far seen convincing evidence that these disturbances are maintained primarily by baroclinic processes acting at latitudes higher than those associated with the more familiar high-frequency disturbances. We have also learned that the growth of low-frequency disturbances is enhanced by barotropic processes, quite in contrast to the barotropic decay typical of high-frequency disturbances.

We would now like to pursue the question of the maintenance of low-frequency disturbances by examining their life cycle. To do so a method must be found to identify low-frequency modes in the data and follow their development in time. Once this goal is achieved, compositing techniques may be used to describe their typical structure and life cycle. In the following pages we will describe the methodology adopted to achieve these goals and the results we have obtained.

7.1 Methodology of identifying and following low-frequency disturbances

One of the ways to identify a mode of variability in time series of meteorological fields is to gain information on its spatial structure and then systematically look for this structure in the data set. The most commonly used approach is the method of space-time spectra. In our case there exists a strong constraint on choosing the proper method, namely the regional character of the low frequency disturbances. In this situation resorting to the use of a set of global basis functions like zonal or spherical harmonics would be inefficient and unsatisfactory. A more reasonable approach to studying regional variability is to use the eigenvectors of the spectral cross covariance (or correlation) matrix as the set of basis functions. This method was first introduced to the field of atmospheric data analysis by Lorenz (1956). Through the efforts of many investigators, including Kutzbach (1967), and Barnett (1977), the so-called Empirical

Orthogonal Function (EOF) method has become a standard technique in the atmospheric sciences.

The "traditional" EOF analysis is most suitable for examining standing oscillations since it uses a matrix of simultaneous spatial correlations. About a decade ago Wallace and Dickinson (1972) suggested a variation on this method which allowed the use of time-lagged information. This was achieved by projecting the time series onto the complex plane, creating a complex spatial "cross-spectrum" matrix instead of the real covariance matrix, and using the complex eigenvectors as the set of basis functions. Recently, Barnett (1983) has revived this technique and applied it to a global data set. The technique is now known as Complex EOF (CEOF) analysis.

In this work we have followed the method of CEOF analysis suggested by Barnett (1983). The real time series of normalized low-frequency geopotential height anomalies from the OSU AGCM was transformed to a coarse, equally spaced grid superimposed on a polar azimuthal equal area projection of the Northern Hemisphere. The uniform areal resolution of this grid is about 4.25×10^5 km^2. At each point we then augmented the original time series by adding to it a complex part that is virtually equal to the original series in amplitude but shifted in time by one quarter of the temporal phase at each frequency (this series is known in the literature as the "Hilbert transform" of the first one). Using the new complex time series we have calculated the complex spatial cross correlation matrix and found its eigenvectors. These complex eigenvectors contain information on both spatial amplitude and phase. A projection of the data onto each eigenvector leads to the evaluation of the corresponding Principal Component (P.C.) which contains information on the temporal amplitude and phase of the spatial mode described by that eigenvector. The purpose of the analysis is to identify a limited number of spatial modes and their corresponding P.C.s which will economically (in terms of the percentage of total variance) describe the dominant modes of variability in the data set. It is further hoped that the statistically dominant modes will correspond to physically realistic modes of variability in the data field.

To implement Barnett's method we have used the Herrmann (1969) quadrature filter to obtain the Hilbert transform, and subroutine "CH" from the EISPACK collection of the National Energy Software Center at Argon for solving the eigenvectors. For the purpose of interpreting the results we repeat some of Barnett's remarks here. We begin by assuming that a given variable field is described by a function of space and time

$$z(\underline{x},t) = \mathrm{Re}\{Z(\underline{x},t)\} \tag{7.1}$$

where $\underline{x}$ denotes a location in space. Z here is a complex time series which for the purpose of the analysis is constructed from the original series and its Hilbert transform. As a result of the EOF analysis the time series $z(\underline{x},t)$ can be presented as a linear combination of the spatial eigenvectors $E_m(\underline{x})$, where the coefficients of expansion are the principal components $P_m(t)$. In other words

$$z(\underline{x},t) = \mathrm{Re}\{\Sigma_m P_m(t) E_m^*(\underline{x})\} \tag{7.2b}$$

(where * denotes complex conjugate) or if P_m and E_m are expressed in terms of their amplitude and phase:

$$z(\underline{x},t) = p_m(t) e_m(\underline{x}) \cos[\phi_m(t) - \varepsilon_m(\underline{x})] \tag{7.3}$$

where p_m and e_m are the amplitudes and ϕ_m and ε_m are the phases of the P.C. and the eigenvector, respectively. Thus in the case of a simple eastward propagating wave with an amplitude A constant in time and space, a frequency ω and a wavenumber k Eq. (7.3) will simply become the traditional mathematical description of a simple plane wave:

$$z(x,t) = A\cos(\omega t - kx) \tag{7.4}$$

i.e., the single P.C. and eigenvector will have a constant amplitude and phase, in time and space respectively.

Figure 7.1 shows the result of applying CEOF analysis to a cosine wave with a nondimensional wavelength of 10 and frequency of 1/20 propagating in the positive x direction. The square of the amplitude

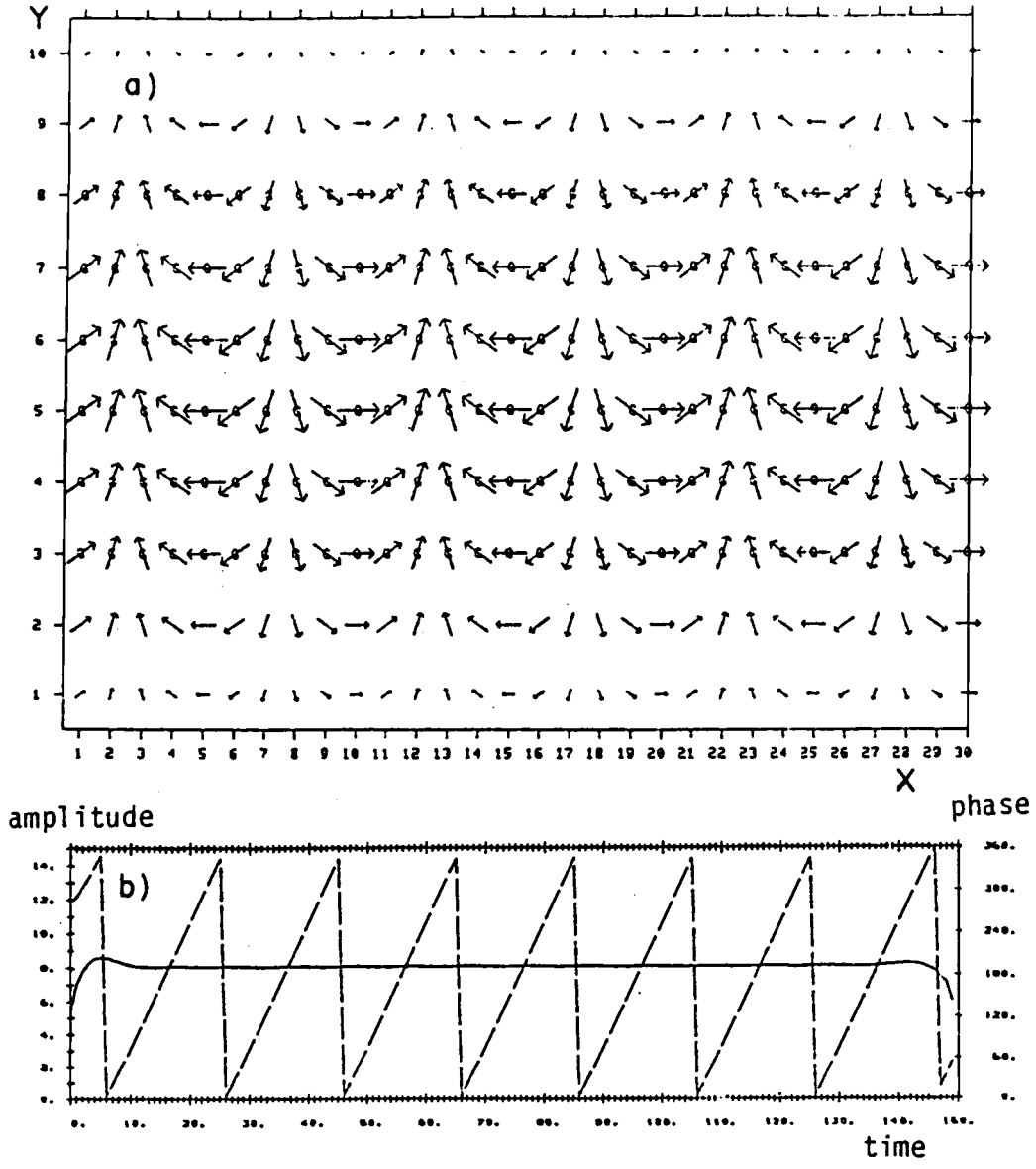

Fig. 7.1. The first and only mode of CEOF analysis applied to a simple eastward propagating wave with a non-dimensional length of 10 in the x-direction and 21 in the y-direction and a period of 20. (a) Amplitude and phase of spatial eigenvector, denoted by the length and direction of the arrows with reference to the x-axis. (b) amplitude and phase of temporal expansion coefficient (principal component), denoted by full and broken lines respectively.

of the P.C. is equal to the amount of total variance explained by the mode. Both spatial and temporal phases are relative (that is they are ambiguous to an additive constant). The upper part of the diagram (Fig. 7.1a) presents the single eigenvector of the field. Here the length of the arrow is proportional to the local spatial amplitude and its direction with respect to the x-axis is its spatial phase (a cosine variation of the amplitude in the y direction was included in the original time series and is depicted in the eigenvector's amplitude). Note that as we move in the positive "x" direction the arrows rotate counterclockwise indicating that the phase of the eigenvector increases eastward. In the lower part of the diagram (Fig. 7.1b) the time amplitude and phase are presented. As expected the amplitude is constant in time and the phase lines have a constant slope (equal to the frequency used, 1/20 days).

If the same analysis is applied to a retrograding wave with the same period, we find that the only difference between this case and the previous one is that the phase of the eigenvector now grows westward. A standing wave will also be described by a single eigenvector as shown in Fig. 7.2. The P.C. corresponding to this eigenvector is exactly similar to that we obtained for the moving wave (we have used the same amplitude and period of oscillation). If we apply a time dependent amplitude to the wave and expose it to CEOF analysis the P.C. phase will remain unchanged, but its amplitude will depict the time changes of the wave's amplitude. A standing wave packet, dispersing energy in the positive-x direction may be described as

$$z(x,t) = A \cos kx \cos(\omega t - \frac{\omega}{C_g} x) \qquad (7.5)$$

where C_g is the group velocity. If we apply CEOF analysis to this time series we again obtain only one eigenvector which is shown in Fig. 7.3 where we have used $C_g = 5$ with the same k and ω as before. What we find is that the resulting mode is a product of a long travelling wave of wavelength 100 and a short standing wave of wavelength 10, exactly as implied by Eq. (7.5). The P.C. of this eigenvector

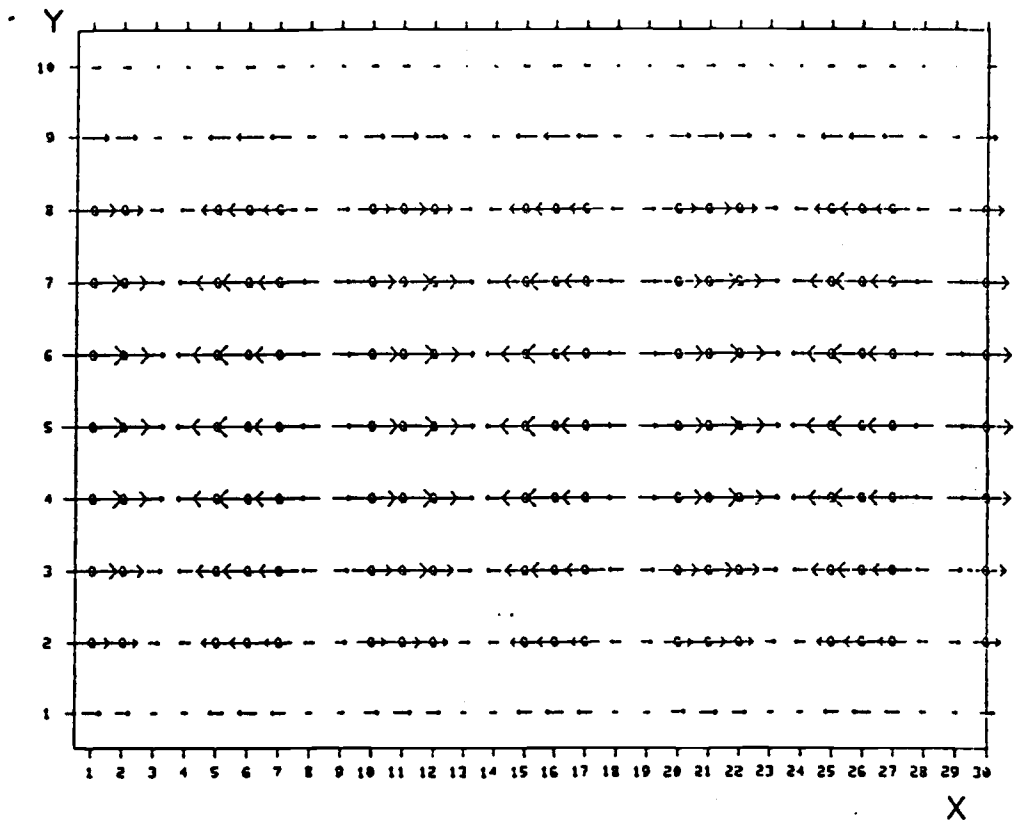

Fig. 7.2. The spatial eigenvector of CEOF analysis applied to a standing wave of length 10 in the x-direction and 21 in the y-direction.

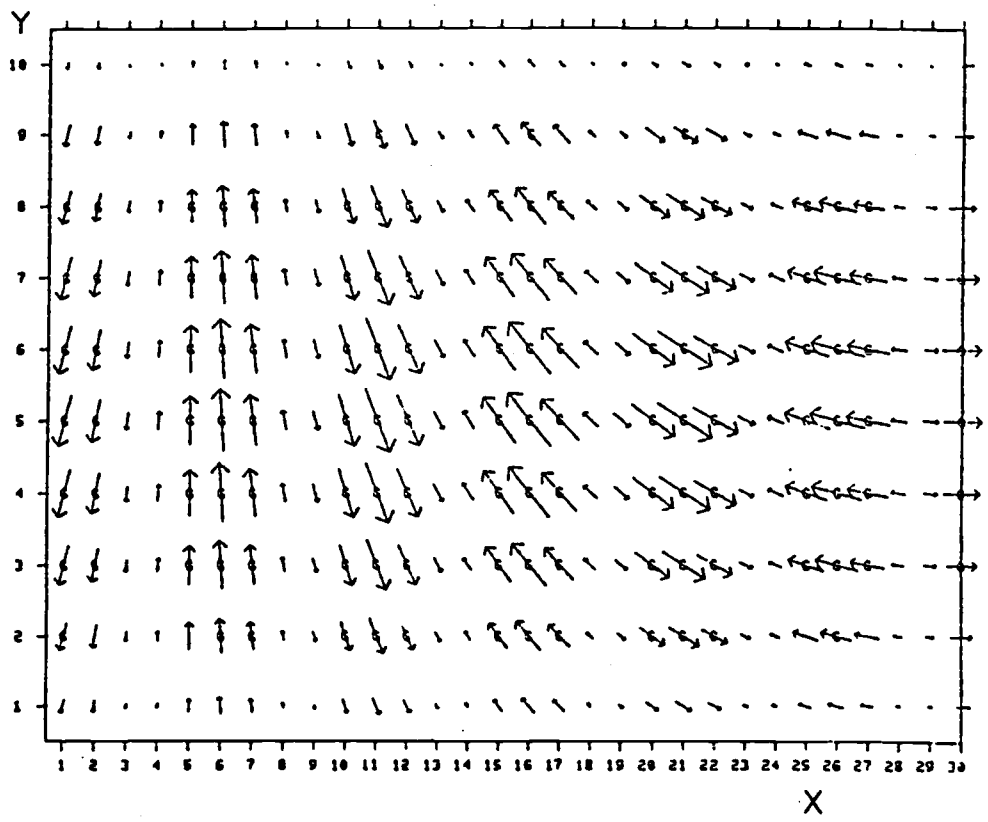

Fig. 7.3. The spatial eigenvector of CEOF analysis applied to a standing wave packet propagating energy in the x-direction with a group velocity of 5.

will again be of constant amplitude and a phase which increases linearly with time.

When we apply CEOF analysis to the model's low-frequency 400 mb geopotential height anomaly over the Northern Hemisphere between 10 and 58°N, we find that the first eigenvector explains only 14% of the total normalized variance. (The second mode explains about 11% of the variance.) This low percentage is the result of the regional character of the variability. The regionality of the first eigenvector is clearly shown in Fig. 7.4. The amplitude is large over the greater part of the North Pacific basin, except for a narrow region over the central western Pacific. Over the region between about 110°W and the date line the amplitude is almost constant (varying between 0.07 and 0.1). The region of minimum amplitudes in the western Pacific seems to have the shape of the jet stream there. It is surrounded by sharp gradients in the EOF amplitude. Over the other parts of the hemisphere the amplitude is quite small except for several circular features isolated from each other extending eastward over the Atlantic from the Gulf of Mexico. Between these circular features there are regions of amplitude minima. The phase of the eigenvector is depicted by the direction of the arrow which should be measured with respect to the side of the page. We note that over the North Pacific the arrows rotate in a clockwise direction when we move along any latitude circle from the date line eastward. Remembering the simple examples presented earlier we can conclude that the first eigenvector represents a planetary-scale wave retrograding over the eastern North Pacific more or less from the coasts of California and Mexico towards northwestern Siberia. Another part of the wave seems to be retrograding more slowly over the subtropics. The wave has a zonal wavelength of about 120° longitude and a meridional wave length of about 80° latitude. Over the Atlantic the phase shifts by about 180° between each of the previously mentioned circular features. In fact, the structure here is similar to the pattern of the simple energy-propagating standing wave we have examined in Fig. 7.3.

The time series of the P.C. corresponding to the first eigenvector is shown in Fig. 7.5, where the solid line represents the

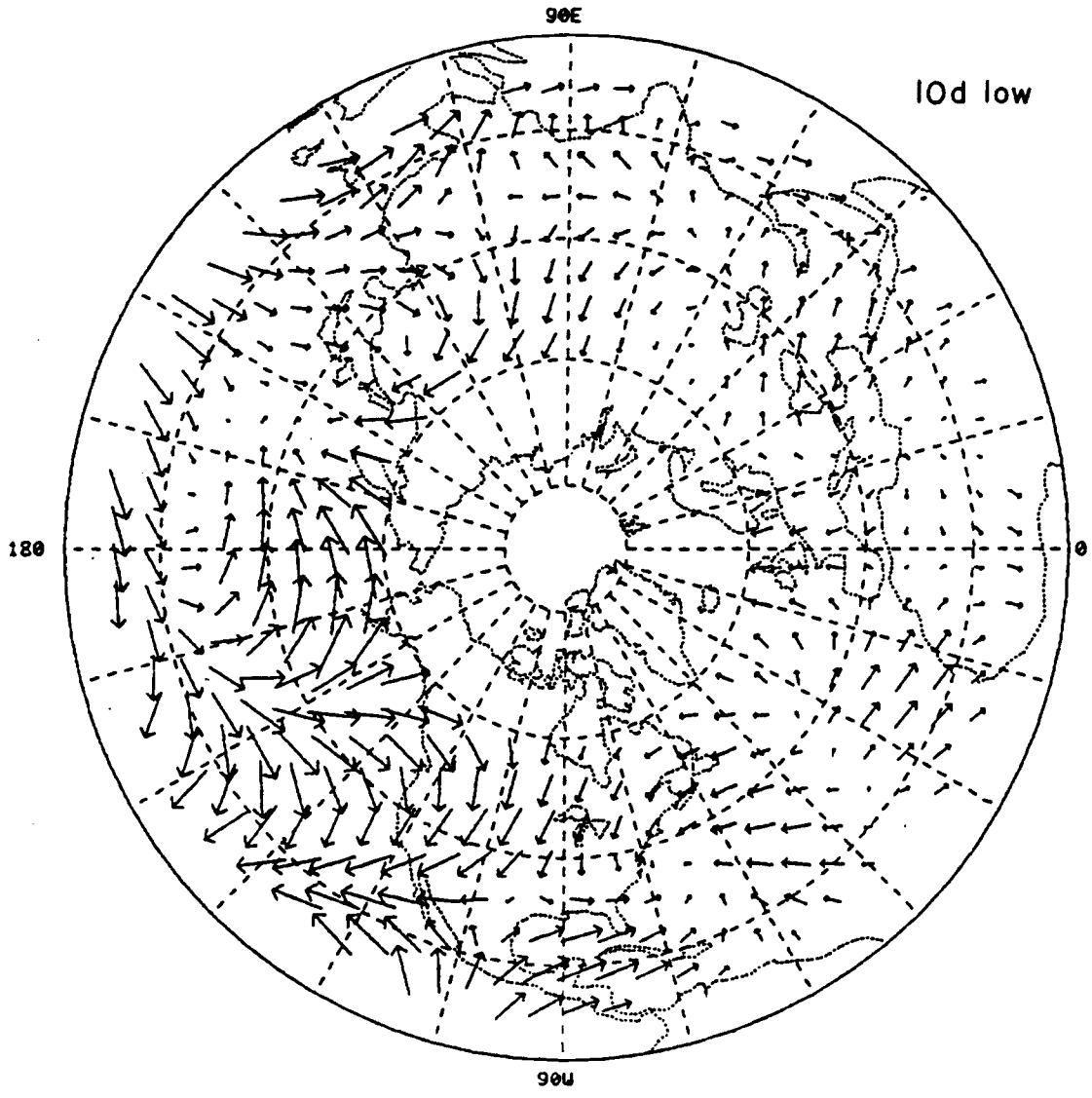

Fig. 7.4. The first eigenvector of a CEOF expansion of the normalized 10 day low-pass simulated geopotential height anomaly over the Northern Hemisphere between 10 and 58°N. The length of the arrow is proportional to the local amplitude and the direction with respect to the side of the page is the relative phase. This mode explains 14.05% of the total normalized variance.

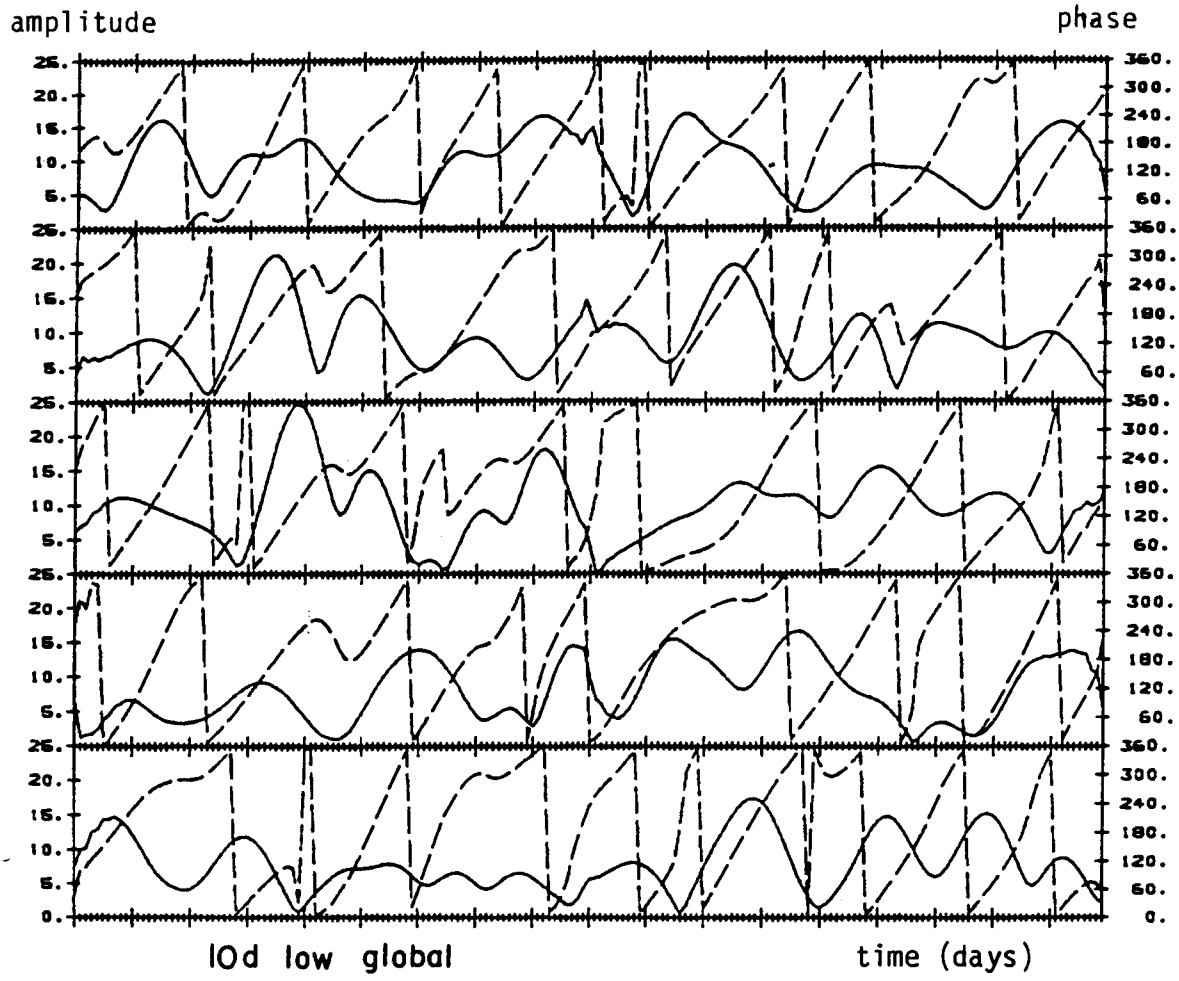

Fig. 7.5. The amplitude and phase of the principal component corresponding to the first hemispheric eigenmode of 10 day low-pass geopotential height anomaly of Fig. 7.4. Amplitude is read on the left ordinate and phase (in degrees) on the right. The time interval between two consecutive tic-marks on the abscissa is one day.

P.C. amplitude and the broken line its phase. We notice that the mode goes through a series of intensification and decay periods. During each of these periods the phase seems to vary quite linearly in time indicating a constant frequency. The typical duration of what we might call an "outbreak" of the mode is about 20 days, during which the implied period (the slant of the phase lines) is also about 20 days.

Following Wallace and Dickinson's (1977) and Barnett's (1983) advice to use relatively narrow frequency bands, we have applied the analysis to a part of the low-frequency signal, removing all fluctuations with periods longer than 40 days. (This was accomplished using the filtering method discussed in Chapter 3.) The results of applying the CEOF analysis to the 10 to 40 day series are remarkably similar to those we have just discussed. The amount of variance explained by the first mode has increased slightly to 16% and the P.C. time series was less "noisy." Very similar results were also obtained when the unnormalized geopotential heights were used.

Since the first eigenvector of the low-frequency and the 10 to 40 day band (intermediate frequency) geopotential height is dominated by the Pacific pattern, we decided to concentrate on the Pacific sector of the Northern Hemisphere. We also decided for reasons that will become clearer later, to use the 10 to 40 day part of the signal only. Not surprisingly, the first eigenvector of this part of the data now explains 27.3% of the total variance ("total" now referring to the Pacific sector of the Northern Hemisphere). The second eigenvector explains now only 13% of the variance. The first eigenvector and its P.C. are shown in Fig. 7.6 and 7.7 respectively. The time series of the P.C. now shows even more clearly that the cycles of the mode are accompanied by a regular linear increase of the phase with time. There is a very close agreement between the life-time of the mode and its period, both averaging about 20 days. Our strategy is to use this information to look at other variables and to determine their behavior during the life-cycle of the mode.

Returning to the theory behind this type of analysis (see Barnett, 1983) we recall that the time series of the P.C.s have the following property

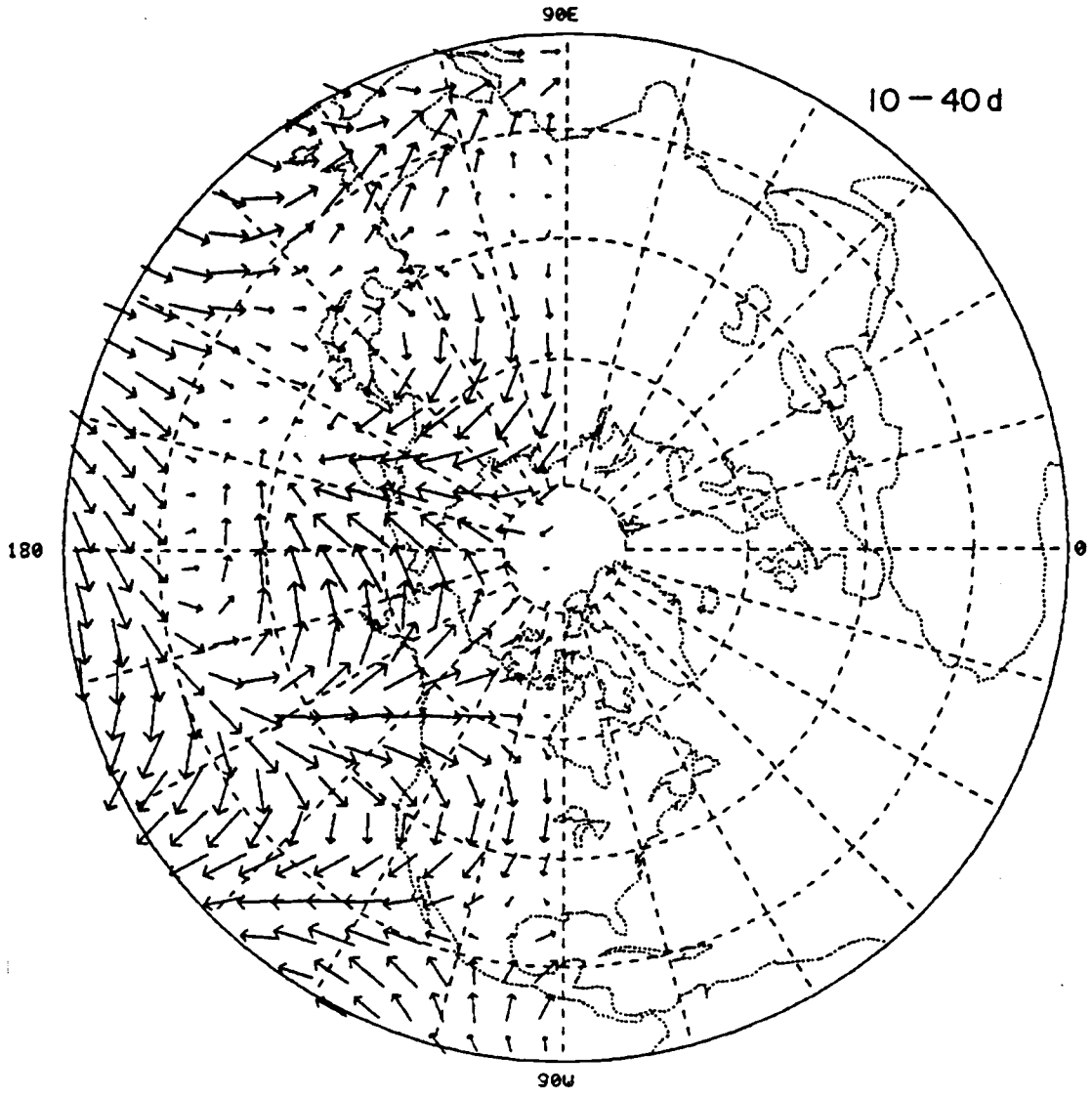

Fig. 7.6. The first eigenvector of a CEOF expansion of the normalized 10 to 40 day band-pass simulated geopotential height anomaly over the Pacific quadrant of the Northern Hemisphere. The length of the arrow is proportional to the local amplitude and the direction with respect to the side of the page is the relative phase. This mode explains 27.31% of the total normalized variance.

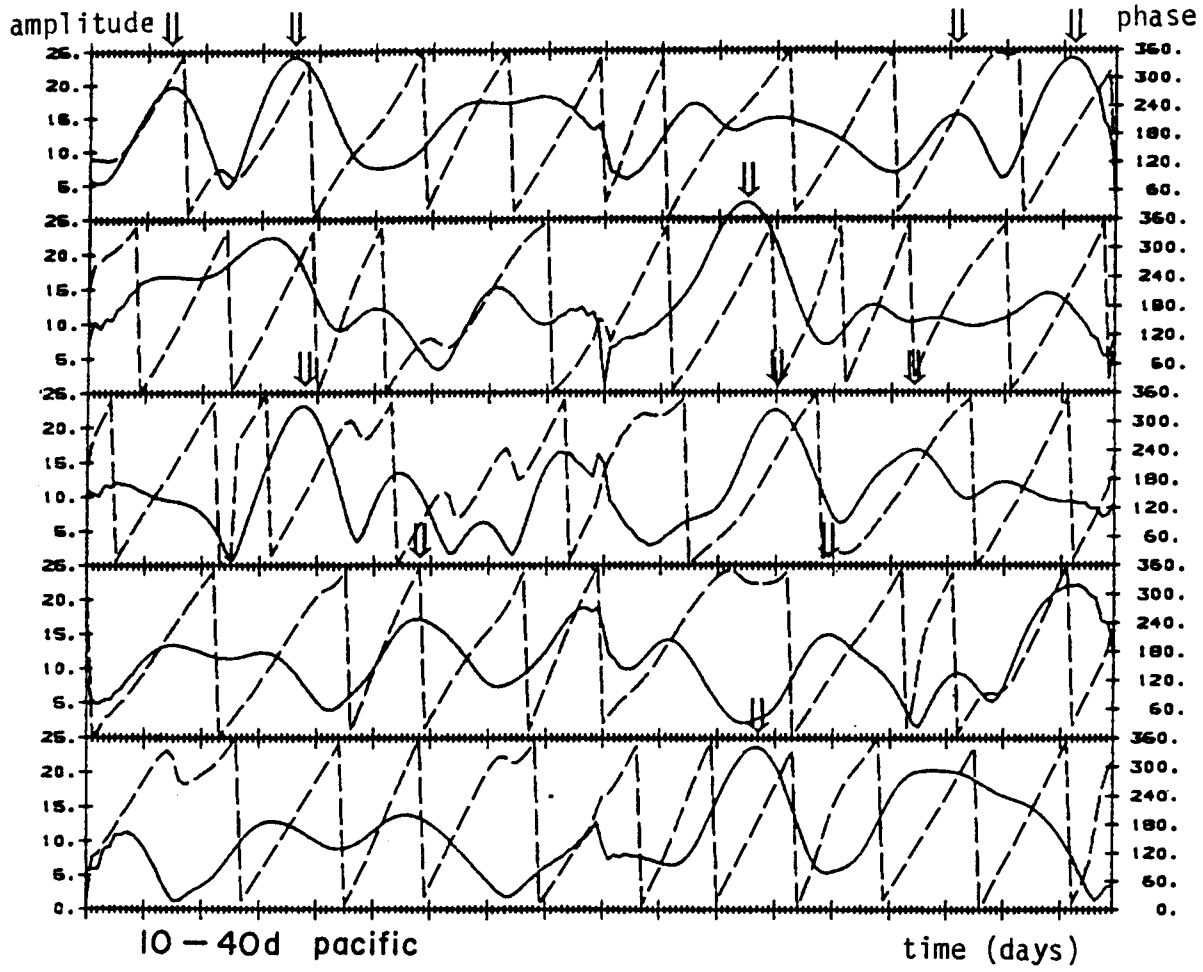

Fig. 7.7. The amplitude and phase of the principal component corresponding to the first Pacific eigenmode of 10 to 40 day band-pass geopotential height anomaly of Fig. 7.6. Amplitude is read on the left ordinate and phase (in degrees) on the right. The time interval between two consecutive tic-marks on the abscissa is one day. The small arrows indicate the peaks of the cycles chosen for later composites.

$$\left\langle P_m(t)P_n^*(t)\right\rangle_t = \lambda_m^2\delta_{mn} \tag{7.6}$$

where $\langle\ \rangle_t$ represents time averaging and λ_m^2 is the eigenvalue corresponding the the m-th mode (the part of the total variance explained by this mode) and is the "Kronecker" delta function. Thus if we multiply both sides of Eq. (7.2) in its complex form by P_n^* and average over time, we obtain:

$$\left\langle P_n^*(t)Z(\underline{x},t)\right\rangle_t = \lambda_n^2 E_n^*(\underline{x}) \tag{7.7}$$

Based on this equation we may define the unnormalized eigenvector $\hat{E}_n^Z(\underline{x})$ as

$$\hat{E}_n^Z(\underline{x}) = \frac{1}{\lambda_n}\left\langle P_n^*(t)Z(\underline{x},t)\right\rangle_t^* \tag{7.8}$$

$\hat{E}_n^Z(\underline{x})$ will have the units of Z which is now allowed to be any field variable, and not necessarily that used to solve for the eigenvalues.

Equation (7.8) is the basis for the compositing method we have used here. For all dependent variable fields, namely the geopotential height, horizontal wind velocity components, temperature and vertical pressure velocity, all at 800 and 400 mb and on the full-resolution model grid (4 x 5 degrees), we have calculated the complex correlation with the P.C. of the first eigenvector of the Pacific sector variability (this was done after first augmenting each time series by its Hilbert transform). The resulting set of "spatial vectors," $E_1(\underline{x})$, contain all the information on the three-dimensional structure of the first Pacific mode and its "dynamical" properties. The temporal information is contained in the P.C. series and is one and the same for all the variables. The amplitude and phase of all the dynamical variables at a particular moment in time can be reconstructed by applying the equation

$$z_1(\underline{x},t) = \frac{1}{\lambda_1}p_1(t)\hat{e}_1^Z(\underline{x})\cos\left[\phi_1(t) - \varepsilon_1^Z(\underline{x})\right] \tag{7.9}$$

where the subscript "1" now refers to the first Pacific mode, z is any dynamical variable, p_1 and ϕ_1 are the amplitude and phase of the first Pacific principal component and $\hat{e}_1^z$ and ϵ_1^z the amplitude and phase of the unnormalized spatial vector constructed using Eq. (7.8)

In the following section we will present the results of applying this method of compositing, examine the structure and properties of the different spatial vectors and try to determine whether they describe a realistic mode of low-frequency variability.

7.2 The structure of the North Pacific low-frequency disturbances

As explained in section 7.1, all the information on the mutual phase relationships of all dynamic variables corresponding to the first Pacific eigenvector are described by their spatial "vector," $\hat{E}^z(\underline{x})$. These relationships are thus constrained to remain fixed throughout the life cycle of the mode; all that changes are the phases of each variable field with respect to the underlying geography and more importantly, the underlying circulation. Examining the first P.C. time series in Fig. 7.7 we note that there is no particular phase at which the mode "prefers" to start or to peak. Thus there seems to be no preferable cycle of phases that the disturbance depicted by this mode tends to take with respect to the underlying geography. This fact is illustrated by Fig. 7.8 which shows the location of several peak values of the P.C. on the complex plane. From these we have picked 11 cases which are marked by small arrows on Fig. 7.7 and on Fig. 7.8. We have averaged the full 10 to 40 day signal of geopotential height anomaly on these 11 days. The results shown in Fig. 7.9a show a planetary-scale system similar to that depicted by the first Pacific eigenvector (see description in section 7.1). We have then averaged the values of the P.C. on the same 11 days in the following way

$$\overline{P(t_0)} = \frac{1}{11} \sum_{j=1}^{11} p_j(t_0)\{\cos\phi_j(t_0) + i\sin\phi_j(t_0)\} \qquad (7.10)$$

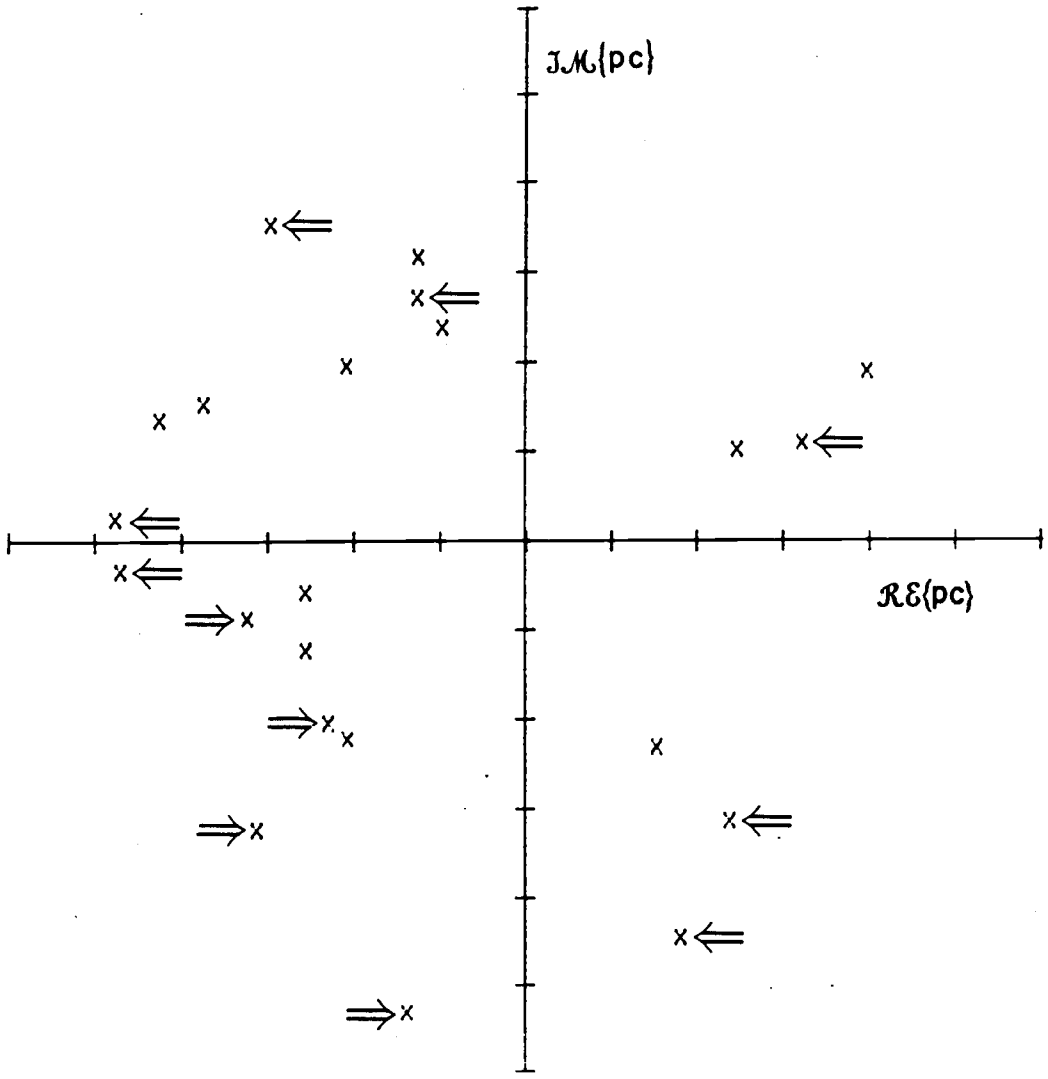

Fig. 7.8. The phase and amplitude of the principal component of the Pacific eigenmode at the peak of its 'outbreak', projected on the complex plain. The arrows point at the days used for later composites.

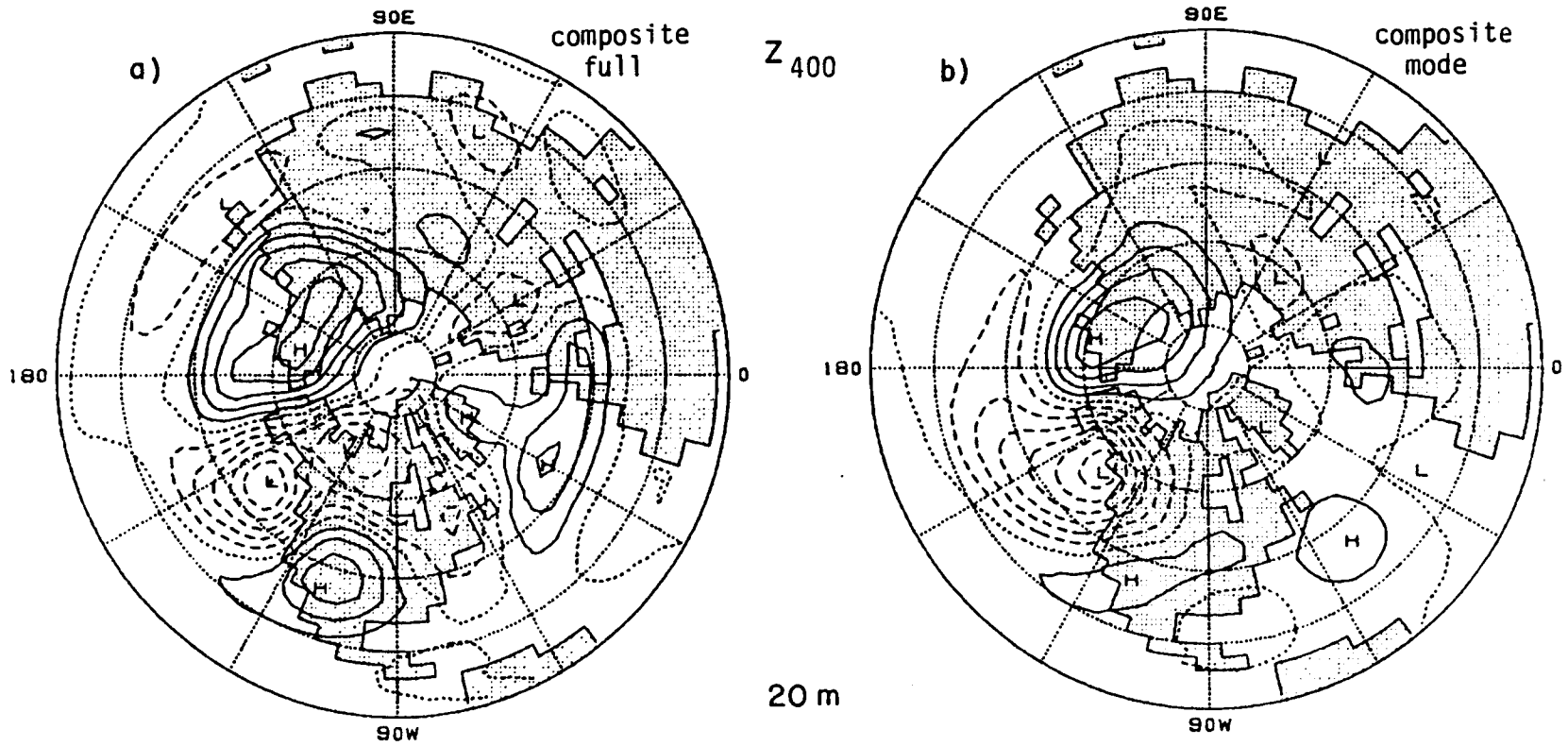

Fig. 7.9. (a) The average geopotential height anomaly in the 11 days of peak Pacific mode amplitudes chōsen for compositing (see Fig. 7.7). (b) The reconstructed average pacific mode for the same 11 days (see text for further details). Contour interval 20 m; negative contours are dashed and the zero line is dotted.

where $i = \sqrt{-1}$, j is the case index and t_0 indicates the time (day) of the peak. We have then reconstructed the height field corresponding to this average P.C. value. The result, presented in Fig. 7.9b corresponds to an average of the part of the 10 to 40 day signal described by the first eigenmode only. We find that over the Pacific quadrant the field based upon the value of the average P.C. of all peak P.C. values is remarkably similar to the average height anomaly for these 11 days. The resulting mode has a smaller amplitude but this could be explained by the fact that the first eigenvector explains only 27% of the total variance (which is only 50% of the amplitude). The agreement in phase between the two patterns is very good in the Pacific sector (note the positions of the extrema). The amplitude of the mode over the other sector is rather small except for a "wave-train" like feature over the central Atlantic (remember that this feature was a part of the first hemispheric eigenvector).

We now examine the phase relationships between the various variable fields as described by the different $\hat{E}_1{}^z$'s, by reconstructing their fields at day zero, defined as the day of peak amplitude. The large variability in the phase of the P.C. at the time of its peak leads to a cancelling effect between individual cases during the averaging. To sharpen the composites we have averaged over the amplitudes only, assigning an average phase of 200° to the results (about equal to the phase of $\overline{P}$ calculated using Eq. (7.10)). This is equivalent to rotating all the phases of the P.C. so that their amplitudes peak at the phase of 200° degrees before averaging.

The 400 mb geopotential height field reconstructed this way is shown in Fig. 7.10. This field differs from that of Fig. 7.9b mainly in its amplitude (the same $E_1{}^z$ and $\phi(t_0)$ were used here and there). Because of the larger amplitude the features of the mode are clearer. We note that the mode's structure agrees with what we have previously learned about the low-frequency modes, namely, that it is zonally elongated at low latitudes and circular or meridionally elongated over high latitudes (see Fig. 5.6b). The wave pattern trailing into the Atlantic is more symmetric in shape. An examination of the time behavior of the mode (not shown), reveals that over western North

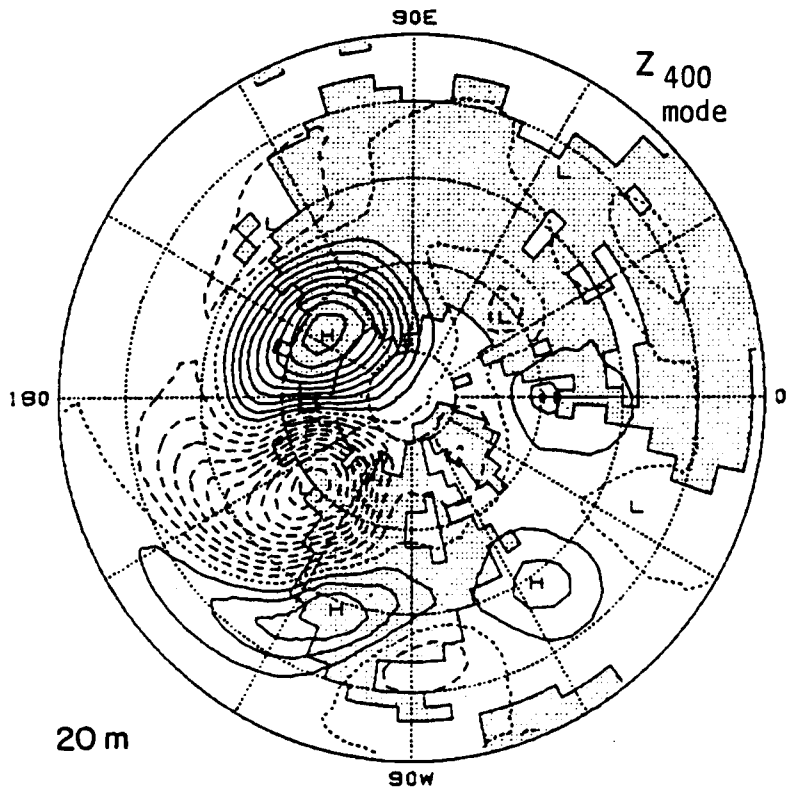

Fig. 7.10. The reconstructed 400 mb 10 to 40 day geopotential height anomaly of a typical, fully developed Pacific mode. Contour interval 20 m; negative contours are dashed and the zero contour is dotted.

America and the Pacific the mode retrogrades (with a period of about 20 days), but over the Atlantic it is stationary. This behavior is clearly depicted by the first hemispheric eigenvector in Fig. 7.5a and can also be seen in one-point-correlation fields with base points over the northeastern Pacific. This behavior suggests that the Atlantic pattern is caused by a packet of Rossby waves dispersing energy from the northeastern Pacific.

The reconstructed 800 mb geopotential height field is shown in Fig. 7.11. Over the northeastern tip of Asia the wave is baroclinic with the 800 mb height leading the 400 mb height by 15 to 20° longitude. The baroclinicity is smaller over the other parts of the wave.

The velocity field at 400 mb is shown in Fig. 7.12a (the u field) and b (the v field). The wind components are clearly consistent with the height field. Note that over the lower middle latitudes the amplitude of the zonal component is largest but over the higher latitudes the meridional wind dominates. This is in good agreement with the low-frequency velocity components' variance fields shown in Chapter 5 (Fig. 5.2c and d). As we remember, the first Pacific eigenvector has very small amplitudes over the jet stream thus its related u field does not include the jet stream features shown by the $\overline{u'^2}$ field. The Atlantic wave train is seen clearly in the v field.

The reconstructed 800 mb temperature field shown in Fig. 7.13. We note that the 800 mb height field leads the Asian part of the temperature field by about 30° latitude which is equivalent to about 1/4 of the wavelength of the disturbance. This implies a positive correlation between the meridional wind and the temperature field. The phase lag decreases southeastward.

The vertical pressure-velocity field presented in Fig. 7.14 contains a region of strong orographically induced upward motion just west of the Rockies. This rising motion is induced by the eastward anomaly in the zonal-wind field there. Other features are of a dynamical origin like the strong sinking motion over Alaska and the Bering Sea which is associated with the convergence of the meridional wind component there.

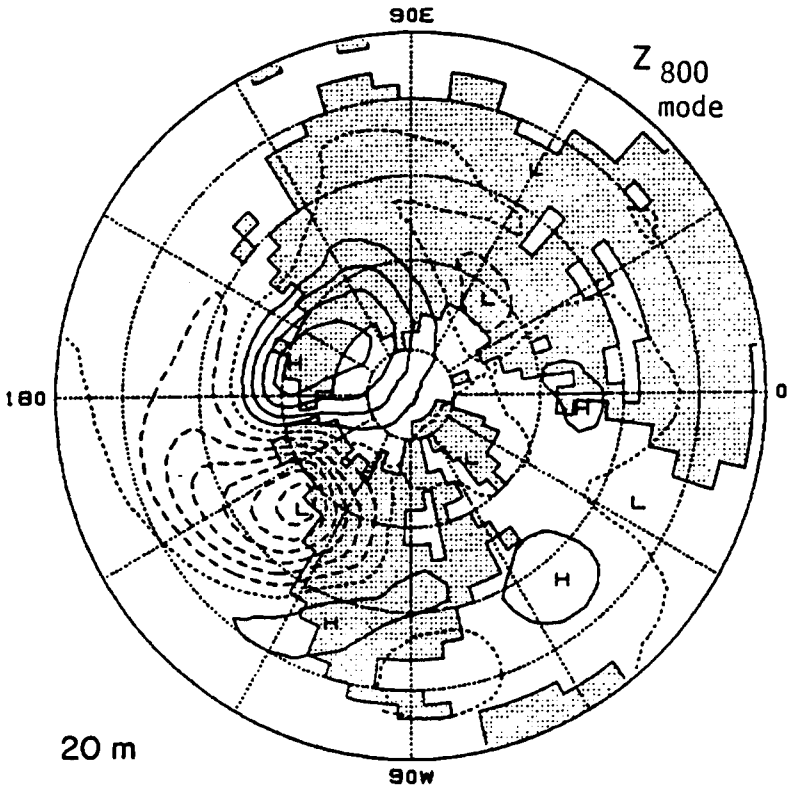

Fig. 7.11. The reconstructed 800 mb 10 to 40 day geopotential height anomaly of a typical, fully developed Pacific mode. Contour interval 20 m; negative contours are dashed and the zero contour is dotted.

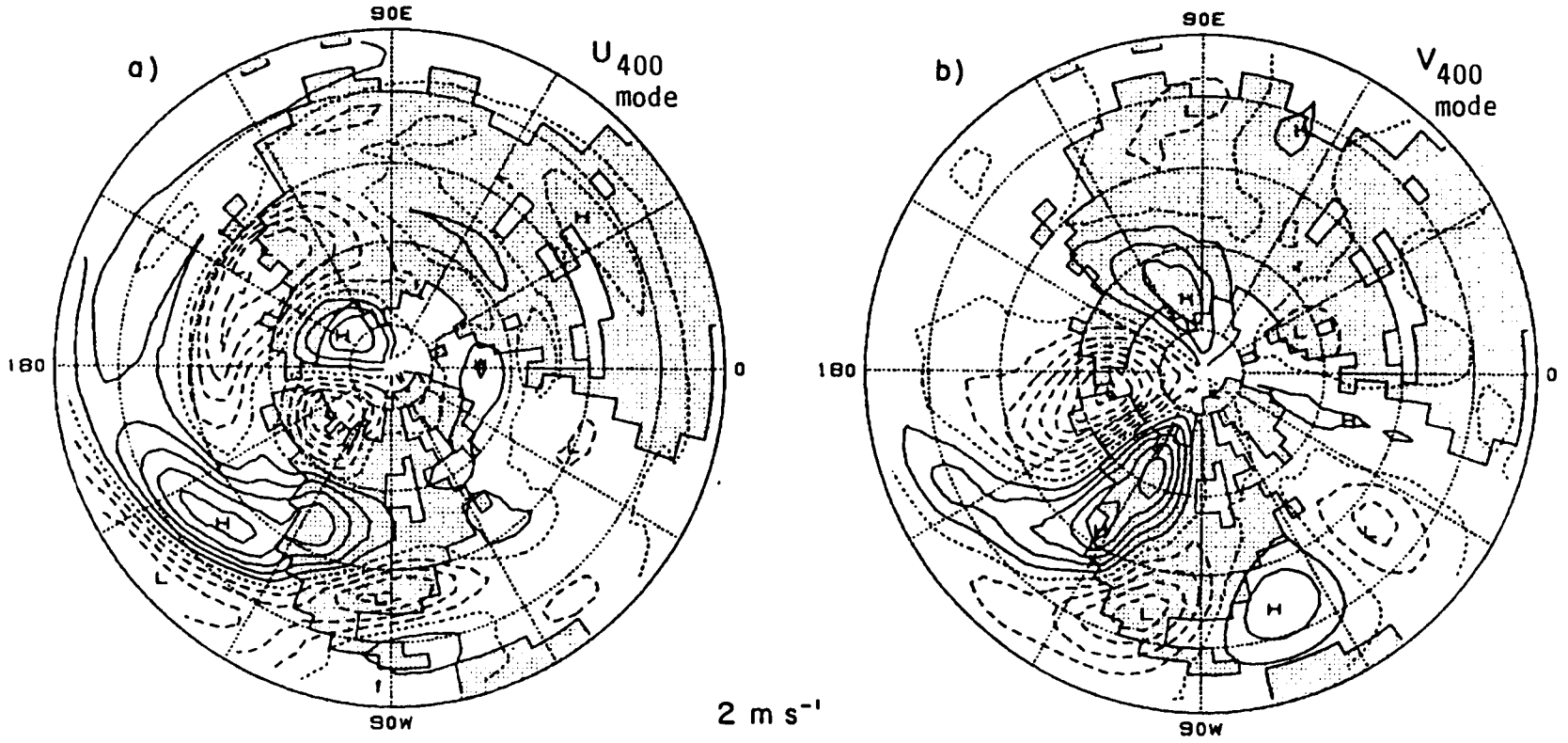

Fig. 7.12. The reconstructed 400 mb 10 to 40 day velocity field of a typical, fully developed Pacific mode. (a) zonal component. (b) meridional component. Contour interval 2 m s^{-1}; negative contours are dashed and the zero contour is dotted.

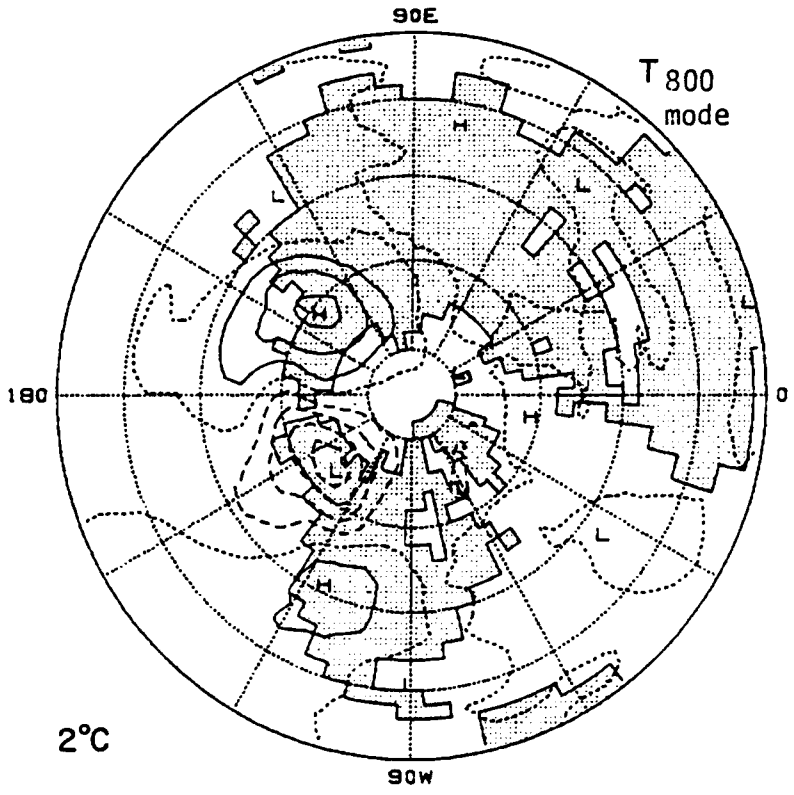

Fig. 7.13. The reconstructed 800 mb 10 to 40 day temperature anomaly of a typical, fully developed Pacific mode. Contour interval 2 °C; negative contours are dashed and the zero contour is dotted.

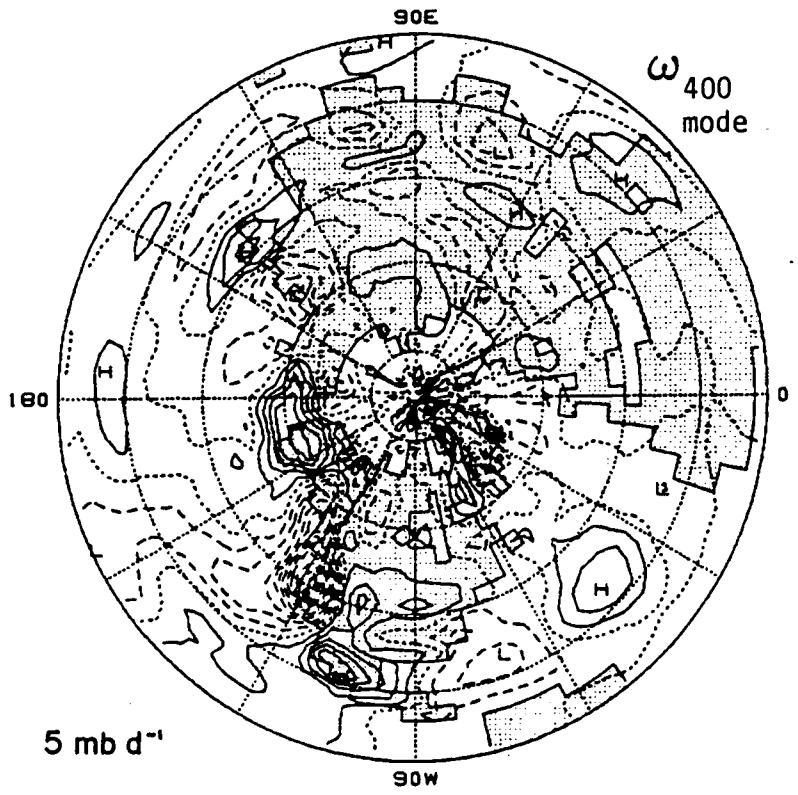

Fig. 7.14. The reconstructed 400 mb 10 to 40 day vertical pressure velocity anomaly of a typical, fully developed Pacific mode. Contour interval 5 mb day^{-1}; negative contours (rising motion) are dashed and the zero contour is dotted.

Finally the diabatic heating field at 800 mb is shown in Fig. 7.15. There is a relatively good correspondence between the regions of heating in this field and those of upward motion in the ω field, and between regions of cooling and those of sinking motion. This means that adiabatic cooling tends to play an important role in balancing diabatic heating.

From all the above results it appears that the method chosen here to isolate and composite the three dimensional structure and dynamical character of the first Pacific eigenvector operates quite well. Thus we may now proceed and examine the energetics of this mode.

7.3 The life cycle and maintenance of North Pacific low-frequency disturbances

We now examine the life cycle and maintenance of the North Pacific mode isolated by the CEOF analysis. To achieve this goal we take the approach of Chapter 6, that is we study the energetics of the mode. This time, however, we can use the information given in the P.C. to follow the terms in the energy equations 6.1 and 6.2 through the life cycle of the mode. By averaging the daily values of these terms in space over a region including at least one wavelength we obtain a measure for the energies and their conversions and their time evolution.

Before carrying out this computational task we examine the 10 winter time series of the 10 to 40 day band kinetic energy over the Pacific sector. This time series is shown in Fig. 7.16. A comparison between this time series and the first Pacific P.C. reveals that there is a fair correspondence between the two. In the kinetic energy time series there appear relatively low-frequency undulations with a period of about 20 days which seem to peak when the P.C. amplitude series peaks. The higher frequency fluctuations in the kinetic energy time series have a period of about 10 days and are a result of kinetic energy being a quadratic quantity of fluctuating velocity field with a period of 20 days.

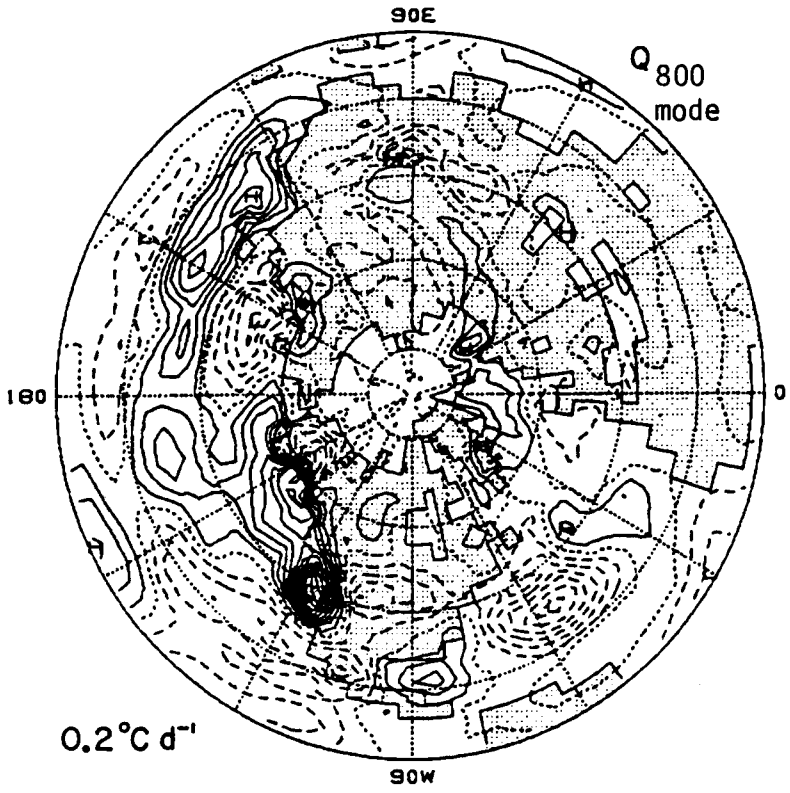

Fig. 7.15. The reconstructed 800 mb 10 to 40 day diabatic heating rate anomaly of a typical, fully developed Pacific mode. Contour interval 0.2 °C day^{-1}; negative contours are dashed and the zero contour is dotted.

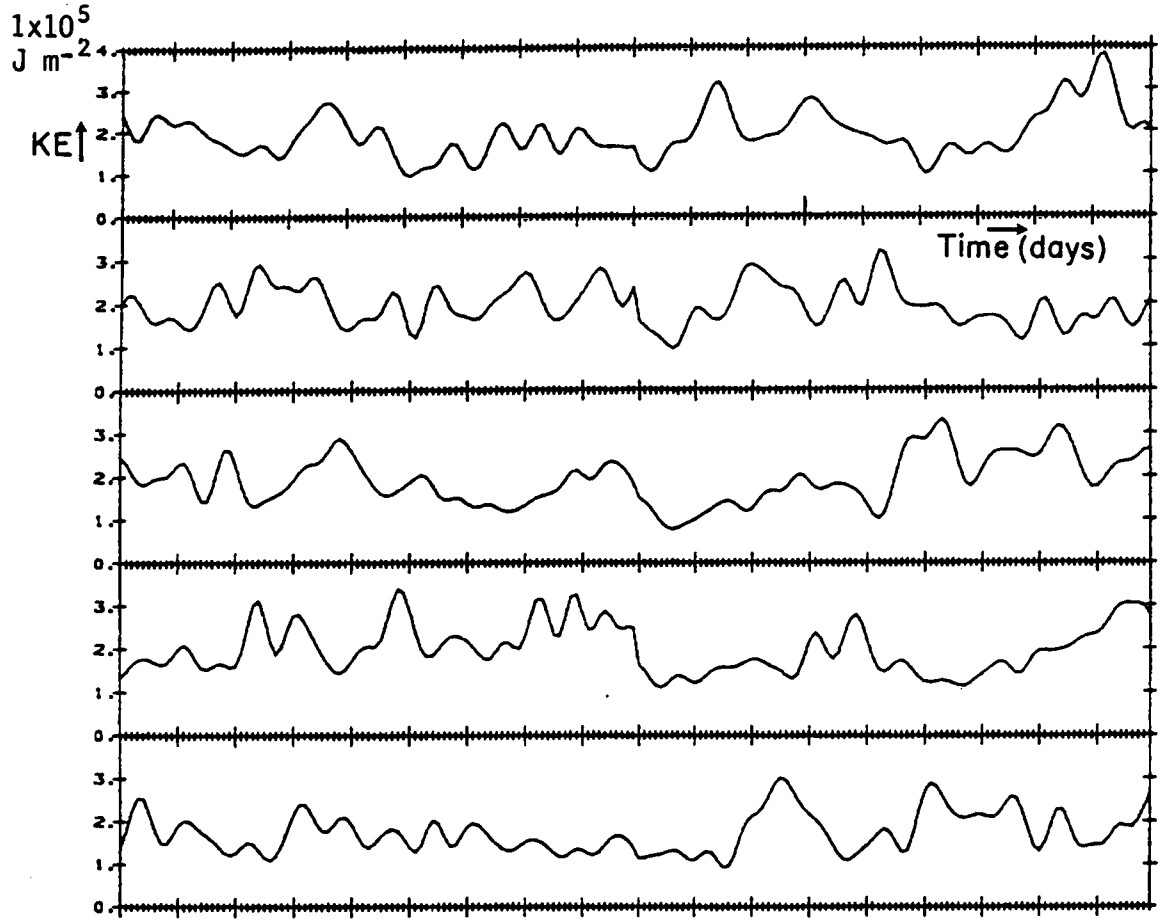

Fig. 7.16. A time series of the vertically integrated kinetic energy of simulated 10 to 40 day fluctuations averaged over the Northern Hemisphere Pacific sector. Units are in 10^5 J m^{-2}.

To calculate the energetics of the North Pacific mode we have reconstructed the full time history (for the 10 winters) of the dynamical variables from the first Pacific P.C. and its corresponding spatial patterns. The reconstructed values were then used to calculate the eddy variance and covariance fields and the daily history of the fields of KE and AE, and the energy terms GAE, HFC and AEKE (see Chapter 6, Eqs 6.1 and 6.2). The fields of the conversion terms AAEH + AAEV (hereafter referred to AAE) and KKEH + KKEV (referred to as KKE) were calculated from the daily values of the eddy covariances and the gradient of the daily total 40 day lowpass fields (daily normals + 40 day low-pass anomaly). In doing this we have considered these fields slowly changing as the basic state during the life cycle of the mode. Using the time series of the major terms in the eddy energetics of the mode we have calculated their seasonal mean and compared them with similar fields based on the total 10 to 40 day signal. This corresponds to a comparison between the average energetics of the "mode only" 10 to 40 day signal to the total signal. The results are shown in Figs. 7.17 and 7.18 for the full signal and the first eigenmode only, respectively. Note that the energetics of the 10 to 40 day band eddies in Fig. 7.17 are quite similar to those of the total 10 day lowpass eddies (see Fig. 6.4) in spatial distribution and relative magnitude of the process described. The comparison between 7.17 and 7.18 reveals that the first Pacific mode energetics resemble that of the total band over the Pacific sector. The magnitude of various features in the different fields of the mode energetics is between 30 and 50% of their full-band counterparts.

Finally we have composited the time development of the energy terms over the 11 chosen cycles of the North Pacific mode. The compositing was done so that all the fields on the days of the peak amplitudes (D_0) were averaged together, and similarly for each of the +n and -n days from D_0 (n = 1, 10). We have then area averaged the resulting fields in space over the Pacific sector from longitude 90°E eastward to longitude 60°W. The resulting 21-day time series of area averaged energy terms is shown in Fig. 7.19. The figure represents the composite life-cycle of a prevailing form of low-frequency

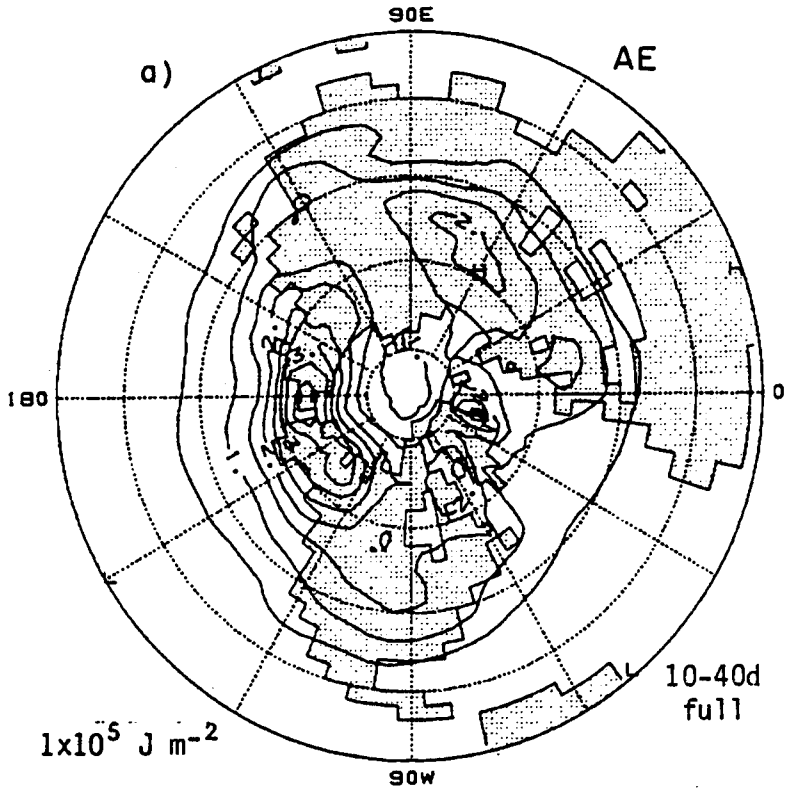

Fig. 7.17. The horizontal distribution of leading terms in the energy budget of the total simulated 10 to 40 day disturbances. (a) APE. (b) Kinetic energy. (c) Time-mean to eddy APE conversion. (d) APE to kinetic energy conversion. (e) Time-mean to eddy kinetic energy conversion. (f) Geopotential flux convergence. (g) Eddy APE generation through diabatic processes. Contour interval in (a) and (b) is 1×10^5 J m^{-2}, in (c), (d) and (f) 1 W m^{-2}, in (e) 0.5 W m^{-2} and in (g) 0.25 W m^{-2}.

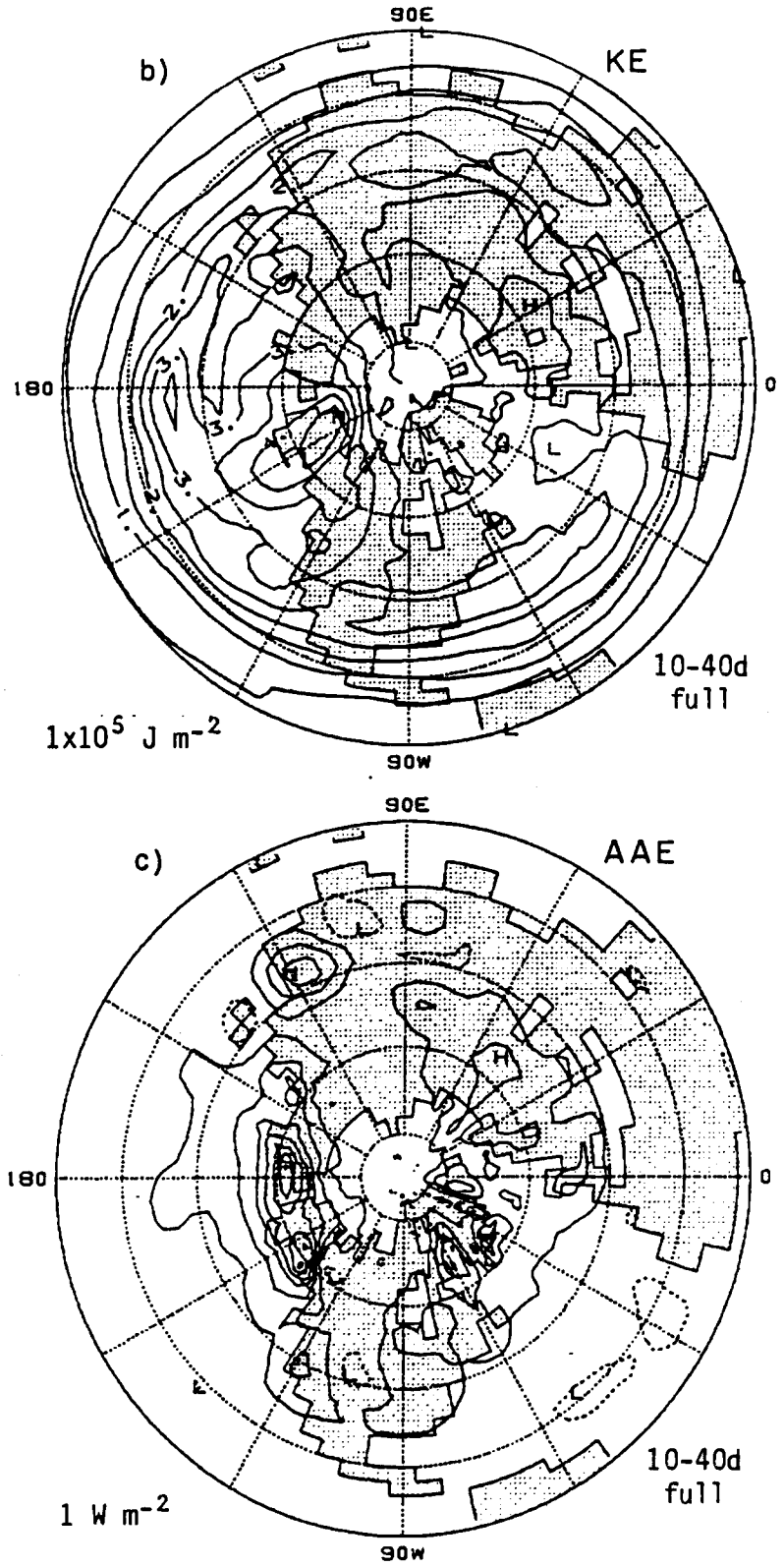

Fig. 7.17 (continued)

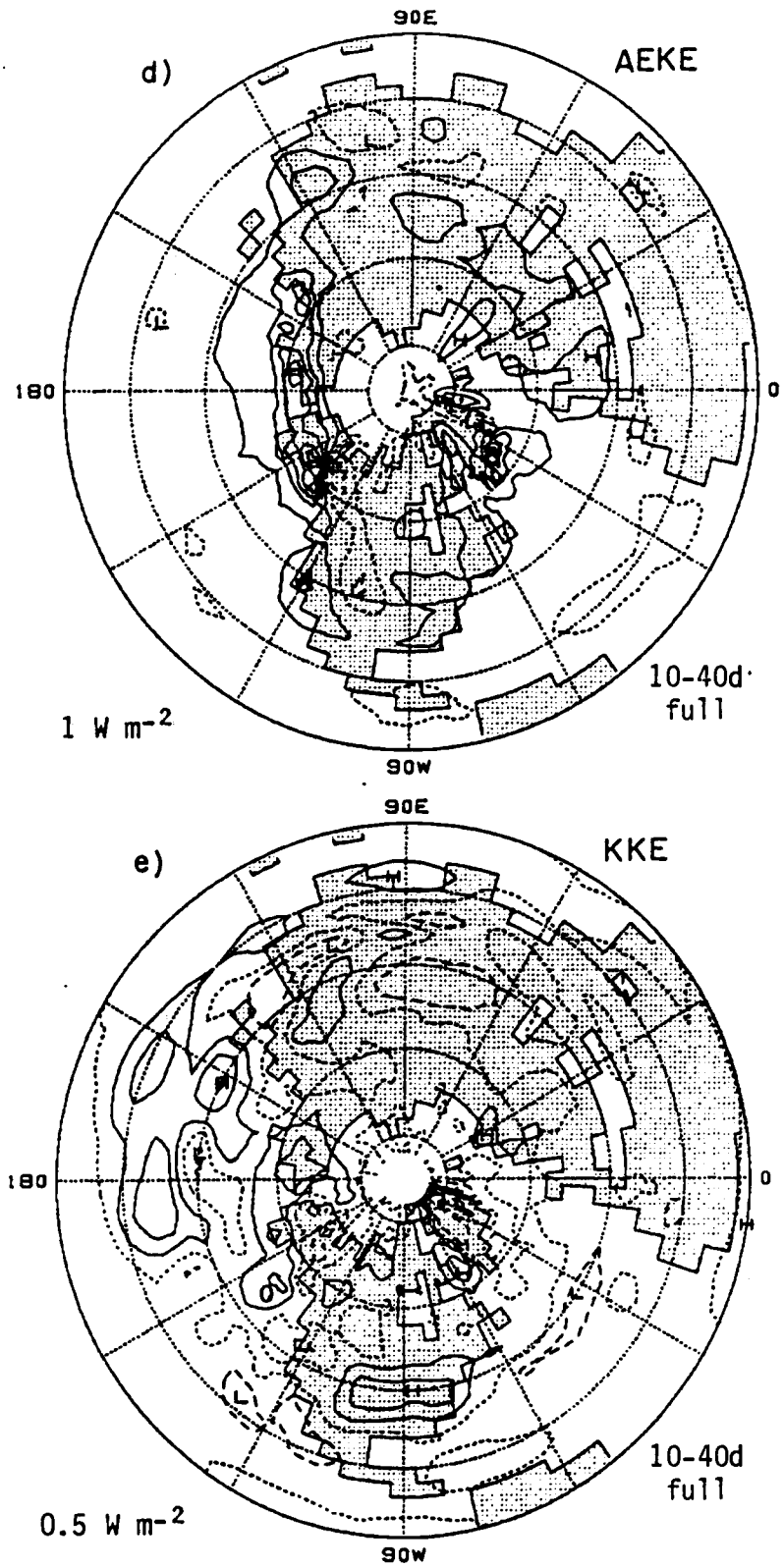

Fig. 7.17 (continued)

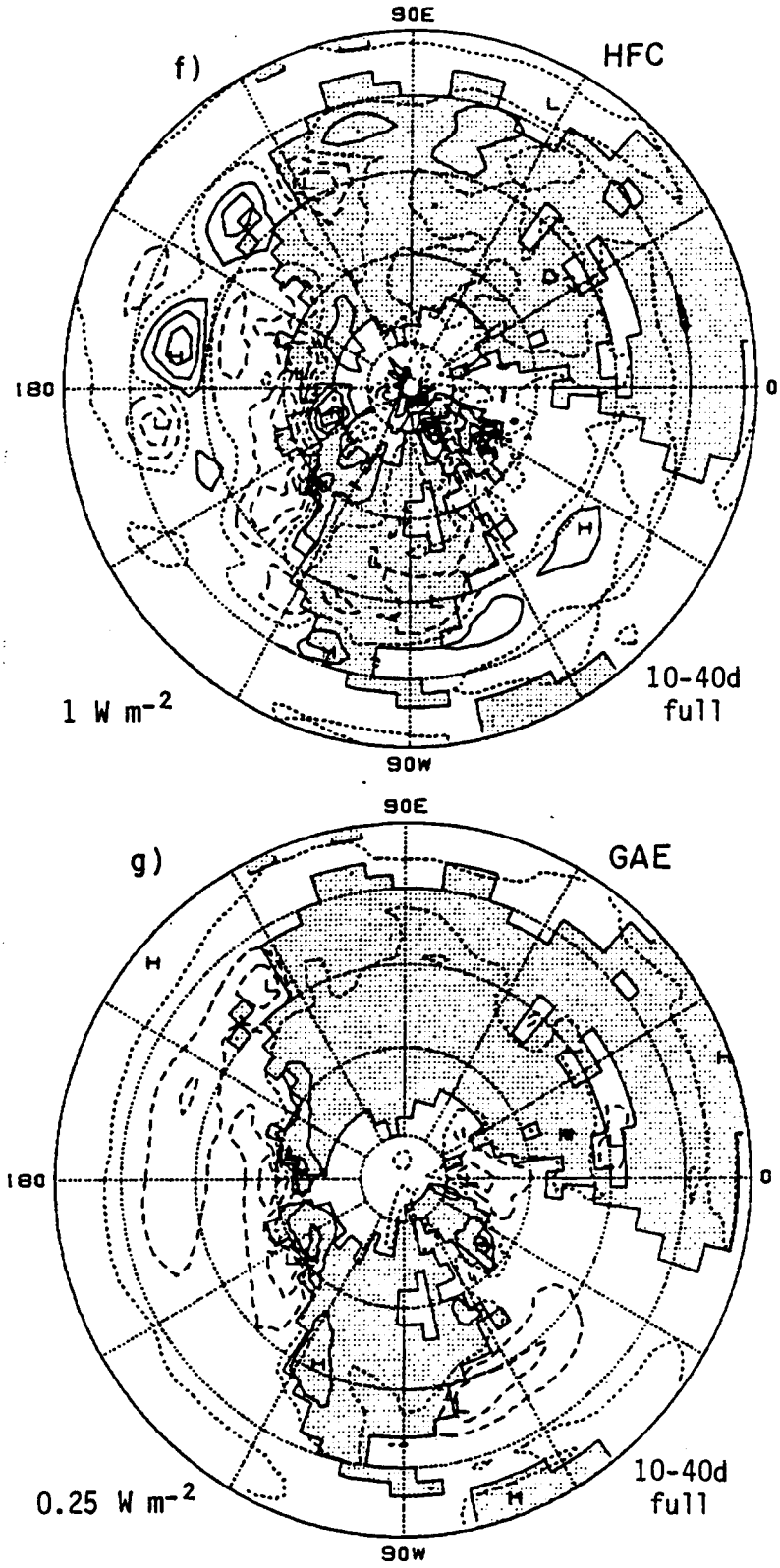

Fig. 7.17 (continued)

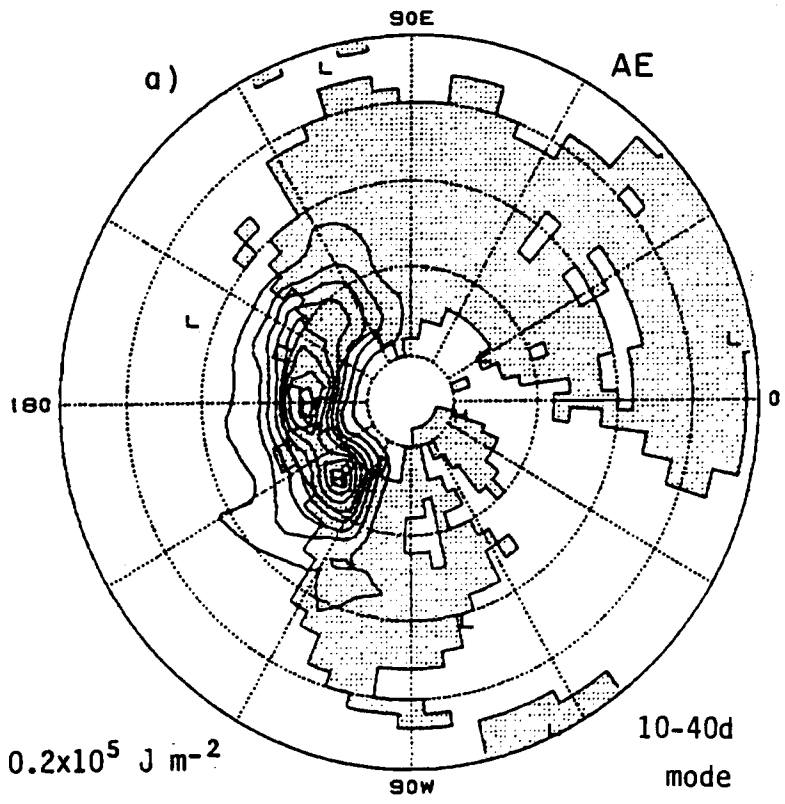

Fig. 7.18. The horizontal distribution of leading terms in the energy budget of the simulated 10 to 40 day disturbances corresponding only to the Pacific mode. (a) APE. (b) Kinetic energy. (c) Time-mean to eddy APE conversion. (d) APE to kinetic energy conversion. (e) Time-mean to eddy kinetic energy conversion. (f) Geopotential flux convergence. (g) Eddy APE generation through diabatic processes. Contour interval in (a) and (b) is 0.2×10^5 J m^{-2}, in (c), (d) and (f) 0.4 W m^{-2}, in (e) 0.2 W m^{-2} and in (g) 0.1 W m^{-2}.

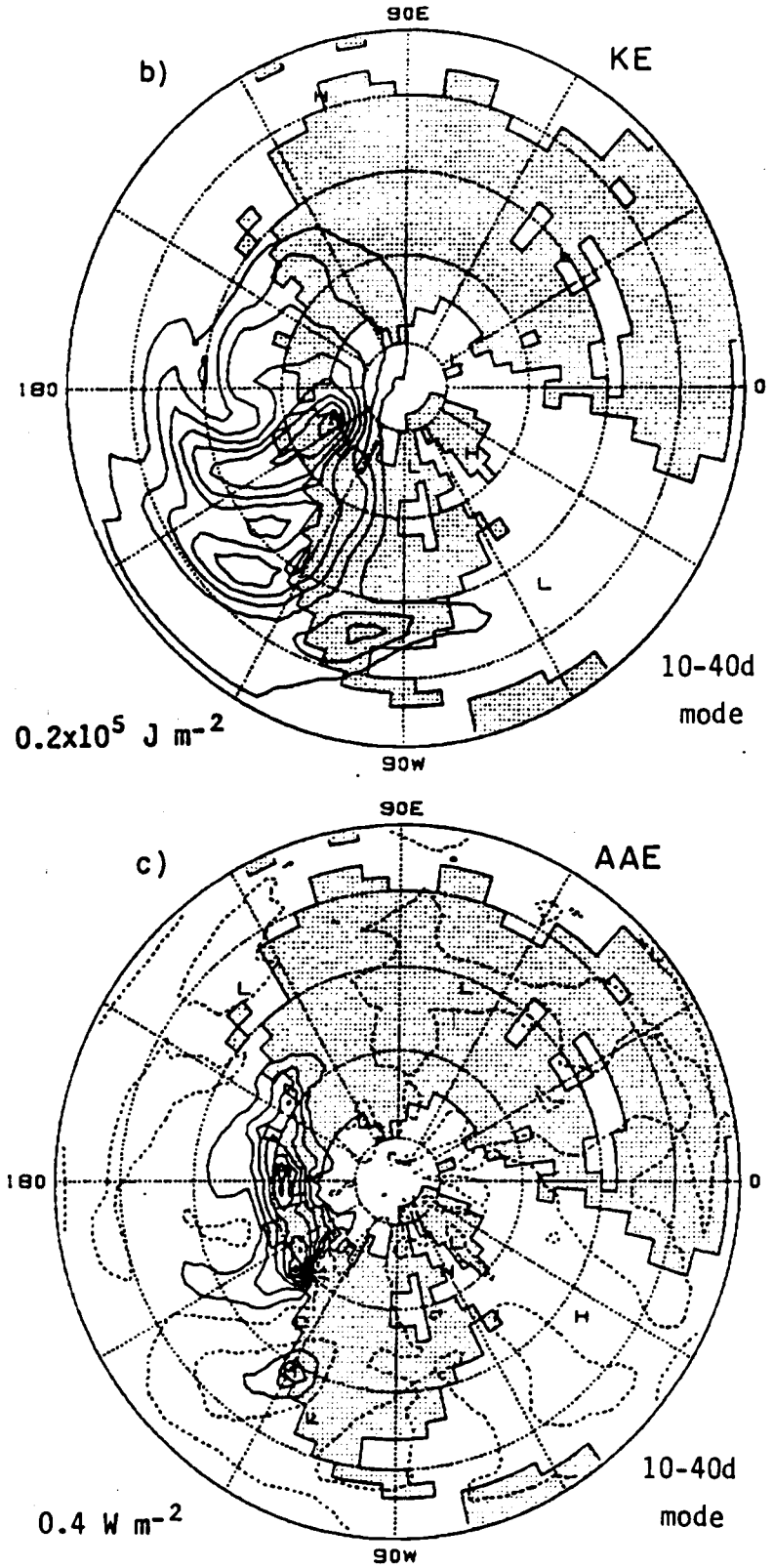

Fig. 7.18 (continued)

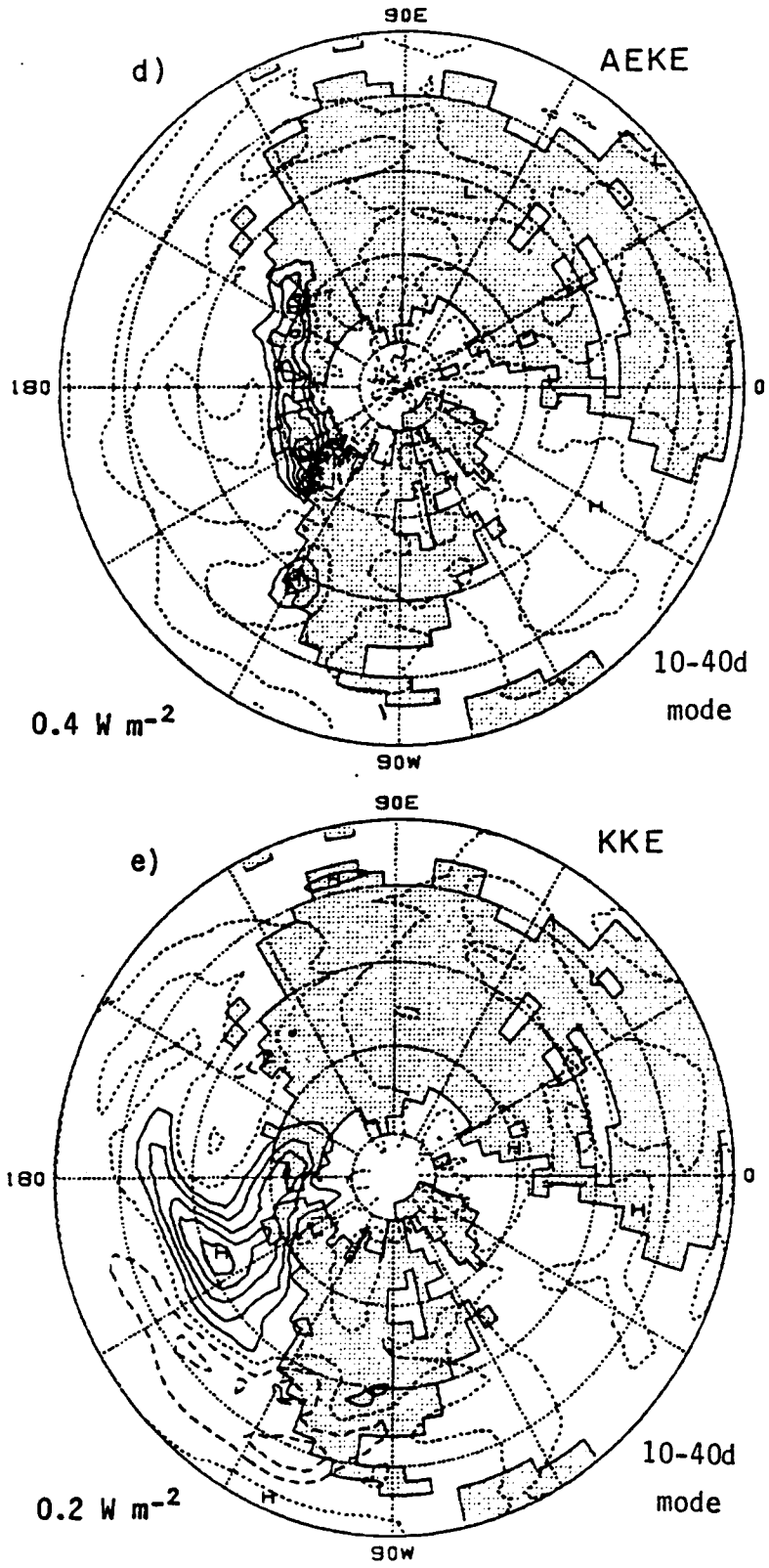

Fig. 7.18 (continued)

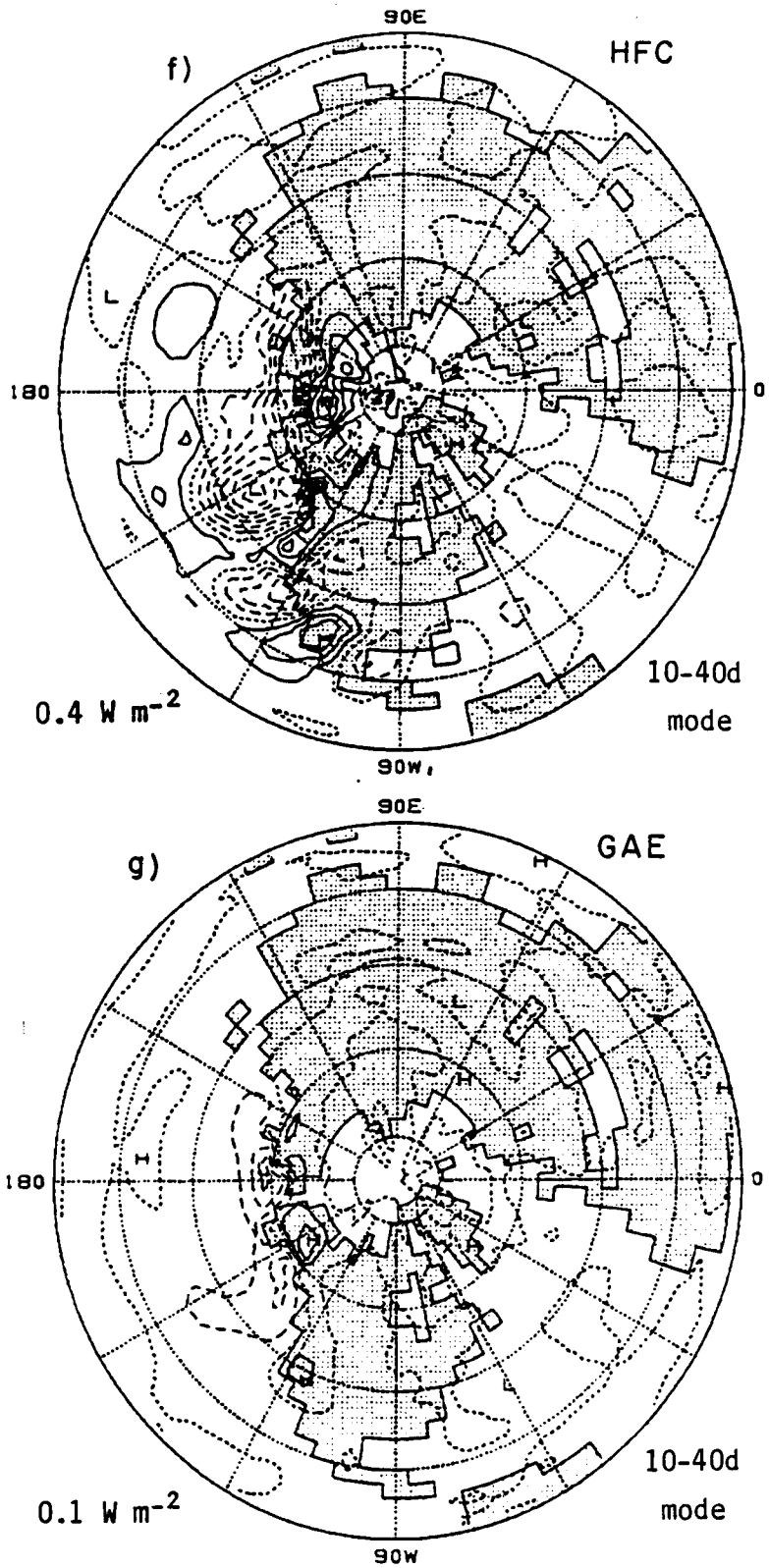

Fig. 7.18 (continued)

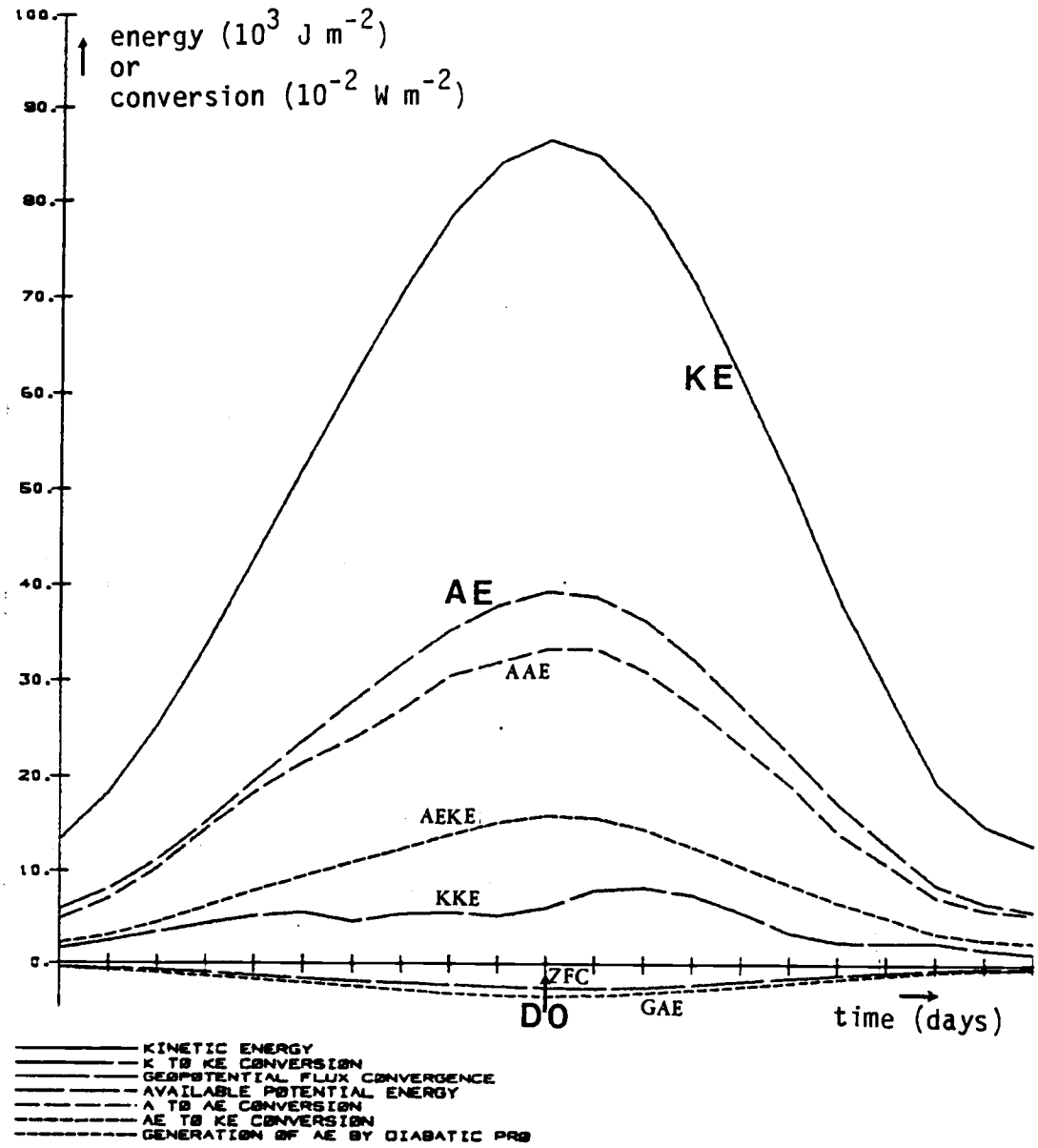

Fig. 7.19. The composite energy cycle of disturbances described by the first Pacific mode. Kinetic energy and APE are in units of 10^3 J m^{-2} and the conversion terms are in 10^{-2} W m^{-2}. The abscissa is in days where day zero denotes the day of maximum mode amplitude. The values represent an area average over the Pacific Quadrant of the Northern Hemisphere from 90°E eastward to 60°W.

disturbances over the northern Pacific basin. It clearly shows the dominance of a baroclinic energy cycle. The baroclinic conversion terms AAE and AEKE increase simultaneously in time as do the kinetic energy and the APE. As was indicated by the seasonally averaged energetics of this mode and the full 10 to 40 day signal these disturbances also grow by barotropic processes. Diabatic processes destroy APE but very weakly so, and kinetic energy is transported out of the region apparently to the Atlantic Ocean, as indicated by the Atlantic wave train in the geopotential height field.

CHAPTER 8: SUMMARY, CONCLUSION AND SUGGESTIONS FOR FURTHER RESEARCH

In this study the statistical properties of northern hemisphere tropospheric wintertime variability on short and long time scales were reviewed and their dynamical characteristics studied. The relative importance of key dynamical processes in the maintenance of the systems causing this variability was evaluated with the primary goal of achieving a better understanding of atmospheric low-frequency, subseasonal variability.

The data used in this study were generated by a 10-year simulation with the OSU atmospheric GCM. The completeness and the full internal consistency of GCM data is expected to provide sound, quantitative measures for the simulated variability and its maintenance. The relative simplicity of the OSU GCM allows a concise representation of the atmospheric state and more importantly, a straight-forward comparison with results of a large class of theoretical models. It was shown that although the simulation of subseasonal atmospheric variability by this GCM suffers from deficiencies, these are mainly quantitative not qualitative. In other words, the model appears to offer a good simulation of the dynamical characteristics of northern hemisphere wintertime variability even though the simulation is not geographically or quantitatively exact. Moreover, the comparison of differences between the model features and observations seems to lead to a better dynamical understanding of the real atmosphere.

The major conclusions from our study may be summarized as follows:

In accordance with observations we have found that subseasonal tropospheric wintertime variability is dominated by two different types of fluctuations. These two types of fluctuations can be classified on the basis of their time scales, short and long, separated in this case as in most observational studies by a 10-day cut off. We have found that the differences between the short and long time-scale fluctuations may be summarized in terms of their maximum intensity, three-dimensional structure and propagation characteristics. Using these criteria, we find that the long time-scale fluctuations are

stronger than the short time-scale fluctuations everywhere, especially over the high latitudes. Short time-scale fluctuations are basically a middle-latitude phenomenon. Long time-scale fluctuations have larger zonal dimensions but a more complex meridional structure than their short time-scale counterparts. In the vertical, the short time-scale fluctuations have a noticeable westward tilt while those at long time scales tilt less in the vertical in most regions (but not in their region of origin). Short time-scale fluctuations show rapid eastward phase propagation while those at long time scales are stationary or slightly retrograding in phase. An interesting feature which stands out in the low-frequency fields is the suggestion of the existence of eastward wave-energy dispersion in the fields of time-lagged spatial correlation analysis.

The transport properties of the eddies causing the wintertime variability and their energetics reveals that the above two categories of fluctuations owe their existence to large-scale dynamical mechanisms on their respective time scales. Moreover, both short and long time-period fluctuations appear to be maintained by similar processes - baroclinic energy cycles in which the eddies grow mainly by extracting potential energy from their environment, converting it in turn into kinetic energy. The major difference between the two types of eddies is in the regions where these cycles are prominant. While at short time scales these energy cycles occur over the major jet streams, those at long time scales occur over the extreme northern parts of the oceanic basins and Siberia. Another important difference between the two eddy categories is the role barotropic processes play in their maintenance. While short time-scale eddies lose their energy through barotropic processes, these processes serve as a source for the long-time-scale eddy kinetic energy. In either case barotropic processes play only a secondary role in the eddy energetics.

Finally, by applying complex EOF analysis to time series of the geopotential height anomaly at low frequencies, we have been able to isolate a class of low-frequency disturbances in the geopotential height field over the North Pacific Ocean. These disturbances are large scale waves with a dipole-like meridional structure. The phase

of the wave retrogrades slowly with a speed of about 5° per day which is equivalent to a period of about 20 days.

We are able to isolate the signal of the disturbance in other dynamical variable fields by correlating them with the principal component of the geopotential height mode. These data enable the calculation of the energy cycle of the disturbances. It is found that these disturbances grow primarily through a baroclinic energy conversion. As in the general case of low-frequency disturbances, barotropic energy conversion also contributes to eddy growth. Throughout the life cycle of the mode, energy seems to be transported out of the large part of the North Pacific basin.

Our results suggest that the primary source for the model wintertime variability is a baroclinic energy conversion of potential energy from the stationary part of the flow to the eddies. That this is the case also in the real atmosphere is hinted by the observed strong northward heat transport in the low-frequencies, over the northern ocean basins (see Blackmon et al., 1977, Fig. 11b). Holopainen et al. (1972) have shown that low-pass eddies exert a strong dissipative effect on the time mean flow through thermal processes equivalent to a baroclinic energy conversion. In their data the strongest forcing also happens over the northern ocean basins.

As we have previously mentioned there also exists theoretical evidence for the existance of low-frequency planetary-scale modes of baroclinic instability. In the studies of Frederiksen (1982 and 1983) it was shown that in situations with a relatively strong static stability, baroclinic instability in a two-level linear, spherical quasi-geostrophic model gives rise to relatively large scale modes with long periods (14 days to ∞) and a dipole-like meridional structure. Frederiksen proposed that these modes grow on both baroclinic and barotropic processes and should be considered as a precursor for blocking situation. In fact, his Pacific modes show a remarkable resemblance the Pacific disturbance isolated by our CEOF analysis. The study of Hartmann (1979) also shows that low-frequency, planetary scale waves with a dipole-like meridional structure are modes of baroclinic instability on a sphere, over high latitudes.

These results were obtained for a typical southern hemisphere zonal wind profile but similar conditions probably exist locally over the northern hemisphere high latitudes.

In the context of combining our results with the observational and theoretical evidence presented above, we propose the following explanation for the characteristics of the observed and modeled wintertime variability. In the stationary part of the wintertime flow there exist three major regions that are strongly baroclinically unstable. These are the regions of the jet streams where the flow has strong horizontal temperature gradients and vertical shears. Because of the geographical location, static stability and the meridional wind shear of the jet stream, the fastest growing baroclinic modes over these regions are high-frequency, eastward-propagating, relatively short waves with a monopole-like meridional structure. Over the higher latitudes, weaker yet significant (because of the larger Coriolis parameter) horizontal thermal gradients and vertical shears are combined with very weak gradients of absolute vorticity of the quasi-stationary flow. These cause the baroclinic growth of larger-scale waves with a dipole-like meridional structure and long periods which propagate slowly westward. The middle-latitude short monopole-like baroclinic waves propagate their energy eastward at velocities almost equal to their phase velocity and thus do not exhibit clear dispersion patterns. The retrograding high-latitude longwave baroclinic disturbances disperse their energy southeastward because of their higher meridional structure, in accordance with the theory of Rossby-wave dispersion on a sphere. It is for these reasons that these waves clearly exhibit the effects of wave dispersion. This also explains why low-frequency disturbances have a relatively baroclinic structure in high latitudes and a more barotropic structure in middle latitudes (see Fig. 4.3b).

This interpretation does not touch upon the mechanisms which generate low-frequency disturbances; our analysis was not tailored to achieve this goal. Mechanisms such as remote forcing by tropical or middle latitude heating, while not important in the maintenance of the energetics of large-amplitude low-frequency eddies could still be a

trigger for this outbreak. So also could be shorter waves with higher frequencies that grow explosively and become longer and slower moving as envisioned by Frederiksen (1983) and suggested by the composite study of Dole (1983).

We also have not examined explicitly the role of interband interactions in the maintenance of low-frequency eddies, a mechanism suggested by Egger and Schilling (1983). Some of our results, however, indicate that these effects are small and probably lead to destruction of low-frequency energy. Another mechanism not evaluated in our study is the role of orography, for example in the sense suggested by Charney and Devore (1979).

In light of the similarity in period and energetics between the low frequency disturbances studied here and theoretical and observed vascillation cycles it seems plausible that these are one-and-the-same phenomenon.

To explore further the various mechanisms that maintain low-frequency variability and their relative importance, some of the analysis methods used here should also be applied to observations. Another possibility would be to look at simulations by GCMs with better vertical resolution.

The CEOF method should also be used to isolate modes responsible for low-frequency variability over the Atlantic and Siberia and the results compared with the Pacific mode. More effort should be put towards describing and comparing the development of simulated and observed low-frequency modes defined by CEOF and other types of analysis. It would also be important to examine the way NWP models handle these low-frequency modes and the effects that initialization procedures have on their prediction.

Much remains to be done. We believe, however, that the results of this study are encouraging in two ways. They point at the benefits of using GCMs in the study of large-scale atmospheric circulation systems, and thus providing investigators with a powerful dynamical tool. They also give reason for optimism with regard to our ability to achieve the goal set by Carl Gustave Rossby and his colleagues, that is to be able to follow and predict the slow fluctuations of the planetary circulation.

REFERENCES

Arakawa, A., 1961: The variation of general circulation in the barotropic atmosphere. *J. Meteor. Soc. Jpn., 39,* 49-58.

Arakawa, A., 1966: Computational design for long-term numerical integration of the equations of fluid motion: Two-dimensional incompressible flow. Part I. *J. Computational Phys., 1,* 119-143.

Barnett, T. P., 1977: The principal time and space scales of the Pacific Trade Wind field. *J. Atmos. Sci., 34,* 221-235.

Barnett, T. P., 1983: Interaction of the Monsoon and Pacific Trade Wind system at interannual time scales. Part I: The Equatorial zone. *Mon. Wea. Rev., 111,* 756-773.

Bjerkness, J. and J. Holmboe, 1944: On the theory of cyclones. *J. Meteor., 1,* 1-22.

Blackmon, M. L., 1976: A climatological spectral study of the 500 mb geopotential height of the Northern Hemisphere. *J. Atmos. Sci., 33,* 1607-1623.

Blackmon, M. L., J. M. Wallace, N.-C. Lau and S. L. Mullen, 1977: An observational study of the Northern Hemisphere wintertime circulation. *J. Atmos. Sci., 34,* 1040-1053.

Blackmon, M. L., R. A. Madden, J. M. Wallace and D. S. Gutzler, 1979: Geographical variations in the vertical structure of geopotential height fluctuations. *J. Atmos. Sci., 36,* 2450-2466.

Blackmon, M. L. and N.-C. Lau, 1980: Regional characteristics of the Northern Hemisphere wintertime circulation: A comparison of the simulation of a GFDL general circulation model with observations. *J. Atmos. Sci., 37,* 497-514.

Blackmon, M. L., Y.-H. Lee and J. M. Wallace, 1984a: Horizontal structure of 500 mb height fluctuations with long, intermediate and short time scales. *J. Atmos. Sci., 41,* 961-979.

Blackmon, M. L., Y.-H. Lee, J. M. Wallace and H.-H. Hsu, 1984b: Time Variations of 500 mb height fluctuations with long, intermediate and short time scales as deduced from lag-correlation statistics. *J. Atmos. Sci., 41,* 981-991.

Branstator, G., 1983: Horizontal energy propagation in a barotropic atmosphere with meridional and zonal structure. *J. Atmos. Sci, 40,* 1689-1708.

Charney, J. G., 1947: The dynamics of long waves in a baroclinic westerly current. *J. Meteorol., 4,* 135-162.

Charney, J. G. and J. G. Devore, 1979: Multiple flow equilibria in the atmosphere and blocking. *J. Atmos. Sci.*, *36*, 1205-1216.

Charney, J. G., J. Shukla and K. C. Mo, 1981: Comparison of a barotropic blocking theory with observation. *J. Atmos. Sci.*, *38*, 762-779.

Cressman, G. P., 1948: On the forecasting of long waves in the upper westerlies. *J. Meteor.*, 44-57.

Cressman, G. P., 1949: Some effects of wave-length variations of the long waves in the upper westerlies. *J. Meteor.*, *6*, 56-60.

Cressman, G. P., 1950: Variations in the structure of the upper westerlies. *J. Meteor.*, *7*, 39-47.

Cressman, G. P., 1958: Divergence and very long atmospheric waves. *Mon. Wea. Rev.*, *86*, 293-297.

Dole, R. M., 1983: Persistent anomalies of the extratropical Northern Hemisphere wintertime circulation. In *Large-Scale Dynamical Processes in the Atmosphere* (B. Hoskins and R. Pearce, Eds.). Academic Press, New York, New York, 397 pp.

Eady, E. T., 1949: Long wave and cyclone waves. *Tellus*, *1*, 33-52.

Egger, J. and H.-D. Scilling, 1983: On the theory of the long-term variability of the atmosphere. *J. Atmos. Sci.*, *40*, 1073-1085.

Frederiksen, J. S., 1978: Instability of planetary waves and zonal flows in two-layer models on a sphere. *Quart. J. Roy. Meteor. Soc.*, *104*, 841-872.

Frederiksen, J. S., 1980: Zonal and meridional variations of eddy fluxes induced by long planetary waves. *Quart. J. Roy. Met. Soc.*, *106*, 63-84.

Frederiksen, J. S., 1982: A unified three-dimensional instability theory of the onset of blocking and cyclogenesis. *J. Atmos. Sci.*, *39*, 969-982.

Gall, R., 1976: A comparison of linear baroclinic instability with the eddy statistics of a general circulation model. *J. Atmos. Sci.*, *33*, 34 9-373.

Gates, W. L., E. S. Batten, A. B. Kahle and A. B. Nelson, 1971: A documentation of the Mintz-Arakawa two-level atmospheric general circulation model. R-877-ARPA, The Rand Corporation, Santa Monica, CA, 408 pp.

Ghan, S. J., J. W. Lingaas, M. E. Schlesinger, R. L. Mobley and W. L. Gates, 1982: A documentation of the OSU two-level atmospheric general circulation model. Report No. 35, Climatic Research Institue, Oregon State University, Corvallis, 395 pp.

Green, J. S. A., 1977: The weather during July 1976: Some dynamical considerations of the drought. *Weather, 32,* 120-125.

Grose, W. L. and B. J. Hoskins, 1979: On the influence of orography on the large-scale atmospheric flow. *J. Atmos. Sci., 36,* 223-234.

Hartmann, D. L., 1974: Time spectral analysis of mid-latitude disturbances. *Mon. Wea. Rev., 102,* 348-362.

Hartmann, D. L., 1979: Baroclinic instability of realistic zonal-mean states to planetary waves. *J. Atmos. Sci., 36,* 2336-2349.

Hayashi, Y. and D. G. Golder, 1977: Space-time spectral analysis of mid-latitude disturbances appearing in a GFDL general circulation model. *J. Atmos. Sci., 34,* 237-262.

Hendon, H. H. and Hartmann, D. L., 1982: Stationary waves on a sphere: Sensitivity to therma feedback. *J. Atmos. Sci., 39,* 1906-1920.

Herrmann, O., 1969: Transversal filter for Hilbert-transformation. *Arch. Elektr. Ubertragung, 23,* 581-587.

Hide, R., 1953: Some experiments on thermal convection in a rotating liquid. *Quart. J. Roy. Meteor. Soc., 79,* 161.

Holopainen, E. O., L. Rontu and N.-C. Lau, 1982: The effect of large-scale transient eddies on the time-mean flow in the atmosphere. *J. Atmos. Sci., 39,* 1972-1984.

Horel, J. D. and J. M. Wallace, 1981: Planetary scale atmospheric phenomena associated with the Southern Oscillation. *Mon. Wea. Rev., 109,* 813-829.

Hoskins, B. J., 1983: Dynamical processes in the atmosphere and the use of models. *Quart. J. Roy. Meteor. Soc., 109,* 1-21.

Hoskins, B. J., A. J. Simmons and D. G. Andrews, 1977: Energy Dispersion in a barotropic atmosphere. *Quart. J. Roy. Meteor. Soc., 103,* 553-567.

Hoskins, B. J. and D. J. Karoly, 1981: The steady linear response of a spherical atmosphere to thermal and orographic forcing. *J. Atmos. Sci., 38,* 1179-1196.

Hoskins, B. J., I. N. James and G. H. White, 1983: The shape, propagation and mean-flow interaction of large-scale weather systems. *J. Atmos. Sci., 40,* 1595-1612.

Kang, I.-S., 1984: Quasi-Stationary Atmospheric Response to Large-Scale Forcing. Ph.D. Thesis, Oregon State University, Corvallis, 140 pp.

Kaylor, R. E., 1977: Filtering and decimation of digital time series. Technical Note BN850, Inst. Phys. Sci. Tech., University of Maryland, College Park, 42 pp.

Kim, J.-W. and J.-T. Chang, 1982: The atmospheric moisture balance simulated for January and July by the OSU two-level atmospheric general circulation model. Report No. 40, Climatic Research Institute, Oregon State Univ., Corvallis, 45 pp.

Kutzbach, J. E., 1967: Empirical eigenvectors of sea-level pressure, surface temperature and precipitation complexes over North America. *J. Appl. Meteor., 6,* 791-802.

Lau, N.-C., 1978: On the three-dimensional structure of the observed transient eddy statistics of the Northern Hemisphere wintertime circulation. *J. Atmos. Sci., 35,* 1900-1923.

Lau, N.-C., 1979a: The structure and energetics of transient disturbances in the Northern Hemisphere wintertime circulation. *J. Atmos. Sci., 36,* 982-995.

Lau, N.-C., 1979b: The observed structure of tropospheric stationary waves and the local balances of vorticity and heat. *J. Atmos. Sci., 36,* 996-1016.

Lau, N.-C., 1981: A diagnostic study of recurrent meteorological anomalies appearing in a 15-year simulation with a GFDL general circulation model. *Mon. Wea. Rev., 109,* 2287-2311.

Lau, N.-C., G. H. White and R. L. Jenne, 1981: Circulation statistics for the extratropical Northern Hemisphere based on NMC analyses. NCAR Technical Note 171 + STR, 138 pp.

Lau, N.-C. and E. O. Holopainen, 1984: Transient eddy forcing of the time-mean flow as identified by geopotential tendencies. *J. Atmos. Sci., 41,* 313-328.

Lau, N.-C. and K.-M. Lau, 1984: The structure and energetics of midlatitude disturbances accompanying cold-air outbreaks over Esat Asia. *Mon. Wea. Rev., 112,* 1309-1327.

Lorenz, E. N., 1956: Empirical orthogonal functions and statistical weather prediction. Sci. Rep. No. 1, Contract AF19-(604) 1566, Dept. Meteor., MIT.

Lorenz, E. N., 1963a: The predictability of hydrodynamic flow. *Trans. New York Acad. Sci., Ser. II, 25* (4), 409-432.

Lorenz, E. N., 1963b: The mechanics of vacillation. *J. Atmos. Sci., 20*, 448-464.

Madden, R. A., 1979: Observations of large-scale traveling waves. *Rev. Geophys. Space Phys., 17*, 1935-1949.

McGuirk, J. P. and E. R. Reiter, 1976: A vacillation in atmospheric energy parameters. *J. Atmos. Sci., 33*, 2079-2093.

Moura, A. D. and P. H. Stone, 1976: The effects of spherical geometry on baroclinic instability. *J. Atmos. Sci., 33*, 602-616.

Mullen, S. L., 1980: Analysis of the regional characteristics of the Northern Hemisphere wintertime circulation simulated by the two-level OSU general circulation model: A comparison with observations. Report No. 19, Climatic Research Institute, Oregon State University, Corvallis, 41 pp.

Namias, J., 1950: The index cycle and its role in the general circulation. *J. Meteor., 7*, 130-139.

Namias, J., 1953: Thirty day forcasts: A review of a ten-year experiment. *Am. Meteor. Soc., Meteor. Monogr., 6*, 83pp.

Namias, J. and P. F. Clapp, 1944: Studies on the motion and development of long waves in the westerlies. *J. Meteor., 1*, 57-77.

Namias, J. and D. R. Cayan, 1981: Large-scale air-sea interactions and short-period climatic fluctuations. *Science, 214*, 869-876.

Newell, R. E., D. G. Vincent, T. G. Dopplick, D. Ferrazza and J. W. Kidson, 1970: The Energy Balance. The Global Circulation of the atmosphere, T. A. Corby, Ed. Roy. Meteor. Soc., 42-90.

Nicholls, N., 1980: Long-range weather forecasting: value, status and prospects. Rev. Geophys. and Space Phys., 18, 771-788.

Oort, A. H., 1964: On estimates of the atmospheric energy cycle. *Mon. Wea. Rev., 92*, 483-493.

Pedloski, J., 1964: The stability of currents in the atmosphere and ocean: Part I. *J. Atmos. Sci., 21*, 201-219.

Phillips, N. A., 1954: Energy transformations and meridional circulations associated with simple baroclinic waves in a two-level, quasi-geostrophic model. *Tellus, 6*, 273-286.

Pratt, R. W. and J. M. Wallace, 1976: Zonal propagation characteristics of large-scale fluctuations in the middle troposphere. *J. Atmos. Sci., 33,* 1184-1194.

Qiu, G.-Q. and S. K. Esbensen, 1984: Teleconnection patterns simulated by the OSU AGCM. Report No. 51, Climatic Research Institute, Oregon State Univ., Corvallis, 42 pp.

Quinet, A., 1974: A numerical study of vacillation. *Adv. in Geophys., 17,* 101-186.

Rex, D. F., 1950a: Blocking action in the middle troposphere and its effect upon regional climate. I. An aerological study of blocking action. *Tellus, 2,* 196-211.

Rex, D. F., 19510b Blocking action in the middle troposphere and its effect on regional climate. II. The climatology of blocking action., *Tellus, 3,* 275-301.

Rossby, C.-G., 1939: Relation between variations in the intensity of the zonal circulation of the atmosphere and the displacement of the semi-permanent centers of action. *J. Marine Res., 2,* 38-55.

Rossby, C.-G., 1945: On the propagation of frequencies and energy in certain types of oceanic and atmospheric waves. *J. Meteor., 2,* 187-204.

Sawyer, J. S., 1970: Observational characteristics of atmospheric fluctuations with a time scale of a month. *Quart. J. Roy. Meteor. Soc., 96,* 610-625.

Schlesinger, M. E. and W. L. Gates, 1980: The January and July performance of the OSU two-level atmospheric general circulaton model. *J. Atmos. Sci., 37,* 1914-1943.

Shapiro, R. and F. Ward, 1960: The time-space spectrum of the geostrophic meridional kinetic energy. *J. Meteor., 17,* 621-626.

Simmons, A. J., 1982: The forcing of stationary wave motion by tropical diabatic heating. *Quart. J. Roy. Meteor. Soc., 108,* 503-534.

Simmons, A. J. and B. J. Hoskins, 1976: Baroclinic instability on a sphere: Normal modes of the primitive and quasi-geostrophic equations. *J. Atmos. Sci., 33,* 1454-1477.

Simmons, A. J. and B. J. Hoskins, 1978: The life cycle of some nonlinear baroclinic waves. *J. Atmos. Sci., 35,* 414-432.

Simmons, A. J., J. M. Wallace and G. Branstator, 1983: Barotropic wave propagation and instability and atmospheric teleconnection patterns. *J. Atmos. Sci ., 40,* 1363-1392.

Smith, P. J., 1980: The energetics of extratropical cyclones. *Rev. Geophys. and Space Phys., 18,* 378-386.

Thompson, P. D., 1957: A heuristic theory of large-scale turbulence and long-period velocity variations in barotropic flow. *Tellus, 9,* 69-91.

Walker, G. T. and E. W. Bliss, 1982: World Weather V. *Mem. Roy. Meteor. Soc., 4,* 53-84.

Wallace, J. M. and R. E. Dickinson, 1972: Empirical orthogonal representation of time series in the frequency domain. Part I: Theoretical considerations. *J. Appl. Meteor., 11,* 887-892.

Wallace, J. M. and D. S. Gutzler, 1981: Teleconnections in the geopotential height field during the Northern Hemisphere winter. *Mon. Wea. Rev., 109,* 1150-1162.

Ward, F. and R. Shapiro, 1961: Meteorological periodicities. *J. Meteor.,* 635-656.

Webster, P. J., 1981: Mechanisms determining the atmospheric response to sea surface temperature anomalies. *J. Atmos. Sci., 38,* 554-571.

Webster, P. J. and J. L. Keller, 1975: Atmospheric variations: Vacillations and index cycles. *J. Atmos. Sci., 32,* 1283-1300.

Willet, H. C., 1948: Patterns of world weather changes. *Trans. Amer. Geophys. Union, 29,* 803-809.

APPENDICES

APPENDIX: Eddy Energy Equations

a. Kinetic energy equation

Consider the zonal and meridional momentum equations

$$\frac{\partial u}{\partial t} + \frac{u}{a\cos\phi}\frac{\partial u}{\partial \lambda} + \frac{v}{a}\frac{\partial u}{\partial \phi} + \omega\frac{\partial u}{\partial p} - \frac{uv\tan\phi}{a} = -\frac{1}{a\cos\phi}\frac{\partial \Phi}{\partial \lambda} + fv + F_\lambda \quad (A.1)$$

$$\frac{\partial v}{\partial t} + \frac{u}{a\cos\phi}\frac{\partial v}{\partial \lambda} + \frac{v}{a}\frac{\partial v}{\partial \phi} + \omega\frac{\partial v}{\partial p} + \frac{u^2\tan\phi}{a} = -\frac{1}{a}\frac{\partial \Phi}{\partial \phi} - fu + F_\phi \quad (A.2)$$

and the mass continuity equation:

$$\frac{1}{a\cos\phi}\frac{\partial u}{\partial \lambda} + \frac{1}{a}\frac{\partial v}{\partial \phi} - \frac{v\tan\phi}{a} + \frac{\partial \omega}{\partial p} = 0 \quad (A.3)$$

Here u, v and ω are the three velocity components in the pressure coordinate system, λ and ϕ are the longitude and latitude angles respectively and a is the radius of the earth. Φ is the geopogential, F_λ and F_ϕ are the zonal and meridional components of friction and f is the Coriolis parameter.

Let a dependent variable A be represented by its time average part $\overline{A}$ and the deviations from it A' in the form:

$$A(x,y,p,t) = \overline{A}(x,y,p,t) + A'(x,y,p,t) \quad (A.4)$$

where we have allowed $\overline{A}$ to change with time, as the averaging in time may be a running average (or other low-pass filter). Thus $\overline{A}$ may be considered as a low-pass part of the field. We will assume however that the Reynolds averaging may be used, that is:

$$\overline{A'(x,y,p,t)} = 0 \quad (A.5)$$

and

$$\overline{A'(x,y,p,t)\overline{A}(x,y,p,t)} = 0 \quad (A.6)$$

The second assumption will hold only if A has a typical time scale which is much longer than that of A'.

Using this time-mean eddy presentation (A.1) becomes:

$$\frac{\partial \bar{u}}{\partial t} + \frac{\partial u'}{\partial t} + \frac{\bar{u}}{a\cos\phi}\frac{\partial \bar{u}}{\partial \lambda} + \frac{u'}{a\cos\phi}\frac{\partial \bar{u}}{\partial \lambda} + \frac{\bar{u}}{a\cos\phi}\frac{\partial u'}{\partial \lambda} + \frac{u'}{a\cos\phi}\frac{\partial u'}{\partial \lambda}$$

$$+ \frac{\bar{v}}{a}\frac{\partial \bar{u}}{\partial \phi} + \frac{v'}{a}\frac{\partial \bar{u}}{\partial \phi} + \frac{\bar{v}}{a}\frac{\partial u'}{\partial \phi} + \frac{v'}{a}\frac{\partial u'}{\partial \phi} + \bar{\omega}\frac{\partial \bar{u}}{\partial p} + \omega'\frac{\partial \bar{u}}{\partial p} + \omega'\frac{\partial u'}{\partial p}$$

$$- \frac{\bar{u}\bar{v}'\tan\phi}{a} - \frac{u'\bar{v}\tan\phi}{a} - \frac{\bar{u}v'\tan\phi}{a} - \frac{u'v'\tan\phi}{a}$$

$$= -\frac{1}{a\cos\phi}\frac{\partial \bar{\Phi}}{\partial \lambda} - \frac{1}{a\cos\phi}\frac{\partial \Phi'}{\partial \lambda} + f\bar{v} + fv' + \bar{F}_\lambda + F_\lambda' \qquad (A.7)$$

Taking the time average (or the low-pass) of (A.7) we obtain the equation for the time-average (or low-pass) zonal momentum:

$$\frac{\partial \bar{u}}{\partial t} + \frac{\bar{u}}{a\cos\phi}\frac{\partial \bar{u}}{\partial \lambda} + \frac{\bar{v}}{a}\frac{\partial \bar{u}}{\partial \phi} + \bar{\omega}\frac{\partial \bar{u}}{\partial p} - \frac{\bar{u}\bar{v}}{a}\tan\phi = -\frac{1}{a\cos\phi}\frac{\partial \bar{\Phi}}{\partial \lambda} + f\bar{v} + \bar{F}_\lambda$$

$$- \left\{\overline{\frac{u'}{a\cos\phi}\frac{\partial u'}{\partial \lambda}} + \overline{\frac{v'}{a}\frac{\partial u'}{\partial \phi}} + \overline{w'\frac{\partial u'}{\partial p}} - \overline{\frac{u'v'}{a}\tan\phi}\right\} \qquad (A.8)$$

The negative of the sum of the "Reynolds-stress" terms in the parentheses will be hereafter referred to $\mathcal{F}_\lambda$ (the zonal component of the eddy velocity Reynolds stress).

By subtracting (A.8) from (A.7) we obtain the equation for the eddy component (high-pass part) of the zonal wind:

$$\frac{\partial u'}{\partial t} + \frac{\bar{u}}{a\cos\phi}\frac{\partial u'}{\partial \lambda} + \frac{\bar{v}}{a}\frac{\partial u'}{\partial \phi} + \bar{\omega}\frac{\partial u'}{\partial p} = -\frac{1}{a\cos\phi}\frac{\partial \Phi'}{\partial \lambda} + fv'$$

$$- \left\{\frac{u'}{a\cos\phi}\frac{\partial \bar{u}}{\partial \lambda} + \frac{v'}{a}\frac{\partial \bar{u}}{\partial \phi} + \omega'\frac{\partial \bar{u}}{\partial p} - \frac{u'\bar{v}}{a}\tan\phi - \frac{\bar{u}v'}{a}\tan\phi\right\}$$

$$+ (\mathcal{F}_\lambda - \bar{\mathcal{F}}_\lambda) \qquad (A.9)$$

Applying the same procedure to (A.2) we obtain the equations for time-mean (low-pass) and time-eddy (high-pass) meridional velocity components:

$$\frac{\partial \bar{v}}{\partial t} + \frac{\bar{u}}{a\cos\phi}\frac{\partial \bar{v}}{\partial \lambda} + \frac{\bar{v}}{a}\frac{\partial \bar{v}}{\partial \phi} + \bar{\omega}\frac{\partial \bar{v}}{\partial p} + \frac{\bar{u}^2}{a}\tan\phi = -\frac{1}{a}\frac{\partial \bar{\Phi}}{\partial \phi} - f\bar{u} + F_\lambda$$

$$- \left\{\overline{\frac{u'}{a\cos\phi}\frac{\partial v'}{\partial \lambda}} + \overline{\frac{v'}{a}\frac{\partial v'}{\partial \phi}} + \overline{\omega'\frac{\partial v'}{\partial p}} + \overline{\frac{u'u'}{a}\tan\phi}\right\} \qquad \text{(A.10)}$$

and:

$$\frac{\partial v'}{\partial t} + \frac{\bar{u}}{a\cos\phi}\frac{\partial v'}{\partial \lambda} + \frac{\bar{v}}{a}\frac{\partial v'}{\partial \phi} + \bar{\omega}\frac{\partial v'}{\partial p} = -\frac{1}{a}\frac{\partial \Phi'}{\partial \phi} - fu' + F_\phi'$$

$$- \left\{\frac{u'}{a\cos\phi}\frac{\partial \bar{u}}{\partial \lambda} + \frac{u'}{a}\frac{\partial \bar{u}}{\partial \phi} + \omega'\frac{\partial \bar{u}}{\partial p} + 2\frac{u'\bar{u}}{a}\tan\phi\right\} + (\mathcal{F}_\phi - \bar{\mathcal{F}}_\phi) \qquad \text{(A.11)}$$

where $\mathcal{F}_\phi$ is the meridional component of the velocity Reynolds-stress vector.

Let us now assume that the eddies we have are confined to one frequency band and that the overbar represents a seasonal (wintertime) average. In that case we can form the seasonally averaged equation for the eddy kinetic energy by multiplying (A.9) by u' and (A.11) by v', summing them up and averaging over the whole season. Defining K_E as:

$$K_E = \frac{1}{2}(\overline{u'^2} + \overline{v'^2}) \qquad \text{(A.12)}$$

we then have:

$$\left(\frac{\partial}{\partial t} + \frac{\bar{u}}{a\cos\phi}\frac{\partial}{\partial \lambda} + \frac{\bar{v}}{a}\frac{\partial}{\partial \phi} + \bar{\omega}\frac{\partial}{\partial p}\right)K_E =$$

$$= -\left\{\overline{\frac{u'}{a\cos\phi}\frac{\partial \Phi'}{\partial \lambda}} + \overline{\frac{v'}{a}\frac{\partial \Phi'}{\partial \phi}}\right\} - \left\{\overline{\frac{u'u'}{a\cos\phi}}\frac{\partial \bar{u}}{\partial \lambda} + \overline{\frac{u'v'}{a}}\frac{\partial \bar{u}}{\partial \phi}\right.$$

$$+ \overline{\frac{u'v'}{a\cos\phi}}\frac{\partial \bar{u}}{\partial \lambda} + \overline{\frac{v'v'}{a}}\frac{\partial \bar{v}}{\partial \phi} - (\overline{u'u'}\bar{v} - \overline{u'v'}\bar{u})\frac{\tan\phi}{a} + \overline{u'\omega'}\frac{\partial \bar{u}}{\partial p}$$

$$\left. + \overline{v'\omega'}\frac{\partial \bar{u}}{\partial p}\right\} + \overline{\mathbb{V}'\cdot\mathcal{F}_e'} + \overline{\mathbb{V}'\cdot\mathbb{F}'} \qquad \text{(A.13)}$$

where $\mathcal{F}_e' = (\mathcal{F}_e - \overline{\mathcal{F}}_e)$ is the velocity Reynolds-stress vector and $\mathbb{F}$ is the friction vector.

The terms that describe the advection of geopotential height can be put into their flux converence form by using the eddy form of the continuity equation (B.3). Thus:

$$- \left\{ \overline{\frac{u'}{\cos\phi} \frac{\partial \Phi'}{\partial \lambda}} + \overline{\frac{v'}{a} \frac{\partial \Phi'}{\partial \phi}} \right\} - \overline{\omega' \frac{\partial \Phi'}{\partial p}} + \overline{\omega' \frac{\partial \Phi'}{\partial p}} =$$

$$= - \nabla \cdot \overline{\mathbb{V}' \Phi'} - \frac{\partial}{\partial p} \overline{\omega' p'} - \overline{\omega' \alpha'} \qquad \text{(A.14)}$$

where we have first added and subtracted a vertical advection term and later used the hydrostatic equation $\frac{\partial \Phi'}{\partial p} = - \alpha$

The terms in the second pair of parenthesis on the r.h.s. of (A.13) act like energy conversion terms between the time mean kinetic energy $K = \frac{1}{2} (\overline{u}^2 + \overline{v}^2)$ and the eddy kinetic energy. This can be shown by forming the time mean kinetic energy equation from (A.8) and (A.10), multiplied by $\overline{u}$ and $\overline{v}$ respectively. The term representing the vector dot product of the time mean velocity $\overline{\mathbb{V}}$ and the eddy Reynolds stress vector $\overline{\mathcal{F}}_e$ then become an energy conversion term. By rearranging terms and performing a horizontal average over a closed domain it becomes equal and magnitude and opposite in sign to the energy conversion term in (A.13).

The term $\overline{\mathbb{V}' \cdot \mathcal{F}_e'}$ may be expressed in flux convergence form using the continuity equation to become:

$$\overline{V' \cdot \mathcal{F}} = - \{ \nabla \cdot \overline{v' K_E} + \frac{\partial}{\partial p} \overline{\omega' K_E} \} \qquad \text{(A.15)}$$

To deal with inter-band energy conversions we go back to the low-pass momentum equations (B.8) and (B.10). We then assume that the overbar represents a low-pass filtering operation and that we may now break any dependent variable $\overline{A}$ into two parts:

$$\overline{A}(x,y,p,t) = \overline{\overline{A}}(x,y,p,t) + \overline{A}'(x,y,p,t) \qquad \text{(A.16)}$$

where $\overline{A}'$ is a "band-pass" anomaly part of A and the double bar represents a seasonal average or another low-pass filtering operation. Following the same procedure as we have used for arriving at the eddy momentum energy equations (A.9) and (A.11) we obtain the equations for the band-pass anomaly velocity fields. In these equations we will now have additional terms which will represent the effect of the high frequency Reynolds stresses on the low frequency part of the field. These terms will be equal to the band pass part of $\overline{\mathcal{F}_\lambda}$ and $\overline{\mathcal{F}_\phi}$ in (A.8) and (A.10). When we form the kinetic energy equations for the band-pass anomaly (which is now $\overline{(u'^2 + v'^2)/2}$), we obtain an equation similar to (A.13) with an extra terms representing the dot product of the high-frequency part of the velocity field and the band-pass part of the Reynolds stress vector . By using the continuity equation these terms can be put into the form:

$$\left\langle \overline{\mathbf{V}}' \cdot \overline{\mathcal{F}_e}' \right\rangle_t = \left\langle -\left\{ \frac{\overline{u}'}{a\cos\phi} \frac{\partial \overline{u'u'}'}{\partial\lambda} + \frac{\overline{u}'}{a} \frac{\partial \overline{u'v'}'}{\partial\phi} + \frac{\overline{v}'}{a\cos\phi} \frac{\partial \overline{u'v'}'}{\partial\lambda} + \frac{\overline{v}'}{a} \frac{\partial \overline{u'v'}'}{\partial\phi} \right.\right.$$

$$\left.\left. + \overline{u}' \frac{\partial \overline{w'u'}'}{\partial p} + v' \frac{\partial \overline{w'v'}'}{\partial p} + \left(\overline{u'v'}'\overline{u}' - \overline{u'u'}'\overline{v}'\right) \frac{\tan\phi}{a} \right\} \right\rangle_t \quad \text{(A.17)}$$

Where we have replaced the double bar by $\langle \rangle_t$ this expression represents the energy lost by the band-pass eddies to the high-pass eddies. Note that the r.h.s. of (A.17) resembles the term representing the time-mean to eddy kinetic energy conversion in the simple case in which the eddies are concentrated in one band only. A similar term to this will appear in the high-frequency kinetic energy equation. Both terms will be exactly equal under area averaging over a closed domain.

b. The temperature variance equation

Here we use the thermodynamic energy equation

$$\frac{\partial T}{\partial t} + \frac{u}{a\cos\phi} \frac{\partial T}{\partial\lambda} + \frac{v}{a} \frac{\partial T}{\partial\Phi} + w \frac{\partial T}{\partial p} = Q + \frac{\kappa}{p} wT \quad \text{(A.18)}$$

where T is the temperature, Q is the heating rate (in deg/sec) and κ is the ratio between the gas constant and the specific heat in constant pressure.

The temperature variance equation is obtained by following a similar procedure to that in the previous section i.e., separating the time-mean and eddy parts of temperature and multiplying the eddy equation by T' thus forming the following equation:

$$\frac{\partial}{\partial t}\left(\frac{1}{2}\overline{T'^2}\right) + \frac{\bar{u}}{a\cos\phi}\frac{\partial(\overline{T'^2})}{\partial\lambda} + \frac{\bar{v}}{a}\frac{\partial(\overline{T'^2})}{\partial\phi} + \bar{\omega}\frac{\partial(\overline{T'^2})}{\partial p}$$

$$= \overline{Q'T'} + \frac{\kappa}{p}\overline{\omega'T'}\,\bar{T} + \frac{\kappa}{p}\bar{\omega}\,\overline{T'^2} + \frac{\kappa}{p}\overline{\omega'T'T'}$$

$$-\left\{\frac{\overline{u'T'}}{a\cos\phi}\frac{\partial\bar{T}}{\partial\lambda} + \frac{\overline{v'T'}}{a}\frac{\partial\bar{T}}{\partial\phi} + \overline{\omega'T'}\frac{\partial\bar{T}}{\partial p}\right\}$$

$$-\left\{\frac{\overline{T'u'}}{a\cos\phi}\frac{\partial T'}{\partial\lambda} + \frac{\overline{T'v'}}{a}\frac{\partial T'}{\partial\phi} + \overline{T'\omega'}\frac{\partial T'}{\partial p}\right\} \qquad \text{(A.19)}$$

The terms in the first parentheses on the r.h.s. represent the conversion from the energy of the time-mean flow, $\bar{T}^2$ to that of the eddies. The terms in the second parentheses on the r.h.s. of (A.19) represent the Reynolds-stress effects on the temperature variance equations and we will symbolize them by $\overline{T'Q'_e}$. Remembering that in the kinetic energy equation a term $-\frac{R}{p}\overline{\omega'T'}$ appeared we can by multiplying (A.19) by $\frac{C_p}{\bar{T}}$, obtain an equation in which a conversion from the energy related to the temperature variance is converted to kinetic energy. This form of (A.19) was used in Chapter 6.

The inter-band conversion terms are found by the same procedure used in the previous chapter, i.e. by breaking the time averages of the dependent variables into two parts. They again acquire a form similar to that of the time-mean to eddy conversion term in (A.19).